COUPLING OF PERIDYNAMICS AND THE FINITE ELEMENT METHOD AND STUDY OF THE DAMPING PROPERTY OF POLYMER COMPOSITES

by

Shank S. Kulkarni

A dissertation submitted to the faculty of
The University of North Carolina at Charlotte
in partial fulfillment of the requirements
for the degree of Doctor of Philosophy in
Mechanical Engineering

Charlotte

2019

Approved by:

Dr. Alireza Tabarraei

Dr. Ronald Smelser

Dr. Harish Cherukuri

Dr. Vincent Ogunro

Dr. Yuri Godin

ABSTRACT

SHANK S. KULKARNI. Coupling of peridynamics and the finite element method and Study of the damping property of polymer composites. (Under the direction of DR. ALIREZA TABARRAEI)

Part - I: Coupling of peridynamics and the finite element method and modeling of creep

One of the important modes of unpredicted failure for large complex structures such as power stations, turbines, processing plants, refineries is a failure due to creep. The ability to predict the evolution of damage due to creep is important. Classical continuum based damage models are used widely for this purpose along with some numerical techniques such as the Finite Element Method (FEM). Although this gives a better prediction of creep strain, when the material is near failure, the finite element method is not easily able to predict crack initiation and propagation. Special care has to be taken for crack propagation such as, re-meshing or use of extended FEM which either lose accuracy or increase the computational cost. These disadvantages can be overcome by using Peridynamics (PD) instead of the finite element method due to its integral formulation and the ability to model the crack as the material response. Therefore one of the aims of this dissertation is to develop a peridynamic formulation equivalent to classical stress-based damage models. We have chosen the Liu-Morakami damage model for our study. In order to check the robustness of the new method, numerous examples are simulated and the results are compared with finite element simulations and show good agreement.

Although peridynamics is a very powerful method in predicting crack propagation, it still has some disadvantages such as very high computational cost and an error in solution near the boundary of the domain. Also, the application of loads and boundary conditions in peridynamics is a tedious process. Therefore, in order to remove these disadvantages, peridynamics can be coupled with the finite element

discretization. The aim is to use PD near crack and the FEM everywhere else. This allows advantage to be taken of both methods giving accurate results with optimum resources. The main challenge in the coupling of peridynamics and the finite element method is a generation of spurious reflections of waves at the interface of peridynamics and the finite element domain. To understand this problem in detail, we use an analytical approach to study the propagation of a plane wave and its spurious reflection in a peridynamic bar using the two different methods. In the first method, a coupled peridynamic–finite element approach is used in which the peridynamic formulation is used in one part of the domain and the finite element is used in the other part. In the second method, the peridynamic formulation is used in the entire domain, but the bar is discretized by two grids of different sizes. In both cases, the size of the grid of each zone does not change and the two grids share one node with each other. The incident wave travels from the finer grid toward the coarser grid. For the case when peridynamics is used on the entire domain, the size of the peridynamics horizon changes based on the size of the gird. For both cases, we investigate the impact of the relative size of the girds on the amplitude and energy of the transmitted and reflected waves. Our analytical and numerical results show that more spurious reflections occur when the size mismatch between the two grids is large. In both cases, the issue of spurious wave reflection becomes more severe when the peridynamic horizon size increases. For the case of a coupled peridynamic–finite element grid, even when the size of the two grids is the same, spurious wave reflection occurs which is due to the change in the formulation from a nonlocal to a local continuum. The spurious reflection reduces when the wavelength of the incident wave is large compared with the coarse grid.

Part - II: Study of the damping property of polymer composites

Visco-elastic materials are used in many applications such as building dampers, bunkers or protective casing for an external hard drive. This is because visco-elastic materials have very good damping capacity and can absorb a huge amount of energy without failure due to their polymeric nature. Polyurea is an example of one such material which is commercially available. Two main problems with the use of such materials are, i) their behavior is very complex and hence it is hard to develop a constitutive model which is simple to use and also accurate, and ii) these materials lack strength and hence need an addition of some fillers in order to provide strength.

In this dissertation, a nonlinear hyper–viscoelastic constitutive model obtained by the superposition of a hyperelastic and a viscoelastic model is proposed to model the behavior of polyurea under both tensile and compressive loading conditions at various strain rates. The incompressible Ogden model is used to model the strain-dependent response of polyurea while a three parameter standard linear solid (SLS) model and nonlinear K-BKZ modes are used to model the strain rate dependent behavior of polyurea. The material parameters of the model are found by curve fitting of the proposed model to the experimental data. Comparison of the proposed model and the experimental data shows that the proposed model can closely reproduce the stress-strain behavior of polyurea under a wide range of strain rates (-6500 to 294 /s).

We also use finite element modeling to investigate the damping property of polymer composites consisting of a viscoelastic matrix and randomly dispersed elastic particles. The dynamic correspondence principle of viscoelasticity is used to solve boundary value problems. The impact of vibration frequency and inclusion size and volume fraction on the damping capability of polymer composites are studied. Results obtained by finite element simulations are compared with results obtained from popular micromechanics methods such as the rules of mixtures, Halpin-Tsai, Hashin-Shtrikman, and Mori-Tanaka. It is shown that micromechanics methods give accurate

predictions only when inclusion volume fraction is small. Our results show that the loading frequency and inclusion volume fraction significantly impact the damping capability of polymer composites. In contrast, the impact of the size of inclusions on the damping properties of polymer composites is negligible. The effect of domain boundary conditions on the simulation results is studied by conducting finite element modeling on representative volume elements (RVEs) which are subjected to periodic or mixed boundary conditions. The modeling results indicate that both boundary conditions lead to similar predictions for damping. Sensitivity analyses are conducted to assess how material properties influence the damping property. The sensitivity analyses show that an increase in the stiffness of the composite matrix leads to a reduction in the damping capability of polymer composites. In contrast, an increase in the stiffness of inclusions results in an increase in the damping capability of polymer composites. Moreover, the damping properties are improved if the relaxation time of the viscoelastic matrix is increased.

ACKNOWLEDGEMENTS

Prof. Alireza Tabarraei,

Dr. Xiaonan Wang,

Prof. Harish Cherukuri,

Prof. Ronald Smelser,

Prof. Vincent Ogunro,

Prof. Yuri Godin,

Prof. Martin Hodgins,

Prof. Tanmay Bhandakkar,

Mech Dept - TA,

Graduate school - GASP,

Graduate school - Fellowship,

Manira, Sujithra, Pedram, Pavitra Varad, Nitesh, Amey, Pratik, Nihar,

Parents and meme Devika.

DEDICATION

to gege and meme...

TABLE OF CONTENTS

LIST OF FIGURES

LIST OF TABLES

LIST OF ABBREVIATIONS

PD Peridynamics

FEM Finite element method

XFEM Extended finite element method

SFEM Stochastic finite element method

SPH Smooth particle hydrodynamics

CT Compact tension

RVE Representative volume element

SLS Standard linear solid

SPUA Spray polyurea elastomer technology

WLF William-Landel-Ferry

RSA Random sequential absorption

MC Monte Carlo

PBC Periodic boundary conditions

SA Sensitivity analysis

LHS Latin hypercube sampling

PI Prediction interval

CI Confidence interval

PMC Polymer Matrix Composites

LIST OF SYMBOLS

α	multi-axiality parameter
$\bar{\mathbf{P}}$	first Piola-Kirchhoff stress tensor
$\boldsymbol{\eta}$	deformed bond vector
$\boldsymbol{B}$	left Cauchy-Green deformation tensor
$\boldsymbol{C}$	right Cauchy-Green deformation tensor
$\boldsymbol{E}$	Green strain tensor
$\boldsymbol{X}$	initial configuration
$\boldsymbol{x}$	current/deformed configuration
$\boldsymbol{\nabla}$	gradient operator
$\boldsymbol{\sigma}$	stress tensor
$\boldsymbol{\xi}$	original bond vector
δ	horizon of point
δ_{ij}	Kronecker delta
Γ_s	traction free boundary
Γ_t	traction prescribed boundary
Γ_u	displacement prescribed boundary
Λ	fictitious damping coefficient
λ_i	principle stretches
$\mathcal{B}$	continuum body

μ	shear modulus
ν	Poisson's ratio
ψ	strain energy density
ρ	mass density
σ_1	maximum principle stress
σ_h	hydrostatic stress
σ_r	rapture stress
σ_{eq}	von Misses stress
θ	volume dilatation
$\underline{\omega}$	influence function
$\underline{\mathbf{T}}$	force state
$\underline{\mathbf{Y}}$	deformation state
$\underline{e}$	extension scalar state
$\underline{e}^d$	deviatoric part of extension state
$\underline{t}$	magnitude of $\underline{\mathbf{T}}$
$\bar{\mathbf{t}}$	traction vector
$\hat{\mathbf{n}}$	unit normal vector
ε^c	creep strain
ε^e	elastic strain
ε^{total}	total strain

$\mathbf{B}$ shape functions derivatives

$\mathbf{b}$ body force per unit mass

$\mathbf{C}^{ep}$ compliance matrix

$\mathbf{F}$ deformation gradient

$\mathbf{f}^{ext}$ external force vector

$\mathbf{f}^{int}$ internal force vector

$\mathbf{I}$ Identity matrix

$\mathbf{K}$ global stiffness matrix

$\mathbf{u}$ displacement field

A cross section area

C_m secondary creep constant in Liu-Morakami model

c_0 micromodulus function

D Damage variable

D^{critical} critical damage

D_m tertary creep constant in Liu-Morakami model

E Young's modulus

f_{broken} fraction representing number of broken bonds

h thickness

H_x neighborhood

K bulk modulus

l	length scale
M_i	Mooney-Rivlin parameters
N	shape function
n_2	secondary creep constant in Liu-Morakami model
p	hydrostatic pressure
p	tertary creep constant in Liu-Morakami model
q	weighted volume
q_2	tertary creep constant in Liu-Morakami model
r_p	spacing between nodes
s	bond stretch
S_{ij}	deviatoric stress
v_{IJ}	volume fraction
W	strain energy function

Part I

Coupling of peridynamics and the finite element method and modeling of creep

CHAPTER 1: INTRODUCTION

1.1 Background and motivation

Creep is one of the important reasons of failure for metal components working at a high temperature such as power plants and turbines. To ensure high efficiency and safety of the working environment, it is extremely important to predict failure due to creep in advance. In order to do so, creep tests are performed on the specimen to understand it's creep properties. The specimen is loaded with a constant tensile load or stress at elevated temperature, and the relation between observed creep strain and time is plotted as a creep curve. In general, the creep curve is divided into three parts namely, primary creep, secondary creep, and tertiary creep. Primary creep will follow the sudden elastic elongation. In this stage, the strain will increase with decelerating strain rate as time increases. Next is secondary creep, which occupies the largest region of the creep curve. In this stage strain increases with an almost constant strain rate obeying the Norton power law. The last stage is a tertiary creep, in this region, strain increases with increasing strain rate finally leading to fracture [5]. Although creep tests provide insight about creep failure, they are costly and time-consuming as creep is slow process. Therefore many researchers focused their efforts on numerical simulations of creep as its cheaper than experiments and saves time. In general, numerical methods to simulate creep failure can be divided into two categories, i. e. i) based on fracture mechanics and ii) based on damage mechanics. Fracture mechanics based methods use parameters such as the stress intensity factor K, J - integral or C^* integral to predict crack growth [6–8]. Whereas, damage mechanics based methods use damage parameter D which varies between 0 (no damage) to 1 (failure) to predict crack growth [9].

Damage based models can be further divided into two types, stress based and strain based. Kachanov-Robotnov model [10, 11] and Liu-Morakami model [12–14] are the most widely used stress based models. These models can predict all three stages of creep with great accuracy but need all parameters to be calibrated experimentally with great care. Also, a large number of parameters have to be used. On the other hand, strain based models use a few number of parameters, but this decreases the accuracy of the model [15–17]. In a stain based model, it is assumed that the damage parameter becomes unity at some critical strain value.

The finite element method (FEM) is the most widely used numerical method to model creep because of its simplicity and commercially available software. Murakami et al. [12, 14, 18] used FEM to simulate crack growth and showed the effect of a local and nonlocal formulation. Also using the Liu-Morakami model along with FEM, Hyde et al. [3, 4, 19–22] simulated a uniaxial creep test and crack propagation in a compact tension (CT) specimen. They also showed that results are in good agreement with experimental data. Simulations were performed on different materials and at different temperatures to ensure the robustness of the model. Simple strain based models were also used along with FEM to simulate creep [23, 24]. Although widely used, FEM performs poorly in predicting the crack speed and growth path [25]. Pandey et al. [26] used the extended finite element method (XFEM) [27] to simulate creep of CT as well as C-shaped tension specimen. Kaupilla et al. [28] developed a continuum damage model for creep from the balance laws and implemented using ANSYS [29].

Some popular methods other than XFEM for accurate modeling of crack propagation are, the cracking particle mesh-free method [30, 31], phantom node method [32], edge based cutting method [33,34], phase field method [35], and peridynamics [36,37]. As peridynamics (PD) has a better ability to model damage, one of the aims of this dissertation is to come up with a peridynamic formulation equivalent to classical stress based damage models for creep. We chose Liu-Morakami model for our study

as it has some advantages over Kachanov-Rabatnov in terms of the selection of the time step for numerical analysis. A comparative study can be found in [38].

Peridynamics theory [36, 37] has been introduced to overcome the difficulties associated with local continuum methods in modeling fracture and damage in materials. Although there are quantum mechanics based methods available such as molecular dynamics [39–42] which gives more accuracy while modeling cracks [43–46], they are much more expensive and hence not able to solve realistic simulation problems. The main issue of using classical continuum theory in modeling crack nucleation and propagation is related to the presence of the spatial derivatives of displacement in the equilibrium equations. Since the displacement field is not continuous across cracks, the derivatives of the displacement field are not defined at these points; hence the equilibrium equations are not described. This issue translates to the computational methods such as a finite element method based on a classical continuum formulation. If the crack path is not known a priori, modeling crack nucleation and propagation using the finite element method requires remeshing [47, 48] which is a cumbersome process and reduces the computational accuracy. Other local based continuum techniques such as extended finite element method (XFEM) [27, 49] have been developed more recently to eliminate the remeshing requirement. However, using XFEM for modeling cases such as fragmentation when several cracks are available in the domain is very challenging. Meshless methods such as the element-free Galerkin method [30, 50], smooth particle hydrodynamics (SPH) [51–53] and reproducing kernel particle methods [54] which construct the approximation fields entirely in terms of nodes are other classes of numerical techniques used to model crack propagation. Such techniques remove the re-meshing requirements and can model the growth of cracks with arbitrary and complex geometries. Peridynamics based meshfree methods have been developed [55, 56] and successfully used to model fracture and damage in various materials and systems. Silling et al. used peridynamics to reproduce Kalthoff-Winkler

experimental results [57] and to model damage due to impact [55, 58]. Gerstle et al. [59] modeled damage in reinforced concrete structures using peridynamics. Xu et al. [60] employed peridynamics to model a crack in laminated composites. Bobaru et al. [61–63] used peridynamics to model dynamic fracture in brittle materials and captured crack branching and kinking in the crack path. Wu and Ren [64] modeled ductile failure during metal machining. Hu et al. [65] used peridynamics to model dynamic fracture in fiber reinforced composites. Amani et al. [66] used peridynamics to model thermoplastic fracture using a Johnson-Cook constitutive model. Ha et al. [67] and Wang et al. [68] have used peridynamics to model fracture in rocks under compressive loading. More recently, multiple groups have used peridynamic to model damage in metals due to the corrosion [69–72]. Peridynamics performance has been validated by applying it to several sophisticated applications including dynamic fracture analysis [73–79], polycrystal fracture [80], membrane fracture [81], fracture of composite materials [82–86], modeling of corrosion damage [87–89], fatigue formulation [90–93], modeling of structural response under extreme loading [94], material fragmentation under impact [95], simulation of the kinetic of phase transformation [96], modeling of geomaterials [97], viscoplasticity [98, 99], thermal diffusion [100], laminated glass beam failure [101] , modeling of metal creep using classical stress based damage models [102], and modeling heat transition in bodies with evolving cracks [66, 103–106]. Hattori et al. [107] developed a framework of peridynamics for anisotropic materials. Zhang et al. [108] increased the horizon of peridynamics theory by developing an axisymmetric ordinary state based peridynamic model for elastic solids. Behzadinasab et al. [109] solved a shock wave perturbation decay problem in granular material using peridynamics. Nguyen et al. [110] used peridynamics so predict the damage in offshore structures.

In addition to the numerical verifications, rigorous mathematical analysis has been used to examine the properties of peridynamics. Silling and Lehoucq [111] showed

that in the limit when the nonlocal region around a point goes to zero, peridynamics converges to classical elasticity theory. Du and Zhou [112] developed a functional analytical framework for peridynamics and demonstrated the connections between peridynamics and classical elastic theory. Alali and Lipton [113] analytically investigated the multiscale dynamics of heterogeneous media using peridyanmic formulation. Mikata [114] studied peristatic and peridynamic problems in a 1D bar. Lindsay et al. [115] came up with a multi-time step model for peridynamics. Kulkarni et al. [116,117] analytically studied wave propagation in peridynamics and also the issue of spurious reflections when coupled with FEM. Mutnuri and Gopalakrishnan [118] studied the wave dispersion between peridynamics and a discrete material in a 1D domain. Madenci et al. [119] proposed a alternative peridynamic formulation based on differential operations.

Although peridynamics can model crack nucleation and propagation effectively; however, due to its nonlocal formulation, it is computationally more expensive than classical continuum mechanics. Two main techniques have been proposed to reduce the computational costs associated with using peridyanmics. In the first approach, peridynamics is coupled with a local method such as a finite element method [120–129]. In this method, peridynamics is used in critical zones such as close to crack tips to model crack propagation and the finite element method is used in the rest of the domain. Since the finite element is used in most of the domain, the computational cost reduces. Moreover, since robust techniques for imposing boundary conditions and modeling contact phenomena using finite element are available, such techniques can be directly employed when a coupled peridynamics and finite element method is used. The main challenge associated with developing coupling techniques is the elimination of the fictitious interface effects. For dynamic problems, the main source of numerical artifacts is the spurious wave reflections at the interface of peridynamics and finite element zones. The main source of spurious wave reflection is due to the change in

the grid size [130] and the change of formulation from local to nonlocal [131–133].

In the second approach, peridynamics is used everywhere in the domain but the size of the peridynamics grid adaptively changes [1, 134, 135]. This approach is similar to the adaptive mesh refinement in finite elements where a finer grid is used in sensitive zones such as the vicinity of defects and coarser grids are used in other regions. By using this approach the total number of nodes in the domain is reduced which leads to a reduction in the computational cost. The change in the grid size which is usually associated with the change in the size of the horizon induces spurious wave reflection at the transition point from the fine to the coarse grid.

Therefore, we study the issue of spurious wave reflection for the above two mentioned approaches using an analytical approach. The main motivation is to provide a better understanding of the concept of wave reflection and to gain insights toward resolving this issue. We study the propagation of a plane wave and investigate how the size of grids and the size of the horizon impact the amplitude of the reflected and transmitted waves. A solution to this issue of spurious reflections is proposed by Wang et al. [136, 137] and proposed solution was incorporated in commercial finite element software [138].

1.2 Original features of dissertation

Formulation of metal creep using state-based peridynamics and studying the problem of spurious wave reflection analytically while coupling PD and FEM are the main contributions of this part of dissertation.

In order to come up with PD formulation for metal creep , we take reference of metal creep formulation using finite element and propose equivalent steps in PD. A new PD formulation is checked by solving numerous examples including a uniaxial tension test, crack propagation under mode I loading and a bending test. All the results are compared with the results from FEM and experiments. Problems are solved by developing proprietary C++ codes.

In an analytical study of spurious wave reflection, the effect of a number of parameters such as mesh size, the wavelength of the wave and size of the horizon is understood. Analytical results were checked with numerical simulations and found in good agreement with each other. The same problem was also studied for nonuniform PD mesh and some interesting results were observed. The analytical solution was obtained by writing code in MATLAB [139].

1.3 Outline of dissertation

The outline of the dissertation is as follows, Chapter 1 provides the background and motivation for the research. Chapter 2 describes the theoretical background of peridynamics, finite element methods, and creep models. Both bond based and state-based PD models are discussed. Next chapter 3 highlights some important peridynamic fundamentals such as dynamic to static conversion, discretization methods, and skin effects. the following chapter 4 starts with the formulation of the creep evaluation using finite elements and progresses towards the formulation of creep evaluation using state-based peridynamics. A new algorithm is given in terms of a flow chart for a better understanding. Finally, the chapter ends with a description of a new influence function which considers damage as well and how the parameters of this influence function can be selected. Chapter 5 shows various examples solved using the proposed method and its comparison to finite element method and experiments. Uniaxial tension under plane strain, 3D uniaxial tension, 2D crack propagation under mode I loading and bending problems are some examples solved.

Then chapter 6 talks about the analytical solution of spurious waves reflected at the interface of PD and FEM while coupling both methods together in order to take advantage of both methods. It starts with the discussion of wave propagation in PD and then showing the actual problem with an example. Results are obtained for uniform as well as nonuniform discretization. Energy flux calculations are also carried out in the same chapter. Chapter 7 deals with the analytical solution for nonuniform

PD meshes coupled together. Results are verified with numerical examples.

Finally, part I of the dissertation concludes in chapter 8 with conclusions from the study. Appendixes are given to further explain some concepts and to give detailed derivations.

CHAPTER 2: THEORETICAL BACKGROUND

2.1 Finite element formulation

The strong form of the boundary value problem for the elastostatic formulation with domain Ω can be given as

$$\boldsymbol{\nabla} \cdot \boldsymbol{\sigma} + \mathbf{b} = 0 \quad \text{in } \Omega, \tag{2.1}$$

where $\boldsymbol{\nabla}$ is the gradient operator, $\boldsymbol{\sigma}$ is the stress tensor, and $\mathbf{b}$ is the body force per unit volume. The boundary conditions can be prescribed as,

$$\boldsymbol{\sigma} \cdot \hat{\mathbf{n}} = \bar{\mathbf{t}} \qquad \text{on} \qquad \Gamma_t, \tag{2.2a}$$

$$\mathbf{u} = \bar{\mathbf{u}} \qquad \text{on} \qquad \Gamma_u, \tag{2.2b}$$

where, $\hat{\mathbf{n}}$ denotes the unit normal vector on the domain boundary, $\mathbf{u}$ is the displacement field, Γ_t is the portion of the boundary with prescribed tractions $\bar{\mathbf{t}}$, and Γ_u is the portion of the boundary with prescribed displacement field as shown in Fig. 2.1.

The weak form is obtained by using the principle of virtual work by assuming the domain undergoes an arbitrary displacement field $\delta\mathbf{u}$ which gives rise to compatible virtual strains $\delta\boldsymbol{\epsilon}$ and can be written as

$$\int_\Omega \boldsymbol{\sigma} : \delta\boldsymbol{\epsilon} d\Omega = \int_\Omega \mathbf{b} \cdot \delta\mathbf{u} d\Omega + \int_{\Gamma_t} \bar{\mathbf{t}} \cdot \delta\mathbf{u} d\Gamma. \tag{2.3}$$

The weak form is discretized in space using the finite element approximation of the

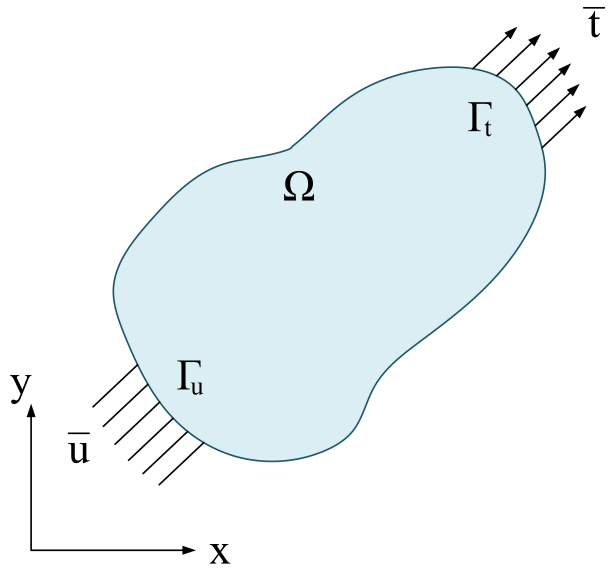

Figure 2.1: Domain Ω under loading and boundary conditions.

displacement field and can be written as

$$\int_{\Omega} \mathbf{B}^T \boldsymbol{\sigma} d\Omega = \int_{\Omega} \mathbf{N}^T \mathbf{b} d\Omega + \int_{\Gamma_t} \mathbf{N}^T \bar{\mathbf{t}} d\Gamma, \tag{2.4}$$

where $\mathbf{N}$ is the matrix of shape functions. By discretizing the domain into finite elements and multiplying the Eq. (2.4) by a weight function $\mathbf{w}$ we get

$$\sum_{e=1}^{n_{el}} \mathbf{w}^{e^T} \left[\int_{\Omega^e} h \mathbf{B}^T \mathbf{C}^{ep} \mathbf{B} d\Omega^e - \int_{\Omega^e} h \mathbf{N}^T \mathbf{b} d\Omega^e + \int_{\Gamma_t^e} h \mathbf{N}^T \bar{\mathbf{t}} d\Gamma_t^e \right] = 0, \tag{2.5}$$

which can also be written as

$$[\mathbf{K}]\{\Delta \mathbf{u}\} = \{\Delta \mathbf{f}\} = \{\mathbf{f}_{ext}\} - \{\mathbf{f}_{int}\}, \tag{2.6}$$

where $\mathbf{K}$ is the global stiffness matrix, $\Delta \mathbf{u}$ is the incremental displacement vector and $\mathbf{f}_{ext}$, $\mathbf{f}_{int}$ are incremental, external and internal force vectors respectively.

For plain stress problem, the stress strain relationship is written as

$$\begin{bmatrix} \sigma_{xx} \\ \sigma_{yy} \\ \sigma_{xy} \end{bmatrix} = \frac{E}{1-\nu^2} \begin{bmatrix} 1 & \nu & 0 \\ \nu & 1 & 0 \\ 0 & 0 & \frac{1-\nu}{2} \end{bmatrix} \begin{bmatrix} \epsilon_{xx} \\ \epsilon_{yy} \\ \epsilon_{xy} \end{bmatrix}, \tag{2.7}$$

and the stiffness matrix and force vector are given by

$$\mathbf{K}^e = \int_{\Omega^e} h\mathbf{B}^T\mathbf{C}^{ep}\mathbf{B}d\Omega^e, \tag{2.8a}$$

$$\mathbf{f}^e_{ext} = \int_{\Omega^e} h\mathbf{N}^T\mathbf{b}d\Omega^e + \int_{\Gamma^e_t} h\mathbf{N}^T\bar{\mathbf{t}}d\Gamma^e_t, \tag{2.8b}$$

where, $\mathbf{B}$ is shape functions derivatives, $\mathbf{C}^{ep}$ is elasticity tensor and h is the thickness.

2.1.1 Finite formulation for a one–dimensional bar

If a one–dimensional domain is discretized with linear finite elements of length h, the equation of motion of node k in the absence of body forces can be written as

$$\rho h\ddot{u}_k = \frac{E}{h}(u_{k+1} - 2u_k + u_{k-1}), \tag{2.9}$$

where E is the Young's modulus and ρ is the mass density.

2.2 Overview of peridynamic theory

An alternative approach to classical continuum mechanics is peridynamic theory [36, 95]. Peridynamics is a nonlocal continuum theory in which a point $\mathbf{x}$ interacts with other points in its vicinity. As shown in the Fig. 2.2, the interaction zone of point $\mathbf{x}$ is its spherical neighborhood $H_x = \{\mathbf{x}' \mid 0 < \|\mathbf{x} - \mathbf{x}'\| \leq \delta\}$, where δ is the horizon of point $\mathbf{x}$. The vector from a point $\mathbf{x}$ to point $\mathbf{x}' \in H_x$ is called a bond defined by $\boldsymbol{\xi} = \mathbf{x}' - \mathbf{x}$ and the bond length is denoted by $\underline{\xi} = |\boldsymbol{\xi}|$.

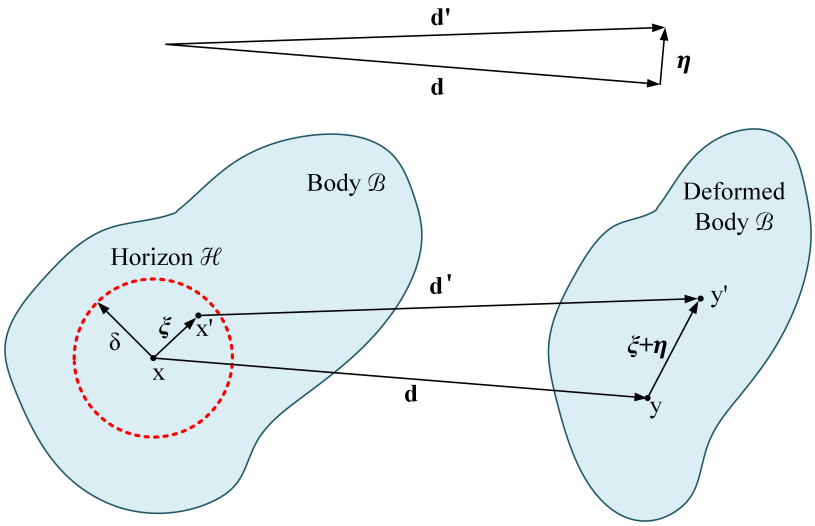

Figure 2.2: A peridynamic domain before and after deformation.

2.2.1 Bond based peridynamics

All material points inside the horizon of some specific material point will exert a certain amount of force on each other, this is equivalent to having a bond between them, hence the name 'Bond based peridynamics'. The total force acting on a material point is the sum of the forces acting on it by all the points within its horizon. In the absence of a body force, the peridynamics equations of motion can be written as [36]

$$\rho \frac{\partial^2 \boldsymbol{u}(\boldsymbol{x}, t)}{\partial t^2} = \int_{\mathcal{H}} \boldsymbol{f}(\boldsymbol{u}(\boldsymbol{x}', t) - \boldsymbol{u}(\boldsymbol{x}, t), \boldsymbol{x}' - \boldsymbol{x}, t) dV_{x'}, \tag{2.10}$$

where $\boldsymbol{x'}$ are position vectors of points within the horizon $\mathcal{H}$ of point $\boldsymbol{x}$, $\boldsymbol{u}$ is the displacement vector, ρ is the mass density and t is time. In Eq. (2.10), $\boldsymbol{f}$ is the pairwise force between point $\boldsymbol{x}$ and $\boldsymbol{x'}$. The value of the force function $\boldsymbol{f}$ depends on the relative position $\boldsymbol{\xi} = \boldsymbol{x'} - \boldsymbol{x}$ of the two interacting material points and their relative displacement $\boldsymbol{\eta} = \boldsymbol{u(x', t)} - \boldsymbol{u(x, t)}$. For a linear elastic material, force

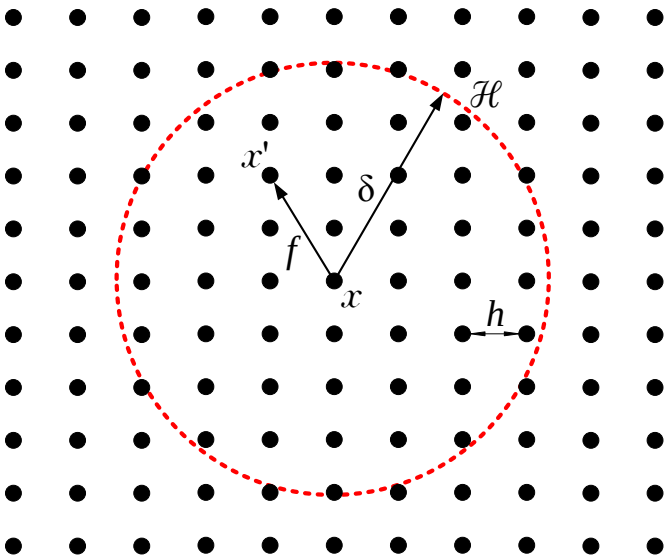

Figure 2.3: Interaction of material points inside the horizon of peridynamic region.

function $\boldsymbol{f}$ can be written as

$$\boldsymbol{f}(\boldsymbol{\xi}, \boldsymbol{\eta}) = \frac{\boldsymbol{\xi} + \boldsymbol{\eta}}{|\boldsymbol{\xi} + \boldsymbol{\eta}|} c_0 s, \tag{2.11}$$

where s is the bond stretch defined as

$$s = \frac{|\boldsymbol{\xi} + \boldsymbol{\eta}| - |\boldsymbol{\xi}|}{|\boldsymbol{\xi}|}, \tag{2.12}$$

and c_0 is known as micromodulus function and represents the bond elastic stiffness. An expression for the micromodulus function c_0 can be found by equating peridynamics elastic energy density with the classical elasticity energy density [57]. Some common forms of micromodulus functions are shown in Fig. 2.4. Details of the derivation of different micromodulus functions can be found in [1].

2.2.1.1 Peridynamic formulation for a one–dimensional bar

For a one–dimensional linear elastic bar, c_0 can be expressed as [1]

$$c_0 = \frac{2E}{\delta^2 A}, \tag{2.13}$$

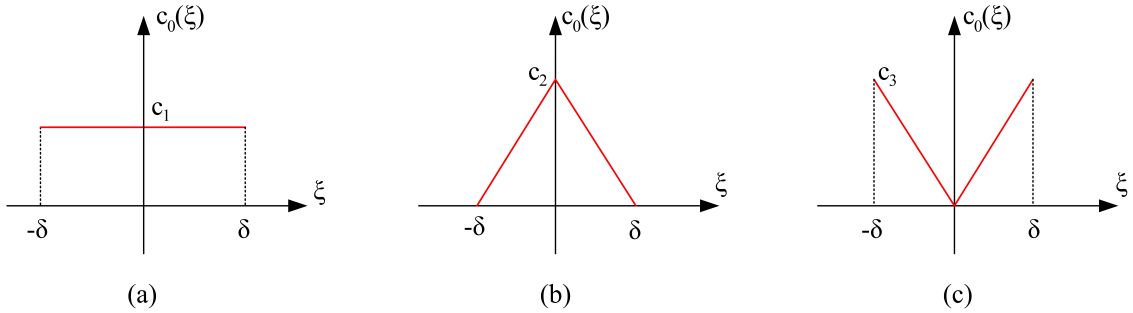

Figure 2.4: Examples of micromodulus functions. (a) constant, (b) triangular and (c) inverted triangular [1].

and the force function can be written as

$$f(\boldsymbol{u}, \boldsymbol{u'}, \boldsymbol{x}, \boldsymbol{x'}) = c_0 \frac{\boldsymbol{u'} - \boldsymbol{u}}{|\boldsymbol{x'} - \boldsymbol{x}|}, \tag{2.14}$$

where E is the Young's modulus, A is the cross sectional area of bar, $\boldsymbol{u'}$ is the displacement of point $\boldsymbol{x'}$ and $\boldsymbol{u}$ is the displacement of point $\boldsymbol{x}$. If the bar is discretized with N nodes, the equation of motion of node k can be obtained by discretizing Eq. (2.10)

$$\rho \ddot{u}_k = \sum_j c_0 \frac{u_j - u_k}{|x_j - x_k|} V_{jk}, \tag{2.15}$$

where V_{jk} is the volume of node j overlapping with the horizon of node k.

2.2.2 State based peridynamics

Previously explained bond based PD suffered from the following difficulties [37]:

1. Deformation of any single bond from one particular point, is always independent of deformation of all other bonds connected to the same point. This resulted in an equivalent Poisson's ratio of 0.25. Materials with different Poisson's ratio can not be modeled.

2. Already available classical continuum mechanics models can not be used directly in the peridynamic realm.

3. Material can undergo permanent deformation undergoing volumetric strain. This is inconsistent with experimental observation which says, material can not undergo plastic deformation without shear loading.

In order to remove these above mentioned limitations of PD theory, in 2007 Silling et al. proposed a new formulation of PD, and they named it, 'State based peridynamics.' This new formulation overcame all the limitations of bond based PD.

2.2.2.1 Definition of state

In this formulation a "State" is defined as, a function which when operated on by a vector, creates an unique image of that vector which gives a tensor whose order is equal to the order of the state. A state of order 1 is called as vector state and state of order 0 is called as scaler state. This operation can be written as $\underline{\mathbf{Y}}\langle\boldsymbol{\xi}\rangle$, which means state $\underline{\mathbf{Y}}$ is operating on vector $\boldsymbol{\xi}$. A state is not necessarily continuous or a linear function. Details of the operations of states such as addition, multiplication, derivatives etc. can be found in [37].

2.2.2.2 Deformation state

The deformation state of a bond $\boldsymbol{\xi}$ at time t is defined as

$$\underline{\mathbf{Y}}[\mathbf{x},t]\langle\boldsymbol{\xi}\rangle = \mathbf{y}(\mathbf{x}+\boldsymbol{\xi},t) - \mathbf{y}(\mathbf{x},t), \tag{2.16}$$

where

$$\mathbf{y}(\mathbf{x},t) = \mathbf{x} + \mathbf{u}(\mathbf{x},t), \tag{2.17}$$

and $\mathbf{u}$ is the displacement vector field. $\underline{\mathbf{Y}}[\mathbf{x},t]$ acts on bond $\boldsymbol{\xi}$ and produces the image of the bond under a deformation. The extension scalar state $\underline{e}$ measures the change in the bond length due to deformation

$$\underline{e} = \underline{y} - \underline{x} = |\boldsymbol{\eta}|, \qquad \underline{y} = |\mathbf{y}' - \mathbf{y}| = |\boldsymbol{\xi}+\boldsymbol{\eta}|, \qquad \underline{x} = |\boldsymbol{\xi}|. \tag{2.18}$$

The volume dilatation θ at point $\mathbf{x}$ is obtained from

$$\theta(\underline{e}) = \frac{3}{q}(\underline{\omega x}) \bullet \underline{e} = \frac{3}{q}\int_{H_x} \underline{\omega x}\underline{y} dV_{\mathbf{x}'} - 3, \tag{2.19}$$

where q is the weighted volume defined by

$$q = (\underline{\omega x}) \bullet \underline{x} = \int_{H_x} \underline{\omega x}^2 dV_{\mathbf{x}'}, \tag{2.20}$$

where H_x denotes the horizon of point $\mathbf{x}$ and $\underline{\omega}$ is the influence function which depends on $|\boldsymbol{\xi}|$, $\underline{\omega} = 1$ for an unbroken bond and $\underline{\omega} = 0$ for a broken bond. The $\bullet$ operator denotes the inner product between two states and is defined in [37].

The deviatoric part $\underline{e}^d$ of extension state $\underline{e}$ is defined by

$$\underline{e}^d = \underline{e} - \frac{\theta \underline{x}}{3}. \tag{2.21}$$

2.2.2.3 Equations of motion and numerical discretization

The peridynamic equation of motion of point $\mathbf{x}$ is

$$\rho(\mathbf{x})\ddot{\mathbf{u}}(\mathbf{x},t) = \int_{H_x} (\underline{\mathbf{T}}[\mathbf{x},t]\,\langle \mathbf{x}' - \mathbf{x}\rangle - \underline{\mathbf{T}}[\mathbf{x}',t]\,\langle \mathbf{x} - \mathbf{x}'\rangle) dV_{\mathbf{x}'} + \mathbf{b}(\mathbf{x},t) = \mathbf{f}_p^{\text{int}}(\mathbf{x},t) + \mathbf{b}(\mathbf{x},t), \tag{2.22}$$

where $\underline{\mathbf{T}}$ is the force state. The force state $\underline{\mathbf{T}}[(\mathbf{x},t)]$ takes the bonds connected to point $\mathbf{x}$ as input and produces a force density vector as the output. Since $\underline{\mathbf{T}}$ acts on a vector and produce a vector, $\underline{\mathbf{T}}$ is similar to a tensor with the difference that $\underline{\mathbf{T}}$ is not necessarily linear or continuous. $\mathbf{f}_p^{\text{int}}(\mathbf{x},t)$ is the equivalent of the classical internal force acting at point $\mathbf{x}$.

Numerical implementation of the peridynamic continuum model requires the discretization of the domain. The most common discretization scheme employed in peridynamics is the meshfree method proposed in [95]. As opposed to the finite el-

ement discretization, in the mesh free method the domain is discretized by nodes instead of elements. In a meshfree discretization nodes are not connected to each other by elements or any other geometrical constraints. The discretized form of the peridynamic equations of motion of node I is

$$\begin{aligned}\rho(\mathbf{x}_I)\ddot{\mathbf{u}}(\mathbf{x}_I,t) &= \sum_{J=1}^{L}(\underline{\mathbf{T}}[\mathbf{x}_I,t]\,\langle\mathbf{x}_J-\mathbf{x}_I\rangle - \underline{\mathbf{T}}[\mathbf{x}_J,t]\,\langle\mathbf{x}_I-\mathbf{x}_J\rangle)V_{cJ} + \mathbf{b}(\mathbf{x}_I,t)\\ &= \left(\mathbf{f}_I^{\text{int}}\right)_p(t) + \mathbf{b}(\mathbf{x}_I,t),\end{aligned} \tag{2.23}$$

where $\mathbf{x}_I$ denotes a peridynamic discrete node, $\mathbf{x}_J$ is a node whose volume overlaps with the horizon of $\mathbf{x}_I$ and L is the total number of nodes whose volume overlaps with the horizon of $\mathbf{x}_I$. V_{cJ} is the portion of volume of $\mathbf{x}_J$ which in the initial configuration is within the horizon of $\mathbf{x}_I$, as shown in Fig. 2.5a. V_{cJ} can be given as $V_{cJ} = v_{IJ}V_J$, where V_J is the volume of $\mathbf{x}_J$ in the initial configuration and v_{IJ} is the volume fraction given by

$$v_{IJ} = \begin{cases} 1 & \text{if} \quad |\mathbf{x}_J-\mathbf{x}_I| \le \delta - \frac{r_p}{2}, \\ \frac{1}{2} + \frac{\delta - |\mathbf{x}_J-\mathbf{x}_I|}{r_p} & \text{if} \quad \delta - \frac{r_p}{2} < |\mathbf{x}_J-\mathbf{x}_I| < \delta + \frac{r_p}{2}, \\ 0 & \text{if} \quad |\mathbf{x}_J-\mathbf{x}_I| \ge \delta + \frac{r_p}{2}, \end{cases} \tag{2.24}$$

where r_p represents the spacing between nodes. As shown in Fig. 2.5, the volume fraction v_{IJ} continuously reduces from 1 to 0. The discretized equations of motion can be integrated in time using an explicit time integration scheme such as the velocity Verlet method.

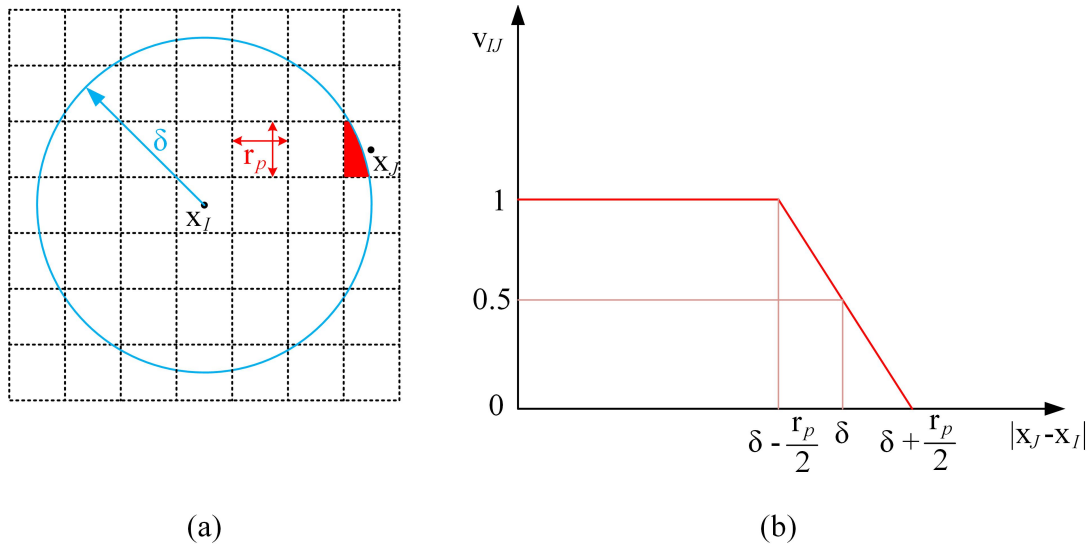

Figure 2.5: (a) Discretization of domain in to PD points (only partial volume of point $\mathbf{x}_J$ is inside horizon of point $\mathbf{x}_I$), (b) v_{IJ} as a function of distance.

2.2.2.4 Linear elasticity using peridynamic formulation

For elastic materials $\underline{\mathbf{T}}$ only depends on $\underline{\mathbf{Y}}([\mathbf{x}, t])$ and can be obtained from the strain energy density function $\psi^{PD}(\underline{\mathbf{Y}})$ given by

$$\underline{\mathbf{T}}(\underline{\mathbf{Y}}) = \nabla \psi^{PD}(\underline{\mathbf{Y}}), \tag{2.25}$$

where ∇ denotes the Fréchet derivative with respect to $\underline{\mathbf{Y}}$. The strain energy density function of a linear elastic material is

$$\psi^{PD}(\theta, \underline{e}^d) = \frac{K\theta^2}{2} + \frac{15\mu}{2q}(\underline{\omega e}^d) \bullet \underline{e}^d, \tag{2.26}$$

where K and μ are respectively the bulk modulus and shear modulus of the material.

Elastic materials can be represented in peridynamics using an ordinary model. In an ordinary model, $\underline{\mathbf{T}} = \underline{t}\mathbf{M}$, where $\mathbf{M}$ is the unit vector along the deformed bond direction and $\underline{t}$ is the magnitude of $\underline{\mathbf{T}}$. Using Eq. (2.26) in Eq. (2.25) the magnitude

of the force state vector acting along the deformed bond direction is

$$\underline{t} = \frac{3K\theta}{q}\underline{\omega x} + \frac{15\mu}{q}\underline{\omega e}^{d}. \tag{2.27}$$

2.2.2.5 Plane stress peridynamic

The volume dilatation in a plane stress state is [140]

$$\theta = \frac{2(2\nu-1)}{(\nu-1)}\frac{\underline{\omega x} \bullet \underline{e}}{q}, \tag{2.28}$$

and the force state is [140]

$$\underline{t} = \frac{2(2\nu-1)}{(\nu-1)}\left(k'\theta - \frac{\beta}{3}(\underline{\omega e}^{d}) \bullet \underline{x}\right)\frac{\underline{\omega x}}{q} + \beta\underline{\omega e}^{d}, \tag{2.29}$$

where

$$\beta = \frac{8\mu}{q}, \tag{2.30a}$$

$$k^{'} = k + \frac{\mu}{9}\frac{(\nu+1)^2}{(\nu-1)^2}. \tag{2.30b}$$

2.3 Elastic creep analysis

Creep is permanent deformation of material operating at elevated temperature whose stress is below the yield stress. In general, the creep curve is divided in three parts namely, primary creep, secondary creep and tertiary creep as shown in Fig. 2.6. Primary creep will follow the sudden elastic elongation. In this stage strain will increase with decelerating strain rate as time increases. Next is secondary creep, which occupies the largest region of the creep curve. In this stage, strain increases with almost constant strain rate obeying a Norton power law. The last stage is

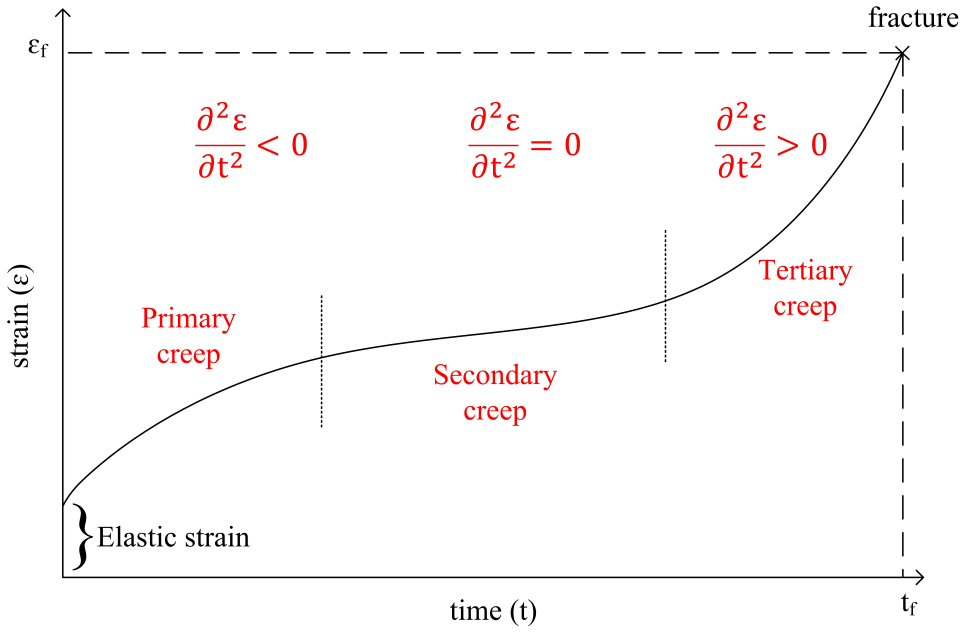

Figure 2.6: Creep strain curve and various stages of creep.

tertiary creep, in this region strain increases with increasing strain rate finally leading to fracture. Creep strain is highly dependent on temperature and applied loading. As temperature increases, creep strain increases and as applied load increases, the creep strain increases as shown in Fig. 2.7. For small strain problems, the total strain is assumed to be divided into two parts, namely elastic strain ε^e and creep strain ε^c as,

$$\varepsilon^{total} = \varepsilon^e + \varepsilon^c. \tag{2.31}$$

Elastic strain is related to stress as,

$$\varepsilon^e = (\mathbf{C}^{ep})^{-1}\sigma, \tag{2.32}$$

whereas, creep strain is related to stress by the Liu-Morakami creep damage model given in following section.

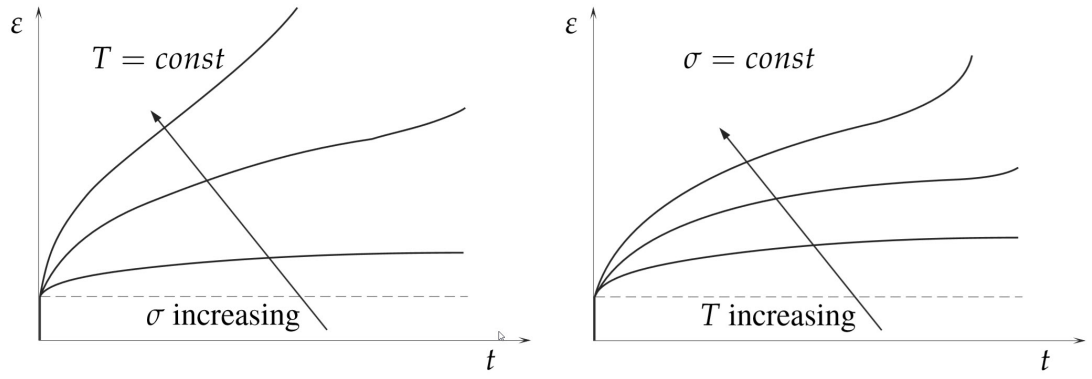

Figure 2.7: Creep strain curve for (a) various stress with constant temperature and (b) various temperatures with stress constant [2].

2.3.1 Liu-Morakami creep damage model

Creep strain rate in the multiaxial form using the Liu-Morakami model can be given as,

$$\dot{\varepsilon}^{c}_{ij} = \frac{3}{2} C_m \sigma^{n2}_{eq} \frac{S_{ij}}{\sigma_{eq}} \exp\left(\frac{2(n_2+1)}{\pi\sqrt{1+3/n_2}} \left(\frac{\sigma_1}{\sigma_{eq}}\right) \cdot D^{\frac{3}{2}} \right), \tag{2.33}$$

where, C_m and n_2 are material constant. $\dot{\varepsilon}^{c}_{ij}$,$\sigma_{eq}$, S_{ij} and σ_1 are creep strain rate, von Misses stress, deviatoric stress and maximum principle stress respectively. Deviatoric stress S_{ij} can be given as,

$$S_{ij} = \sigma_{ij} - \frac{1}{3}\delta_{ij}\sigma_{kk}, \tag{2.34}$$

where, δ_{ij} is Kronecker delta defined as,

$$\delta_{ij} = \begin{cases} 1 & \text{if} \quad i = j, \\ 0 & \text{if} \quad i \neq j, \end{cases} \tag{2.35}$$

and $\sigma_{kk} = 3\sigma_h$, where σ_h is hydrostatic stress, defined as:

$$\sigma_h = \frac{\sigma_{11} + \sigma_{22} + \sigma_{33}}{3}. \tag{2.36}$$

The damage variable D is evaluated by the equation,

$$\dot{D} = D_m \frac{(1 - e^{-q_2})}{q_2} \sigma_r^p e^{q_2 D}, \tag{2.37}$$

where, D_m, q_2, and p are material constants. σ_r is the rapture stress, which can be given as,

$$\sigma_r = \alpha\sigma_1 + (1 - \alpha)\sigma_{eq}, \tag{2.38}$$

where, α is the multi-axiality parameter. For a uniaxial condition α is zero.

2.3.1.1 Calculation of creep parameters

The Liu- Morakami model consists of a total of six parameters (C_m, n_2,D_m, q_2, p, and α) which have to be found by careful testing of a specimen under creep. The procedure to find these parameters can be given in brief as follows [3].

1. Uniaxial material constants: C_m, n_2,D_m, q_2, and p can be found using uniaxial tension tests of a creep specimen.

   (a) C_m and n_2: These constants represents secondary creep behavior and hence can be obtained by approximating the initial creep response as

   $$\dot{\varepsilon}^c = C_m \sigma^{n_2}. \tag{2.39}$$

   By taking log of both sides, we get,

   $$\log(\dot{\varepsilon}^c) = n_2 \log(\sigma) + \log(C_m). \tag{2.40}$$

   By curve fitting a straight line through the creep data, C_m and n_2 can be obtained as shown in Fig. 2.8.

(b) D_m, and p: In order to find these constants, we can rewrite Eq. (2.37) as,

$$\frac{dD}{e^{q_2 D}} = Q dt, \tag{2.41}$$

where $Q = D_m \frac{(1-e^{-q_2})}{q_2} \sigma^p = constant$. Now integrating Eq. (2.41) for limits of 0 to 1 for D and 0 to total time to failure t_{tf} for time gives us,

$$\int_0^1 e^{-q_2 D} dD = Q \int_0^{t_{tf}} dt. \tag{2.42}$$

After simplifying Eq. (2.42) with substitution of Q, we get

$$t_{tf} = \frac{\sigma^{-p}}{D_m}. \tag{2.43}$$

Taking the log of both sides of Eq. (2.43), we get

$$\log(t_{tf}) = -p\log(\sigma) + \log(\frac{1}{D_m}). \tag{2.44}$$

By curve fitting a straight line through the creep data, p and D_m can be obtained as shown in Fig. 2.9.

(c) q_2: After calculation of first four constants using the above mentioned process, we know all other constants required for uniaxial creep curve apart from q_2. Therefore q_2 can be easily found by curve fitting Eq. (2.33) in data of ε^c vs time.

2. Multi axial material constant α: The most commonly used method to calculate α involves creep testing on a notched specimen. The creep test is carried out to find the total time to failure t_{tf}. Using Eq. (2.37) , the total time to failure can be written as,

$$t_{tf} = \frac{1}{D_m(\alpha\sigma_1 + (1-\alpha)\sigma_{eq})^p}. \tag{2.45}$$

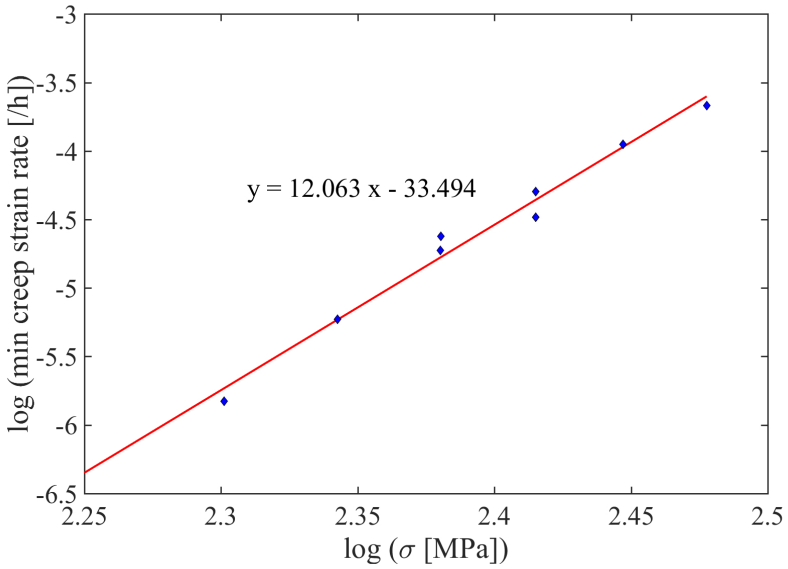

Figure 2.8: Example of creep plot to calculate creep constants C_m and n_2 [3].

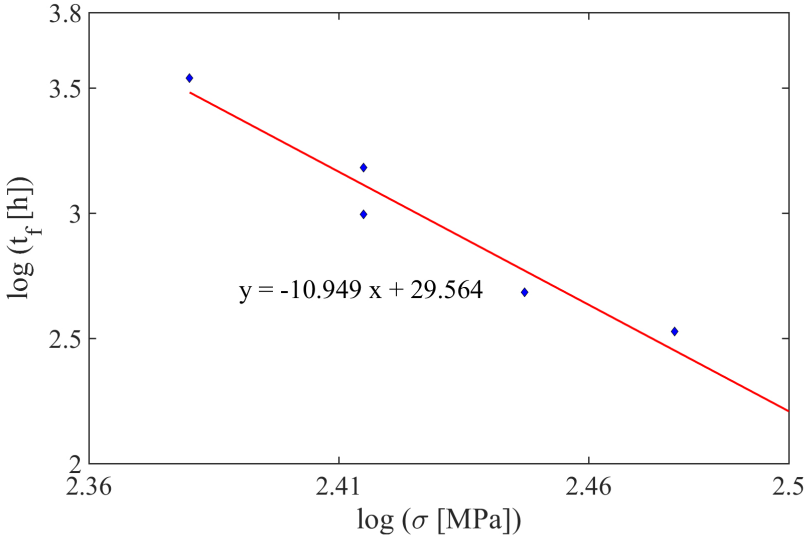

Figure 2.9: Example of creep plot to calculate creep constants D_m, and p [3].

Then multiple finite element simulations can be carried out with different values of α and total time to failure t_{tf} can be calculated. The value of α that will be selected whose t_{tf} value match the value from Eq. (2.45).

CHAPTER 3: PERIDYNAMIC FUNDAMENTALS

In this chapter we will discuss some important peridynamic fundamentals that we will need for creep formulation.

3.1 Dynamic to Static conversion

The peridynamic formulation is by itself a dynamic formulation. Therefore in order to solve a static problems with a peridynamic formulation some special attention has to be paid. Few of the most used methods to convert a dynamic formulation into a static formulation are described in brief below.

3.1.1 Stability estimation/ Averaging method

Numerical results obtained from a peridynamic equation will fluctuate across some value due to it's dynamic nature. In order to find stable values of coordinates, the average is considered of the maximum and minimum values. This is the simplest way to obtain a steady state value. This method is introduced in [141, 142] and used for peridynamics problem successfully in [143, 144]. This method works perfectly when the fluctuation frequency is very high but, when the fluctuation frequency is low this method is no longer accurate due to the long wavelength.

3.1.2 Energy minimization method

Another method is based on the total potential energy of a system. At steady state, the total force acting on each PD node must be equal to zero. At this point the total potential energy of the system is minimum. This can be achieved by an iterative minimization method based on the conjugate gradient method [145]. This method is used in the peridynamic realm by Le et al. [140].

3.1.3 Dynamic relaxation method

The dynamic relaxation method was introduced long ago to solve static non-linear problems [146, 147]. This method is based on the fact that, the steady state solution of the transient solution is static part. In order to do so a fictitious damping term will be added in the equation of motion along with fictitious density as [148, 149],

$$\rho(\mathbf{x})\ddot{\mathbf{u}}(\mathbf{x},t) + \Lambda\rho(\mathbf{x})\dot{\mathbf{u}}(\mathbf{x},t) = \mathbf{f}_p^{\text{int}}(\mathbf{x},t) + \mathbf{b}(\mathbf{x},t), \tag{3.1}$$

where, Λ is the value of fictitious damping coefficient. Selection of this fictitious damping coefficient was not always an easy choice as it will also affect the convergence speed. Large value can leave the system over damped or a small value can take many iterations to converge. This method was used in the peridynamics area by Rabczuk et al. [150] to simulate quasi-static fracture in rocks.

3.1.4 Adaptive dynamic relaxation method

To improve the convergence, the concept of adaptive dynamic relaxation was introduced in which a damping coefficient changes for every iteration [151, 152]. This method was introduced in peridynamics formulation by Kilic et al. [153, 154]. The effectiveness of this method was demonstrated by solving static problems involving structural components under tensile and bending loadings and comparing the results with finite element results [154]. Later many other researchers used this approach to solve different peridynamics problems such as, brittle fracture [155].

3.2 Discretization method

In peridynamics, a homogeneous domain is discretized in a finite number of material points with finite volume. Many different discretization methods were used in the past [95, 156], but most commonly the domain will be divided with a square grid in the case of 2D and a cubical grid in the case of 3D. There are two ways of discretizing

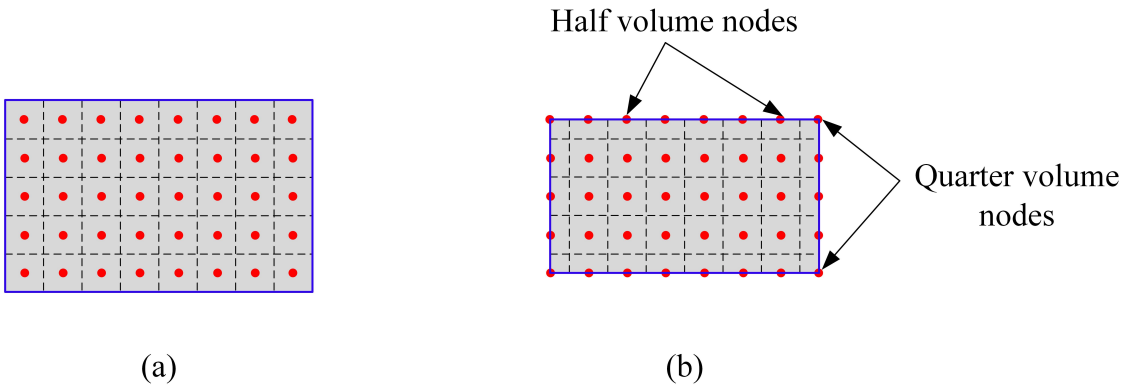

Figure 3.1: Two ways of discretization of PD domain. (a) Cell edges on the domain boundary, (b) nodes on the domain boundary

the domain boundary. Consider a simple example of the rectangular domain as shown in Fig. 3.1. The solid blue line represents a domain boundary and the dotted black lines are cell boundaries. As shown in the figure, the two ways are:

1. Align the boundary of a cell to a domain boundary. In this case there will not be any nodes on the actual domain boundary, but all nodes will have the same volume. The main disadvantage of this way is that the applied boundary conditions will be applied to nodes somewhat inside boundary as there are no nodes on the boundary. This causes an increase in the error of the solution.

2. Align the nodes to the domain boundary. In this case, nodes on the edge will have a half volume and corner nodes will have a quarter volume.

In this study, we chose the discretization shown in Fig. 3.1 b.

3.3 Skin effect

Possession of the full neighborhood for any PD node is extremely important for accurate results as PD parameters such as the deformation state in the case of the state based PD or micro-modulus function in the case of the bond based PD are calculated assuming a node has a complete neighborhood volume. The elastic strain energy density matches with the elastic strain energy density from the classical elasticity model.

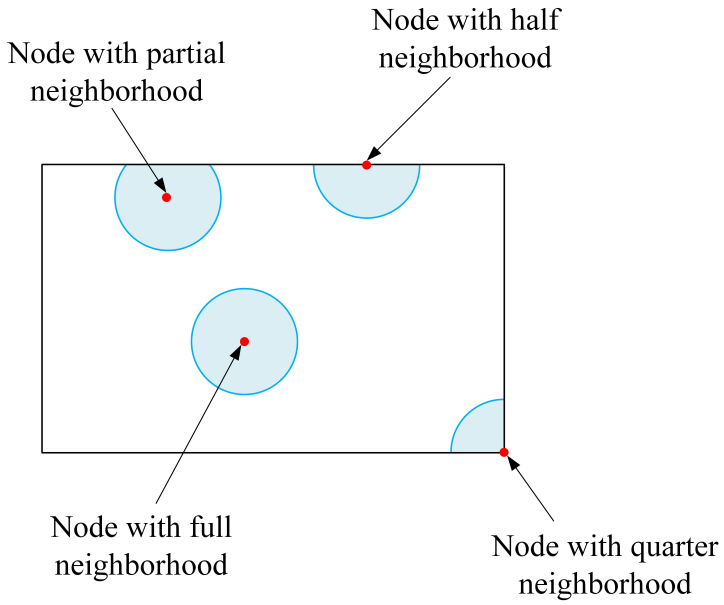

Figure 3.2: Partial neighborhood of PD nodes near the domain boundary.

Due to this solutions obtained using PD matches with the classical continuum mechanics solutions for homogeneous deformations. But as shown in Fig. 3.2, nodes near the domain boundary do not have a full neighborhood. Because of this nodes near the domain boundary will result in slightly different behavior from the nodes inside the bulk. This is called a "skin effect" or "surface effect". As nodes get closer to the domain boundary, their neighborhood starts to decrease and becomes half for nodes laying exactly on boundary. Corner nodes will have only quarter neighborhood making them the least accurate nodes.

Many methods have been proposed in the literature to reduce this skin effect [157–160]. A few of them are as follows:

1. The volume method: In this method the micromodulus value for nodes near the boundary is increased in a such a way that boundary node has the same strain energy density as an inner point.

2. The force density method: This is similar to the volume method. Micromodules for a boundary node is multiplied with the multiplication parameter such that

the materials behave as in the bulk.

3. The energy method: In this method, the strain energy density of the boundary nodes is adjusted to match the inner nodes.

4. Fictitious node method: In this method, the ghost or dummy nodes are added on the outside of the boundary till all the actual nodes have full neighborhood. This is a very effective method which reduces error due to the skin effect to be almost negligible.

In this study we will use the 'fictitious node method' as this one is the most efficient in reducing error in stress calculations. Details of all methods can be found in [160], which reviews and compare all the methods.

CHAPTER 4: NUMERICAL IMPLEMENTATION

The concept of peridynamic constitutive correspondence was introduced in [37] to take advantage of the large number of constitutive models which are already available in classical continuum mechanics. For a peridynamic material model to be equivalent to a classical material model, the strain energy density of both models should match each other under the same deformations.

In the PD formulation, the deformation gradient can be approximated by

$$\mathbf{F} = \left[\int_H \underline{\omega}(\mathbf{Y}\langle\xi\rangle \otimes \xi) dV_\xi\right]\mathbf{K}^{-1}, \tag{4.1}$$

where, $\underline{\omega}$ is the influence function and $\mathbf{K}$ is the shape tensor given by

$$\mathbf{K} = \int_H \underline{\omega}(\xi \otimes \xi) dV_\xi. \tag{4.2}$$

The force state using this correspondence principal is obtained by

$$\underline{\mathbf{T}}\langle\xi\rangle = \underline{\omega}\mathbf{P}\mathbf{K}^{-1}\xi, \tag{4.3}$$

where, $\mathbf{P}$ is the first Piola-Kirchhoff stress tensor. The correspondence principle is used to incorporate many classical continuum mechanics models in peridynamics such as rate dependent plasticity or viscoelasticity [98]. Many attempts have been made to incorporate other classical damage models in PD like the Johnson-Cook damage model [66, 161]. The general framework of incorporating any classical damage model into PD is discussed in [162]. In this study we will use this correspondence principle to incorporate the classical creep damage model in the PD.

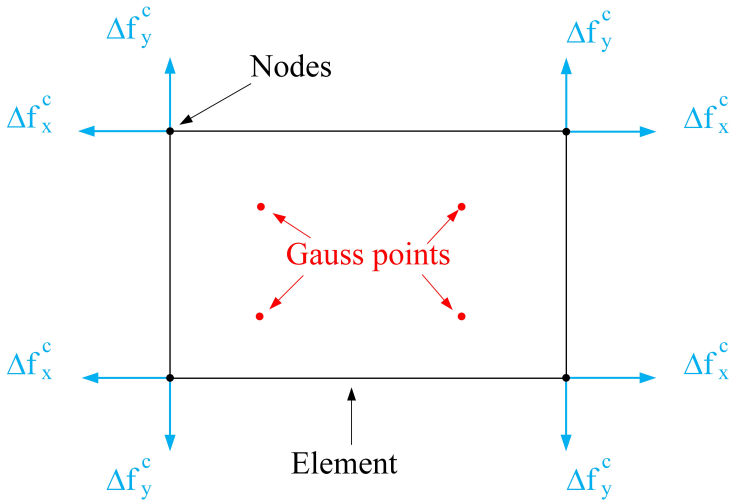

Figure 4.1: Application of incremental creep force on all points in the neighborhood of PD node.

A forward Euler time integration scheme is used for calculation of the damage parameter and creep strain.

4.1 Creep evaluation in finite element methods

The iterative scheme for creep growth using the finite element method is as follows,

1. Discretize the domain in uniform mesh, at time $t = 0$, initialize the damage variable $D = 0$ at all Gauss points in all elements.

2. Carry out elastic-static analysis to find the displacement field $\mathbf{u}$

   (a) Calculate the element stiffness matrix and element force matrix

   (b) Assemble the element matrices to obtain the global stiffness $[\mathbf{K}]_{global}$ and the force $\{\mathbf{f}\}_{global}$ matrices.

   (c) Apply the appropriate boundary conditions.

   (d) Calculate the displacement at each node using,

$$[\mathbf{K}]_{global}\{\mathbf{d}\} = \{\mathbf{f}\}_{global}. \tag{4.4}$$

3. Calculate the stress and strain at each Gauss point in all elements.

4. For creep analysis, the time increment Δt is decided.

   (a) Evaluate σ_1 , σ_{eq} and σ_r at each Gauss point.

   (b) Calculate the damaged $\mathbf{C}^{ep}$ as $(\mathbf{C}^{ep})_{damage} = (1 - D)\mathbf{C}^{ep}$.

   (c) Using the Liu-Morakami model, compute the damage rate $\dot{D}$, calculate the incremental damage variable and update as

$$(\Delta D)^t = \Delta t(\dot{D}) \qquad \text{and} \qquad (D)^{t+\Delta t} = (D)^t + (\Delta D)^t. \tag{4.5}$$

   (d) Compute the creep strain rate $\dot{\epsilon}^c$ and calculate the increment in creep strain and update as

$$(\Delta \epsilon^c)^t = \Delta t(\dot{\epsilon^c}) \qquad \text{and} \qquad (\epsilon^c)^{t+\Delta t} = (\epsilon^c)^t + (\Delta \epsilon^c)^t. \tag{4.6}$$

   (e) Evaluate the force vector due to incremental creep strain as

$$(\Delta \mathbf{f}^c)^t = \int_\Omega \mathbf{B}^T (\mathbf{C}^{ep})_{damage} \Delta \epsilon^c d\Omega, \tag{4.7}$$

   and calculate global the force matrix accordingly as shown in Fig. 4.1.

   (f) Calculate the change in the displacement due to the creep force.

   (g) Update the time to $t = t + \Delta t$ and repeat step 4 till the final time is achieved.

4.2 Creep evaluation in peridynamics

The iterative scheme for creep growth using peridynamics is as follows,

1. Discretize the domain, at time $t = 0$, initialize the damage variable $D = 0$ at all PD nodes and calculate the shape tensor $\mathbf{K}$ using Eq. (4.2) for each node.

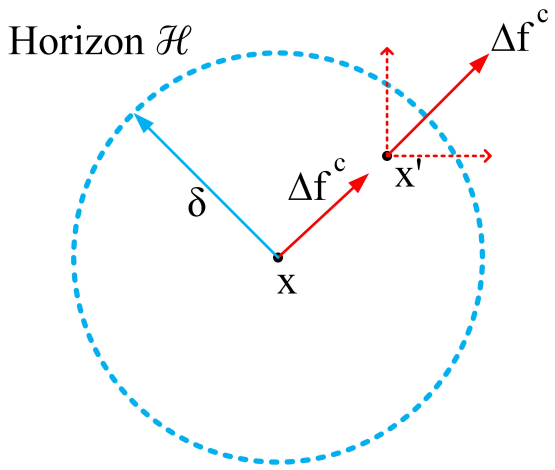

Figure 4.2: Application of incremental creep force on all points in the neighborhood of PD node.

2. Apply the appropriate boundary conditions and loads. (If necessary convert surface loading into body force and apply on several layers of nodes.)

3. Carry out the elastic-static analysis by incorporation of the damping term into the equation of motion of each node as

$$\rho(\mathbf{x})\ddot{\mathbf{u}}(\mathbf{x},t) + \Lambda\rho(\mathbf{x})\dot{\mathbf{d}}(\mathbf{x},t) = \mathbf{f}_p^{\text{int}}(\mathbf{x},t) + \mathbf{b}(\mathbf{x},t), \tag{4.8}$$

where Λ is the damping coefficient selected based on experience.

4. The equation of motion is to be solved using the velocity Verlet method until a steady state solution is reached.

5. Calculate the stress at each node using the approximate deformation gradient as

$$\sigma = \mathbf{C}^{ep}\epsilon, \tag{4.9}$$

where $\mathbf{C}^{ep}$ is known from the material properties and ϵ can be given as

$$\epsilon = \frac{1}{2}(\mathbf{F}^T + \mathbf{F}) - \mathbf{I}, \tag{4.10}$$

where $\mathbf{F}$ is given by Eq. (4.1).

6. For creep analysis, the time increment Δt is decided.

   (a) Evaluate σ_1 , σ_{eq} and σ_r at each PD node.

   (b) Calculate the damaged $\mathbf{C}^{ep}$ as $(\mathbf{C}^{ep})_{damage} = (1 - D)\mathbf{C}^{ep}$.

   (c) Using the Liu-Morakami model, compute the damage rate $\dot{D}$, calculate the incremental damage variable and update as

$$(\Delta D)^t = \Delta t(\dot{D}) \qquad \text{and} \qquad (D)^{t+\Delta t} = (D)^t + (\Delta D)^t. \tag{4.11}$$

   (d) Similar to the step above, compute the creep strain rate $\dot{\epsilon^c}$, calculate the incremental creep strain and update as

$$(\Delta \epsilon^c)^t = \Delta t(\dot{\epsilon^c}) \qquad \text{and} \qquad (\epsilon^c)^{t+\Delta t} = (\epsilon^c)^t + (\Delta \epsilon^c)^t. \tag{4.12}$$

   (e) Evaluate the force vector because of the incremental creep strain as

$$(\Delta \mathbf{f}^c)^t = \underline{\omega}(\mathbf{C}^{ep})_{damage}(\Delta \epsilon^c)^t \mathbf{K}^{-1}\xi, \tag{4.13}$$

   and apply those forces as the body force at corresponding nodes as shown in Fig. 4.2.

   (f) Evaluate the updated displacement by solving the equation of motions for each PD node until a new steady state is achieved.

   (g) Update the time as $t = t + \Delta t$ and repeat step 6 until the final time is achieved.

The same steps can be given in the form of flow chart as shown in Fig. 4.3.

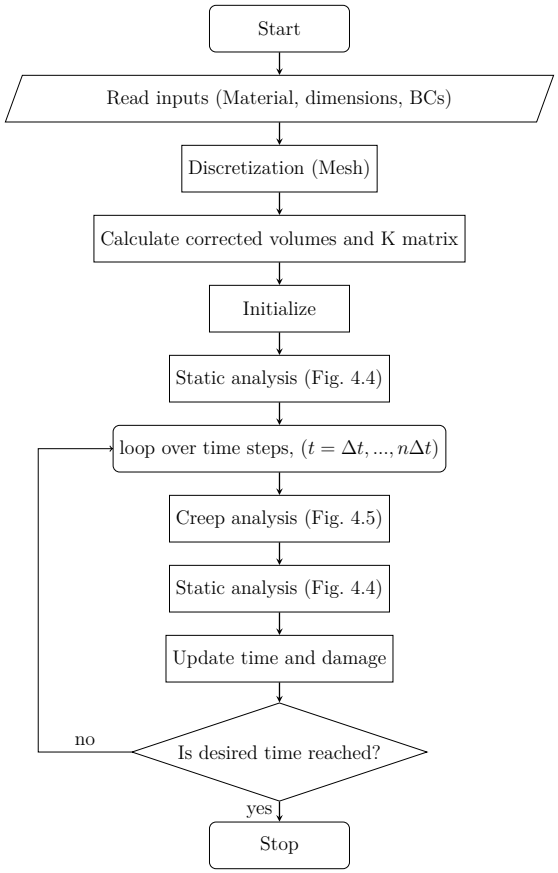

Figure 4.3: Flow chart of steps of numerical implementation

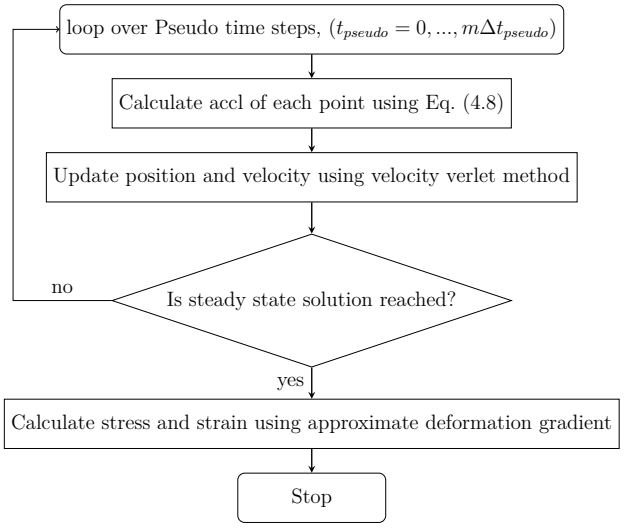

Figure 4.4: Flow chart of steps of achieving steady state solution

4.3 Time marching method

The time integration in the equation of motion is conducted using the velocity Verlet algorithm. Let us say, we know the position x_n for the current time step, and

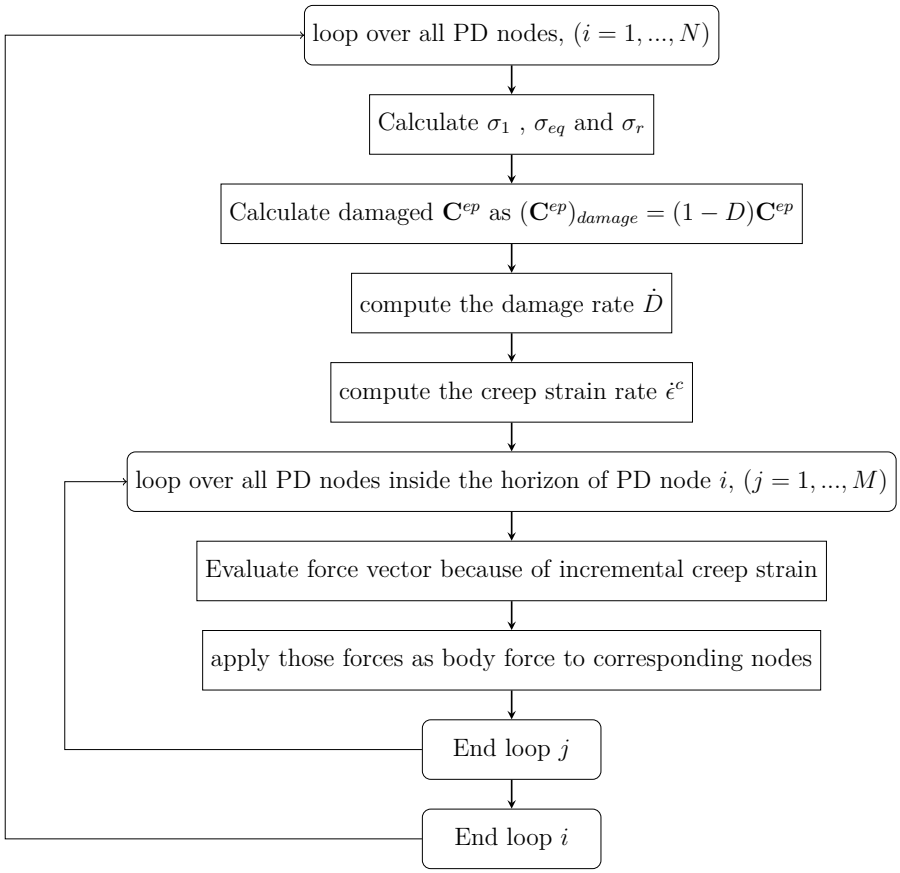

Figure 4.5: Flow chart of steps of creep analysis

we know the position, velocity and acceleration for the past time step as x_{n-1}, v_{n-1} and a_{n-1} respectively. We first calculate velocity for current time step n as,

$$v_n = \frac{x_n - x_{n-1}}{dt}, \tag{4.14}$$

where dt is the size of the time step. Then using this value of velocity, we calculate the acceleration for the current time step a_n as,

$$a_n = \frac{\mathbf{f}^{int} + \mathbf{b} - \Lambda v_n}{\rho}, \tag{4.15}$$

and finally, using this acceleration value, we can calculate the position for the future time step $n+1$ as,

$$x_{n+1} = 2x_n - x_{n-1} + dt^2 a_n, \tag{4.16}$$

The forward Euler time integration scheme is used for the calculation of the damage parameter and creep strain as,

$$\begin{aligned} \frac{dD}{dt} &= \frac{D_n - D_{n-1}}{\Delta t}, \\ \frac{d\varepsilon^c}{dt} &= \frac{\varepsilon^c_n - \varepsilon^c_{n-1}}{\Delta t}. \end{aligned} \tag{4.17}$$

4.4 Selection of influence function

The PD formulation provided in section 2.2 incorporates two damage parameters. One is the damage parameter D given in the classical damage model and other is the influence function $\hat{\omega}$ in the PD formulation. Use of both damage criteria will lead to nonphysical instabilities in the numerical computations [161]. For example, nodes with full damage impose unrealistic high strains at all points within their horizon. This will eventually lead to further propagation of damage causing diffusion of damage, where as in reality damage should be localized [161]. To avoid this, we modify the influence function such that the influence function is now dependent on the classical damage parameter D of both nodes as well along the bond length. This is given as

$$\underline{\omega} = \hat{\omega}(|\xi|, D, D'), \tag{4.18}$$

where D and D' are the classical damage parameters at point $\mathbf{x}$ and $\mathbf{x}^{'}$ respectively. In a simplified form, the above equation can be written as [161]

$$\hat{\omega}(|\xi|, D, D') = \omega_\xi(|\xi|)\omega_D(D, D'), \tag{4.19}$$

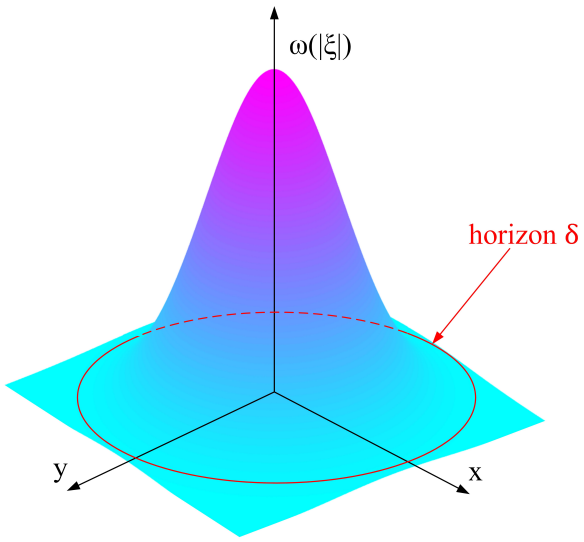

Figure 4.6: Representation of Gaussian influence function for two dimensional case.

where D and $D' \in [0,1]$ and $\omega_\xi(|\xi|)$ is the PD influence function whose value depends only on the bond length. The value of ω_D has to be zero if any one of its argument is grater than the critical damage D^{critical} i. e. when any points of the bond has full damage, the value of ω_D is zero and can be given as

$$\omega_D(D, D') = \begin{cases} 0 & \text{if} \quad D > D^{\text{critical}} \quad \text{or} \quad D' > D^{\text{critical}}, \\ 1 & \text{otherwise.} \end{cases} \tag{4.20}$$

Different forms of PD influence functions have been used in the past [1, 92]. Here we choose the following Gaussian form [75, 161],

$$\omega_\xi(|\xi|) = e^{-\frac{|\xi|^2}{l^2}}, \tag{4.21}$$

where l is length scale. Selection of the length scale is explained in next section. Fig. 4.6 shows the general representation of the Gaussian influence function given by Eq. (4.21). It has been shown that the influence function given by Eq. (4.19) does not affect the satisfaction of the balance laws by the equation of motion [161].

4.4.1 Calculation of length scale

The length scale is a measure of non-locality, and as the value of the length scale decreases, material becomes more and more non local in nature.

Consider a PD node and a finite element of the same dimension under the same stress σ_x along the x –direction as shown in Fig. 4.7. For simplicity, we are considering the stress in only one direction here. To achieve this stress in the FEM element, let us say we have to apply force F_c on each node of the element in the positive and negative x –direction as shown. Now to achieve same stress at a PD node, we have to apply forces on all nodes inside the horizon of the center node. We can calculate the force state at the center PD node using the known stress value from Eq. (4.3). This will give us the force acting on each neighbor node required to obtain the same stress as the FEM element if the center point has only that neighbor node. But, in reality all nodes inside the horizon are interacting with the center PD node. Therefore, to get same stress, the following equality must be valid,

$$\sum_{1}^{n} f_x = 2F_c, \tag{4.22}$$

where, f_x is the force on the PD node, F_c is force on the FEM node and n is the number of PD nodes inside the horizon of the center node.

Using Eq. (4.3), we can write above equality as,

$$\sum_{1}^{n} e^{-\frac{|\xi|^2}{l^2}} \bar{\mathbf{P}}\mathbf{K}^{-1}\xi = 2F_c. \tag{4.23}$$

Therefore Eq. (4.23) is used to calculate the value of length scale. It must be noted that, value of the length will be the same for a specific material with a specific mesh size.

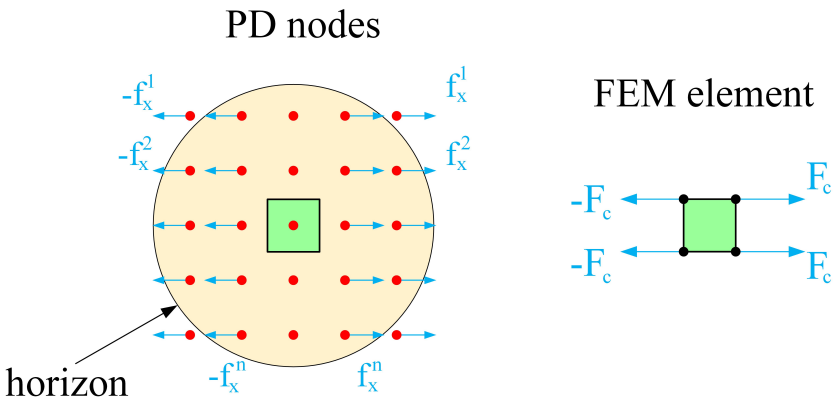

Figure 4.7: Equivalence of PD and FEM stress at node.

4.4.2 Crack representation

The number of bonds associated with any PD node is equal to the number of nodes inside its neighborhood. Since all bonds do not break simultaneously, rather each bond breaks when the damage criteria for that particular bond is reached. Therefore, we have to define a new parameter for each node indicating the number of broken bonds at each node. This parameter f_{broken} is defined as the fraction of the number of broken bonds to the total number of bonds for any node,

$$f_{broken} = \frac{\text{number of broken bonds}}{\text{total number of nodes inside horizon}}. \tag{4.24}$$

At $t = 0$, the number of broken bonds is zero, and hence, the f_{broken} is zero. The maximum value of f_{broken} is 1. A plot of f_{broken} gives us the crack path.

CHAPTER 5: NUMERICAL EXAMPLES OF CREEP MODELING

To demonstrate the performance of the peridynamic formulation presented in the previous section, creep studies are performed on 316 stainless steel at 600° C temperature. Material properties of 316 stainless steel are given in Table 5.1, while creep constants are given in Table 5.2.

5.1 Selection of damping coefficient

In this paper, we are using the dynamic relaxation method with a value of damping coefficient of $\Lambda = 5$. This value is chosen through a parametric study where the damping coefficient value was varied within certain range.

In order to select a value of the damping coefficient Λ and also to check if the developed C++ code is correct, we solve a simple problem of a plate with a circular hole at the center as shown in Fig. 5.1. The plate has dimensions of 100 mm by 50 mm, and the diameter of hole is 20 mm. As shown in Fig. 5.1, the left side is fixed, and on the right side, a tensile stress of 1 MPa is applied. The bulk modulus is set to be 100 GPa and Poisson's ratio is set to be 0.4. The plate is meshed with nodes with a size of 0.1 mm. the time step is chosen to be 1 ms. Static analysis is done with different values of damping coefficient ranging from 0.3 to 5.

Results of this parametric study are shown in Fig. 5.2, where the displacement of point 'A' on right edge is plotted against time. As can be seen from Fig. 5.2, the value of $\Lambda = 5$ gives the optimum damping without overshoot or over-damping.

We also plot the displacement of all nodes on the vertical center line of plate (shown in bottom right corner of Fig. 5.3). These displacement values are compared with results from the finite element method using ABAQUS as shown in Fig. 5.3. We can

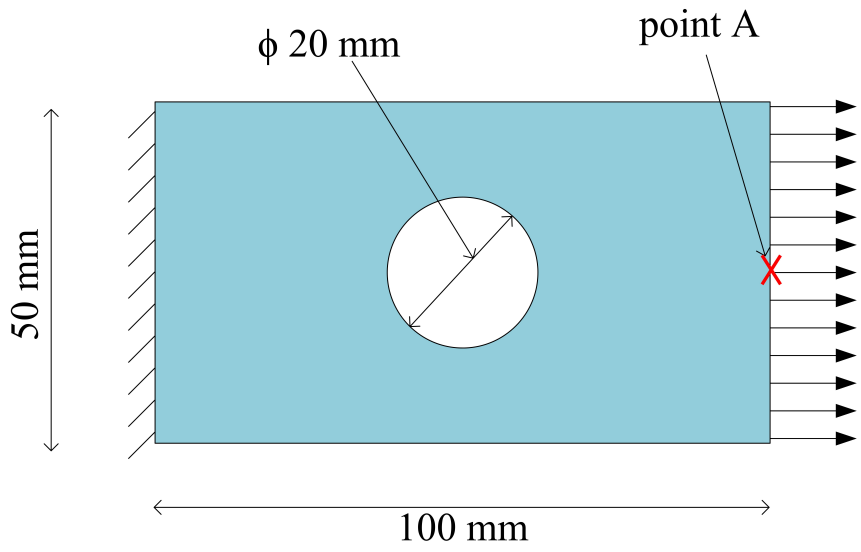

Figure 5.1: Geometry of problem of plate with hole. Plate is under uniaxial tension.

Table 5.1: Tensile properties of 316 stainless steel at 600° C. [4]

E (GPa)	v
148	0.3

Table 5.2: Creep constants of 316 stainless steel at 600° C. [4]

C_m	n_2	D_m	p	q_2	α
1.47×10^{-29}	10.147	2.73×10^{-30}	10.949	6.35	0.47845

see the results are in excellent agreement with each other, and hence, we can say that the chosen value of damping coefficient is reasonable.

5.2 Uniaxial tension test (Plain stress condition)

As shown in Fig. 5.4a the steel plate is under a uniaxial stress of 240 MPa. Dimensions of the plate are 1 cm × 10 cm. Plane stress conditions are assumed.

The mesh is generated with the seed size of 0.05 cm. Load and fixed boundary conditions are applied on 5 layers of nodes each. Although the density of the steel is not required for this kind of problem, but due to the dynamic formulation, we have to assume some value for density. Here density is assumed to be 1000 kg/m^3.

Horizon size for the PD formulation is chosen to be four times the seed size, i.e.

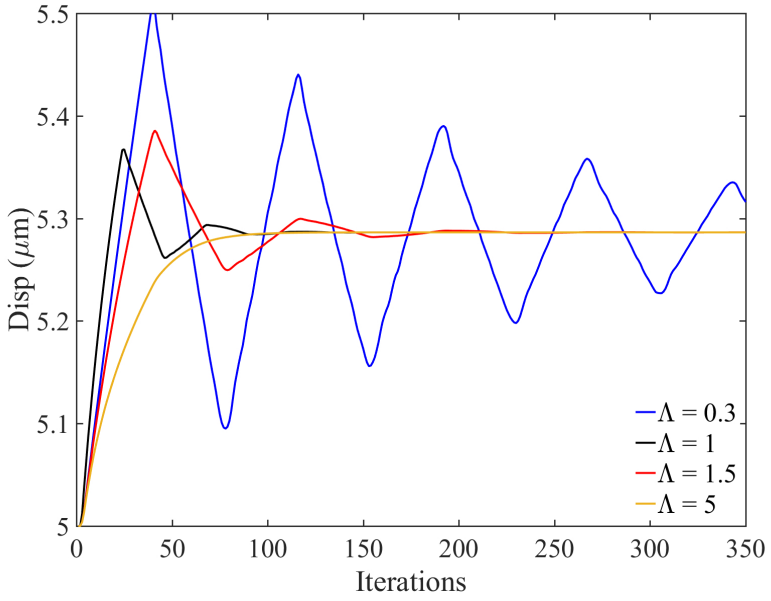

Figure 5.2: Results of parametric study in order to chose optimum value of damping coefficient.

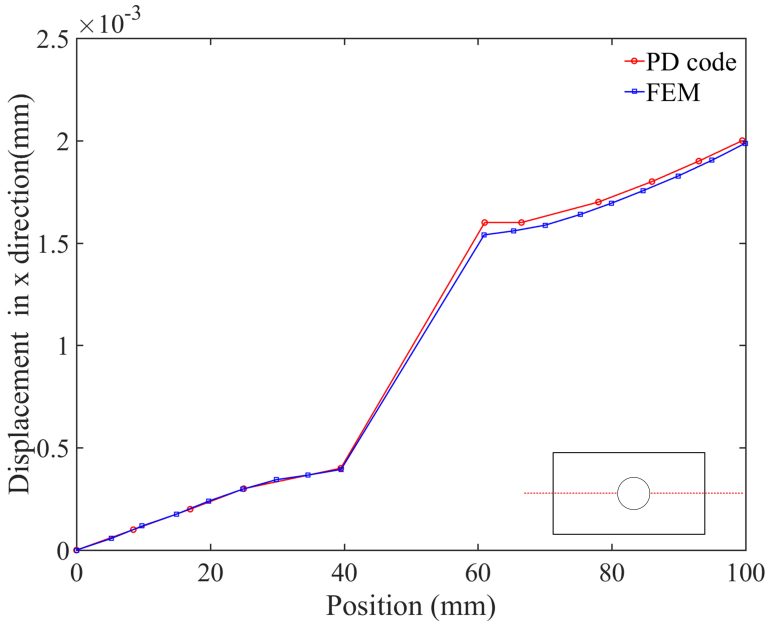

Figure 5.3: Geometry of problem of plate with hole. Plate is under uniaxial tension.

0.2 cm. The real time step is chosen to be 100 s and pseudo time step is 10^{-3} s.

The example was solved by writing code with C++ which was run on the university cluster with 1 processor, and the computational time was approximately 30 hours.

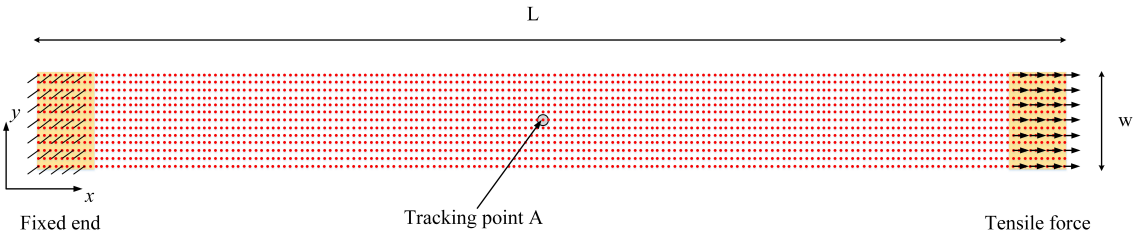

Figure 5.4: Plate under uniaxial loading

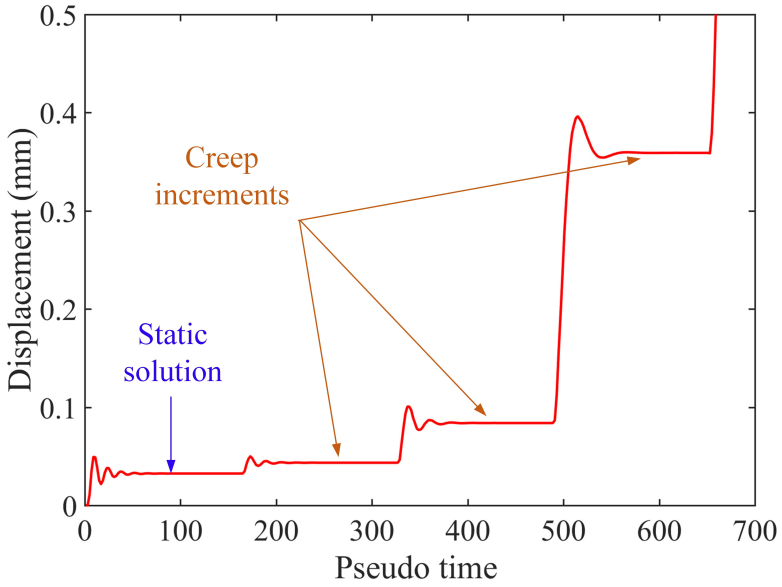

Figure 5.5: Displacement of point 'A' with respect to pseudo time.

The same problem was also solved using FEM. the same mesh size was used in the FEM as well for ease of comparison. The FEM solution was obtained using MATLAB code.

Fig. 5.6a shows the displacement of point A which is at the center of plate as shown in Fig. 5.4. The initial displacement observed at time $t = 0$ s is due to elastic static analysis. Then an almost linear increase is observed as time increases. This behavior shows secondary creep. When the time exceeds 2500 hours significant increase in the displacement is observed which represents tertiary creep finally ending in failure. Fig. 5.6b shows the evolution of damage parameter D with respect to time. It can be seen that it shows a similar behavior to the displacement curve. At $t = 0$ s value

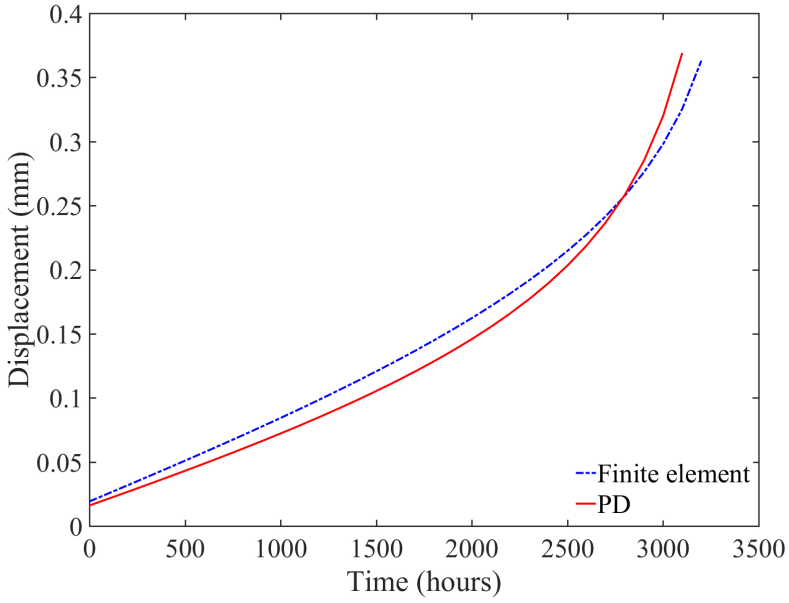

(a)

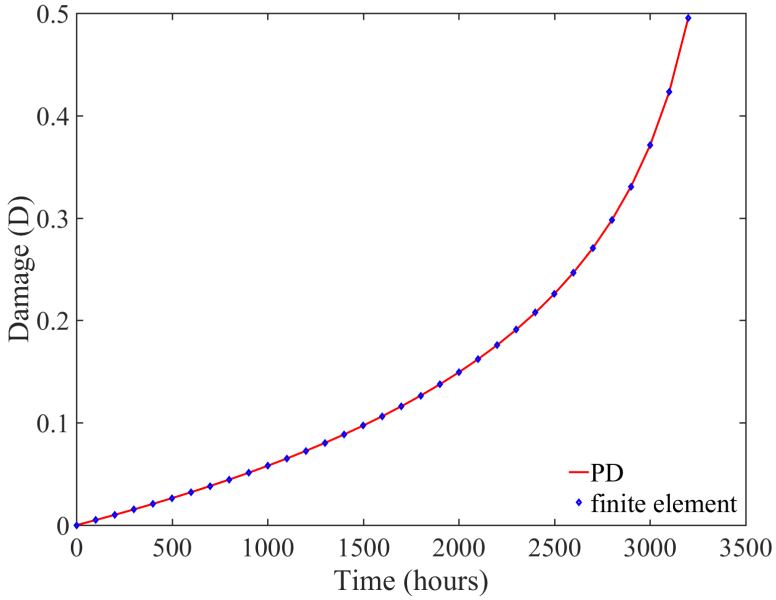

(b)

Figure 5.6: Comparison of FEM and PD results of point A for (a) Displacement with respect to time and (a) Evolution of damage parameter D with respect to time.

of D is zero and increases with respect to time. Results shows very good agreement with the finite element method.

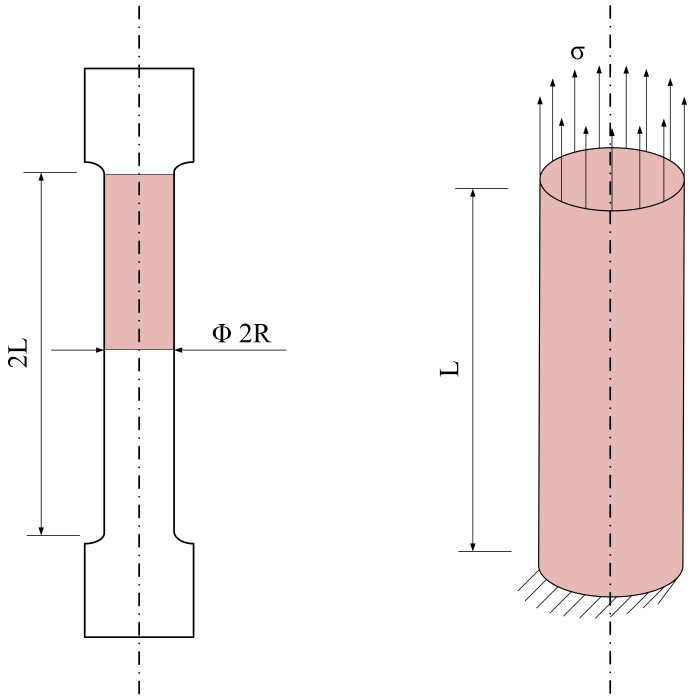

Figure 5.7: Uniaxial creep specimen

5.3 3D uniaxial tension

In order to check the robustness of the proposed method, we also simulate a uniaxial creep tension test. The geometry of the uniaxial creep specimen in shown in Fig. 5.7. A cylindrical part, denoted by the red color, is chosen for our simulation because of symmetry. The length of cylinder is $L = 50$ mm and the radius is $R = 5$ mm. Again, the same material i.e. 316 stainless steel is used. The value of the applied load is 240 MPa, 260 MPa, 280 MPa and 300 MPa respectively. The horizon size for the PD formulation is chosen to be four times the seed size, i.e. 0.2 cm. A real time step is chosen to be 100 s, and a pseudo time step is 10^{-3} s.

As the number of peridynamic nodes inside the horizon of any PD node increases by one order for a 3D domain than a 2D domain, the computational time increases exponentially. In order to save computational time the 3D examples are solved by writing code with Fortran 2003 as Fortran is shown to be 30 % faster than C++.

Fig. 5.8 shows a comparison of results with experimental data obtained by Hyde

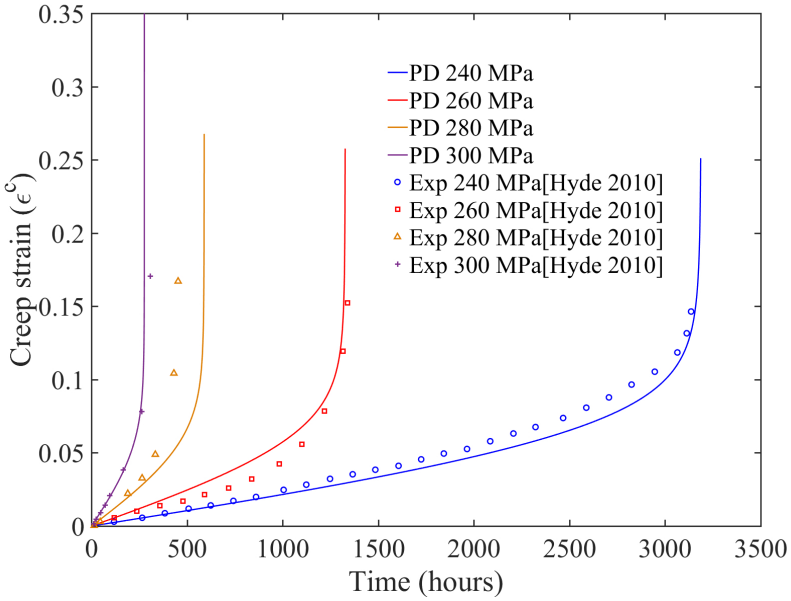

Figure 5.8: Comparison of creep strain for point 'A' obtained using proposed PD model and experimental results from Hyde et al. [4] for different load values.

et al. [4]. Four different loading conditions are applied (240 MPa,260 MPa,280 MPa and 300 MPa). Results are in good agreement with experiments.

We also solved the same example using FEM with the help of ABAQUS along with it's user subroutine CREEP. The FEM results are consistent with the PD results. Fig. 5.9a shows the displacement field in the loading direction at time $t = 20$ hours and Fig. 5.9b shows the stress distribution at the same time. As expected, the stress is uniformly distributed in the body with a value of the applied load, in this case 240 MPa.

In both uniaxial examples (2D and 3D), critical damage is not reached. We are doing the analysis until the damage parameter $D = 0.5$. The reason behind this is as the material is uniform and ideal, the damage parameter is uniform all over the body; hence, damage at all points will reach the critical value together. In reality, due to some defects in the material, stress concentration will occur causing some points to reach the critical damage before others. In this case, only a single crack can initiate.

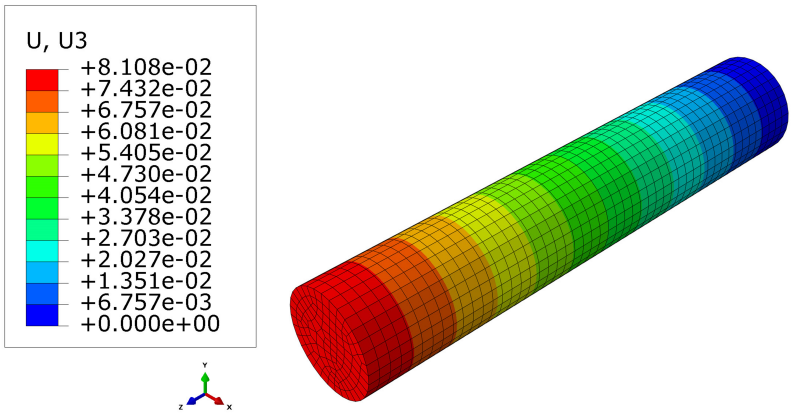

Figure 5.9: Displacement field on creep specimen in direction of loading.

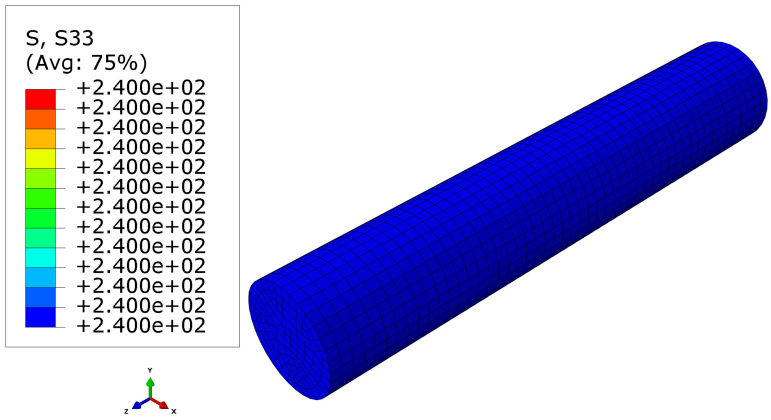

Figure 5.10: Uniform stress field on creep specimen in direction of loading.

5.4 2D Crack propagation (Mode I loading)

Creep crack growth analysis of a specimen under mode I loading is studied. The specimen geometry is shown in Fig. 5.11, and for this problem, we choose $W = L = 40$ mm. The length of the initial crack is 20 mm. The crack is modeled by removing one layer of nodes and breaking all the bonds which cross that removed layer. The material used for the specimen is 316 stainless steel at 600° C, and it is subjected to 11.51 kN force.

5.4.1 Comparison of static analysis with finite element

In the previous examples of uniaxial tension, the stress at every point in body is the same, and hence, the creep strain and damage parameter D is uniform in the

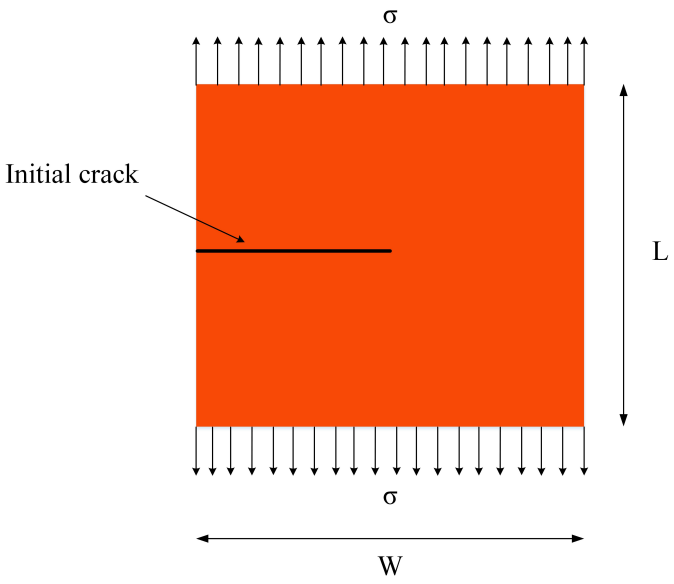

Figure 5.11: Geometry of crack propagation specimen with initial crack.

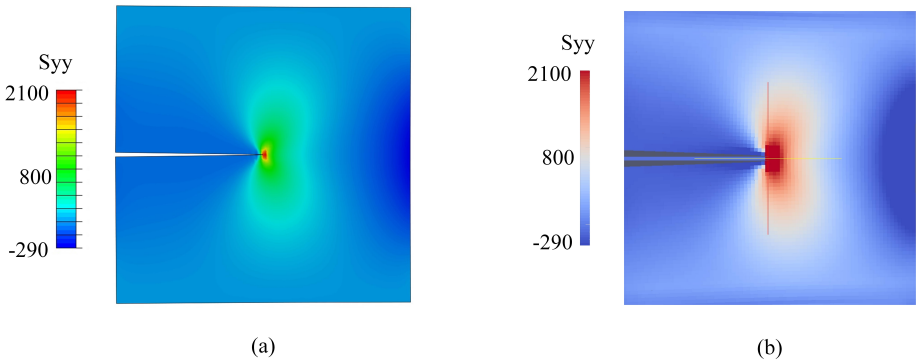

Figure 5.12: Stress distribution in plate with crack for σ_{yy} under tension. (a) shows results from finite element and (b) shows results from peridynamics.

whole body. But in the case of the plate with an initial crack, a nonuniform stress distribution is expected, and hence, it is important to make sure that the stress distribution after the static analysis is correct. In order to do that, we solve the same example using the finite element method. The mesh size is kept the same in the finite element and the PD as 0.1 mm. Linear plane stress elements are used to mesh the domain with FEM.

The normal stress in the x– and y–direction obtained from the finite element and peridynamics simulations are shown in Fig. 5.12 and Fig. 5.13. As expected, the

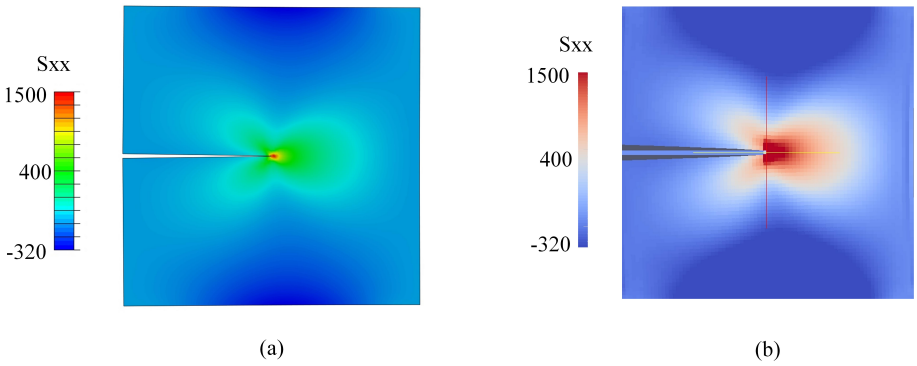

Figure 5.13: Stress distribution in plate with crack for σ_{xx} under tension. (a) shows results from finite element and (b) shows results from peridynamics.

stress intensity is observed near the crack tip. Results from PD and FEM are in close agreement with each other. Stress intensity in the PD is spread over a slightly larger area than the FEM due to the skin effect. All the methods used to reduce the skin effect are only applicable on outer boundaries but cannot be used for the crack tip. Therefore, the primary reasons for the difference between the stress values by the FEM and PD can be summarized as follows:

1. Incomplete neighborhood for the points near the crack tip. The ghost node method is used to reduce the skin effect on boundaries but cannot be used near the crack tip. This is the most dominant reason for error.

2. Boundary conditions in the FEM are applied only on the surface; whereas in the PD, it is applied on several layers of nodes. This definitely does not impact much but still is a source for error.

3. The way in which the crack is modeled in PD and FEM is different. In the PD the crack is formed by removing one layer of nodes; on the other hand in the FEM crack is modeled in the geometry itself. This makes the crack in FEM a bit sharper than the crack in PD.

Despite these sources for errors, overall results are in good agreement with each other.

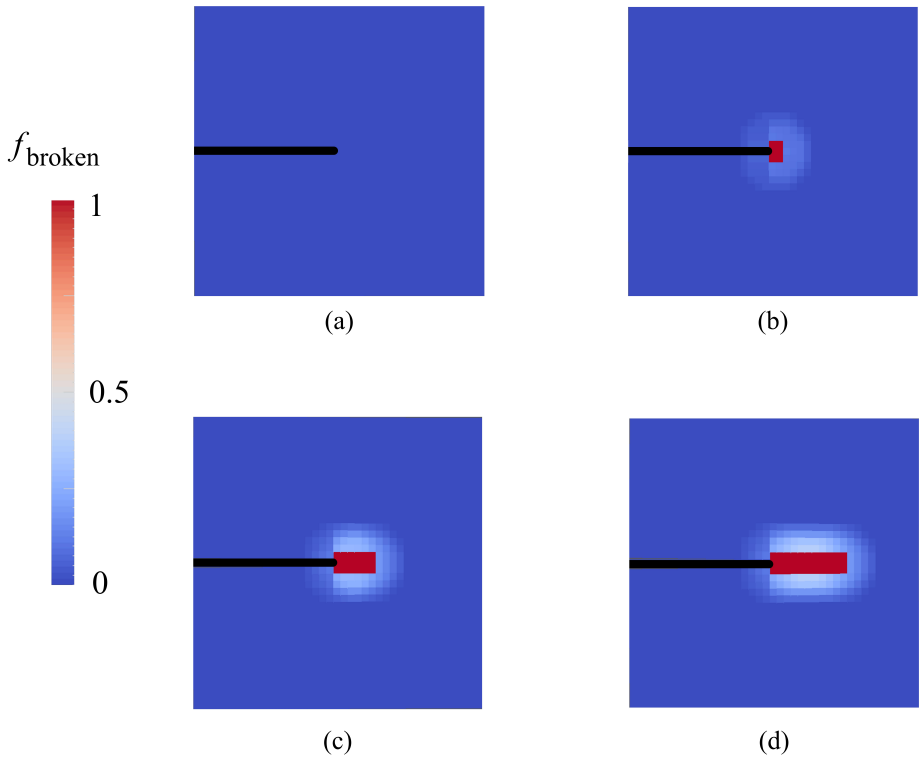

Figure 5.14: Crack propagation under mode I loading due to creep. (a) Initial crack, (b) crack at $t = 100$, (c) crack at $t = 300$, and (d) crack at $t = 500$.

5.4.2 Crack propagation due to creep

The critical value of the damage parameter $D^{\text{critical}} = 0.75$ is chosen as the bond breaking criterion. Therefore, if the damage parameter at a node is 0.75 all bonds attached to that node break. Although this causes loss of total mass in the domain, the amount of lost mass is very small compared to the total mass of the domain and hence can be neglected.

Fig. 5.14 shows the crack at three different times. As we can see, the crack propagates in a straight line, and the crack growth rate increases with respect to time. Although bonds can break due to excess strain, most of the bonds in this case are broken due to the node reaching a critical damage value.

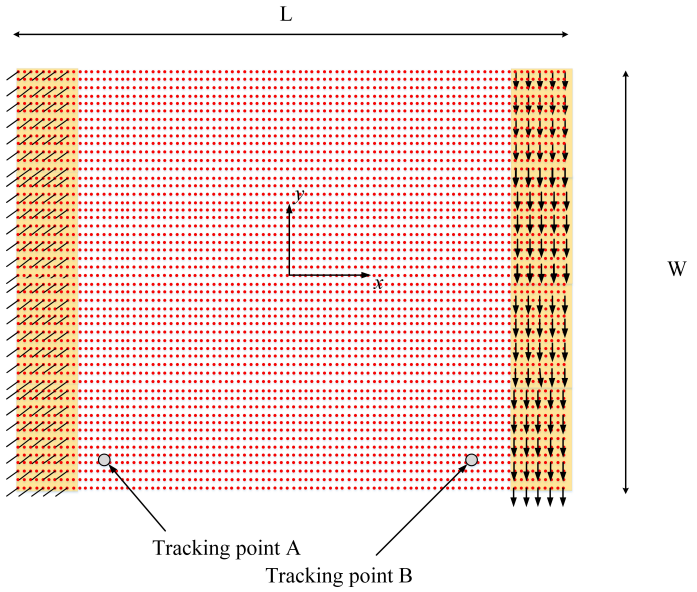

Figure 5.15: Plate under bending

5.5 2D bending example

Finally, we simulate the creep under bending loading in a plane stress condition. Fig. 5.15 shows the plate geometry. Values of L and W are chosen to be the same and is equal to 10 mm. A body force is applied in negative y–direction on the right end of the plate while the left end is fixed. Material parameters are kept the same.

Fig. 5.16 shows the stress distribution over the plate under bending. The plate mostly contains stress along x–direction in upper (tension) and lower (compression) part near the fixed end. As the creep model does not alter the stress, this stress distribution is maintained throughout the simulation. As the stress along y–direction is negligible, the deformation of the plate continues mostly because of the weakening of the material due to the accommodation of the damage near the fixed end and not because of the addition of the extra force. Fig. 5.16c shows the shear stress distribution over the domain.

Fig. 5.17 compares the creep strain and damage values for two specific points 'A' and 'B' on the plate as shown in Fig. 5.15. The tracking points are chosen to be

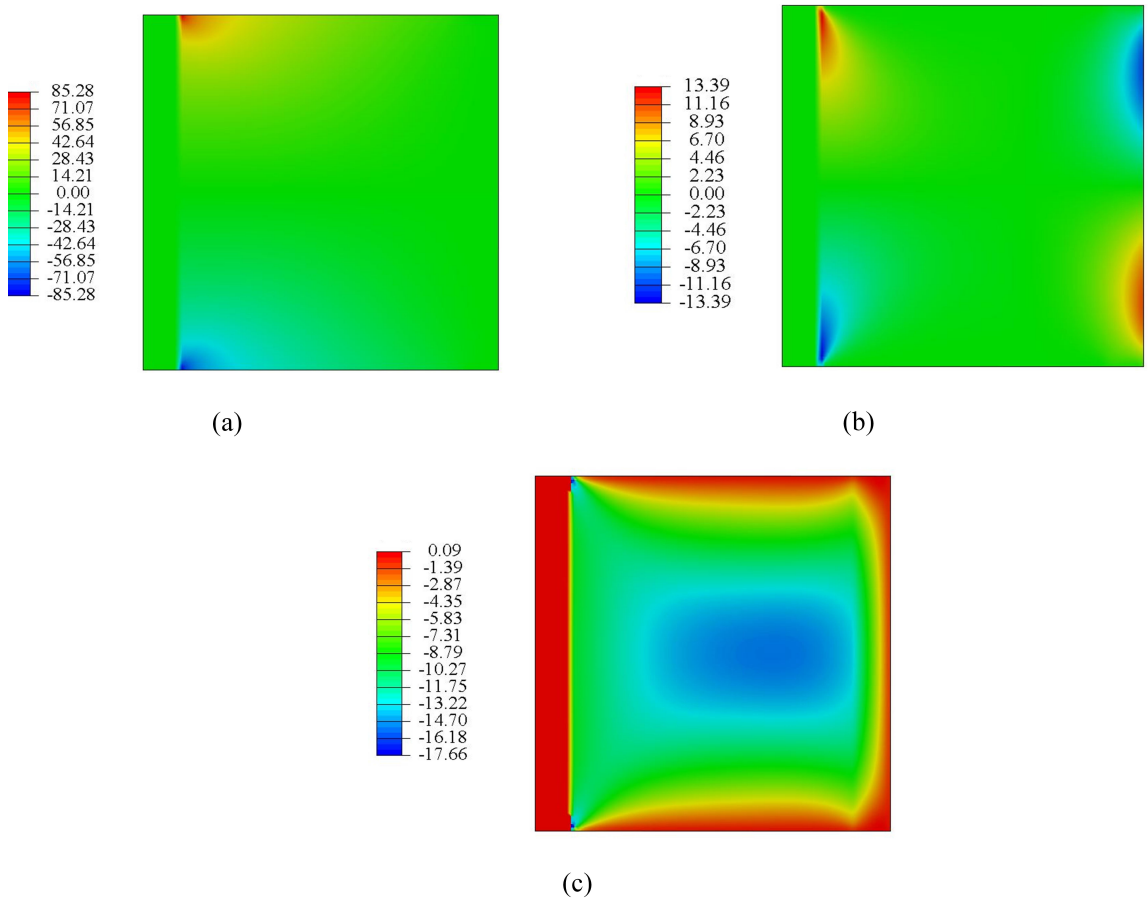

Figure 5.16: Stress contours in plate under bending loading. (a) σ_{11}, (b) σ_{22}, and (c) σ_{12}.

somewhat inside the domain and not on the boundary to avoid the skin effect observed in peridynamics. It is observed that damage and creep strain is accumulated near the high stress region. Results are in good agreement with the finite element method.

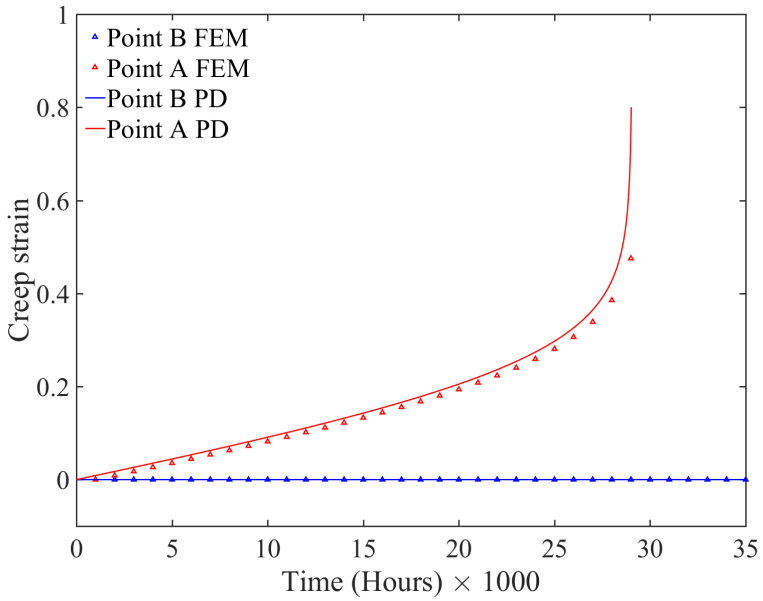

(a)

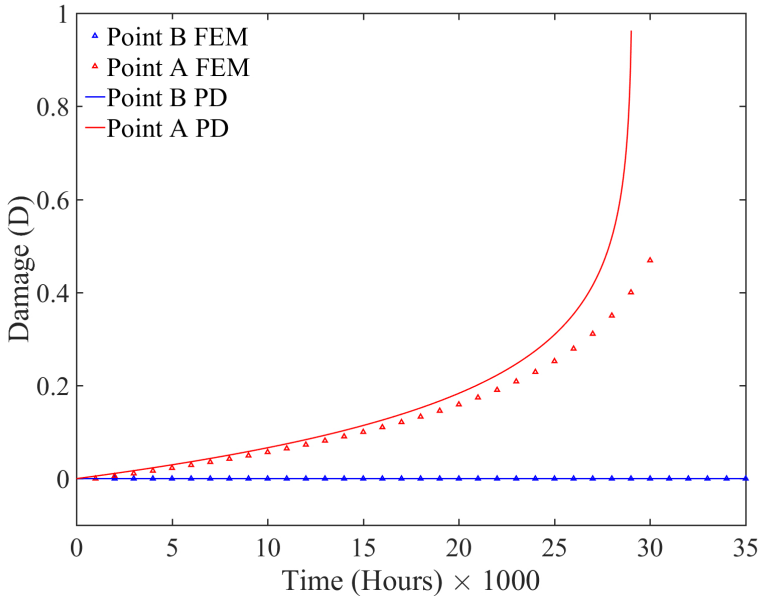

(b)

Figure 5.17: Comparison of (a) creep strain and (b) Damage for points 'A' and 'B' under bending.

CHAPTER 6: ANALYTICAL SOLUTION FOR COUPLING OF PD AND FEM

6.1 Wave propagation in peridynamics

In this section, we study a longitudinal plane wave propagating from the left to right in an infinite homogeneous elastic medium. By assuming that the peridynamic grid is uniform and rectangular, and the wave travels along the grid lines, the three–dimensional problem can be simplified to a one–dimensional wave propagation problem. A plane wave traveling in the positive x–direction can be represented as

$$u(x,t) = A_0 e^{i(\omega t - Kx)}, \tag{6.1}$$

where $u(x,t)$ is the magnitude of the wave at point x at time t, A_0 is the amplitude of the wave, $i = \sqrt{-1}$, K is the wave number and ω is the angular frequency of wave. The wave number K, angular frequency ω, time period T, wavelength λ and wave velocity v are related by

$$v = \frac{\omega}{K} = \frac{\lambda}{T}. \tag{6.2}$$

The one–dimensional peridynamic grid used to study the motion of the wave is shown in Fig. 6.1. We assume the distance between every two peridynamic nodes is h and we number the nodes consecutively as $k = \ldots, -3, -2, -1, 0, 1, 2, 3, \cdots$ with $k = 0$ at the origin of the x–axis. We assume that a time step τ is used to integrate the equations of motion. By using Eq. (6.2) and noting that on this grid $x = kh$, the displacement of node k is due to the propagation of a planar wave Eq. (6.1), at time step n ($t = n\tau$) can be written as

$$u_{k,n} = A_0 e^{i\omega(n\tau - kh/v)}, \tag{6.3}$$

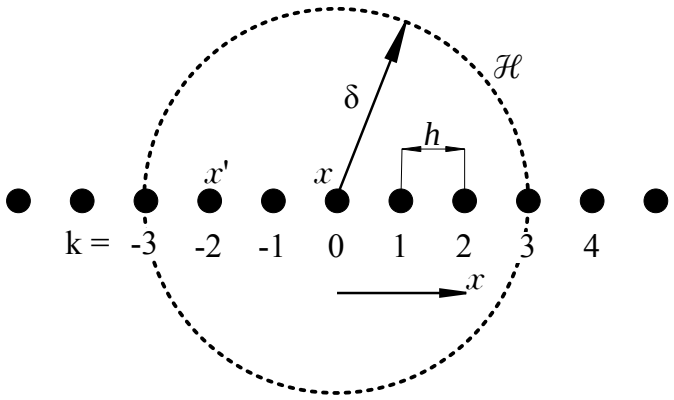

Figure 6.1: Modeling of 1D bar using peridynamic theory.

where $u_{k,n}$ is the magnitude of the wave at time step n at node k.

The equation of motion of node k can be obtained using Eq. (2.15). By assuming the horizon $\delta = 3h$, we obtain

$$\rho \ddot{u}_k = \sum_{j=k-3}^{k+3} c_0 \frac{(u_j - u_k)}{|x_j - x_k|} V_{jk}, \tag{6.4}$$

where V_{jk} is a fraction of the volume of the PD node inside the horizon. The finite difference method can be used to approximate acceleration at time step n using

$$\ddot{u}_{k,n} = \frac{1}{\tau^2}(u_{k,n+1} - 2u_{k,n} + u_{k,n-1}). \tag{6.5}$$

Substituting Eq. (6.5) in Eq. (6.4) and using Eq. (6.3) gives (for detailed steps see Appendix A)

$$\sin^2\left(\frac{\omega\tau}{2}\right) = \frac{E\tau^2}{27\rho h^2}\left[\sin^2\left(\frac{3\phi}{2}\right) + 3\sin^2\phi + 6\sin^2\left(\frac{\phi}{2}\right)\right], \tag{6.6}$$

where,

$$\phi = \frac{\omega h}{v} \tag{6.7}$$

is used to simplify the notation. Using Eq. (6.2) in Eq. (6.7) and noting that $\omega = 2\pi T$

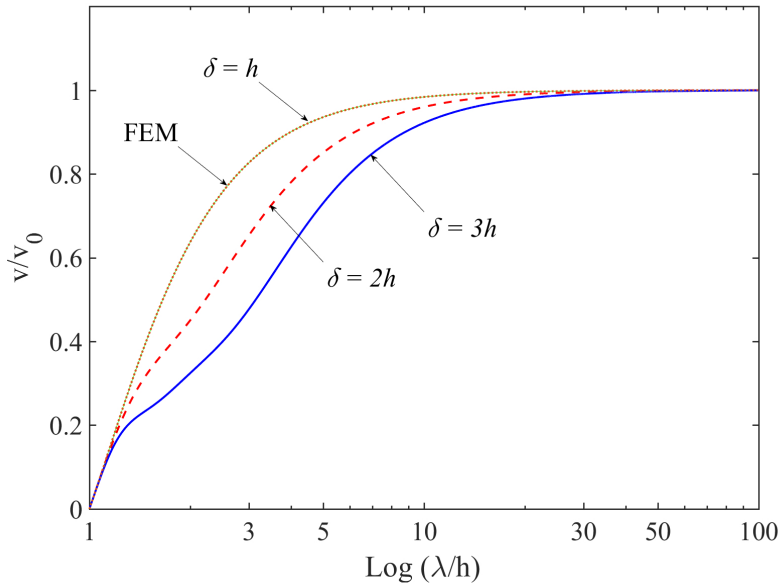

Figure 6.2: Variation of velocity of wave with respect to mesh size for different values of δ.

we obtain

$$\phi = 2\pi \frac{h}{\lambda}. \tag{6.8}$$

By dividing both sides of Eq. (6.6) by $v_0 = \sqrt{\frac{E}{\rho}}$, the wave velocity in a continuous medium, we obtain

$$\frac{v}{v_0} = \frac{2h\left[\sin^{-1}\left(\frac{\tau}{3h}\sqrt{\frac{E}{3\rho}\{\sin^2\left(\frac{3\phi}{2}\right) + 3\sin^2\phi + 6\sin^2\left(\frac{\phi}{2}\right)\}}\right)\right]}{v_0\phi\tau}. \tag{6.9}$$

This equation provides the ratio of the wave velocity obtained from the peridynamic formulation to the theoretical value of the wave velocity v_0 in the continuum domain. It is expected that this ratio be close to one when the problem is solved with high accuracy. Based on Eq. (6.9), besides the material parameters, two other factors affect the wave velocity obtained from the peridynamics formulation. The first one is the ratio of grid size to the wavelength (i.e. ϕ) and the second one is the integration time step τ.

To study the impact of the peridynamic horizon size on the wave velocity predicted by the peridynamic formulation, we repeat the previous procedure for $\delta = 2h$. Following the steps outlined in Appendix A for $\delta = 2h$ we obtain

$$\sin^2\left(\frac{\omega\tau}{2}\right) = \frac{E\tau^2}{8\rho h^2}\left[\sin^2\phi + 4\sin^2\left(\frac{\phi}{2}\right)\right], \tag{6.10}$$

and the ratio of the wave velocity obtained from the discretized peridynamic formulation and the wave velocity in a continuum domain can be obtained from

$$\frac{v}{v_0} = \frac{2h\left[\sin^{-1}\left(\frac{\tau}{2h}\sqrt{\frac{E}{2\rho}\{\sin^2\phi + 4\sin^2(\frac{\phi}{2})\}}\right)\right]}{v_0\phi\tau}. \tag{6.11}$$

Finally, we solve the problem for the case of $\delta = h$. When $\delta = h$, the one–dimensional peridynamics formulation obtained from Eq. (2.15) becomes equivalent to the one–dimensional finite element method with linear elements given in Eq. (2.9). Following steps of Appendix A yields

$$\sin^2\left(\frac{\omega\tau}{2}\right) = \frac{E\tau^2}{\rho h^2}\left[\sin^2\left(\frac{\phi}{2}\right)\right], \tag{6.12}$$

which leads to the following equation for the ratio of wave velocities from the peridynamic formulation and the wave velocity in the continuous medium as

$$\frac{v}{v_0} = \frac{2h\left[\sin^{-1}\left(\frac{\tau}{h}\sqrt{\frac{E}{\rho}\{\sin^2(\frac{\phi}{2})\}}\right)\right]}{v_0\phi\tau}. \tag{6.13}$$

This equation has been previously derived by Bazant et al. [130, 163] for wave propagation in a continuous medium discretized by the linear finite elements.

To study the impact of the grid resolution and size of the horizon on the wave velocity, Eq. (6.9), Eq. (6.11) and Eq. (6.13) are plotted in Fig. 6.2 with value of

$\tau = 1$ ms. The graph shows that when the ratio of λ/h increases, i.e. when the grid resolution is fine with respect to the wavelength, the wave velocity obtained from the peridynamics formulation approaches that of the theoretical value for the continuum medium. By increasing the size of horizon, a finer grid is required for the wave velocity to match the theoretical value. For example, in order for the wave velocity v to match its theoretical value, when $\delta = h$, the wavelength should be at least 10 times larger than the grid spacing, but when $\delta = 3h$ the wavelength should be about 30 times larger than the grid size. This trend clearly shows the necessity of using finer grids when the horizon size increases.

The wave dispersion curves can be obtained by rearranging Eqs (6.6), (6.10) and (6.12) to obtain a relation between the angular frequency ω and wave vector K

$$\omega = \frac{2}{\tau}\sin^{-1}\left[\frac{\tau}{h}\sqrt{\frac{E}{27\rho}\left[\sin^2\left(\frac{3Kh}{2}\right) + 3\sin^2(Kh) + 6\sin^2\left(\frac{Kh}{2}\right)\right]}\right], \quad \text{for} \quad \delta = 3h, \tag{6.14a}$$

$$\omega = \frac{2}{\tau}\sin^{-1}\left[\frac{\tau}{h}\sqrt{\frac{E}{8\rho}\left[\sin^2(Kh) + 4\sin^2\left(\frac{Kh}{2}\right)\right]}\right], \quad \text{for} \quad \delta = 2h, \tag{6.14b}$$

$$\omega = \frac{2}{\tau}\sin^{-1}\left[\frac{\tau}{h}\sqrt{\frac{E}{\rho}}\sin\left(\frac{Kh}{2}\right)\right], \quad \text{for} \quad \delta = h. \tag{6.14c}$$

The dispersion curves for different horizon sizes are plotted in Fig. 6.3. These curves show the same trend as the dispersion curves obtained in Reference [164]. For large wavelengths, all the dispersion curves match with the theoretical values. For small wavelengths, the dispersion curves obtained from the peridynamic formulation do not match with the theoretical curve, and the difference is more significant for larger horizon sizes.

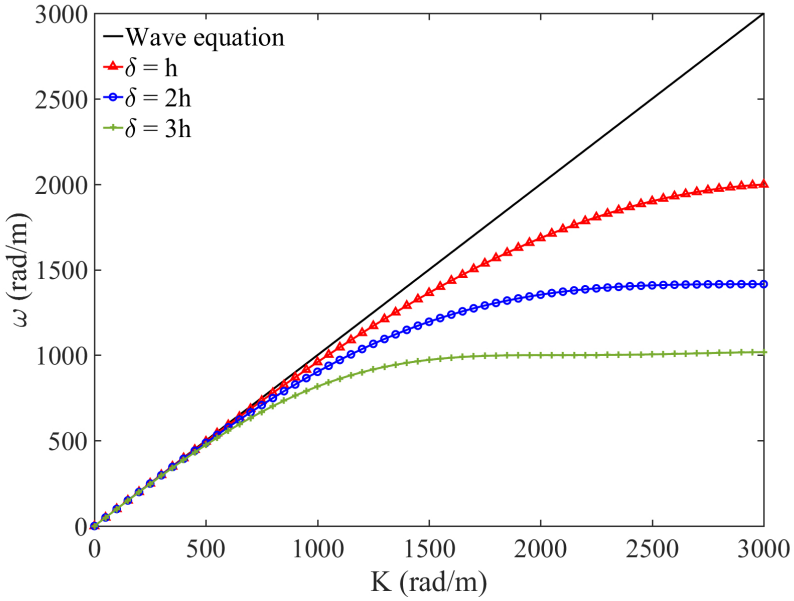

Figure 6.3: Dispersion relations for the different horizon sizes and wave vectors for $h = 1$mm.

To verify the analytical results numerically, the propagation of a longitudinal wave is modeled using the peridynamics formulation. The longitudinal wave is shown in Fig. 6.4a and is composed of a coarse and a fine component represented by

$$u(x,t) = 10^{-4} e^{i(x - \frac{1000\pi t}{32})} + 10^{-5} e^{i(x - 1000\pi t)}. \tag{6.15}$$

The value of λ/h for the low frequency component of the wave is approximately 250 and for the high frequency wave is approximately 8. A time step of 1 ms is used for the time integration of the equations of motion.

The snapshots of the wave propagation obtained using different horizon size are shown in Fig. 6.4. These snapshots show that the velocity of the low frequency (long wavelength) component of the wave is the same for all horizon sizes and is equal to the theoretical value of wave velocity. On the other hand, the high frequency component (short wavelength) of the wave travels at a lower velocity than the low frequency component. By increasing the size of horizon δ from h to $3h$, the velocity of

high frequency wave reduces drastically and it lags further behind the low frequency wave. The numerical results are in agreement with the analytical results presented in Fig. 6.2.

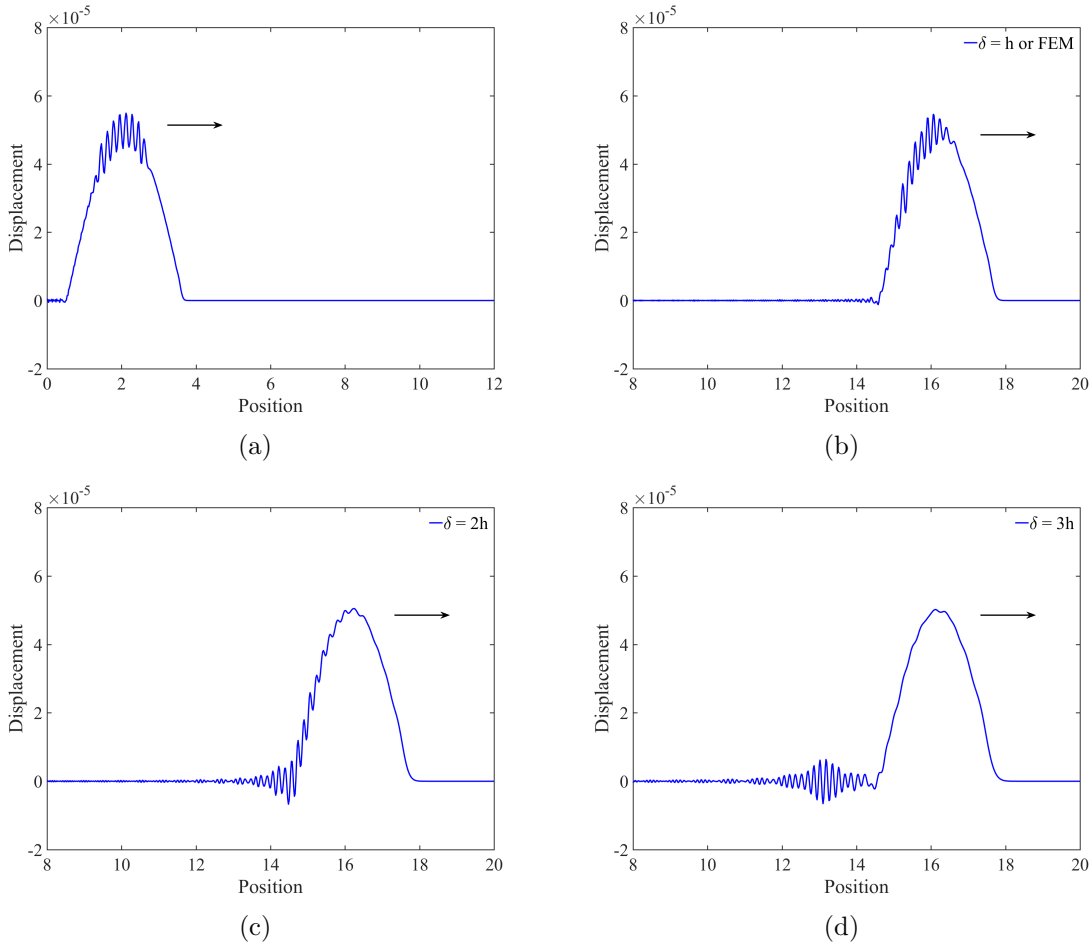

Figure 6.4: Propagation of high and low frequency waves in homogeneous bar for different peridynamic horizons. (a) The initial wave, (b) $\delta = h$, (c) $\delta = 2h$ and (d) $\delta = 3h$. The snapshots of the propagated waves are at $t = 14s$.

6.2 Non-uniform discretization

To reduce the high computational costs associated with using peridynamics, it is advantageous to couple peridynamics and finite elements. In such a coupling method, peridynamics is used in critical zones where crack nucleation and propagation is probable and the finite element method is used elsewhere. Due to the change in the formulation from a nonlocal to a local continuum and because of the difference in the

grid size of the finite element and peridynamic zone, spurious wave reflections happen at the interface between peridynamics and the finite element zone.

To demonstrate the issue of wave reflection, we model wave propagation using a coupled peridynamics–finite element approach. The discretized one–dimensional domain is shown in Fig. 6.5. As shown, the domain is discretized by a peridynamic grid of constant spacing h in the left and a finite element mesh of constant size $H \geq h$ in the right. Peridynamic nodes are shown with solid black circles and finite element nodes are shown with "$\times$". The peridynamics and finite element nodes are marked consecutively as $k = \cdots -3, -2, -1, 0, 1, 2, 3, \cdots$. The peridynamics zone covers the subdomain with $k \leq 0$ and finite element zone covers $k \geq 0$. Therefore, the two zone only overlap at $k = 0$ where the displacement, velocity, and acceleration of the peridynamic node is transferred to the finite element node at $k = 0$. To ensure that the peridynamic nodes close to the interface have the same number of neighbors as the other peridynamics nodes, ghost nodes are added to the right side of the interface. The ghost nodes are shown in red in Fig. 6.5 and their spacing is the same as the original peridynamic grid. The displacement of ghost nodes are obtained be interpolating the displacement of finite element nodes using the finite element shape functions. We model the propagation of the wave presented in Eq. (6.15) from the peridynamic zone to the finite element zone using the described coupling method. The material is linear elastic and for simplicity its cross section and Young's modulus is kept to be unity. To ensure that both the finite element and peridynamic zone have the same material properties, the peridynamic material parameter c_0 is found using Eq. (2.13). The H/h ratio is chosen to be 4.

The snapshot of the wave before and after reaching the interface point is shown in Fig. 6.6a and Fig. 6.6b, respectively. As shown, after reaching the interface, only the low frequency component of the wave can travel into the finite element zone and high frequency component of the wave spuriously reflects back into the peridynamics zone.

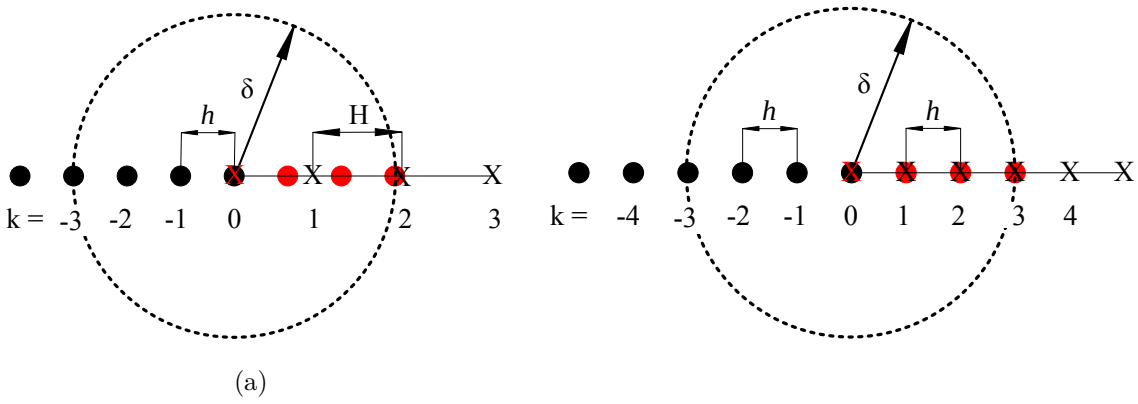

(a)

Figure 6.5: Coupling of peridynamics and finite element for (a) peridynamic grid spacing is h and finite elements size is H, (b) both finite element and peridynamics have the same spacing h. Peridynamic nodes are shown with solid black circles and finite element nodes are shown with "×". Red color indicates ghost node.

The spurious wave reflection of the wave can significantly reduce the computational accuracy and must be prevented. A technique for resolving the issue of spurious wave reflection is proposed in [137]. In this section, we study the impact of the horizon size δ, λ/h ratio and H/h ratio on the spurious wave reflection at the interface. For the simplicity of the presentation, we study the coupling for two cases: a) when the discretization is not uniform between the peridynamic and the finite element domains, i.e. $h \neq H$; and b) when $h = H$, i.e. a uniform discretization is used in both peridynamic and finite element zones.

The coupling of peridynamic and finite element zones when the finite element mesh is coarser than the peridynamic grid is shown in Fig. 6.5a. As described previously, the equation of motion of the nodes with $k \leq 0$ is obtained using the peridynamic formulation and equation of motion of nodes with $k \geq 0$ is obtained using the finite element method. At $k = 0$, information from the peridynamic domain is passed to the finite element zone. Since all the peridynamic nodes should have the same number of nodes in their horizon, ghost PD nodes are added to the right side of the interface. For example, if $\delta = 3h$, three PD ghost nodes are added as shown in Fig. 6.5.

Using Eq. (2.15) and Eq. (2.9), the equation of motion of PD and FE nodes when

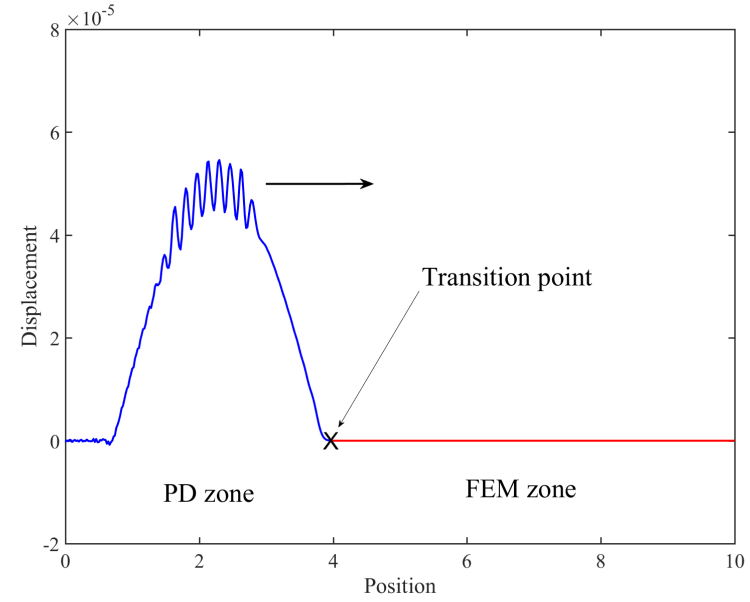

(a)

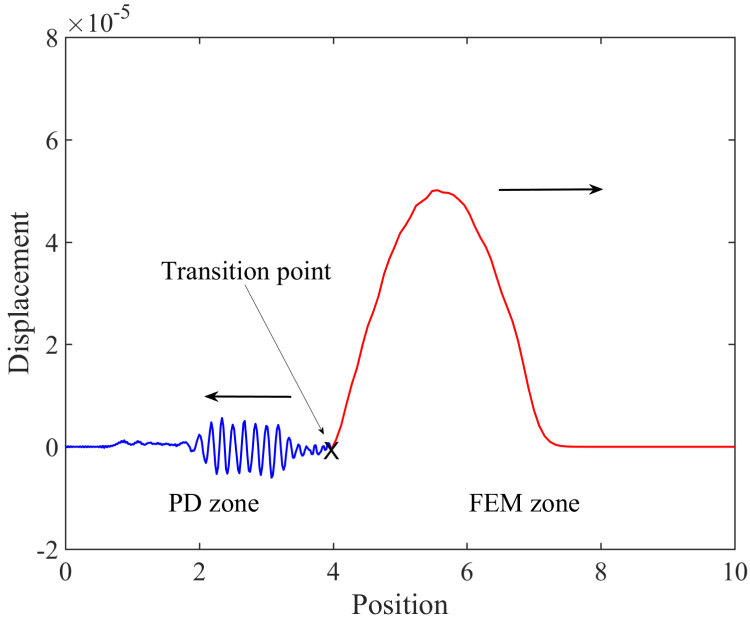

(b)

Figure 6.6: (a) Incident waves and (b) reflection of high frequency wave from transition point.

$\delta = 3h$ can be expressed as

$$\rho\ddot{u}_k = \sum_{j=k-3}^{k+3} c_0 \frac{(u_j - u_k)}{|x_j - x_k|} V_{jk}, \quad \text{for} \quad k \leq 0, \tag{6.16a}$$

$$\rho H\ddot{u}_k = \frac{E}{H}(u_{k+1} - 2u_k + u_{k-1}), \quad \text{for} \quad k \geq 0. \tag{6.16b}$$

To simplify the calculations and without the loss of generality, we assume that the amplitude of the incident wave traveling from the peridynamic zone toward the finite element zone is equal to one. A spurious wave reflection with an amplitude of β occurs at $k = 0$ and a plane wave with amplitude of α transmits into the finite element zone. Therefore, the displacement of each node can be written as

$$u_{k,n} = e^{i\omega(n\tau - {}^{kh}/_{v})} - \beta e^{i\omega(n\tau + {}^{kh}/_{v})}, \quad \text{for} \quad k \leq 0, \tag{6.17a}$$

$$u_{k,n} = \alpha e^{i\omega(n\tau - {}^{kH}/_{V})}, \quad \text{for} \quad k \geq 0, \tag{6.17b}$$

where V is the velocity of wave in the finite element zone. Since the displacement obtained from Eq. (6.17)a and Eq. (6.17)b at $k = 0$ should be the same, we obtain a relation between the amplitude of transmitted and reflected waves as

$$1 - \beta = \alpha. \tag{6.18}$$

Since the angular frequency of the wave does not alter after passing into the finite element zone, by equating frequency of wave using Eq. (6.6) and Eq. (6.12) (by changing FEM element length to H), we obtain a relationship between the wave velocities in the peridynamic and the finite element zones as

$$\sin^2\left(\frac{\Phi}{2}\right) = \frac{1}{27}\left(\frac{H}{h}\right)^2\left[\sin^2\left(\frac{3\phi}{2}\right) + 3\sin^2\phi + 6\sin^2\left(\frac{\phi}{2}\right)\right], \tag{6.19}$$

where, $\Phi = \frac{\omega H}{V}$. Using Eq. (6.16)a, the equation of motion for the PD point at $k = 0$ can be written as

$$\rho\ddot{u}_0 = F_{-3} + F_{-2} + F_{-1} + F_1^* + F_2^* + F_3^*, \tag{6.20}$$

where F_j^* is the force due to ghost nodes in the FEM region. Here the value of k at three ghost nodes can be given as, $k_1^* = {}^{h}/_{H}, k_2^* = {}^{2h}/_{H}$ and $k_3^* = {}^{3h}/_{H}$. Substituting

Eq. (6.17) in Eq. (6.20) gives (details are presented in Appendix B)

$$\sin^2\left(\frac{\Phi}{2}\right)+\frac{(H/h)^2}{108(1-\beta)}\Big[\alpha\left\{e^{-3i\Phi^h/H}+3e^{-2i\Phi^h/H}+6e^{-i\Phi^h/H}\right\}$$
$$+\left\{e^{3i\phi}+3e^{2i\phi}+6e^{i\phi}-20\right\}-\beta\left\{e^{-3i\phi}+3e^{-2i\phi}+6e^{-i\phi}-20\right\}\Big]=0. \tag{6.21}$$

By solving Eqs (6.18),(6.19) and (6.21), the values of α and β for different ratios of λ/H and H/h can be found.

A similar procedure can be conducted to find the amplitude of transmitted and reflected waves for other values of δ. For example, for $\delta = 2h$, the relationship between the wave velocities in the peridynamics and finite element zones is found by equating Eq. (6.10) and Eq. (6.12)

$$\sin^2\left(\frac{\Phi}{2}\right)=\frac{1}{8}\left(\frac{H}{h}\right)^2\Big[\sin^2\phi+4\sin^2\left(\frac{\phi}{2}\right)\Big], \tag{6.22}$$

and by using the equation of motion of the PD node at $k = 0$ we obtain

$$\sin^2\left(\frac{\Phi}{2}\right)+\frac{(H/h)^2}{32(1-\beta)}\Big[\alpha\left\{e^{-2i\Phi^h/H}+4e^{-i\Phi^h/H}\right\}+\left\{e^{2i\phi}+4e^{i\phi}-10\right\}$$
$$-\beta\left\{e^{-2i\phi}+4e^{-i\phi}-10\right\}\Big]=0. \tag{6.23}$$

The values of α and β can be found by solving Eqs (6.18),(6.22) and (6.23) simultaneously. Finally, for $\delta = h$, the PD formulation reduces to the finite element method. This can be easily verified by using Eq. (6.12) to get

$$\sin\left(\frac{\Phi}{2}\right)=\left(\frac{H}{h}\right)\sin\left(\frac{\phi}{2}\right). \tag{6.24}$$

Using the equation of motion of the PD node at $k = 0$ yields

$$\sin^2\left(\frac{\phi}{2}\right) + \frac{(1}{4(1-\beta)}\left[\alpha\left\{e^{-i\Phi^h/H}\right\} + \left\{e^{i\phi} - 2\right\} - \beta\left\{e^{-i\phi} - 2\right\}\right] = 0. \tag{6.25}$$

The values of α and β for different ratios of λ/H and H/h are plotted in Fig. 6.7. As expected for large wavelengths, there is no reflection and the entire wave travels into the finite element zone. But spurious wave reflections occurs for shorter wave lengths. The amplitude of the reflected wave greatly depends on the λ/H ratio. The effect of the change of δ is dominant for small H/h ratios. As we increase the value of δ, spurious reflection decreases for small H/h ratio but remains almost constant for high H/h ratio.

6.3 Energy flux calculation

Besides the amplitude of the transmitted wave, the energy of the reflected and transmitted wave can be used to study the issue of wave reflection. The energy of a wave is the sum of the potential (strain) and kinetic energy. Consider the plane wave given in Eq. (6.1). The potential energy of the wave stored in a differential length dx of the domain is

$$dE_U = \frac{1}{2}\rho\omega^2 u^2 dx, \tag{6.26}$$

where u is the real part of displacement given by Eq. (6.1). By integrating the above equation over the wavelength of the wave, the potential energy stored in one wavelength is obtained as

$$E_U = \int_0^\lambda \frac{1}{2}\rho\omega^2 u^2 dx = \frac{1}{4}\rho\omega^2 A_0^2 \lambda, \tag{6.27}$$

where λ is the wavelength. The kinetic energy of the wave over length dx is

$$dE_K = \frac{1}{2}\rho\dot{u}^2 dx. \tag{6.28}$$

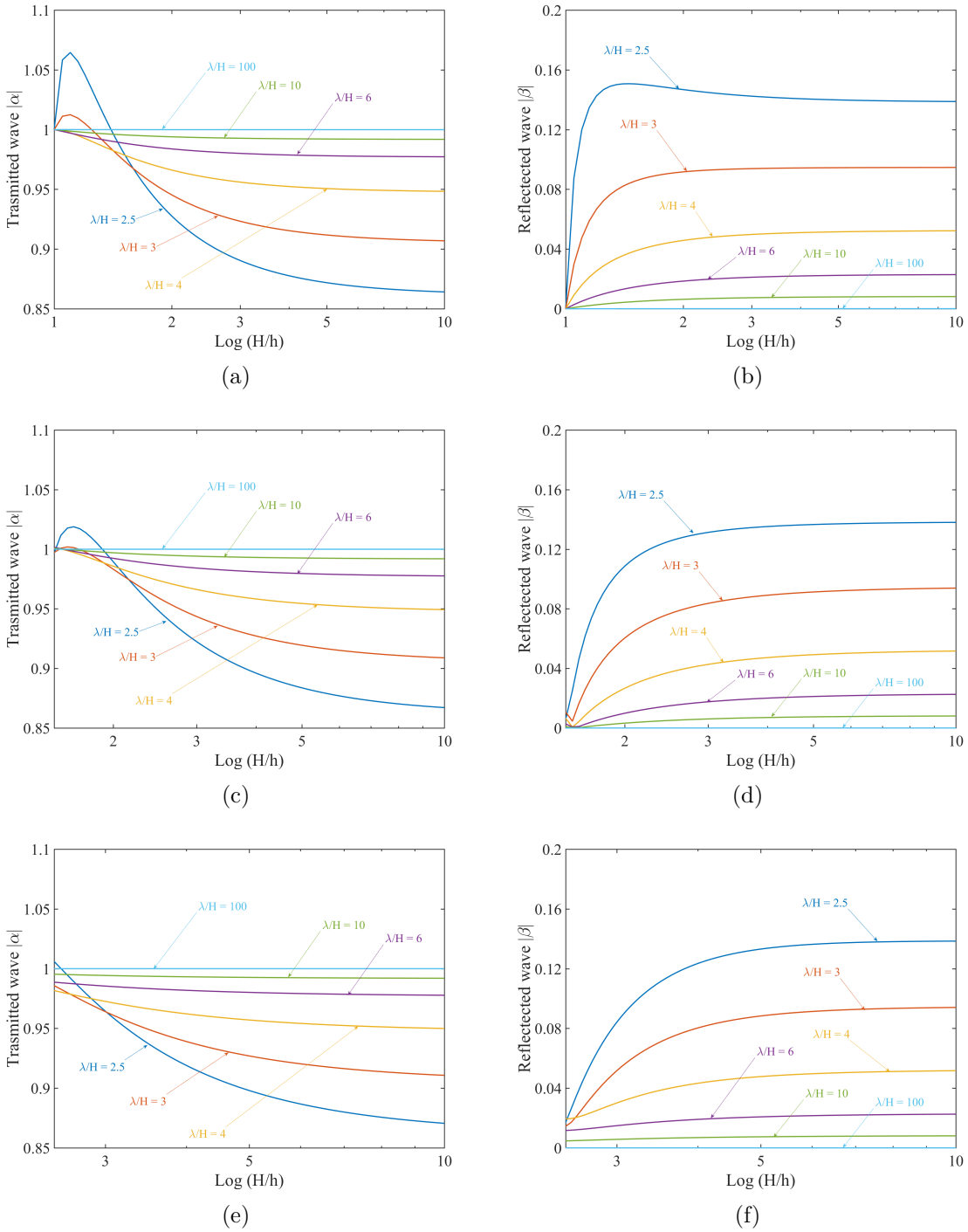

Figure 6.7: Results for amplitude of transmitted wave and reflected wave versus H/h ratio for [(a),(b)] $\delta = h$, [(c),(d)] $\delta = 2h$ and [(e),(f)] $\delta = 3h$ for different λ/H ratios.

The total kinetic energy of the wave in a wavelength λ is

$$E_K = \int_0^\lambda \frac{1}{2}\rho \dot{u}^2 dx = \frac{1}{4}\rho\omega^2 A_0^2 \lambda. \tag{6.29}$$

Hence total energy in one wavelength is

$$E = E_U + E_K = \frac{1}{2}\rho\omega^2 A_0^2 \lambda = \frac{1}{2}\rho\omega^2 A_0^2 vT, \tag{6.30}$$

or the average energy over wave period is

$$\langle P \rangle = \frac{E}{T} = \frac{1}{2}\rho\omega^2 A_0^2 v. \tag{6.31}$$

In the peridynamic zone $v = \frac{\omega h}{\phi}$. Therefore, the average energy of the incident ($A_0 = 1$) and reflected ($A_0 = \beta$) wave can be written as

$$\langle P_I \rangle = \frac{1}{2}\rho\omega^3 \frac{h}{\phi}, \tag{6.32a}$$

$$\langle P_R \rangle = \frac{1}{2}\rho\omega^3 \beta^2 \frac{h}{\phi}. \tag{6.32b}$$

Similarly, in the finite element zone $V = \frac{\omega H}{\Phi}$. Hence the average energy of the transmitted wave ($A_0 = \alpha$) is

$$\langle P_T \rangle = \frac{1}{2}\rho\omega^3 \alpha^2 \frac{H}{\Phi}. \tag{6.33}$$

Hence, the ratios of the energy of the transmitted and reflected waves to the energy of the incident wave can be written as

$$\frac{\langle P_R \rangle}{\langle P_I \rangle} = \beta^2, \tag{6.34a}$$

$$\frac{\langle P_T \rangle}{\langle P_I \rangle} = \alpha^2 \frac{\phi}{\Phi}\left(\frac{H}{h}\right). \tag{6.34b}$$

The above two equations are plotted for different values of λ/H in Fig. 6.8. The results show that very small fraction of energy gets transmitted for high frequency waves. Although the fraction of energy reflecting back in the PD region is small, a huge part of the energy is lost because of a numerical artifact. For low frequency waves almost all energy is transmitted to the FEM part without any energy loss. The sum of the power ratios is always one for higher λ/H ratios, which signifies that there is no energy loss in the system and serves as a check for our calculations.

6.4 Uniform discretization

We study the special case when both the peridynamic and the finite element zone have the same discretization size by setting $h = H$ in Eqs (6.21–6.25). The amplitudes and energies of the transmitted and reflected waves are shown in Fig. 6.9 and Fig. 6.10, respectively. Fig. 6.11 shows the variation in the total energy of the wave with respect to the relative wavelength. The results show that the amplitude of the transmitted wave can be larger than the amplitude of the incident wave. The plots also show that wave reflection happens at low values of λ/h. Since both finite elements and peridynamics have the same grid spacing, the wave reflection occurs due to the change in the domain formulation from a nonlocal to a local continuum. By increasing the value of δ the amplitude of the wave reflection increases which indicates that by increasing the size of horizon the nonlocal effects become more important.

A new coupling method to solve this issue is proposed based on Arlequin method [165–167]. In this method, both the peridynamic domain and finite element domain overlap with each other at the interface. The displacements of the peridynamic nodes are decomposed into two components, first the course displacement, this is the displacement which can be supported by the FE nodes and the second, the fine displacement, this is the displacement which can not be resolved by the FE nodes. A viscous damping is introduced into the equation of motion of the fine displacement part and the fine displacement component is damped out. This results in the

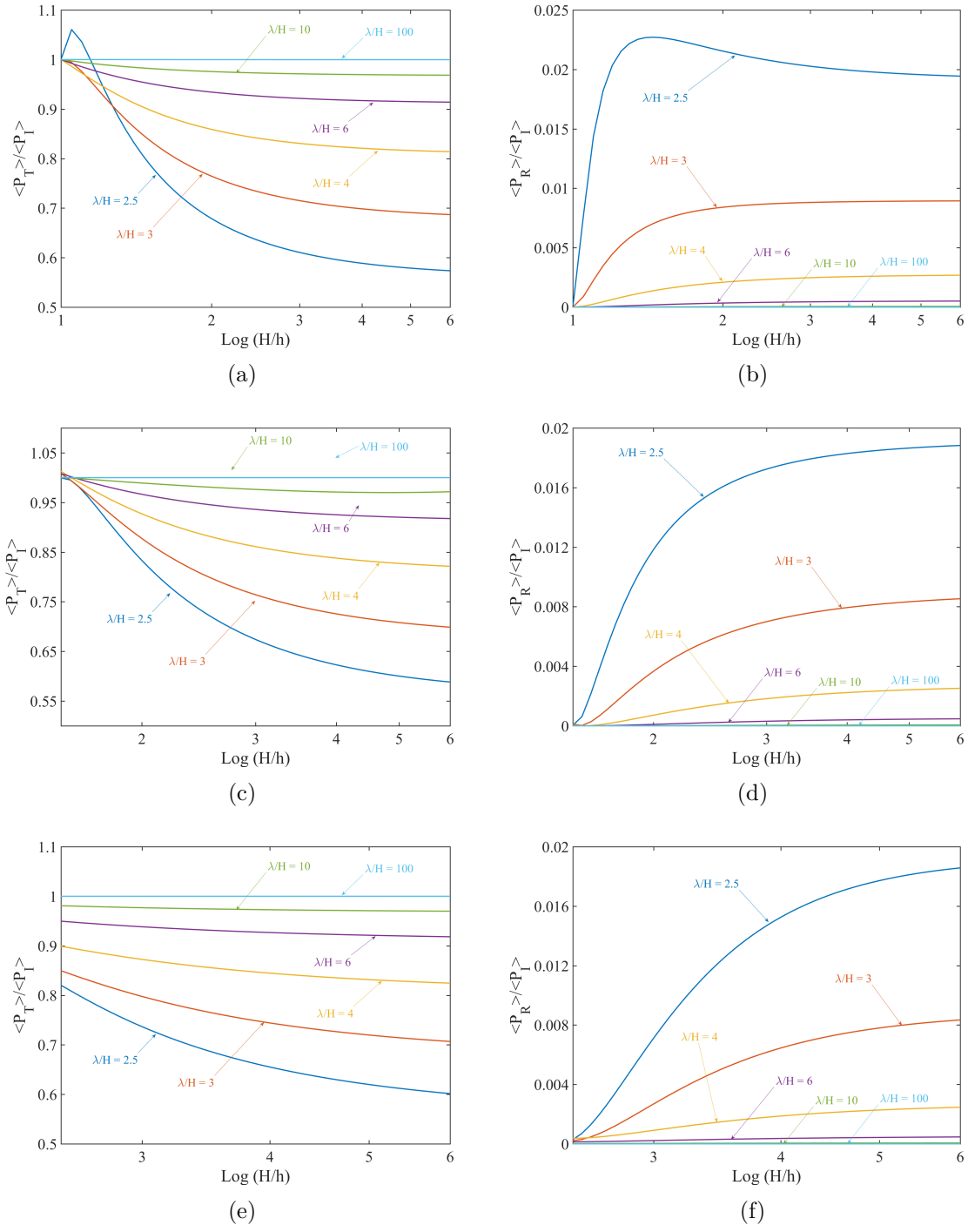

Figure 6.8: Results showing for ratio of average transmitted energy flux and average reflected energy flux to average incident energy flux versus H/h ratio $[(a),(b)]$ $\delta = h$, $[(c),(d)]$ $\delta = 2h$ and $[(e),(f)]$ $\delta = 3h$ for different λ/H ratios.

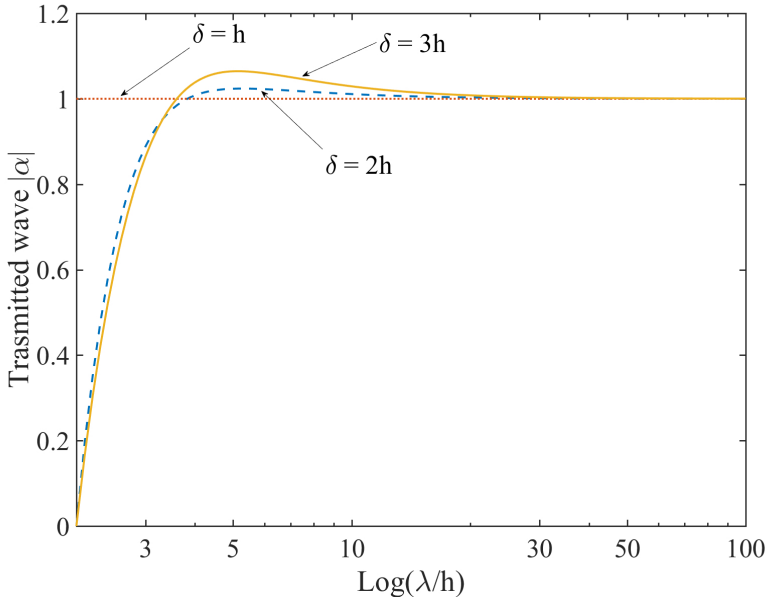

(a)

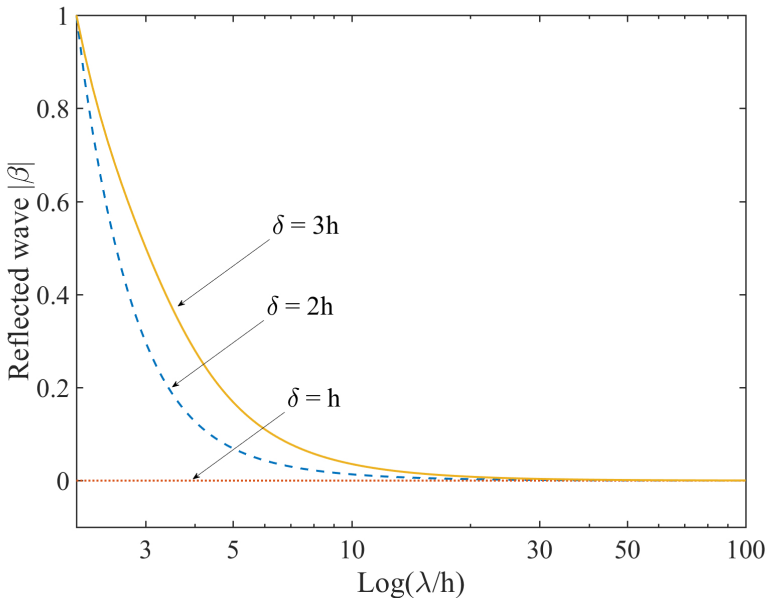

(b)

Figure 6.9: Results for amplitude of (a) transmitted wave and (b) reflected wave versus relative wavelength for uniform mesh.

suppression of the spurious reflection. This method was tested by solving numerous examples and proven to be effective in resolving the issue of spurious reflections. The detailed analysis of this method can be found in [136, 137].

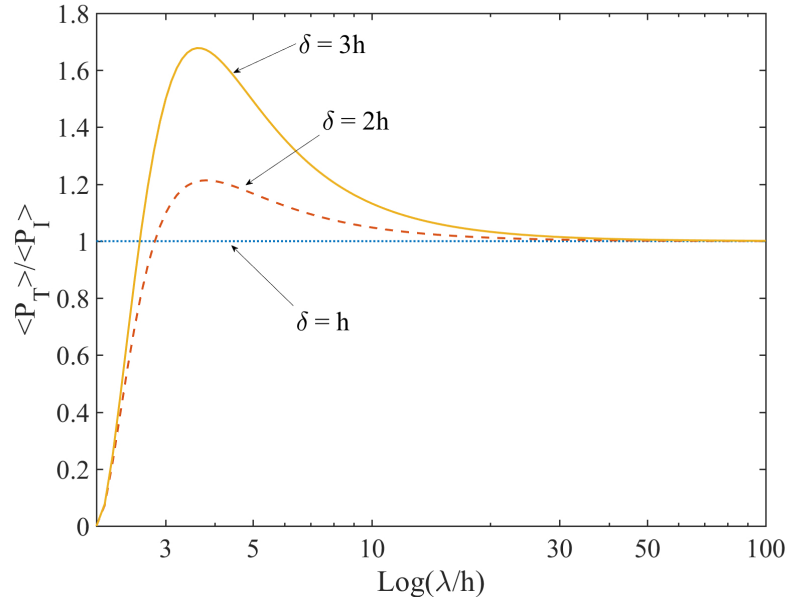

(a)

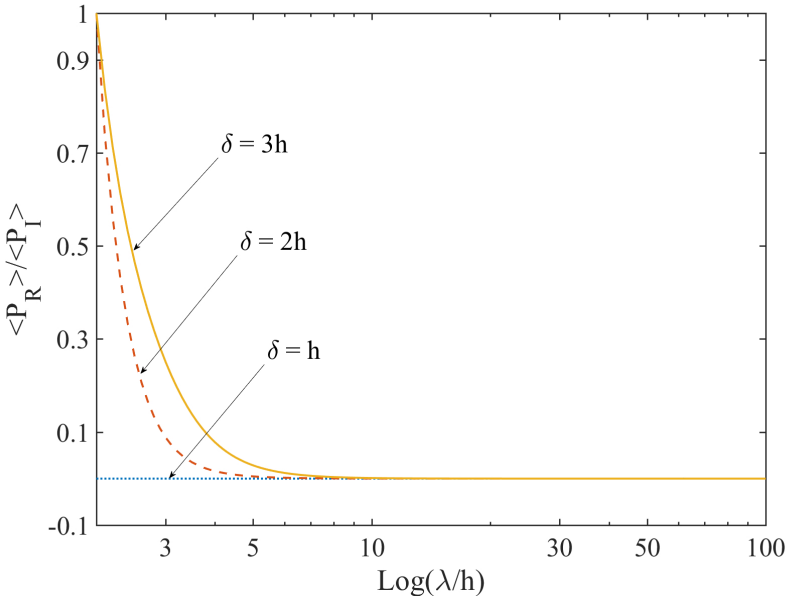

(b)

Figure 6.10: Results for ratio of (a) average transmitted energy flux, and (b) average reflected energy flux to average incident energy flux versus relative wavelength for uniform mesh.

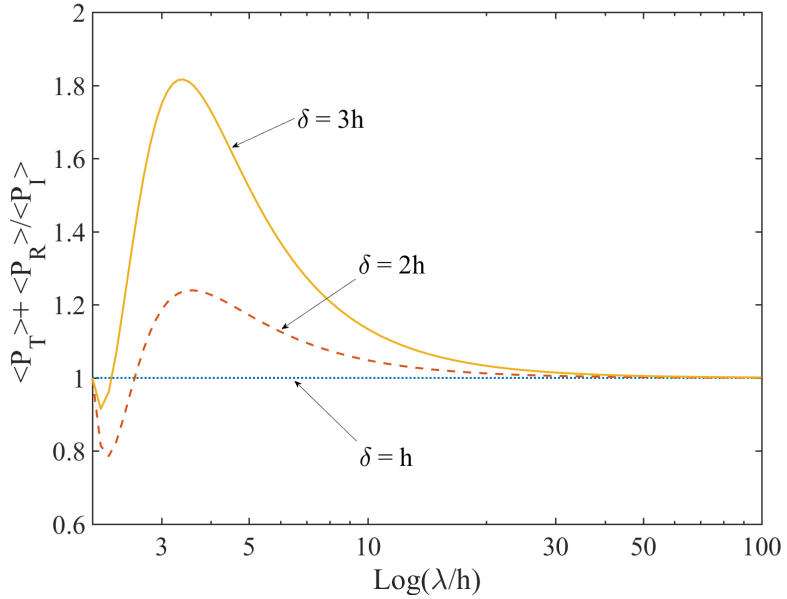

Figure 6.11: Results for ratio of average total energy flux to average incident energy flux versus relative wavelength for uniform mesh.

CHAPTER 7: ANALYTICAL SOLUTION FOR COUPLING OF NONUNIFORM PD

In this chapter, the problem of a one–dimensional elastic wave propagation in a peridynamic grid with uniform spacing everywhere except at one point is analyzed. The PD grid is shown in Fig. 7.1a. As shown, the left and right sides of the domain are discretized with grids of size h and H with $H \geq h$. Similar to previous analysis the nodes are numbered consecutively, and the two grids are connected at node $k = 0$.

We assume that the size of the horizon of the left and right regions of the domain changes according to the grid spacing. For example, if the horizon of the left grid is $\epsilon = 2h$, the horizon of the right grid is $\delta = 2H$. Since $H \geq h$, the nodes of the left region which are close to the interface have fewer nodes in their horizon than the other nodes of the left region. On the other hand, the nodes of the right region which are close to the interface have a greater number of nodes in their horizon than the other nodes of the right region. We assume the node at $k = 0$ has the same horizon

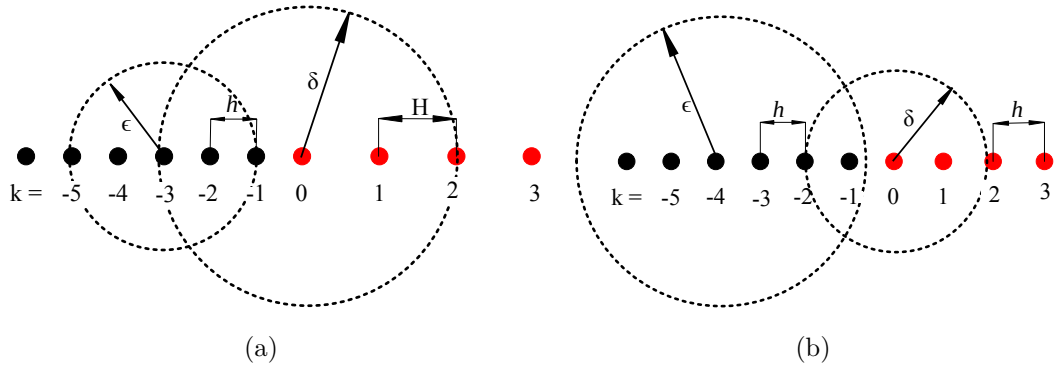

Figure 7.1: Coupling of peridynamics regions for different horizons with (a) different mesh size and (b) same mesh size.

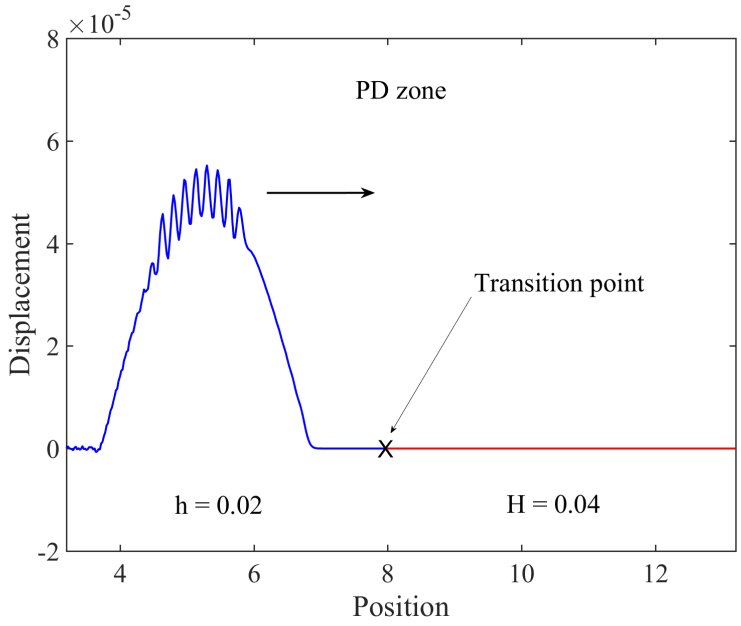

(a)

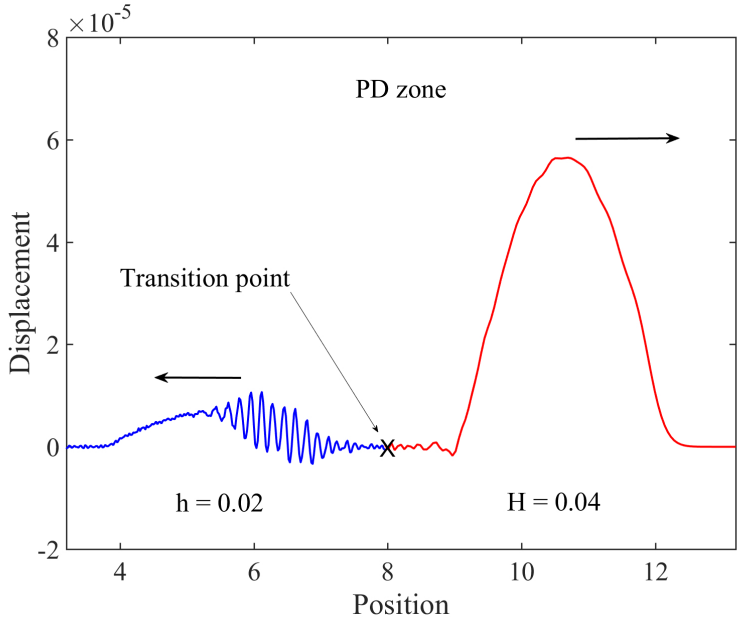

(b)

Figure 7.2: (a) incident waves and (b) reflection of high frequency wave from transition point for nonuniform mesh using only PD.

size δ of the right hand zone.

We model the propagation of the wave presented in Eq. (6.15) from a peridynamic grid with $h = 0.02$ to another grid with $H = 0.04$ using the described coupling method

for a linear elastic material. The snapshot of the wave before and after reaching the interface point is shown in Fig. 7.2a and Fig. 7.2b, respectively. It is interesting to note that the amplitude of the transmitted wave is more than amplitude of the incident wave. Also, as expected, the high frequency wave spuriously reflects back into the peridynamic zone. Additionally, we observe that some part of low frequency wave also reflects from interface point. In what follows we obtain the amplitude of the reflected and transmitted waves as a function of the grid spacings and the peridynamic horizon size. To simplify the calculations, we assume that wave reflection occurs only at $k = 0$.

7.1 Horizon three times the mesh size

Since the angular frequency of the wave does not change by transmission from the left region to the right region, a relation between the wave velocities in two regions can be obtained by using Eq. (6.6)

$$\sin^2\left(\frac{3\phi}{2}\right) + 3\sin^2\phi + 6\sin^2\left(\frac{\phi}{2}\right) = \left(\frac{h}{H}\right)^2\left[\sin^2\left(\frac{3\Phi}{2}\right) + 3\sin^2\Phi + 6\sin^2\left(\frac{\Phi}{2}\right)\right], \quad (7.1)$$

where $\phi = \frac{\omega h}{v}$ and $\Phi = \frac{\omega H}{V}$. the equation of motion of node $k = 0$ can be expressed as

$$\rho\ddot{u} = F_{-3} + F_{-2} + F_{-1} + F_1 + F_2 + F_3, \quad \text{for} \quad 1 \le H/h < 1.333, \quad (7.2a)$$

$$\rho\ddot{u} = F_{-4} + F_{-3} + F_{-2} + F_{-1} + F_1 + F_2 + F_3, \quad \text{for} \quad 1.333 \le H/h < 1.666, \quad (7.2b)$$

$$\rho\ddot{u} = F_{-5} + F_{-4} + F_{-3} + F_{-2} + F_{-1} + F_1 + F_2 + F_3, \quad \text{for} \quad 1.666 \le H/h < 2, \quad (7.2c)$$

$$\rho\ddot{u} = F_{-6} + F_{-5} + F_{-4} + F_{-3} + F_{-2} + F_{-1} + F_1 + F_2 + F_3, \quad \text{for} \quad 2 \le H/h < 2.333, \quad (7.2d)$$

where F_i is the force exerted by node i on node $k = 0$. The forces F_i are given in the right hand side of Eq. (2.15). By using Eq. (6.17) as the displacement field, the equation of motion of node $k = 0$ can be written as

$$\text{for} \quad 1 \le H/h < 1.333 :$$
$$\sin^2\left(\frac{3\Phi}{2}\right) + 3\sin^2\Phi + 6\sin^2\left(\frac{\Phi}{2}\right) + \frac{1}{4\alpha}\Bigg[\left(6\frac{H}{h} - 5\right)(e^{3i\phi} - \beta e^{-3i\phi} - \alpha)$$
$$+3(e^{2i\phi} - \beta e^{-2i\phi} - \alpha) + 6(e^{i\phi} - \beta e^{-i\phi} - \alpha) + 6\alpha(e^{-i\Phi} - 1)$$
$$+3\alpha(e^{-2i\Phi} - 1) + \alpha(e^{-3i\Phi} - 1)\Bigg] = 0,$$

$$\text{for} \quad 1.333 \le H/h < 1.666 :$$
$$\sin^2\left(\frac{3\Phi}{2}\right) + 3\sin^2\Phi + 6\sin^2\left(\frac{\Phi}{2}\right) + \frac{1}{16\alpha}\Bigg[3\left(6\frac{H}{h} - 7\right)(e^{4i\phi} - \beta e^{-4i\phi} - \alpha)$$
$$+8(e^{3i\phi} - \beta e^{-3i\phi} - \alpha) + 12(e^{2i\phi} - \beta e^{-2i\phi} - \alpha) + 24(e^{i\phi} - \beta e^{-i\phi} - \alpha)$$
$$+24\alpha(e^{-i\Phi} - 1) + 12\alpha(e^{-2i\Phi} - 1) + 4\alpha(e^{-3i\Phi} - 1)\Bigg] = 0,$$

$$\text{for} \quad 1.666 \le H/h < 2 :$$
$$\sin^2\left(\frac{3\Phi}{2}\right) + 3\sin^2\Phi + 6\sin^2\left(\frac{\Phi}{2}\right) + \frac{1}{40\alpha}\Bigg[6\left(6\frac{H}{h} - 9\right)(e^{5i\phi} - \beta e^{-5i\phi} - \alpha)$$
$$+15(e^{4i\phi} - \beta e^{-4i\phi} - \alpha) + 20(e^{3i\phi} - \beta e^{-3i\phi} - \alpha) + 30(e^{2i\phi} - \beta e^{-2i\phi} - \alpha)$$
$$+60(e^{i\phi} - \beta e^{-i\phi} - \alpha) + 60\alpha(e^{-i\Phi} - 1) + 30\alpha(e^{-2i\Phi} - 1) + 10\alpha(e^{-3i\Phi} - 1)\Bigg] = 0,$$

$$\text{for} \quad 2 \le H/h < 2.333 :$$
$$\sin^2\left(\frac{3\Phi}{2}\right) + 3\sin^2\Phi + 6\sin^2\left(\frac{\Phi}{2}\right) + \frac{1}{40\alpha}\Bigg[5\left(6\frac{H}{h} - 11\right)(e^{6i\phi} - \beta e^{-6i\phi} - \alpha)$$
$$+12(e^{5i\phi} - \beta e^{-5i\phi} - \alpha) + 15(e^{4i\phi} - \beta e^{-4i\phi} - \alpha) + 20(e^{3i\phi} - \beta e^{-3i\phi} - \alpha)$$
$$+30(e^{2i\phi} - \beta e^{-2i\phi} - \alpha) + 60(e^{i\phi} - \beta e^{-i\phi} - \alpha)$$
$$+60\alpha(e^{-i\Phi} - 1) + 30\alpha(e^{-2i\Phi} - 1) + 10\alpha(e^{-3i\Phi} - 1)\Bigg] = 0. \tag{7.3}$$

The amplitudes of the transmitted wave α and reflected wave β can be found by solving Eqs (6.18), (7.1) and (7.3).

7.2 Horizon two times the mesh size

The relation between wave velocities in the two regions can be obtained by using Eq. (6.10)

$$\sin^2\phi + 4\sin^2\left(\frac{\phi}{2}\right) = \left(\frac{h}{H}\right)^2\left[\sin^2\Phi + 4\sin^2\left(\frac{\Phi}{2}\right)\right]. \tag{7.4}$$

The equation of motion for node $k = 0$ can be given as follows,

$$\rho\ddot{u} = F_{-2} + F_{-1} + F_1 + F_2 \quad \text{for} \quad 1 \leq H/h < 1.5, \tag{7.5a}$$

$$\rho\ddot{u} = F_{-3} + F_{-2} + F_{-1} + F_1 + F_2 \quad \text{for} \quad 1.5 \leq H/h < 2, \tag{7.5b}$$

$$\rho\ddot{u} = F_{-4} + F_{-3} + F_{-2} + F_{-1} + F_1 + F_2 \quad \text{for} \quad 2 \leq H/h < 2.5. \tag{7.5c}$$

By finding the forces F_i using Eq. (2.15) and displacement field from Eq. (6.17), the equation of motion of node $k = 0$ can be written as

$$\text{for} \quad 1 \leq H/h < 1.5 :$$
$$\sin^2\Phi + 4\sin^2\left(\frac{\Phi}{2}\right) + \frac{1}{4\alpha}\Bigg[\left(4\frac{H}{h} - 3\right)(e^{2i\phi} - \beta e^{-2i\phi} - \alpha)$$
$$+4(e^{i\phi} - \beta e^{-i\phi} - \alpha) + 4\alpha(e^{-i\Phi} - 1) + \alpha(e^{-2i\Phi} - 1)\Bigg] = 0,$$

$$\text{for} \quad 1.5 \leq H/h < 2 :$$
$$\sin^2\Phi + 4\sin^2\left(\frac{\Phi}{2}\right) + \frac{1}{6\alpha}\Bigg[\left(4\frac{H}{h} - 5\right)(e^{3i\phi} - \beta e^{-3i\phi} - \alpha) + 3(e^{2i\phi} - \beta e^{-2i\phi} - \alpha)$$
$$+6(e^{i\phi} - \beta e^{-i\phi} - \alpha) + 6\alpha(e^{-i\Phi} - 1) + \frac{3}{2}\alpha(e^{-2i\Phi} - 1)\Bigg] = 0,$$

$$\text{for} \quad 2 \leq H/h < 2.5 :$$
$$\sin^2\Phi + 4\sin^2\left(\frac{\Phi}{2}\right) + \frac{1}{24\alpha}\Bigg[3\left(4\frac{H}{h} - 7\right)(e^{4i\phi} - \beta e^{-4i\phi} - \alpha) + 8(e^{3i\phi} - \beta e^{-3i\phi} - \alpha)$$
$$+12(e^{2i\phi} - \beta e^{-2i\phi} - \alpha) + 24(e^{i\phi} - \beta e^{-i\phi} - \alpha) + 24\alpha(e^{-i\Phi} - 1) + 6\alpha(e^{-2i\Phi} - 1)\Bigg] = 0. \tag{7.6}$$

Eq. (7.6) can be solved along with Eqs (6.18) and (7.4) to obtain amplitudes of reflected and transmitted waves.

7.3 Discussion of the results

The amplitude of the transmitted and reflected wave for two cases of $\lambda/H = 2.5$ and $\lambda/H = 50$ are shown in Fig. 7.3. The discontinuities in the values of α and β observed in the graphs of Fig. 7.3, occurs when the number of nodes within the horizon of node $k = 0$ changes.

The plots of Fig. 7.3 show that when the wave passes between two PD grids of different sizes, a spurious wave reflection occurs. The wave reflection is more severe for higher values of H/h, i.e. when the grid size changes more drastically. An important

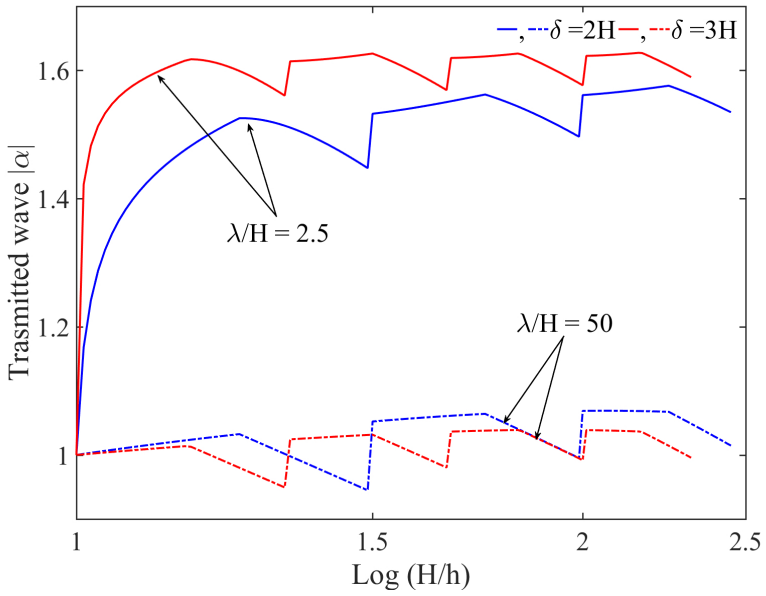

(a)

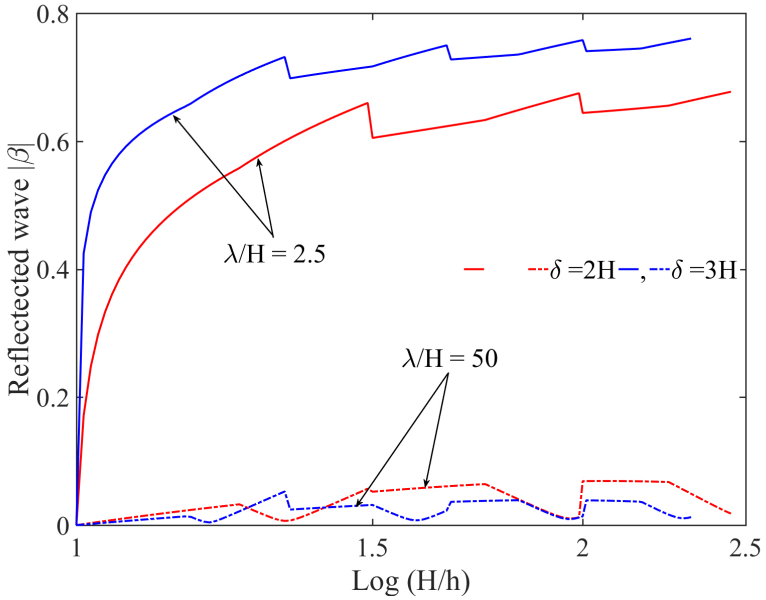

(b)

Figure 7.3: Results for amplitude of (a) transmitted and (b) reflected wave at interface point for PD with non uniform mesh.

observation is that the amplitude of the transmitted wave is higher than the amplitude of the incident wave. When the grids become finer compared with the wavelength, i.e. when λ/H increases, the amplitudes of both the reflected and the transmitted wave

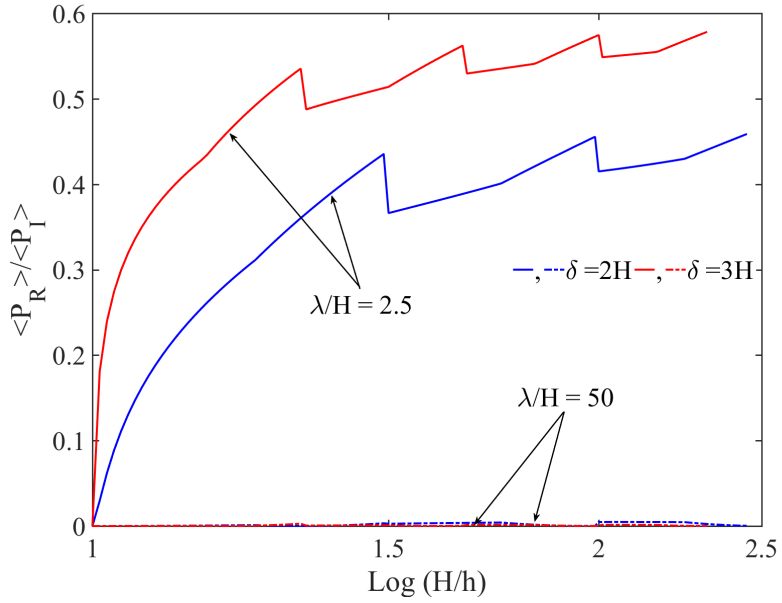

(a)

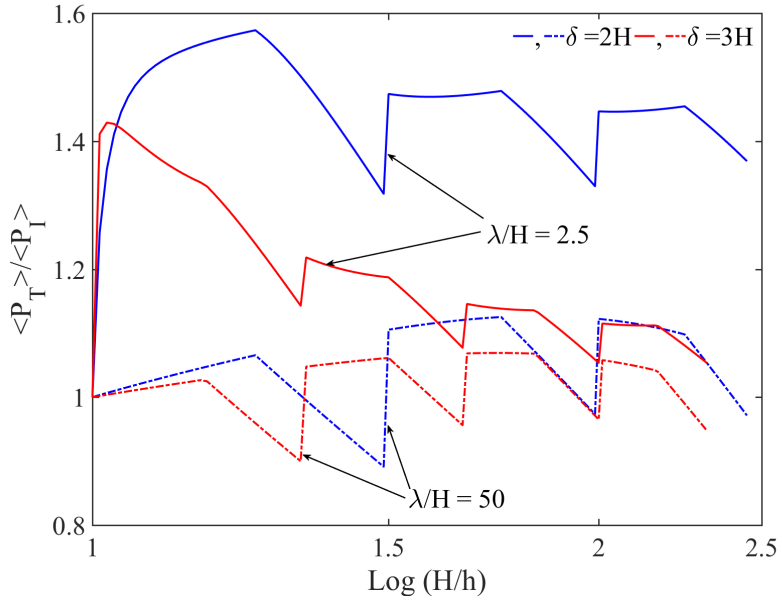

(b)

Figure 7.4: Fraction of energy (a) reflected, and (b) transmitted for non uniform PD for different λ/H ratios and different values of δ.

reduce. However, spurious wave reflections do not disappear even when $\lambda/H = 50$.

The wave reflection is studied further by plotting the ratio of the average energy flux of the reflected and transmitted wave to the average energy flux of the incident

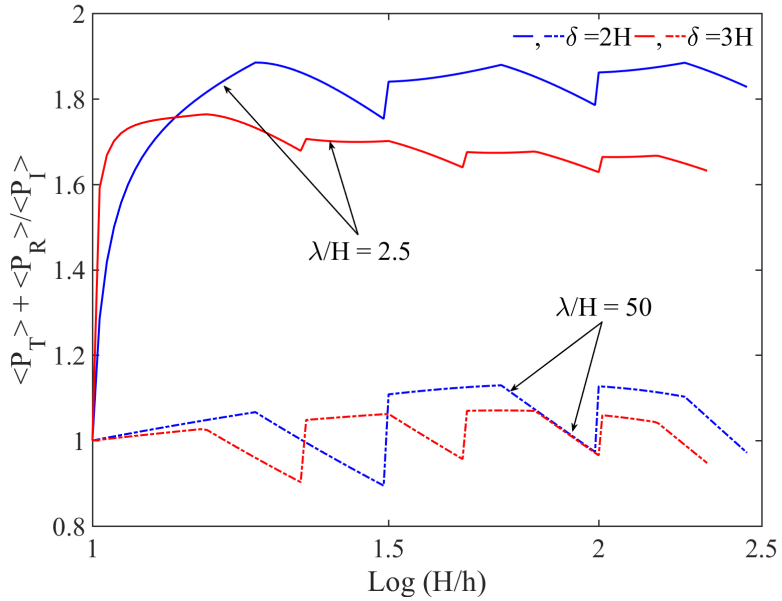

Figure 7.5: Results for ratio of average total energy flux to average incident energy flux versus relative wavelength for non uniform PD for different λ/H ratios and different values of δ.

wave as shown in Fig. 7.4. These graphs show that when $\lambda/H = 50$ the energy of the reflected wave is less than 2% of the energy of the incident wave. On the other hand, when $\lambda/H = 2.5$, the energy of the reflected wave can be as high as 60% percent of the energy of the incident wave. The ratio of the average energy flux of both the transmitted and reflected wave to the average energy flux of the incident wave is shown in Fig. 7.4c. This figure shows that the total energy of the transmitted and reflected waves is higher than the total energy of the incident wave. This is mainly because the amplitude of the transmitted wave is higher than the amplitude of the incident wave.

As a special case, we study the propagation of wave when only the size of the horizon changes and the grid size remains uniform, i.e. $H = h$, as shown in Fig. 7.1b. The peridynamic horizon size for $k < 0$ is $\epsilon = 3h$ and for $k \geq 0$ the horizon $\delta = 2h$. In this case, the relation between the wave velocities in the two regions is obtained

by equating Eq. (6.6) and Eq. (6.10)

$$\sin^2\Phi + 4\sin^2\left(\frac{\Phi}{2}\right) = \frac{8}{27}\left[\sin^2\left(\frac{3\phi}{2}\right) + 3\sin^2(\phi) + 6\sin^2\left(\frac{\phi}{2}\right)\right], \tag{7.7}$$

here $\Phi = \frac{\omega h}{V}$ and $\phi = \frac{\omega h}{v}$, where v and V are the wave velocities in the left and right regions, respectively. After substituting the solution from Eq. (6.17) into the equation of motion for point $k = 0$ using Eq. (6.16) we get,

$$\sin^2\phi + 4\sin^2\left(\frac{\phi}{2}\right) + \frac{1}{4\alpha}\left[\alpha e^{-2i\Phi} + 4\alpha e^{-i\Phi} + e^{2i\phi} + 4e^{i\phi} - \beta e^{-2i\phi} - 4\beta e^{-i\phi} - 10\alpha\right] = 0. \tag{7.8}$$

Eqs (6.18), (7.7) and (7.8) can be used to find the amplitude of the transmitted and reflected waves. These amplitudes along with the ratios of the average energy flux are plotted in Fig. 7.6. These figures show that even when the grid is uniform, wave reflection can occur. This reflection is due to the change in the size of the peridynamic horizon. For λ/h ratio more than 20, the wave passes without any spurious reflection through the transition point. The simplest way to avoid this is by filtering out wavelengths with a λ/H ratio less than 20. Other techniques for resolving the issue of wave reflection due to the change of the grid or horizon size are presented in [134, 135].

7.3.1 Comparison with numerical results

The analytical results of this section are verified with the numerical results. For this purpose the wave propagation in a bar of length 20 mm is modeled. The domain is discretized in the left by a grid with a node spacing of $h = 0.02$ mm. To study the impact of the ratio of H/h, the grid spacing H of the right side of the domain is varied. A plane wave with amplitude of 10^{-4} mm represented by

$$u_k = 10^{-4} e^{i\omega(\tau n - kh/v)}, \tag{7.9}$$

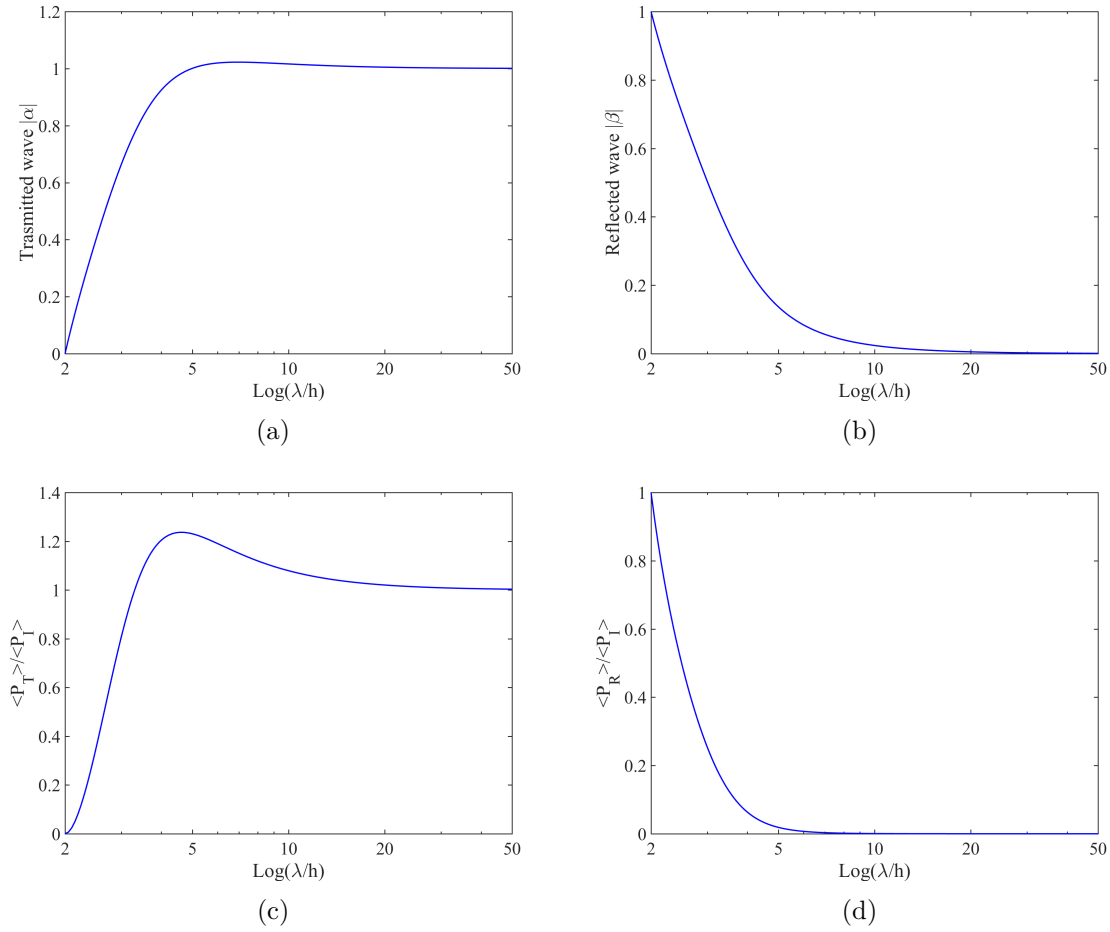

Figure 7.6: Results for dual horizon PD with uniform mesh for (a) transmitted wave, (b) reflected wave, (c) fraction of transmitted average energy flux and (d) fraction of reflected average energy flux.

travels from left to rigth and the amplitudes of the reflected and the transmitted waves are measured. A time step of $\tau = 10^{-3}$ s is chosen for numerical integration.

Results of the numerical simulations are shown in Fig. 7.7 and are compared with the analytical results. We can see that for $\delta = H$ results are in excellent agreement with the analytical predictions. When $\delta = 2H$, the amplitudes of reflected and transmitted waves are following the same trend as is predicted by the analytical method, however the values of the amplitudes are different. This difference between numerical and analytical results can be due to the assumption that wave reflection occurs only at $k = 0$.

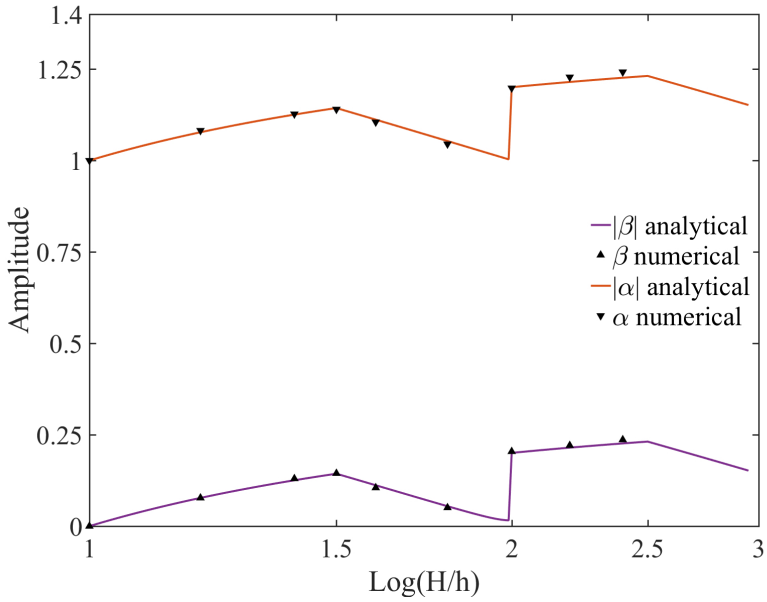

(a)

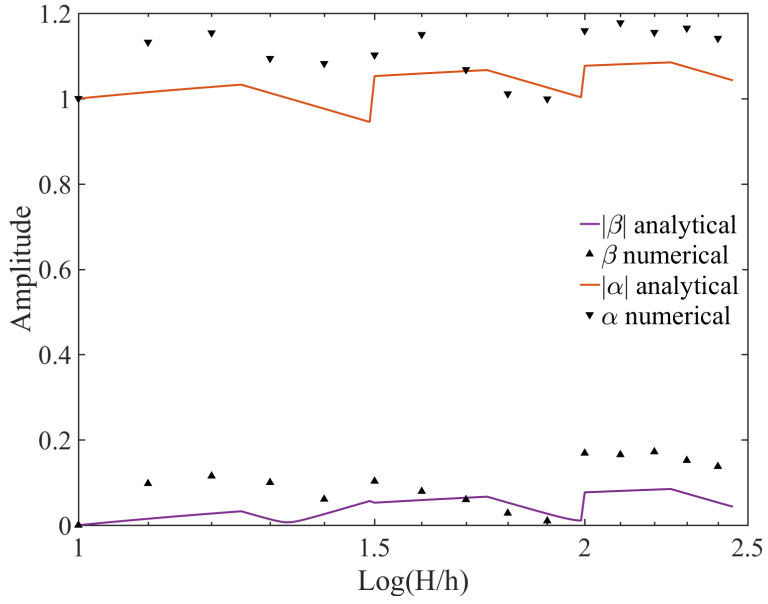

(b)

Figure 7.7: Comparison of numerical results with analytical results for $L/H = 50$ for (a) $\delta = H$ and (b) $\delta = 2H$.

CHAPTER 8: CONCLUSIONS

The Peridynamic formulation to predict the creep in metal using a stress based damage model is presented. The Liu-Morakami creep damage model was used to model creep. The dynamic relaxation method was used to obtain steady state results from the dynamic formulation of PD. The influence function of the peridynamics formulation is modified to incorporate damage from the Liu-Morakami creep model. Robustness of the proposed model was shown by solving a plain stress 2D example and comparing results with finite element models. 316 Stainless steel at 600° C is used as a material for the creep test. Results were in good agreement with the FEM with the maximum error of less than 9%. Also, a 3D uniaxial creep test was simulated using peridynamics and results were compared with the finite element model which shows good agreement with each other.

Crack propagation due to creep was simulated for the same material, 316 stainless steel, for a plane stress condition. As fictitious node method to reduce the skin effect cannot be used at a crack tip or newly formed crack surfaces. Some error was observed for the stress field near the crack tip, but the overall results were in good agreement with FEM. Finally, the bending problem was solved using the new formulation. This new formulation gives an alternative way for modeling creep in metals using peridynamics allowing us to exploit the salient features of PD while modeling creep.

We also studied the one–dimensional wave propagation in a domain composed of two regions. Two cases were considered. In the first case, peridynamics is used in one zone and the finite element method is used in the other zone. In the second case, peridynamics is used everywhere, but the grid spacing and horizon size change

between the two regions. Using an analytical approach, we showed that spurious wave reflections occur in both cases. The amplitude of the spurious waves depends on factors such as the wavelength of the incident wave, the ratio of the grid spacing in the two regions of the domain, and the horizon size of the peridynamic zone. As the ratio of the wavelength to grid size increases, the spurious wave reflection reduces. The wave reflection gets worse when the size of the resolution of the grids changes more drastically, but wave reflection can happen even when the grid spacings are close to each other. The results also showed that an increase in the horizon size leads to more wave reflection at the interface of the two zones.

A difference between the two cases is on the amplitude of the transmitted wave. When the coupled peridynamic–finite element technique was used to model the wave propagation, the amplitude of the transmitted wave into the finite element zone was always less than the amplitude of the incident wave. However, when peridynamics is used on the two different grids, the amplitude of the transmitted wave into the coarser grid can be larger than the amplitude of the incident wave. This means that the energy of the transmitted wave is higher than the energy of the initial wave. This is an artifact of the numerical modeling and significantly reduces the computational accuracy.

Part II

Study of the damping properties of polymer composites

CHAPTER 9: INTRODUCTION

9.1 Background and motivation

Vibrations are inevitably present during the operation of equipments and vehicles. Effective damping of vibrations is essential in the design of structural components since excessive vibrations can damage or adversely affect the in-service performance of equipments and structures. Material damping using polymer composites provides an effective solution to the damping problems of a wide spectrum of industries including automotive [168, 169], aerospace [169], civil engineering [170] and food packaging [171,172]. One example of such material is polyurea. Remarkable strength and adhesion characteristics of polyurea along with its high toughness to density ratio, its ability to resist abrasion, corrosion and impact bring it a wide range of applications including corrosion protection, membranes, containments, and lining. A recent development of spray polyurea elastomer technology (SPUA) has enabled the use of polyurea for direct spray coating on a vast type of surfaces to enhance their mechanical properties and durability [173]. It is shown that implementing the polyurea coating on structural components act as a protective layer which reduces damage to the structures and personnels under blast and impact loading [173–177]. Due to such a wide spectrum of applications, polyurea undergoes different loading conditions at different strain and strain rates. Predicting and understanding the behavior of polyurea coated structures under different loading conditions necessitates the development of a reliable constitutive model for polyurea. The proposed constitutive model should be able to capture the behavior of polyurea at large deformations under different strain rates from quasi-static loadings to high strain rates under impact.

For practical purposes, constitutive models should be simple with few material

parameters which can be determined from standard experiments. In this dissertation, we use the experimental data of Ronald et al. [178] and Serva et al. [179] to propose two frame–independent incompressible hyper-viscoelastic models for both tensile and compressive behavior of polyurea.

Similar to most polymers, polyurea displays strain rate stiffening and strengthening effects even at low and intermediate strain rates [178–182]. Experiments indicate that polyurea is an incompressible elastomer and its stress-strain behavior depends significantly on temperature, pressure and strain rate [175, 183]. Gamonpilas and McCuiston [184] developed a nonlinear constitutive viscoelastic model assuming separable time and strain-dependent behavior. They used a Mooney–Rivlin model to describe the strain-dependent behavior of polyurea and Prony series to capture its time-dependent behavior. Li and Lua [185] proposed a nonlinear hyper-viscoelastic constitutive model for polyurea under compression loading. They employed the Ogden model to describe the the hyperelastic behavior of polyurea under quasi-static loading and a hereditary integral with a Zaps (BKZ) memory function for the viscoelastic behavior. Amirkhizi et al. [175] used the Prony series to model the behavior of polyurea in compression and considered the effects of temperature and pressure using William-Landel-Ferry (WLF) equation. Although the above mentioned constitutive models are comparatively simple, however, since they use constant rate independent material parameters, their application is limited to a narrow range of strain rates. More complicated constitutive models have been developed which can predict the response of polyurea under a wider range of strain rates. Shim and Mohr [181] used the approach of multiplicative decomposition of deformation gradients to propose a nonlinear viscoelastic model for the behavior of polyurea under compression. They used two parallel Maxwell elements and a Gent spring to describe loading and unloading behavior. Elsayed et al. [176] developed a variational constitutive model by decomposing the mechanical response of polyurea into equilibrium and nonequilib-

rium components and used it to model ballistic impact on steel–polyurea composite plates. Although these constitutive models can predict the response of polyurea accurately, however, implementing these models in a finite element code is complicated and they have been developed only for compressive loading mode [186].

Although, these polymers have great damping capacity they lack in strength. Hence it is essential to come up with some technique in order to increase their strength. Therefore, Polymer Matrix Composites (PMCs) are invented in which fillers are added to increase the strength and stiffness of polymers. The addition of inclusions, however, can alter the damping properties of the polymer matrix. Damping properties of PMCs can be tailored by properly choosing the size, shape, volume fraction and constitutive properties of the inclusions. Hence, to design polymer composites which demonstrate high damping capability it is imperative to understand how the properties of inclusions affect the damping properties of polymer matrix composites.

Several efforts have been made in the past to study the damping properties of polymer composites as a function of their constituents properties. Most of these methods are limited to fiber–reinforced or laminated composites under a two–dimensional state of stress. Adams and Bacon [187] developed a micromechanical model to predict damping in unidirectional fiber–reinforced composites. Hwang and Gibson [188] proposed a strain energy–finite element method to study the damping of discontinuous fiber reinforced composites. Kaliske and Rother [189] employed a consistent micromechanical theory of a representative fiber matrix cell to predict material damping of fiber composites. They obtained six damping coefficients corresponding to six stress components. Brinson and Lin [190] used Mori-Tanaka [191] and Halpin-Tsai [192] homogenization techniques to predict the loss and storage modulus of fiber reinforced polymer composites. Although their model shows good agreement with finite element results [193] however they considered only one inclusion in the computation unit cell. As the number of inclusions increases their model loses accuracy since it

does not take into account the interactions between inclusions. More recently, Moore et al. [194] used a multiscale approach to augment the Mori-Tanaka and Halpin-Tsai models by an additional interaction term between inclusions. They assumed that inclusions have a cubic shape and obtained the additional interaction term based on stress concentration factors.

Stochastic Finite Element Method (SFEM) simulations are mostly focused on material and geometric uncertainties. Random variables are treated as Gaussian or non-Gaussian distributions. Kaminski et al. [195] applied stochastic perturbation technique together with the finite element method to calculate effective elastic properties of the rubber-carbon composite. They also studied the effect of interface defects on overall elastic properties [196]. The bonding between filler particles and the matrix is never perfect. Due to the presence of some imperfections such as voids or inconsistencies, material properties near the boundary of filler particles can vary significantly from both filler particle and matrix. This can be modeled by adding a thin layer all around the filler particles. In the past, many experiments have been done to prove the existence of such interphase and its thickness is estimated to be between 30 to 240 nm [197–200]. Therefore it is important to study the effect of interphase on damping properties. In this dissertation affect of interphase is assumed to be negligible. More details about interphase can be found out in [201–204].

9.2 Original features of dissertation

Ogden model and Mooney-Rivlin model are used to represent the hyperelastic behavior of polyurea at low strain rates while standard linear solid (SLS) model and K-BKZ model are used to model its viscoelastic behavior at high strain rates. A distinct feature of the proposed constitutive models is their rate dependent material parameters which allow replicating the experimental results in a wide range of tensile and compressive strain rates. Comparison of the proposed models with the experimental results indicates that proposed hyper–viscoelastic models can accurately

model the behavior of polyurea under various tensile and compressive strain rates.

In this part of dissertation, the finite element method is used to investigate the damping properties of polymer composites aiming at quantifying the key parameters influencing the damping quality of polymer composites. Both two-dimensional and three–dimensional modelings are performed. A wide range of properties for the inclusions and matrix as well as the size of the inclusions are considered. To consider the interaction between inclusions, the representative volume elements (RVEs) used in our modelings include multiple inclusions. The properties of RVEs can be predicted using either a periodic or mixed boundary condition for the RVEs. We also compare the results obtained from periodic and mixed boundary conditions by conducting simulations using both periodic and mixed boundary conditions for the RVEs. Finite element modeling results are compared with results from analytical micromechanics methods such as rules of mixtures, Halpin-Tsai, Hashin-Shtrikman, and Mori-Tanaka. Finally, we conduct sensitivity analyses to determine the material properties that play a more significant role on the damping properties of polymer composites.

9.3 Outline of dissertation

Outline of part II of the dissertation is as follows, first chapter 9 gives the background and motivation of this study. Then chapter 10 describes the theoretical background required for the study. This includes kinematics of continuum mechanics followed by hyper-elastic material models descriptions (Ogden model and Mooney-Rivin model) and visco-elastic material models descriptions (SLS model and K-BKZ model). Next, chapter 11 talks about the proposed hyper-viscoelastic model for polyurea and gives all material parameters in details.

Chapter 12 elaborates the material models used for the study of damping capacity of polymer composites. It also gives predictions of the damping capacity of polymer composites using micro-mechanics analytical methods such as Mori-Tanaka, Halpin-Tsai etc. Chapter 13 lays down the ground for finite element study of damping

properties by explaining the RVE generation algorithm, model geometry and boundary conditions used. Following chapter, chapter 14, explains the results obtained by finite element analysis. Results are obtained for 2D as well as 3D models using different types of boundary conditions. Lastly, chapter 15 shows the results of sensitivity analysis which gives the effect of uncertainty on material parameters on damping property of composite. Finally, part II concludes with chapter 16.

CHAPTER 10: THEORETICAL BACKGROUND

10.1 Kinematics

Consider a continuum body $\mathcal{B}$ which moves in space from an initial (reference) configuration Ω_0 to a current configuration Ω as shown in Fig. 10.1. Let the position vector of particles in the initial and current configurations be denotes with $\boldsymbol{X}$ and $\boldsymbol{x}$, respectively. The motion of body $\mathcal{B}$ is defined by a vector field $\boldsymbol{\Phi}$ which maps points $\boldsymbol{X}$ from the initial configuration Ω_0 to their places $\boldsymbol{x}$ in the current configuration Ω [205]

$$\boldsymbol{x} = \boldsymbol{\Phi}(\boldsymbol{X}, t). \tag{10.1}$$

An important variable in characterizing the deformation is the deformation gradient defined by

$$\boldsymbol{F} = \nabla \boldsymbol{\Phi} = \frac{\partial \boldsymbol{\Phi}}{\partial \boldsymbol{X}}. \tag{10.2}$$

The deformation gradient provides a relationship between vectors in the initial and current configurations. Its determinant $J = \det \boldsymbol{F}$ provides a measure for the change in volume. The deformation gradient can be used to define strain measures.

For example the square of the local changes in distances due to deformation is represented by the right Cauchy-Green deformation tensor ($\boldsymbol{C}$) defined by

$$\boldsymbol{C} = \boldsymbol{F}^T \cdot \boldsymbol{F}, \tag{10.3}$$

which provides an important strain measures in material coordinates. The transpose

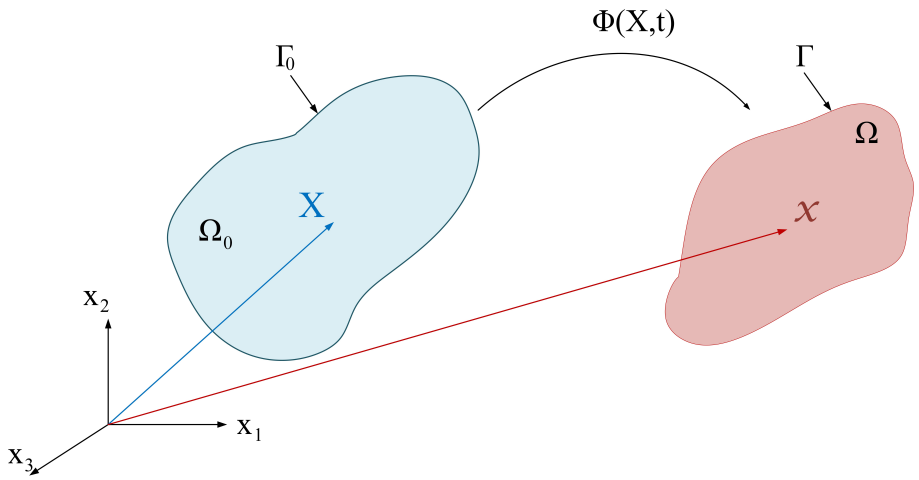

Figure 10.1: Deformation of continuum body.

of tensor $\boldsymbol{C}$ is known as left Cauchy-Green deformation tensor $\mathbf{B}$

$$\boldsymbol{B} = \boldsymbol{F} \cdot \boldsymbol{F}^T, \tag{10.4}$$

and provides a measure of strain in the spatial coordinates. Another measure of strain is given by the Green strain tensor $\boldsymbol{E}$ defined by

$$\boldsymbol{E} = \frac{1}{2}(\boldsymbol{C} - \boldsymbol{I}), \tag{10.5}$$

where $\boldsymbol{I}$ is the unit tensor. The Green strain tensor measures the difference of the square of length of a differential line segment in the current configuration and the initial configuration.

The eigenvalues of tensors $\boldsymbol{B}$ or $\boldsymbol{C}$ are the squares of the principle stretches denoted by $\lambda_i^2, i = 1, 2, 3$, where λ_i are principle stretches.

Tensors $\boldsymbol{B}$ and $\boldsymbol{C}$ have the same invariants which can be written in terms of the

principle stretches as

$$I_1 = I_1(\boldsymbol{B}) = I_1(\boldsymbol{C}) = \lambda_1^2 + \lambda_2^2 + \lambda_3^2, \tag{10.6a}$$

$$I_2 = I_2(\boldsymbol{B}) = I_2(\boldsymbol{C}) = \lambda_1^2\lambda_2^2 + \lambda_2^2\lambda_3^2 + \lambda_3^2\lambda_1^2, \tag{10.6b}$$

$$I_3 = I_3(\boldsymbol{B}) = I_3(\boldsymbol{C}) = J^2 = \lambda_1^2\lambda_2^2\lambda_3^2. \tag{10.6c}$$

10.1.1 Isotropic incompressible materials under uniaxial loading

Consider an incompressible material under uniaxial loading. Let the principle stretch in the direction of loading be denoted by λ_1. Since the material is incompressible, $J = \lambda_1\lambda_2\lambda_3 = 1$. Assuming the material is isotropic, the two other principle stretches are equal, i.e $\lambda_2 = \lambda_3$. Hence, the incompressibility condition yields $\lambda_2 = \lambda_3 = \lambda_1^{-1/2}$. The Corresponding deformation gradient and left Cauchy-Green deformation tensors can be written as

$$\boldsymbol{F} = \begin{bmatrix} \lambda_1 & 0 & 0 \\ 0 & \lambda_1^{-1/2} & 0 \\ 0 & 0 & \lambda_1^{-1/2} \end{bmatrix}, \quad \boldsymbol{B} = \begin{bmatrix} \lambda_1^2 & 0 & 0 \\ 0 & \lambda_1^{-1} & 0 \\ 0 & 0 & \lambda_1^{-1} \end{bmatrix}. \tag{10.7}$$

Therefore, the three invariants of tensor $\boldsymbol{B}$ can be written as

$$I_1 = \lambda_1^2 + \lambda_2^2 + \lambda_3^2 = \lambda_1^2 + 2\lambda_1^{-1}, \tag{10.8a}$$

$$I_2 = \lambda_1^2\lambda_2^2 + \lambda_2^2\lambda_3^2 + \lambda_3^2\lambda_1^2 = \lambda_1^{-2} + 2\lambda_1, \tag{10.8b}$$

$$I_3 = \lambda_1^2\lambda_2^2\lambda_3^2 = 1. \tag{10.8c}$$

10.2 Hyper-elasticity

Elastic materials for which the work of external forces is independent of their path are known as hyperelastic materials. Hyperelastic materials are characterized by the

existence of a strain energy function W defined per unit reference volume. The strain energy function of an isotropic hyperelastic material can be expressed as a function of one variable tensor $\boldsymbol{C}$ or $\boldsymbol{B}$, i.e $W(\boldsymbol{C}) = W(\boldsymbol{B})$. Moreover, it can be shown using the representation theorem of invariants that the strain energy function of isotropic hyperelastic materials can be represented using the invariants of $\boldsymbol{C}$ or $\boldsymbol{B}$

$$W = W(I_1(\boldsymbol{C}), I_2(\boldsymbol{C}), I_3(\boldsymbol{C})) = W(I_1(\boldsymbol{B}), I_2(\boldsymbol{B}), I_3(\boldsymbol{B})). \tag{10.9}$$

Several forms of strain energy functions including Neo-Hookean [206], Arruda-Boyce [207], Mooney-Rivlin [208,209], Yeoh [210] and Ogden [211] have been proposed in the past. In this paper we use Ogden model to model the behavior of polyruea under quasi–static loadings.

10.2.1 Incompresible Hyperelastic Materials

Hyperelastic materials which can sustain large deformations without noticeable change in volume are known as incompressible hyperelastic materials. For such materials $I_3 = J = \lambda_1\lambda_2\lambda_3 = 1$. The general form of the strain energy function of incompressible isotropic hyperelastic materials can be written as

$$W = W(\lambda_1, \lambda_2, \lambda_3) - p(J-1), \tag{10.10}$$

where p is the hydrostatic pressure and acts as an indeterminate Lagrange multiplier. Using the strain energy function, the three principle Cauchy stresses can be obtained using

$$\sigma_i^e = -p + \lambda_i \frac{\partial W}{\partial \lambda_i}, \quad i = 1, 2, 3. \tag{10.11}$$

10.2.1.1 Ogden model

A very sophisticated strain energy function for incompressible materials is presented by Ogden [211]. According to Ogden, the strain density function can be written as

$$W = \sum_{j=1}^{n} \frac{2\mu_j}{\alpha_j^2}\Big(\lambda_1^{\alpha_i} + \lambda_2^{\alpha_i} + \lambda_3^{\alpha_i} - 3\Big), \tag{10.12}$$

where μ_j are constant shear moduli, α_j are dimensionless constants and n is the number of terms in the strain energy function. Using Eq. (10.11) the three principle Cauchy stresses in Ogden model are

$$\sigma_i^e = -p + \sum_{j=1}^{n} \mu_j \lambda_i^{\alpha_j}, \tag{10.13}$$

where the hydrostatic pressure p is determined using incompressibility and boundary conditions.

The hydrostatic pressure p can be obtained using the boundary conditions of σ_2 (or σ_3) be equal to zero. By using this requirement in Eq. (10.13) we obtain

$$p = \sum_{j=1}^{n} \mu_j \lambda_2^{\alpha_j} = \sum_{j=1}^{n} \mu_j \lambda_1^{-\alpha_j/2}. \tag{10.14}$$

Using Eq. (10.14) in Eq. (10.13) gives an equation for σ_1

$$\sigma_1^e = \sum_{j=1}^{n} \mu_j (\lambda_1^{\alpha_j} - \lambda_1^{-\alpha_j/2}). \tag{10.15}$$

10.2.1.2 Mooney-Rivlin model

One more well known form of strain energy potential was proposed by Mooney and Rivlin [208, 209]. According to this model, a strain energy density is a polynomial series. It was found that only first three terms of polynomial are sufficient fit

compressive response [212]. Therefore, strain energy potential can be given as,

$$W(I_1, I_2) = M_1(I_1 - 3) + M_2(I_2 - 3) + M_3(I_1 - 3)(I_2 - 3), \tag{10.16}$$

where, M_1,M_2, and M_3 are unknown parameters to be found out by curve fitting of stress strain response of 1D testings. The constitutive equation can be given as,

$$\sigma^e = -p\mathbf{I} + \alpha_1\mathbf{B} + \alpha_2\mathbf{B}\cdot\mathbf{B}, \tag{10.17}$$

where, coefficients α_1 and α_2 can be given as,

$$\begin{aligned} \alpha_1 &= 2\left(\frac{\partial W}{\partial I_1} + I_1\frac{\partial W}{\partial I_2}\right), \\ \alpha_2 &= -2\frac{\partial W}{\partial I_2}. \end{aligned} \tag{10.18}$$

For uni-axial loading conditions, using Eq. (10.8a) and substituting it in Eq. (10.17) along with Eq. (10.18) we get,

$$\sigma^e = 2\lambda(1 - \lambda^{-3})\Big[M_1\lambda + M_2 + M_3[(\lambda^2 + 2\lambda^{-1} - 3) + \lambda(\lambda^{-2} + 2\lambda - 3)]\Big], \tag{10.19}$$

where λ is stretch in loading direction.

10.3 Visco-elasticity

Basic characteristic of viscoelastic material is the relationship between stress and strain depends on loading history. Hence they show phenomenon such as, creep, stress relaxation and hysteresis. In general viscoelastic materials can be divided in to two categories, linear viscoelastic materials and non-linear viscoelastic materials. Most common method is use of spring and dash-pot to mathematically model viscoelastic material. Following sections describes some most common linear (Maxwell, Kelvin, SLS [213]) as well as non-linear (K-BKZ [214–216]) models for viscoelastic materials.

10.3.1 The Maxwell model

Maxwell model consists of a spring and a dash pot in series as shown in Fig. 10.2. Stress applied will be same on both spring as well as dash pot but strain will be divided in two elements as ε_1 and ε_2. Therefore we can write following equation for spring element which is purely elastic and obeys Hooks law,

$$\varepsilon_1 = \frac{\sigma}{E}. \tag{10.20}$$

Similarly, dash pot is purely viscus material which obeys

$$\dot{\varepsilon_2} = \frac{\sigma}{\eta}, \tag{10.21}$$

this equation. Lastly, addition of strains in both element should be equal to total strain. Therefore,

$$\varepsilon = \varepsilon_1 + \varepsilon_2. \tag{10.22}$$

By taking derivative of Eq. (10.22) and then substituting values of ε_1 and ε_2 from Eq. (10.20) and Eq. (10.21) respectively, we get constitutive equation for Maxwell model as,

$$\dot{\varepsilon} = \frac{\dot{\sigma}}{E} + \frac{\sigma}{\eta}. \tag{10.23}$$

Physically, we can expect that after application of load spring will elongate instantaneously and deformation will keep on increasing with respect to time because of the dash pot. Once load is removed, spring deformation will be recovered but system will have permanent deformation due to dash pot. This shows the creep behavior, under constant load deformation will keep on increasing.

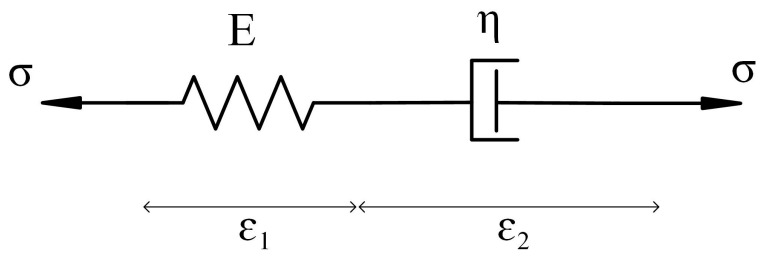

Figure 10.2: Block diagram of Maxwell model.

10.3.2 The Kelvin model

Other two element model, Kelvin model, consists of a spring and a dash pot in parallel as shown in Fig. 10.3. Stress applied will be divided in both spring as well as dash pot as σ_1 and σ_2 but strain ε will be same in two elements. Therefore we can write following equation for spring element which is purely elastic and obeys Hooks law,

$$\varepsilon = \frac{\sigma_1}{E}. \tag{10.24}$$

Similarly, dash pot is purely viscus material which obeys

$$\dot{\varepsilon} = \frac{\sigma_2}{\eta}, \tag{10.25}$$

this equation. Lastly, addition of stress in both element should be equal to total stress applied. Therefore,

$$\sigma = \sigma_1 + \sigma_2. \tag{10.26}$$

By substituting values of σ_1 and σ_2 from Eq. (10.24) and Eq. (10.25) respectively in to Eq. (10.26), we get constitutive equation for Kelvin model as,

$$\sigma = E\varepsilon + \eta\dot{\varepsilon}. \tag{10.27}$$

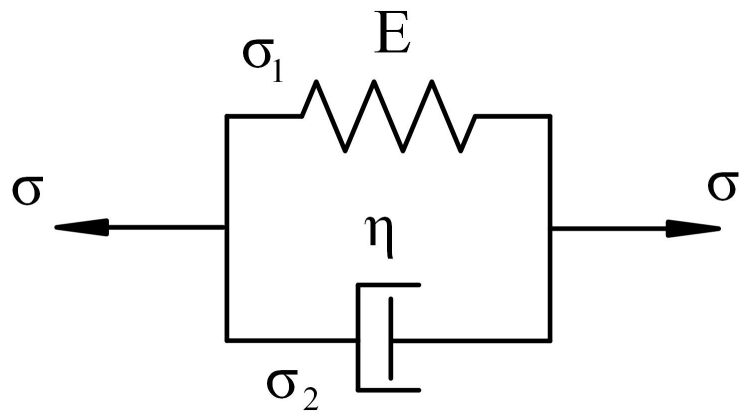

Figure 10.3: Block diagram of Kelvin model.

Physically, we can expect that after application of load deformation will keep on increasing with respect to time because of the dash pot but not in linear way. Once load is removed, due to spring all deformation will be recovered and system will not have any permanent deformation. This shows the relaxation behavior, under constant strain the stress will keep on decreasing.

10.3.3 SLS model

The standard linear solid (SLS) model used in this paper is the three-parameter model shown in Fig. 10.4.This model is a combination of a Kelvin model and a free spring acting in series.

The kinematic equation for this model is

$$\varepsilon = \varepsilon_1 + \varepsilon_2, \tag{10.28}$$

where ε_1 and ε_2 are the strain of the free spring and Kelvin element, respectively. From equilibrium the stress in the free spring σ_1 and the stress in the Kelvin element σ_2 are the same and equal to the remote stress σ^v

$$\sigma^v = \sigma_1 = \sigma_2. \tag{10.29}$$

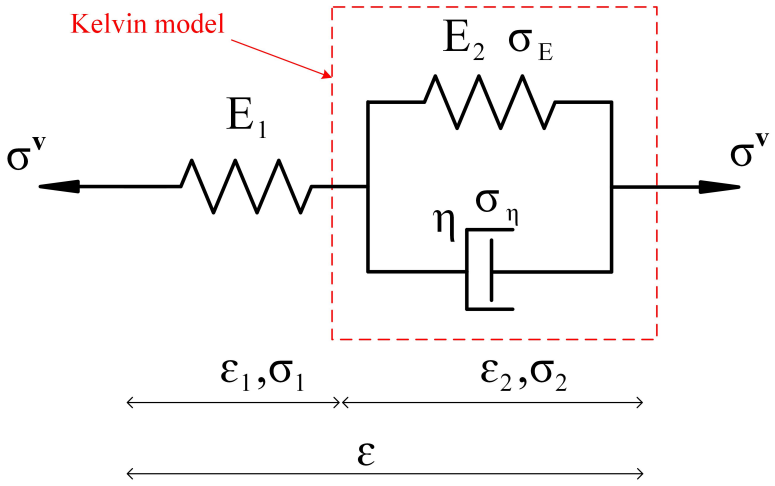

Figure 10.4: Block diagram of standard linear solid (SLS) model.

The relation between stress and strain in the Kelvin model is given by

$$\sigma_2 = \sigma_E + \sigma_\eta = E_2\varepsilon_2 + \eta\dot{\varepsilon_2}, \tag{10.30}$$

where η is the viscosity of dashpot, σ_E and σ_η are respectively the stress in the spring and dashpot of the Kelvin model. By using Eq. (10.29) and Eq. (10.30) in Eq. (10.28) and noting that for the free spring $\sigma_1 = E_1\varepsilon_1$ the constitutive equation of the three parameter model is obtained as

$$(E_1 + E_2)\sigma^v + \eta\dot{\sigma^v} = E_1E_2\varepsilon + E_1\eta\dot{\varepsilon}. \tag{10.31}$$

The three material parameters of the model are E_1, E_2 and η which should be determined using experimental stress-strain response.

The relaxation modulus of this model can be obtained by solving the differential equation (10.31) for a relaxation test of constant strain. The relaxation modulus of the three parameter model can be written as

$$E(t) = \frac{E_1}{E_1 + E_2}\left(E_2 + E_1e^{-t/\tau}\right), \tag{10.32}$$

where $\tau = \eta/(E_1 + E_2)$. The relaxation modulus can be used in a hereditary integral to find the relationship between stress and strain for a general form of loading

$$\sigma^v = \int_0^t E(t-\xi)\frac{d\varepsilon}{d\xi}d\xi, \tag{10.33}$$

where t is total time. By substituting Eq. (10.32) in to Eq. (10.33), the relation between stress and strain can be written in the following integral form

$$\sigma^v = \int_0^t (A_1 + A_2 e^{-(t-\xi)/A_3})\dot{\varepsilon}d\xi, \tag{10.34}$$

where $A_1 = E_1E_2/(E_1+E_2)$, $A_2 = E_1^2/(E_1+E_2)$ and $A_3 = \tau$. Three model parameters A_1, A_2 and A_3 are determined using experimental data from different strain rate under uniaxial loading.

10.3.4 K-BKZ model

Using K-BKZ model Cauchy stress tensor for homogeneous, isotropic, and incompressible material can be written as [214–217],

$$\sigma^v = -p^v\boldsymbol{I} + \boldsymbol{F}(t)\cdot\prod_{\tau=-\infty}^{t}\{\boldsymbol{C}(\tau)\}\cdot\boldsymbol{F}^T(t), \tag{10.35}$$

where σ^v is Cauchy stress tensor, p^v is the pressure for viscoelastic part and $\prod$ is frame-independent matrix function which consider effect of strain rate. Although there are many different forms proposed for function $\prod$, one of the well accepted form is given as,

$$\prod_{\tau=-\infty}^{t}\{\boldsymbol{C}(\tau)\} = \int_{-\infty}^{t}\phi(I_1', I_2')m(t-\tau)\dot{\boldsymbol{E}}(\tau)d\tau, \tag{10.36}$$

where $\phi(I_1', I_2')$ is a damping function, $m(t)$ is relaxation function and $\dot{\boldsymbol{E}}$ can be given as,

$$\dot{\boldsymbol{E}} = \frac{1}{2}(\dot{\boldsymbol{F}}^T\cdot\boldsymbol{F} + \boldsymbol{F}^T\cdot\dot{\boldsymbol{F}}). \tag{10.37}$$

$I_1^{'}$ and $I_2^{'}$ are first and second invariants of strain tensor $\boldsymbol{C}(\tau)$. In case of uniaxial loading we can prove that $(I_1)_{hyperelastic} = (I_1^{'})_{viscoelastic}$ and $(I_2)_{hyperelastic} = (I_2^{'})_{viscoelastic}$. Many different forms of damping function are found in literature, we will use the following in order to reduce number of parameters [218]:

$$\phi(\tau) = B_1 + B_2\Big(I_2^{'} - 3\Big), \tag{10.38}$$

where B_1 and B_2 are undetermined parameters. The relaxation function is usually given in terms of Prony series as,

$$m(t-\tau) = G_\infty + \sum_{i=1}^{n} G_i e^{-(t-\tau)/\omega_i}, \tag{10.39}$$

where n is number of terms in Prony series , G_∞ is long term shear modulus, G_i and ω_i are relaxation shear modulus and relaxation time respectively.

10.4 Hyper- Viscoelasticity model

It is postulated that the stress-strain response of polyurea is a combination of hyperelasticity and viscoelasticity. Therefore, the total stress can be given as the addition of hyperelastic and a viscoelastic components [219–223]

$$\sigma^{total} = \sigma^e + \sigma^v, \tag{10.40}$$

where σ^{total} is the total Cauchy stress, σ^e characterizes the quasi–static hyperelastic response and σ^v is the rate dependent viscoelastic component of stress tensor.

CHAPTER 11: HYPER-VISCOELASTIC CONSTITUTIVE MODEL FOR POLYUREA

11.1 Quasi static response

In first part, we assume that quasi static response of polyurea is purely hyper elastic and hence can be modeled by Ogden or Mooney Rivlin model. We curve fit both the models (Ogden and Mooney Rivlin) to compressive quasi static response of polyurea given in [179]. Curve fitting is done using MATLAB tool, '*cftool*' [224].

The material parameters of Ogden model for polyurea are found by fitting Eq. (10.15) using four pairs of constant μ_j and $\alpha_j (n = 4)$ to the experimental data. Similarly, material parameters of Mooney-Rivlin model are found by fitting Eq. (10.19) to the experimental data. The experimental data from Sarva et al. [179] at a compressive strain rate of 0.0016 /s are used to find the material parameters for compressive loading.

Fig. 11.1 shows comparison between Ogden and Mooney-Rivlin model. As seen in figure, Ogden model is better fit and reason can be number of parameters available in Ogden model are higher than Mooney-Rivlin. Therefore we will use Ogden model for further modeling.

The tensile tests conducted by Ronald et al. [178] on polyurea at a strain rate of 0.09 /s are used to find the material parameters for polyurea under tension. The Ogden material parameters for polyurea under quasi–static loading are shown in Table 11.1. For the purpose of comparison, the experimental data and the stress–strain curves obtained using these material parameters are plotted in Fig. 11.2. The R^2 values which represents goodness of fit for tension and compression response are 0.9998 and 0.9982, respectively. This indicates a good agreement between the proposed Ogden

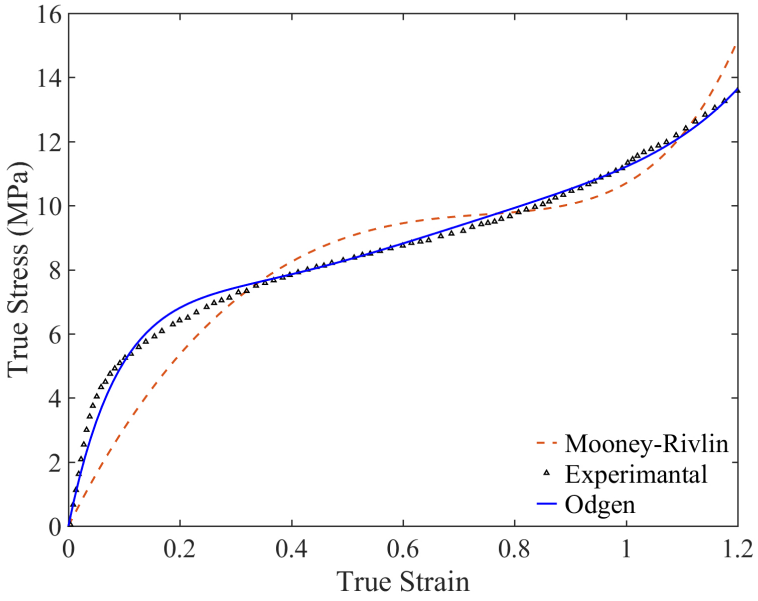

Figure 11.1: Fitting of four term Ogden model and three term Mooney Rivlin model to low strain rate compression (0.0016 /s) data.

Table 11.1: Material parameters for four term Ogden model.

	1	2	3	4
for tension				
μ_i (MPa)	−9.149	−6.346	−7.47	0.001635
α_i	−1.658	4.289	−8.37	7.35
for compression				
μ_i (MPa)	6.114	3.526	9.673	3.421
α_i	9.853	9.853	−4.924	1.067

model with the experimental data for quasi–static response of polyurea for both tension and compression loading conditions.

11.2 High strain rate response

11.2.1 KBKZ + Ogden model

Coefficients of Prony series in K-BKZ model can be found out by approximating master curve obtained by relaxation tests done on polyurea. Using standard WLF function data from relaxation testes at different temperatures can be shifted according to time-temperature shift principle. This is already done by Li et. al. [185] and is

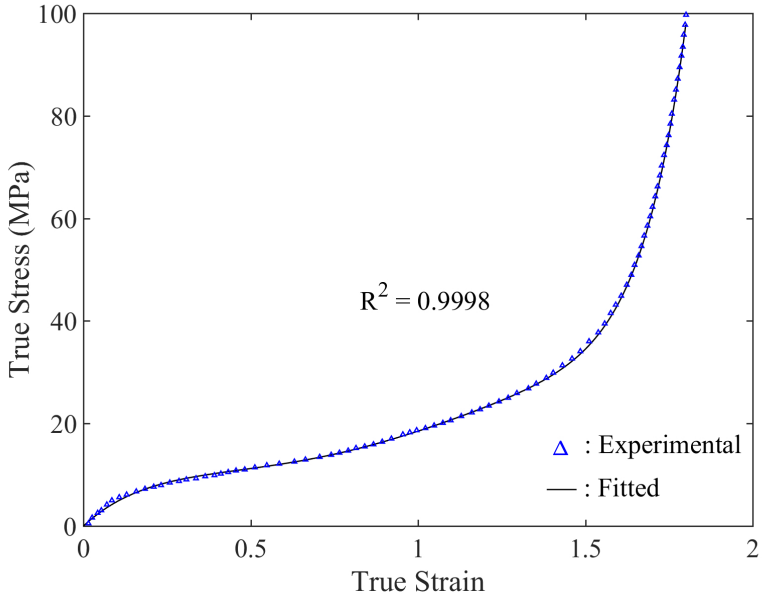

Figure 11.2: Fitting of four term Ogden model to low strain rate tension (0.09 /s) data.

given here in Table 11.2 just for the sake of completeness of constitutive model. Prony series is approximated using six terms along with the value of $G_\infty = 25$ MPa.

Table 11.2: Coefficients of Prony series given by Eq. (12.12)

	1	2	3	4	5	6
G_i (MPa)	15.8879	28.3111	38.1695	44.0718	66.9582	86.1898
ω_i (ms)	301.61	0.13146	1.0556×10^{-3}	4.3933×10^{-5}	2.4659×10^{-6}	1.6715×10^{-7}

By substituting σ^v from K-BKZ model using Eq. (10.35) along with Eq. (12.12) we get,

$$\sigma^{total} = \sigma^e + \frac{1}{2}\lambda^{-1}\int_0^t \lambda^{-2}\Big[B_1 + B_2(I_2-3)\Big]m(t-\tau)\dot{\lambda}d\tau + \lambda^2\int_0^t \lambda\Big[B_1 + B_2(I_2-3)\Big]m(t-\tau)\dot{\lambda}d\tau, \tag{11.1}$$

here two undermined parameters B_1 and B_2 are to be determine by curve fitting.

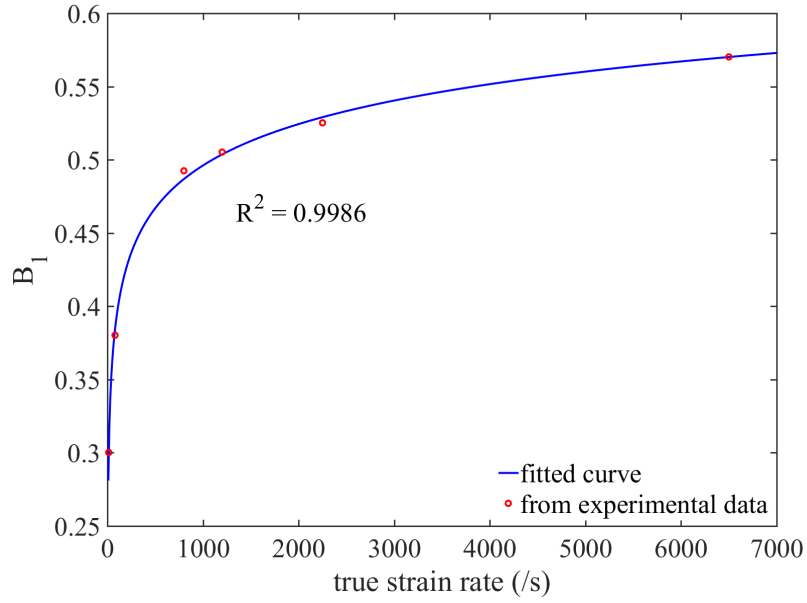

(a)

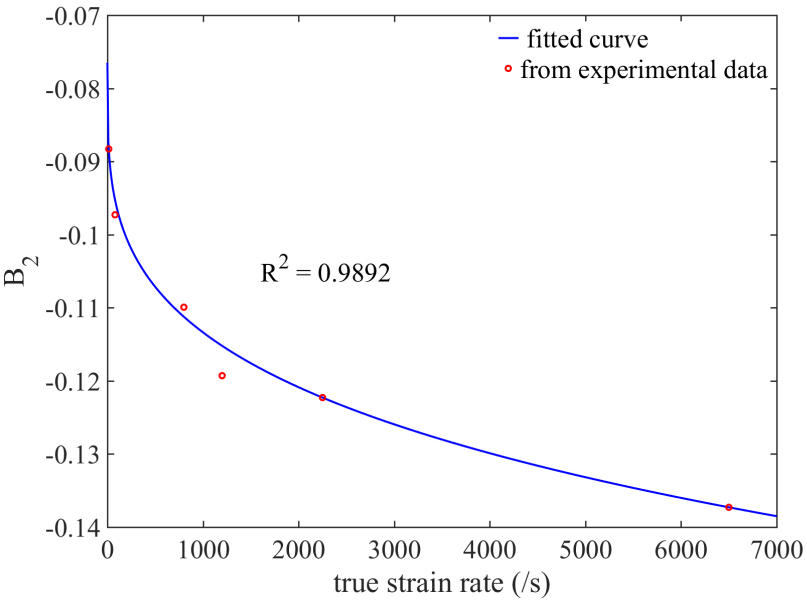

(b)

Figure 11.3: Plots showing relation between true strain rate and material parameters B_1 and B_2 for compression using Ogden + K-BKZ model.

Unlike SLS model K-BKZ model has only two undermined parameters to be found out using curve fitting. This constraints our ability to obtain a very good fit. As

nature of response of polyurea under tension is challenging to capture, we observed that K-BKZ model is inadequate for capturing that response.

Parameters obtained for compression behavior are summarized in Table 11.3 and Eq. (11.3) is plotted for parameters B_1 and B_2 in Fig. 11.3 along with parameter values from experimental data. The values of these parameters for each strain rate are presented in Table 11.4. As R^2 values are very close to 1 , we can say the fit is very good. Fig. 11.4 shows results using these parameters.

Table 11.3: Material parameters for S_i^1, S_i^2 and S_i^3 visco-hyperelastic model using Ogden + B-KBZ model.

$i =$	1	2	3
for compression			
S_i^1	-1.157	-0.05093	1.31
S_i^2	-0.005827	0.2671	-0.07649

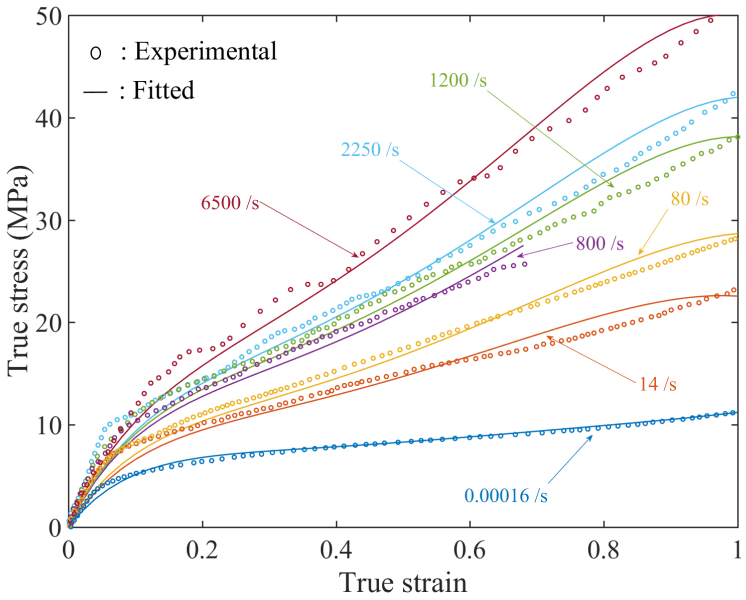

Figure 11.4: Comparison of stress values predicted using proposed constitutive model using Ogden + K-BKZ model and experimental data.

Table 11.4: Material parameters B_1 and B_2 of Ogden + K-BKZ model for different strain rates.

strain rate	B_1(MPa)	B_2(MPa)
for compression		
14	0.30025	−0.088286
80	0.38025	−0.097286
800	0.4925	−0.1099286
1200	0.50525	−0.119286
2250	0.52525	−0.122286
6500	0.57025	−0.137286

11.2.2 SLS + Ogden model

The total visco–hyperelastic stress obtained using Ogden and SLS model is obtained by using Equations (10.15) and (10.34) in Eq. (10.40)

$$\sigma^{total} = \sum_{j=1}^{n} \mu_j(\lambda_1^{\alpha_j} - \lambda_1^{-\alpha_j/2}) + \int_0^t (A_1 + A_2 e^{-(t-\xi)/A_3})\dot{\varepsilon} d\xi, \tag{11.2}$$

The material parameters for Ogden model are presented in Table 11.1. The material parameters of the SLS model are obtained by using the experimental data of Ronald et al. [178] and Sarva et al. [179] at different strain rates. To ensure the accuracy of the model, the viscoelastic material parameters A_1, A_2 and A_3 are found separately for each strain rate. The values of these parameters for each strain rate are presented in Table 11.5. The total stress obtained using Eq. (11.2) by employing the material parameters of Table 11.5 are plotted in Fig. 11.5 and compared with the experimental data. These graphs show that the proposed hyper–viscoelastic equation can capture the behavior of polyurea over a wide range of strain rates under both tensile and compressive loadings.

The values of material parameters shown in Table 11.5 indicate that A_1, A_2 and A_3 are rate dependent. We propose to represent the rate dependence of these material parameters using

$$A_i = S_i^1(|\dot{\varepsilon}|)^{S_i^2} + S_i^3, \quad i = 1, 2, 3 \tag{11.3}$$

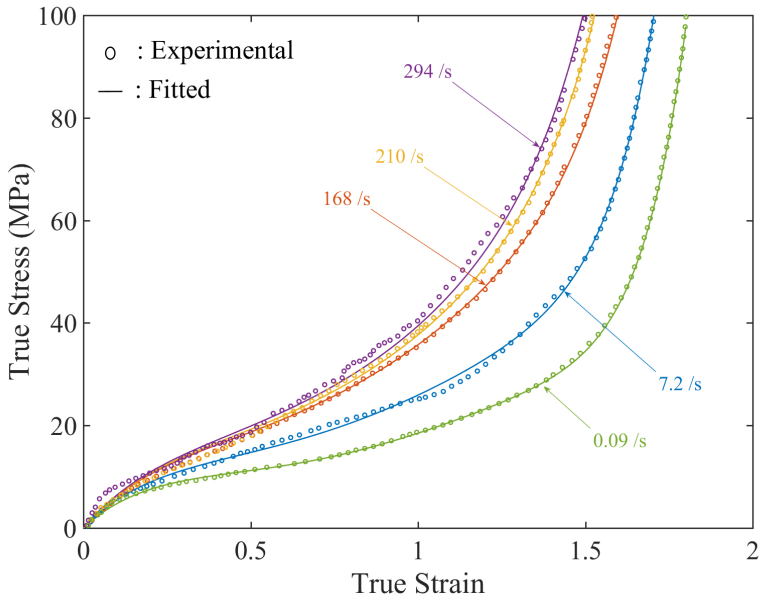

(a)

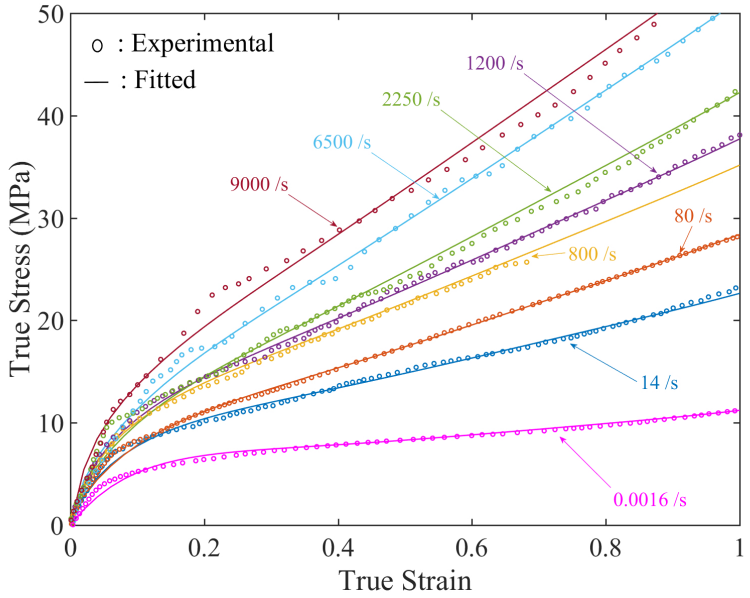

(b)

Figure 11.5: Comparison of curve fitted stress strain curve for proposed hyper-viscoelastic constitutive model using Odgen + SLS model and experimental data for (a) tension and (b) compression.

where S_i^1,S_i^2 and S_i^3 are constants which are found by fitting Eq. (11.3) to the values of A_i presented in Table 11.5. The values of S_i^1,S_i^2 and S_i^3 are shown in Table 11.6 and

Table 11.5: Material parameters A_1, A_2 and A_3 of Ogden + SLS model for different strain rates.

strain rate	A_1(MPa)	A_2(MPa)	A_3
for tension			
7.2	7.007	0.007153	-0.02382
168	14.35	0.19879	-0.0014498
210	15.33	0.2039	-0.001074
294	16.5	0.2239	-0.000755
for compression			
14	12.1	115.0	9.5×10^{-5}
80	16.05	121.0	4.496×10^{-5}
800	22.249	149.86	1.373×10^{-5}
1200	24.407	161.42	1.053×10^{-5}
2250	28.349	183.59	6.4439×10^{-6}
6500	37.06	236.81	1.4031×10^{-6}
9000	40.371	258.35	0.2198×10^{-6}

their capability in reproducing the values of Table 11.5 is demonstrated in Fig. 11.6 to Fig. 11.8. As shown in Figs. 11.6 to 11.8, Eq. (11.3) closely matches with the original values of A_i. The R^2 values which indicate the goodness of the fitting are close to one which indicates the high quality of fitting curve.

Table 11.6: Material parameters S_i^1, S_i^2 and S_i^3 of visco-hyperelastic model using Ogden + SLS model.

$i =$	1	2	3
for tension			
S_i^1	2.8350	0.2870	2.0100
S_i^2	-0.6663	-0.1587	0.4942
S_i^3	-0.1174	-0.7900	0.0005686
for compression			
S_i^1	1.277	0.325	8.863
S_i^2	1.14	0.5364	110.3
S_i^3	281.0	-0.3772	-8.841

The results from both models are very good, but Ogden + SLS model gives slightly better fit than Ogden + K-BKZ model. Also one important thing to note here is k-BKZ model could not give accurate results for response of polyurea under tension. Therefore we can say that Ogden + SLS model is the best option to ahead with.

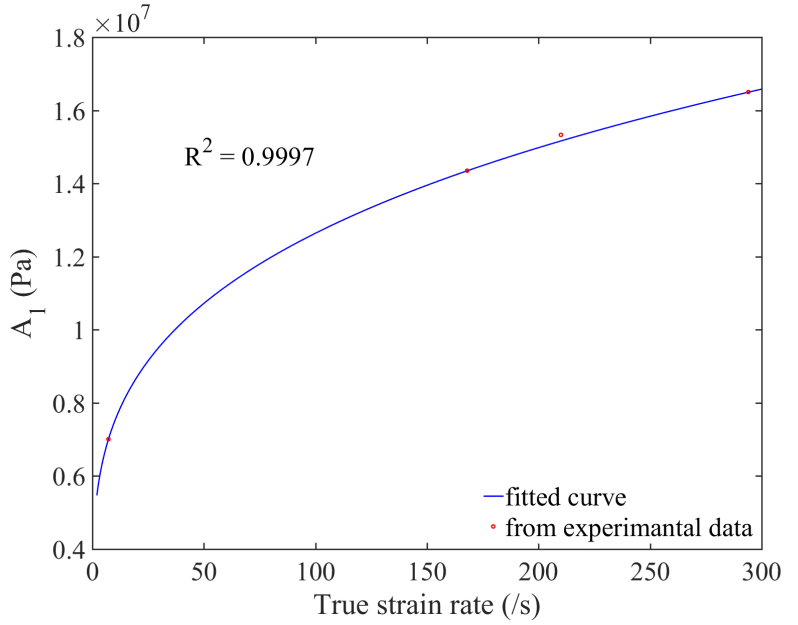

(a)

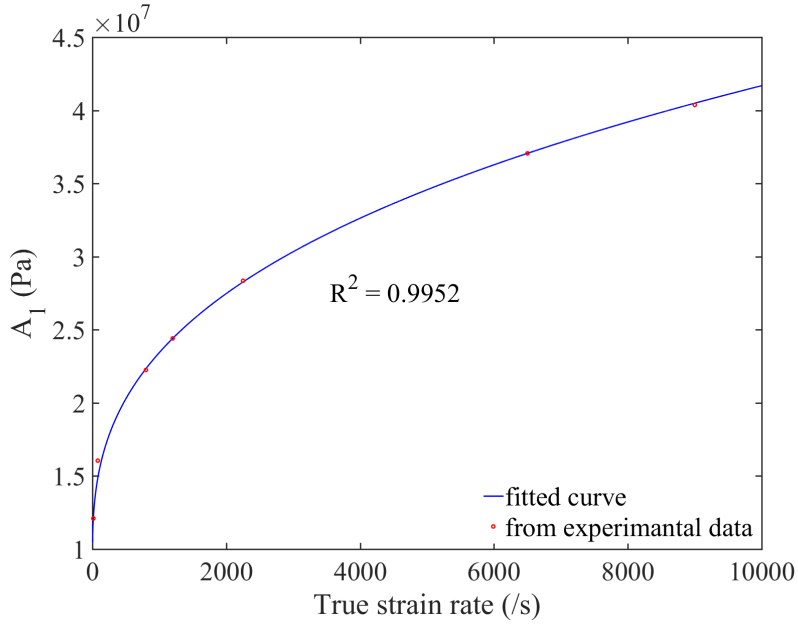

(b)

Figure 11.6: Plots showing relation between true strain rate and material parameter A_1 for (a) tension, and (b) compression for combined Odgen and SLS model.

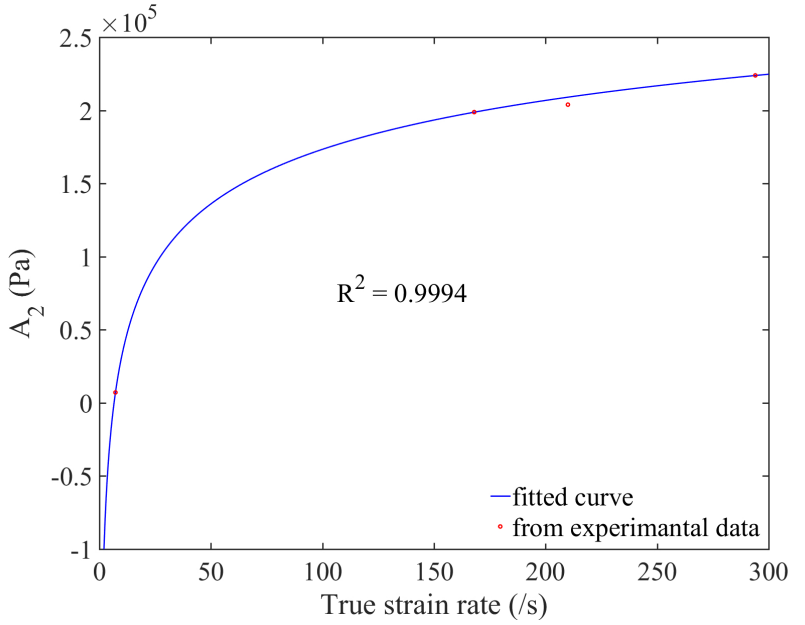

(a)

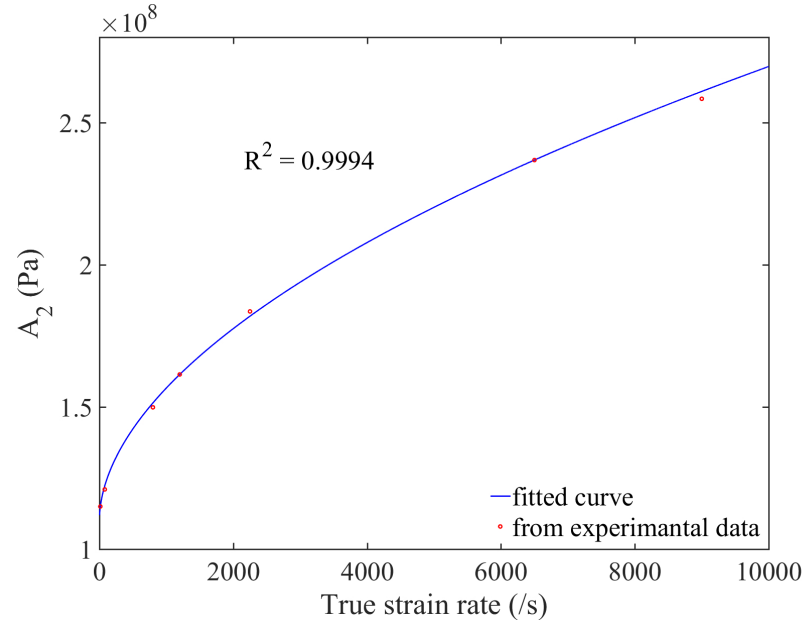

(b)

Figure 11.7: Plots showing relation between true strain rate and material parameter A_2 for (a) tension, and (b) compression for combined Odgen and SLS model.

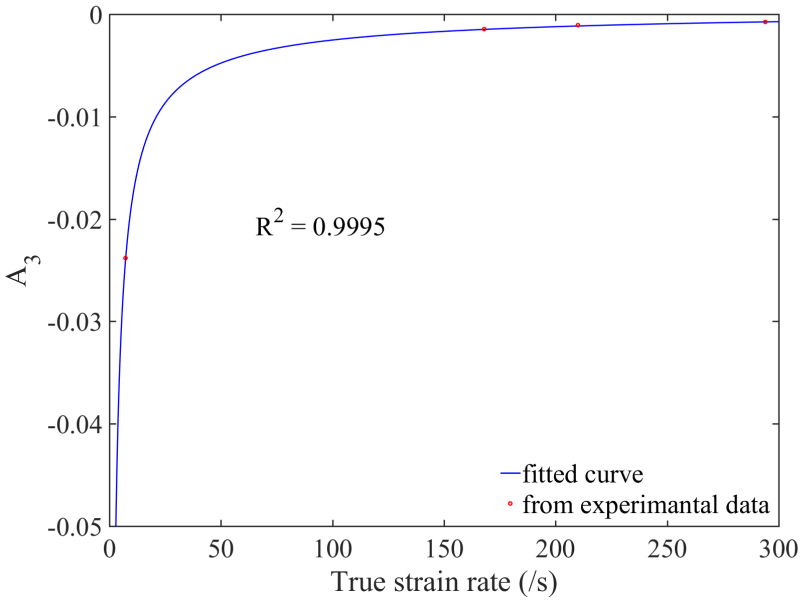

(a)

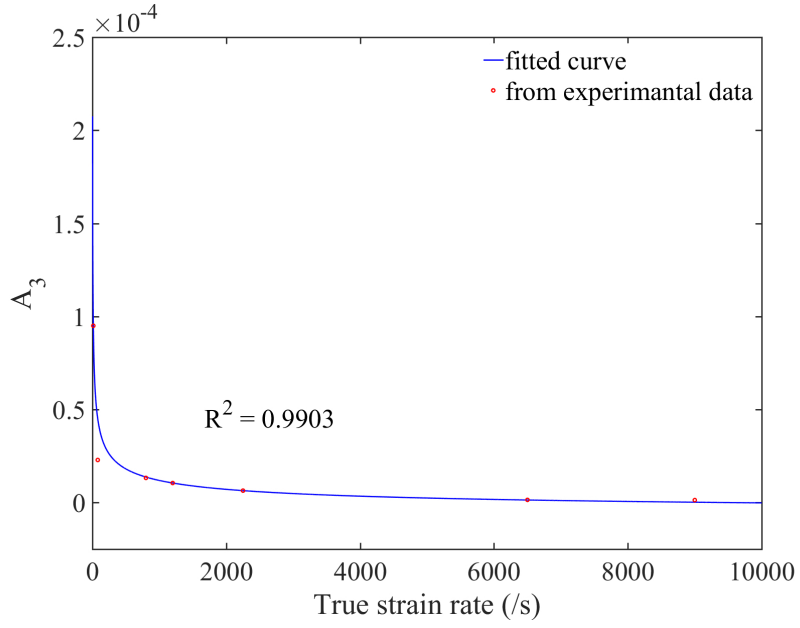

(b)

Figure 11.8: Plots showing relation between true strain rate and material parameter A_3 for (a) tension, and (b) compression for combined Odgen and SLS model.

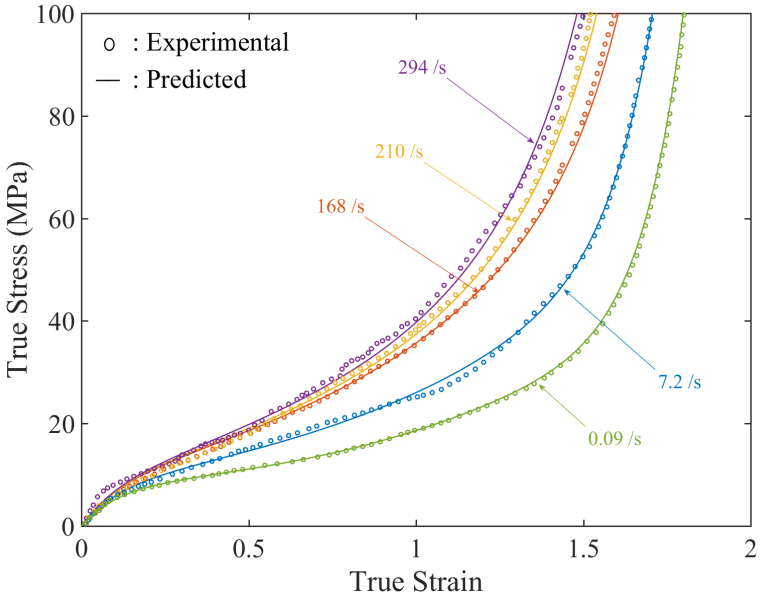

(a)

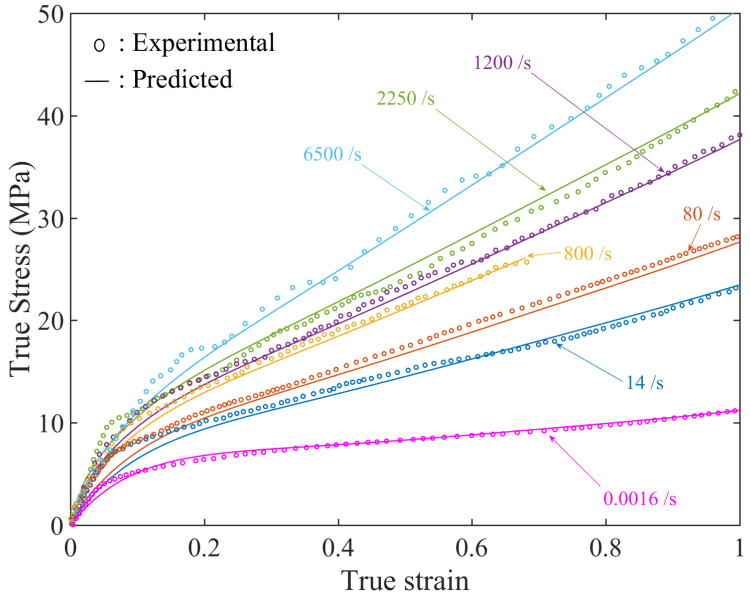

(b)

Figure 11.9: Comparison of stress values predicted using proposed hyper-viscoelastic constitutive model using Odgen + SLS model and experimental data for (a) tension and (b) compression.

CHAPTER 12: PREDICTIONS OF DAMPING PROPERTIES USING ANALYTICAL METHODS

In this chapter, we briefly describe the micormechanics based analytical methods that are commonly used for predicting homogeneous properties of composites.

12.1 Material description

12.1.1 Matrix material model

We assume that the polymer matrix is a linear viscoelastic material. The constitutive relations for a viscoelastic material can be written as

$$\sigma_{ij}(t) = \int_0^t C_{ijkl}(t-\tau)\frac{d\varepsilon_{kl}(\tau)}{d\tau}d\tau, \tag{12.1}$$

where σ_{ij} and ε_{kl} are stress and strain tensors and C_{ijkl} is the time dependent modulus of the material. For a linear viscoelastic material, Eq. (12.1) can be written as

$$\sigma_{ij}(t) = \int_0^t 2G(t-\tau)\frac{d\varepsilon_{ij}}{d\tau}d\tau + \mathbf{I}\int_0^t K(t-\tau)\frac{d\varepsilon_{ij}^{Vol}}{d\tau}d\tau, \tag{12.2}$$

where ε_{ij} is deviatoric strain, ε_{ij}^{Vol} is volumetric strain and $G(t)$ and $K(t)$ are shear and bulk relaxation modulus, respectively.

Under a time harmonic deformation history

$$u_i(\mathbf{x},t) = u_i^0(\mathbf{x},\omega)e^{i\omega t}, \tag{12.3}$$

the strain field is

$$\varepsilon_{ij}(\mathbf{x},t) = \varepsilon_{ij}^0(\mathbf{x},\omega)e^{i\omega t}, \tag{12.4}$$

where ω is the frequency, $\mathbf{x}$ is the position vector and $i = \sqrt{-1}$. Using Eq. (12.4) in Eq. (12.1) and assuming the material is isotropic, the deviatoric and dilatational stress components can be written as

$$\begin{aligned} s_{ij} &= 2G^*(\omega)\varepsilon_{ij}, \\ \sigma_{kk} &= 3K^*(\omega)\varepsilon_{kk}, \end{aligned} \tag{12.5}$$

where $G^*(\omega)$ and $K^*(\omega)$ are the shear and bulk modulus defined in complex form as

$$\begin{aligned} G^*(\omega) &= i\omega \int_0^\infty G(t)e^{-i\omega t}dt, \\ K^*(\omega) &= i\omega \int_0^\infty K(t)e^{-i\omega t}dt. \end{aligned} \tag{12.6}$$

The complex Young's modulus of viscoelastic materials can be obtained using

$$E^*(\omega) = \frac{9K^*G^*}{3K^* + G^*}, \tag{12.7}$$

which can be written in a simplified form as the sum of storage and loss moduli

$$E^*(\omega) = E^{'}(\omega) + iE^{''}(\omega), \tag{12.8}$$

where real and imaginary parts represent the storage and loss moduli, respectively. Storage modulus represents the ability of a viscoelastic material to store energy and loss modulus represents the energy dissipated through conversion to heat. The loss factor ($\tan\delta$) defined as the ratio of loss to storage modulus

$$\tan\,\delta = \frac{E^{''}}{E^{'}}, \tag{12.9}$$

provides a measure of the damping capability of viscoelastic materials [213].

The plane strain complex Young's modulus E^*_{pl} can be obtained using

$$E^*_{pl} = \frac{E^*}{1 - \upsilon^{*2}}, \tag{12.10}$$

where υ^* is complex Poisson's ratio obtained from

$$\upsilon^* = \frac{3K^* - 2G^*}{2(3K^* + G^*)}. \tag{12.11}$$

12.1.2 Prony series

Shear and bulk modulus of a linear viscoelastic materials can be represented by a Prony series as

$$\begin{aligned} G(t) &= G_\infty + \sum_{j=1}^{N} G_j e^{-t/\tau_j}, \\ K(t) &= K_\infty + \sum_{j=1}^{N} K_j e^{-t/\tau_j}, \end{aligned} \tag{12.12}$$

where G_j and K_j are the relaxation shear and bulk modulus, τ_j is the relaxation time and G_∞ and K_∞ are the long term shear and bulk modulus when the material is completely relaxed. By substituting Eq. (12.12) in Eq. (12.6), complex shear and bulk moduli in terms of frequency can be written as

$$\begin{aligned} G^*(\omega) &= G_\infty + i\omega \sum_{j=1}^{N} \frac{G_j \tau_j}{(1 + i\omega\tau_j)}, \\ K^*(\omega) &= K_\infty + i\omega \sum_{j=1}^{N} \frac{K_j \tau_j}{(1 + i\omega\tau_j)}. \end{aligned} \tag{12.13}$$

Details about this conversion of time domain response to frequency domain response can be found in Appendix E.

The relaxation time and moduli of the matrix used in this paper are taken from Reference [190] and are given in Table 12.1. These material parameters are chosen

because they include a broad range of relaxation times. We assume that the density of polymer matrix is 1.0 gr/cm^3.

Table 12.1: Bulk and shear relaxation moduli for matrix material. The units of relaxation moduli and relaxation times are in bar and second, respectively.

$G_\infty = 3.162$			
$K_\infty = 200$			
τ_j^G	G_j	τ_j^G	G_j
0.032	2.512	100.0	19.953
0.100	10.0	316.228	12.589
0.316	56.234	1000.0	2.512
1.0	316.228	3162.278	1.698
3.162	1000.0	10000.0	1.202
10.0	199.526	31622.777	1.148
31.623	50.119	100000.0	1.096
τ_j^K	K_j	τ_j^K	K_j
100	3000	316.228	100

12.1.3 Inclusions

Since the glass inclusions in our model are much stiffer and stronger than the polymer matrix, a linear elastic material model is used to model them. The inclusions are assumed to have a Young's modulus of $E = 64.89$ GPa, a Poisson's ratio of 0.249 and density of 2.47 g/cm^3.

12.2 Rules of mixtures

The rules of mixture provides a simple method for estimating homogeneous properties of composites. Rules of mixtures can be written as

$$\frac{1}{E_h^*} = \frac{v_m}{E_m^*} + \frac{v_f}{E_f}, \tag{12.14}$$

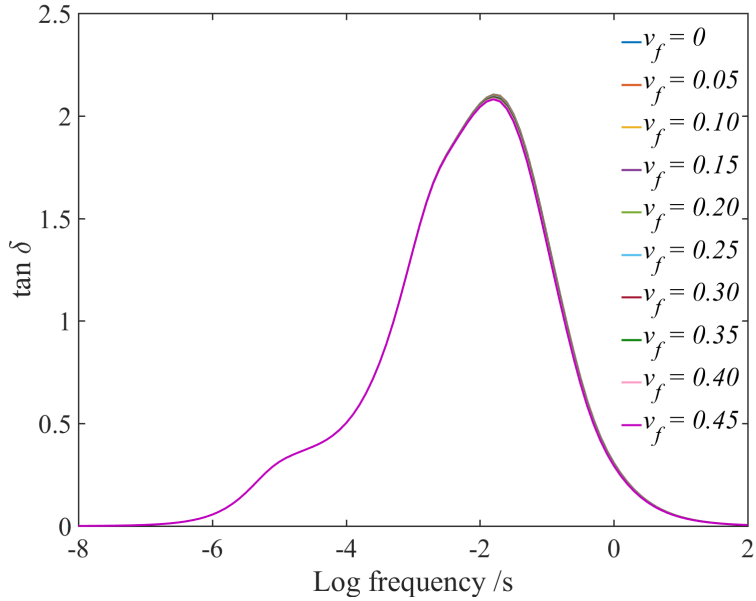

(a)

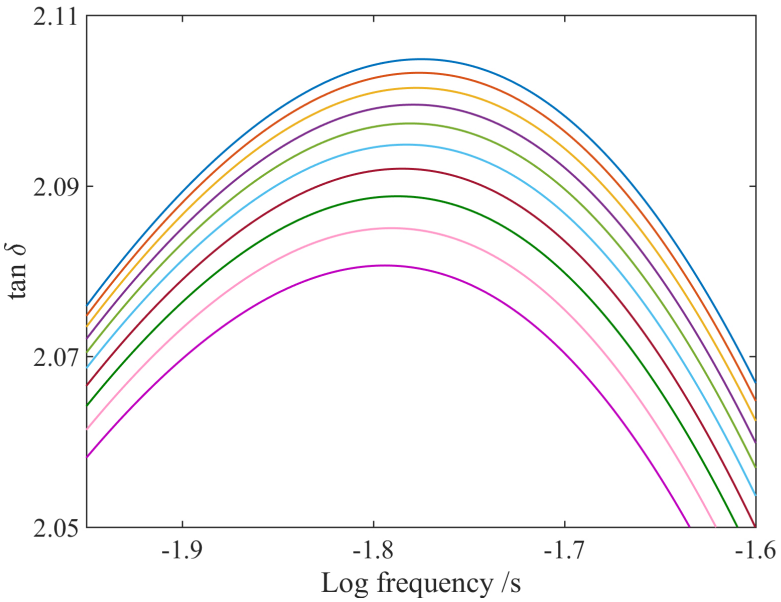

(b)

Figure 12.1: a) Values of $\tan\delta$ obtained using rules of mixtures for different inclusion volume fractions, b). Zoom–in of $\tan\delta$ plots at their peaks.

where E_h^* is the homogenized complex Young's modulus of composite, E_m^* is the complex Young's modulus of matrix, E_f is the Young's modulus of inclusions, and v_m and v_f are volume fractions of matrix and inclusions, respectively.

By using Eqs. (12.13) and (12.7) in Eq. (12.14) the homogenized complex Young's modulus of composite as a function of frequency $E_h^*(\omega)$ is obtained. The $\tan\delta$ of the composite at different frequencies can be obtained by using loss and storage modulus of $E_h^*(\omega)$ in Eq. (12.9). The values of $\tan\delta$ of a polymer composite at various inclusion volume fractions using the material parameters given in Section 12.1 are plotted in Fig. 12.1. As shown in Fig. 12.1(a), the value of $\tan\delta$ significantly depends on the vibration frequency. Fig. 12.1(b) shows the zoomed portion of peak $\tan\delta$ from Fig. 12.1(a). It can be seen in Fig. 12.1(b) that, by increasing the inclusions volume fraction, the peak value of $\tan\delta$ decreases and the frequency at which the peak $\tan\delta$ occurs reduces. Based on this model, the value of $\tan\delta$ is not sensitive to the inclusions volume fraction.

12.3 Hashin-Shtrikman Bounds

Hashin and Shtrikman [225] bounds provide the narrowest possible bounds of homogenized bulk and shear modulus of isotropic elastic composites. Using dynamic correspondence relations Hashin and Shtrikman (H–S) bounds can be extended to obtain lower and upper bounds for homogenized bulk and shear modulus of viscoelastic composites

$$\begin{aligned}
K_L^* &= K_m^* + \frac{v_f}{\frac{1}{K_f - K_m^*} + \frac{(2n+1)v_m}{(2n+1)K_m^* + (3n+1)G_m^*}}, \\
K_U^* &= K_f + \frac{v_m}{\frac{1}{K_m^* - K_f} + \frac{(2n+1)v_f}{(2n+1)K_f + (3n+1)G_f}}, \\
G_L^* &= G_m^* + \frac{v_f}{\frac{1}{G_f - G_m^*} + \frac{(5n+1)v_m(K_m^* + 2G_m^*)}{(4n+1)G_m^*[(2n+1)K_m^* + (3n+1)G_m^*]}}, \\
G_U^* &= G_f + \frac{v_m}{\frac{1}{G_m^* - G_f} + \frac{(5n+1)v_f(K_f + 2G_f)}{(4n+1)G_f[(2n+1)K_f + (3n+1)G_f]}},
\end{aligned} \tag{12.15}$$

where K_m^* and G_m^* are complex bulk and shear modulus of matrix, K_f and G_f are bulk and shear modulus of inclusion, v_m and v_f are matrix and inclusion volume fraction

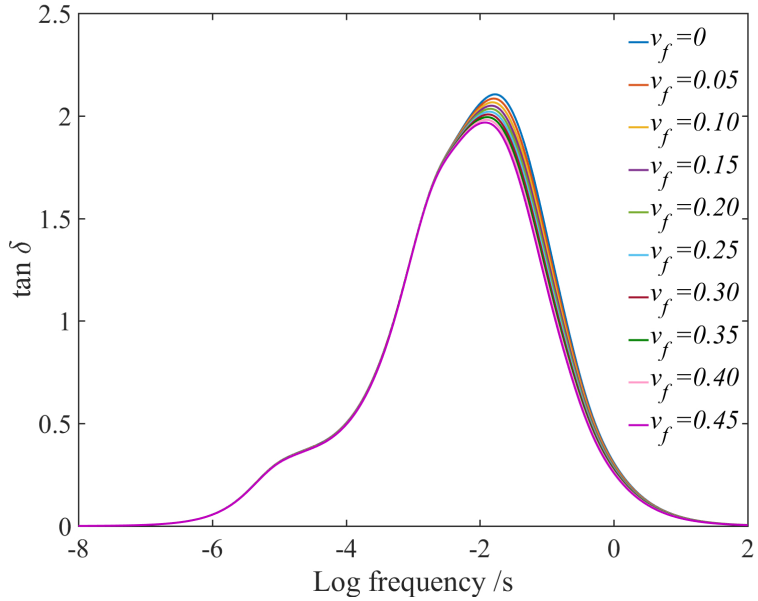

(a)

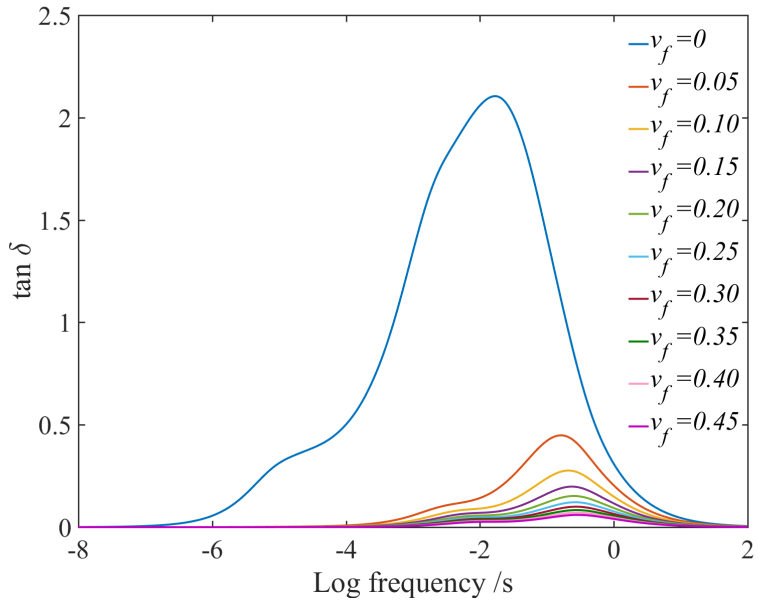

(b)

Figure 12.2: Plots for (a)upper and (b)lower H-S bounds for $\tan\delta$ for different volume fractions.

respectively, K_L^* and G_L^* are lower bounds on bulk and shear modulus , K_U^* and G_U^* are upper bounds on bulk and shear modulus and parameter $n = 0$ corresponds to cylindrical inclusions [226] while $n = 1$ corresponds to spherical inclusions [225].

The upper and lower H–S bounds of $\tan\delta$ for different inclusion volume fractions are plotted in Fig. 12.2. Since inclusions are significantly stiffer than matrix, there is remarkable gap between the upper and lower bounds of $\tan\delta$ hence predicting the value of $\tan\delta$ using H–S bounds is not possible.

12.4 Halpin-Tsai model

Halpin-Tsai model is based on the self-consistent micromechanics method developed by Hill [227]. The Halpin-Tsai equations can be written as

$$\begin{aligned} E_h^* &= E_m^* \frac{1 + 2\zeta v_f \eta^*}{1 - v_f \eta^*}, \\ \eta^* &= \frac{\frac{E_f}{E_m^*} - 1}{\frac{E_f}{E_m^*} + 2\zeta}, \end{aligned} \tag{12.16}$$

where ζ is the aspect ratio of inclusion. The aspect ratio of spherical inclusions is assumed to be 1. The value of $\tan\delta$ can be found using the above equations by separating imaginary and real parts of homogenized Young's modulus. The values of $\tan\delta$ obtained using Halpin-Tsai model are plotted in Fig. 12.3(a). It is observed that values of $\tan\delta$ obtained using Halpin-Tsai model are smaller than values obtained using rules of mixtures.

12.5 Mori-Tanaka method

Mori–Tanaka method is the most widely used analytical method for determining homogenized properties of composites. Since the influence of the shape of inclusions on the overall properties of composites are considered through Eshelby tensor [228], the Mori–Tanaka method provides a more accurate prediction of the homogenized properties of composites than other micromechanical methods. In this method, the homogenized complex modulus is given by

$$\boldsymbol{C^*} = \boldsymbol{C_m^*}\Big(\boldsymbol{I} - v_f[\boldsymbol{S^*}v_m + vf\boldsymbol{I} + (\boldsymbol{C_f} - \boldsymbol{C_m^*})^{-1}\boldsymbol{C_m^*}]^{-1}\Big)^{-1}, \tag{12.17}$$

where $\boldsymbol{C}_{\boldsymbol{m}}^{*}$ and $\boldsymbol{C}_{\boldsymbol{f}}$ are respectively the compliance tensor of matrix and inclusions, $\boldsymbol{I}$ is the identity matrix and $\boldsymbol{S}^{*}$ is the Eshelby's tensor. For plain stress 2D Eshelby's tensor is given as,

$$\boldsymbol{S}^{*} = \begin{bmatrix} \frac{7-5\nu^{*}}{15(1-\nu^{*})} & \frac{5\nu^{*}-1}{15(1-\nu^{*})} & 0 \\ \frac{5\nu^{*}-1}{15(1-\nu^{*})} & \frac{7-5\nu^{*}}{15(1-\nu^{*})} & 0 \\ 0 & 0 & \frac{4-5\nu^{*}}{15(1-\nu^{*})} \end{bmatrix}. \tag{12.18}$$

The values of $\tan\delta$ obtained using Mori–Tanakamethod are plotted in Fig. 12.3(b). In comparison with Halpin–Tsai method, the Mori–Tanaka method predicts lower values for $\tan\delta$. The plots of Fig. 12.3(b) also show that at low vibration frequencies the values of $\tan\delta$ are not affected by the inclusion volume fraction.

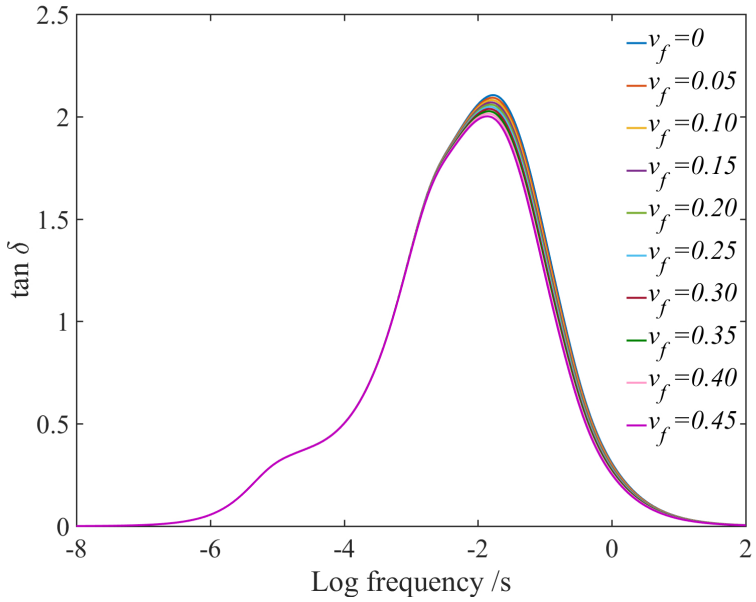

(a)

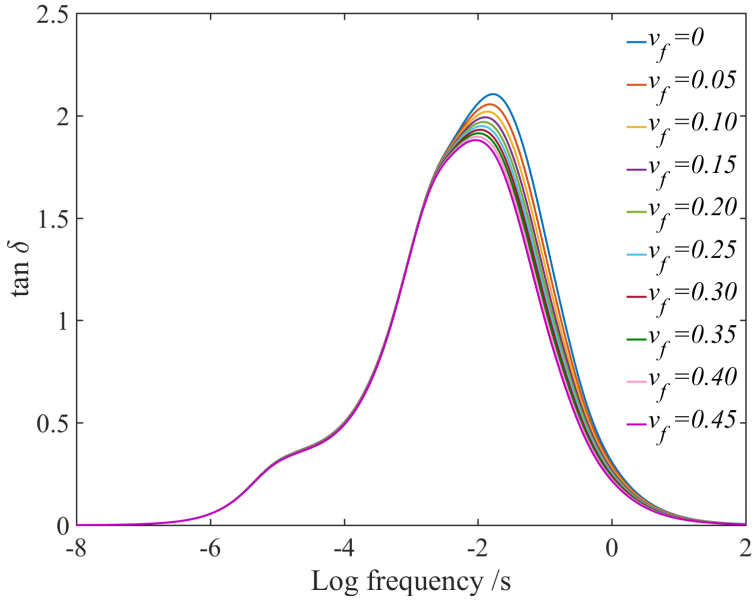

(b)

Figure 12.3: Estimated $\tan\delta$ using (a)Halpin-Tsai and (b) Mori-Tanaka model for different inclusion volume fractions.

CHAPTER 13: FINITE ELEMENT FORMULATION

13.1 RVE generation algorithm

The finite element computations are conducted on a representative volume element (RVE). The RVE is defined as the smallest volume whose properties represent the property of the whole structure. Based on the Hill's definition [227] an RVE should a) be entirely typical of the whole composite on average and b) includes a sufficient number of inclusions such that for macroscopically uniform boundary conditions, the properties of RVE be independent of the value of displacement and traction boundary conditions.

Different techniques for generating computational RVEs have been used in the past. Random sequential adsorption (RSA) schemes [201, 229–231] sequentially add inclusions to the matrix by randomly generating its location, size and orientation. The new inclusion is accepted only if it does not overlap with the previous inclusions. Jamming is an issue associated with RSA schemes which prevents achieving high volume fractions using this technique. Another class of methods which are used for the generation of RVEs are Monte Carlo (MC) based techniques [232–234]. Such techniques are essentially two–step schemes. First all the inclusions are deposited in the simulation box then the location and orientation of inclusions along with the size of RVE are modified to remove intersections and to achieve the desirable volume fraction. Because the movements are random, the removal of the overlaps using MC method is slow. To accelerate the process, molecular dynamics based techniques [235, 236] have been used to remove overlaps. More recently image reconstruction procedures [194, 237, 238] have been used to generate RVEs by extracting data from microstructural images. Such techniques require image analysis tools to reconstruct

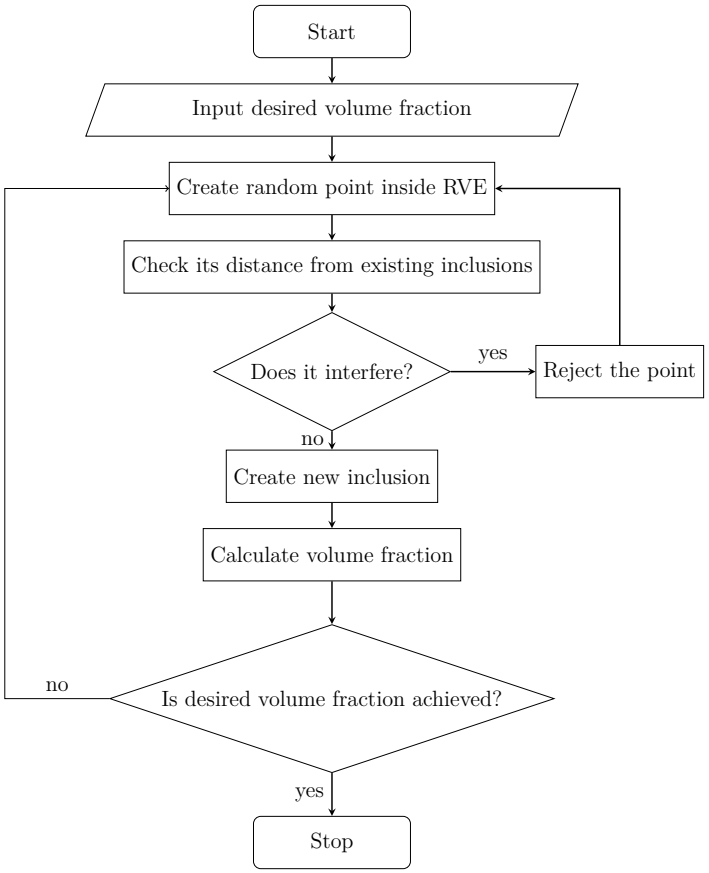

Figure 13.1: Flow chart of RVE generation

the three-dimensional structure of polymer composites.

In this paper we use a random sequential adsorption approach to generate the RVEs employing python scripting in Abaqus [239]. Location of the center of inclusions are randomly generated using random generator function of Python. The distance of the new inclusions from existing particles is checked to prevent intersecting of inclusions with each other. To ensure proper meshing, a minimum gap of 10% of the diameter of inclusion is maintained between any two inclusions. The addition of new particles continues until the desired volume fraction is obtained. Further details can be found in [240, 241].

13.2 Model geometry

We conduct both two–dimensional and three-dimensional simulations. The two–dimensional simulations are conducted under a plane-strain condition representing transverse behavior of unidirectional fibrous composites. The three–dimensional simulations are conducted on polymer composites with spherical inclusions. An example of a two and three–dimensional representative volume element is shown in Fig. 13.2a and Fig. 13.2b, respectively. RVEs are square and cube in two–dimensional and three–dimensional model respectively with an edge size of 2mm. Two–dimensional models are meshed using 6-node and 8-node plane strain elements as shown in Fig. 13.3a. Nodes on the boundary of matrix and inclusion are shared between both materials as shown in Fig. 13.3b. Three dimensional finite element models are meshed using 8-node tetrahedral elements as showed in Fig. 13.4. Similar to two–dimensional models, the nodes at the interface are shared between inclusion and matrix.

Since damping property of polymers is directly related to the value of $\tan\delta$, we use finite element method to calculate $\tan\delta$ by applying the following strain

$$\varepsilon_{yy} = \epsilon^0 \sin(\omega t), \tag{13.1}$$

to the top surface of the RVE. In Eq. (13.1) ϵ^0 is the amplitude of applied strain, ω is the vibration angular frequency and t is time. Since the amplitude of applied strain does not impact the value of $\tan\delta$, in our simulations we choose $\epsilon^0 = 1.0\%$. The impact of vibration frequency on damping is studied by considering a wide range of frequencies from 10^{-8}/s to 10^{2}/s.

The value of $\tan\delta$ can be calculated by comparing the input strain curve of Eq. (13.1) with the output stress curve. A typical input and output of a steady state vibration of Eq. (13.1) is shown in Fig. 13.5. As shown in Fig. 13.5 the angle δ is the phase lag between the input strain curve and output stress curve. The phase lag is related to

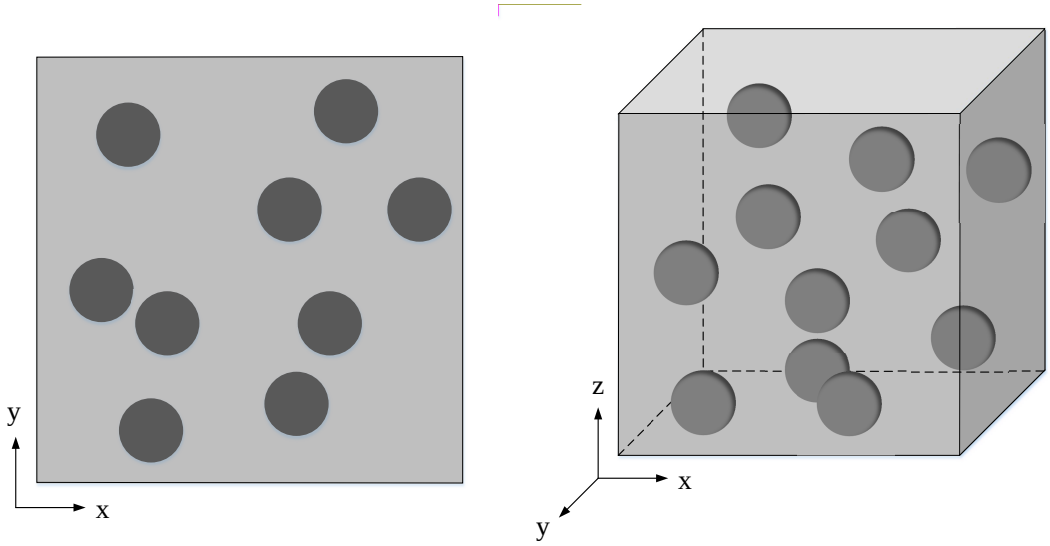

(a) (b)

Figure 13.2: Example of (a) 2D RVE and (b) 3D RVE with inclusion volume fraction 0.10.

the time lag Δt between the strain and stress curves by

$$\delta = 2\pi\Delta t f = \omega\Delta t, \tag{13.2}$$

where f is the loading ordinary frequency.

13.3 Boundary conditions

We use both mixed and periodic boundary conditions in our finite element modelings. Periodic boundary conditions are considered to be the most efficient and accurate choice for calculating the properties of RVEs [242–246]. The prescription of periodic boundary conditions can be challenging for complicated meshes, therefore mixed boundary conditions are used more often in finite element modeling of the damping properties of polymer composites [190, 194, 247]. In this paper, for the purpose of understanding the impact of boundary conditions on the predicted values of the damping of polymer composites, we use both mixed and periodic boundary conditions.

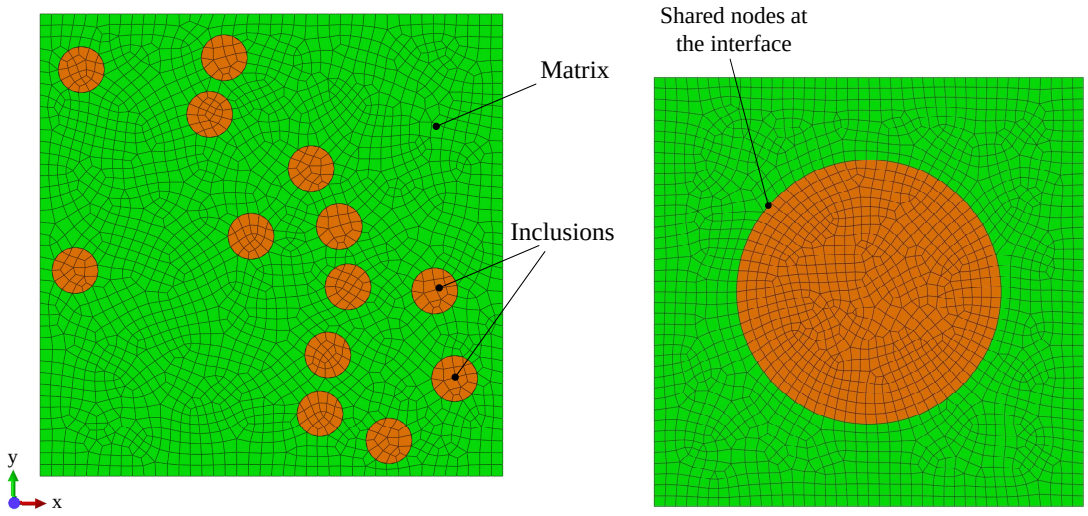

(a) (b)

Figure 13.3: (a) A two–dimensional finite element mesh, and (b) node sharing at the interface between matrix and inclusion.

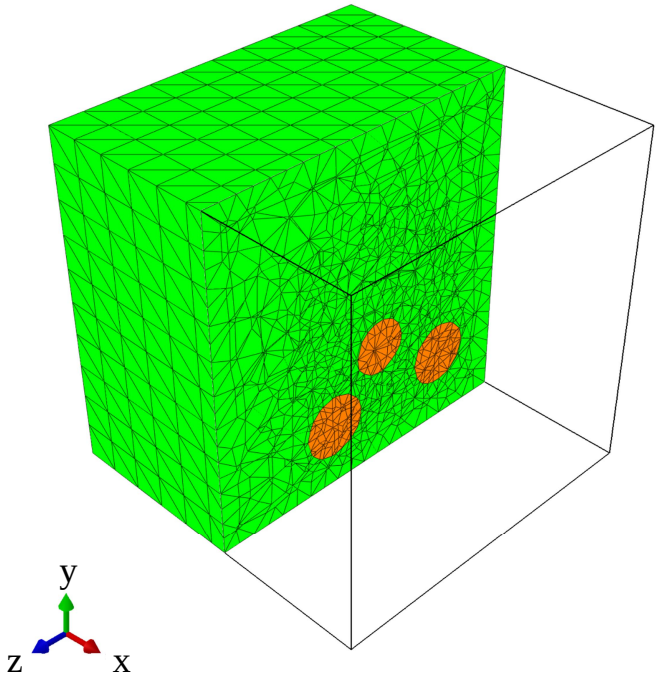

Figure 13.4: Discretization of a three dimensional RVE domain using finite element mesh.

13.3.1 Mixed boundary conditions

Mixed boundary conditions are applied by decomposing the boundary into two parts

$$\Omega = \Omega_{\mathbf{u}} \cup \Omega_{\mathbf{t}}, \tag{13.3}$$

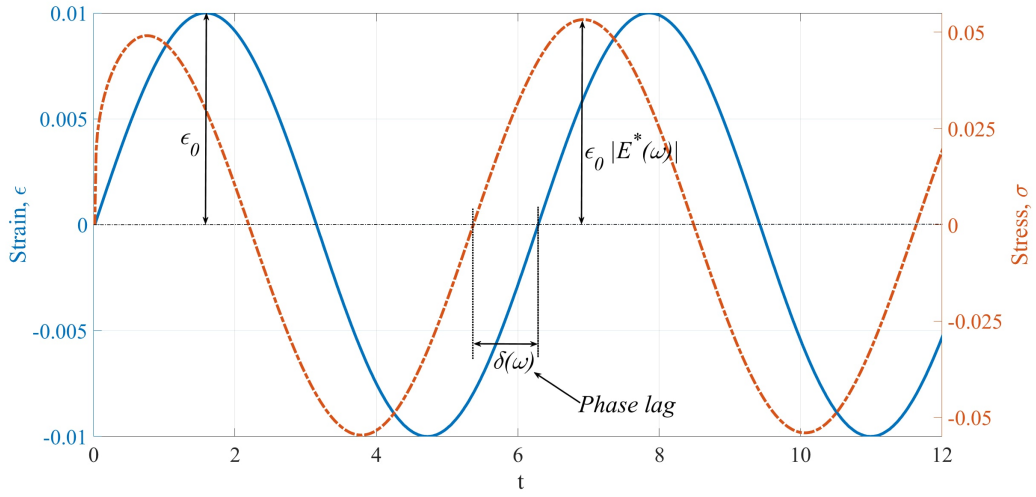

Figure 13.5: Example of input and output of steady state vibration

where displacements are prescribed on $\Omega_{\mathbf{u}}$ and tractions are applied on $\Omega_{\mathbf{t}}$. In this paper, the mixed boundary conditions shown in Fig. 13.6a are applied to the RVEs. As shown in Fig. 13.6a, a normal strain is applied to the top surface of the RVE using Eq. (13.1) while roller supports are applied to the left, bottom and back faces of the RVE as,

$$\begin{cases} u_1 = 0 & \text{on left face,} \\ u_2 = 0 & \text{on bottom face,} \\ u_3 = 0 & \text{on back face,} \end{cases} \tag{13.4a}$$

where, u_1,u_2 and u_3 are displacements in x, y and z direction respectively. The x component of the displacement of the right face of RVE is tied to the corresponding displacement component of edge BC and the z component of the displacement of the front surface of RVE is tied to the corresponding displacement component of edge AB. Such constraints are required to ensure that the RVE surfaces remain plane during deformation and no void is created in the domain as an artifact of numerical

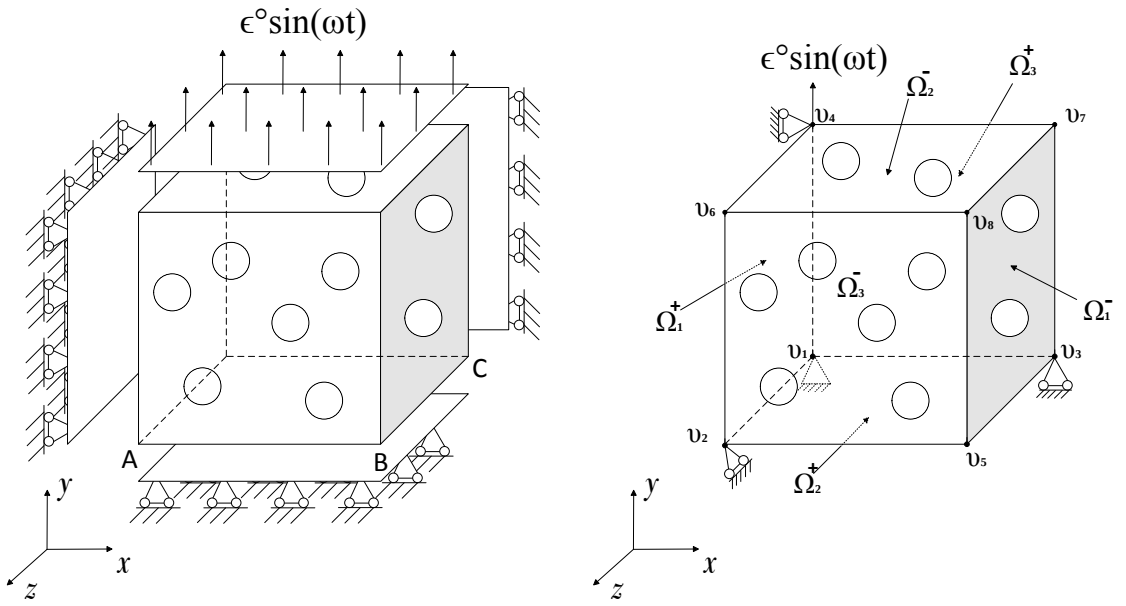

(a) (b)

Figure 13.6: RVE showing (a) Mixed boundary conditions and (b) Periodic boundary conditions.

modeling.

13.3.2 Periodic boundary conditions

To apply periodic boundary conditions (PBCs) to the RVE, the boundary Ω of the RVE is decomposed into two parts, as shown in Fig. 13.6b: Ω^+ and Ω^- such that $\Omega = \Omega^+ \cup \Omega^-$. If a surface belongs to Ω^+ its opposite surface belongs to Ω^-. The imposition of periodic boundary conditions on the RVE is schematically shown in Fig. 13.6b. RVE has eight vertices υ_1 to υ_8 connected by three boundary pairs Ω_p^+ and Ω_p^-, where $p = 1, 2, 3$. To avoid rigid body motion vertex υ_1 is fixed. Roller supports are applied to vertex υ_2, υ_3 and υ_4. Finally loading is applied to vertex υ_4 in y direction.

By assuming that the RVE deforms in a repetitive way identical to its adjacent neighbors, the periodic boundary conditions are obtained by enforcing that the displacement and tractions of opposite surfaces of the RVE should satisfy the following

compatibility condition [248]

$$\mathbf{u}(\mathbf{x}^+) = \mathbf{u}(\mathbf{x}^-) \quad \forall \mathbf{x}^+ \in \Omega^+ \quad \text{and matching} \quad \mathbf{x}^- \in \Omega^-, \tag{13.5a}$$

$$\mathbf{t}(\mathbf{x}^+) = \mathbf{t}(\mathbf{x}^-) \quad \forall \mathbf{x}^+ \in \Omega^+ \quad \text{and matching} \quad \mathbf{x}^- \in \Omega^-, \tag{13.5b}$$

where $\mathbf{u}$ and $\mathbf{t}$ are the displacement and traction vectors, respectively. In a finite element simulations, these conditions are satisfied by enforcing the following relations between the displacements of opposite surfaces [242]

$$\mathbf{u}_{\Omega_1^+} = \mathbf{u}_{\Omega_1^-} - \mathbf{u}_{\upsilon_3} + \mathbf{u}_{\upsilon_1}, \tag{13.6a}$$

$$\mathbf{u}_{\Omega_2^+} = \mathbf{u}_{\Omega_2^-} + \mathbf{u}_{\upsilon_1} - \mathbf{u}_{\upsilon_4}, \tag{13.6b}$$

$$\mathbf{u}_{\Omega_3^+} = \mathbf{u}_{\Omega_3^-} - \mathbf{u}_{\upsilon_2} + \mathbf{u}_{\upsilon_4}, \tag{13.6c}$$

where $\mathbf{u}_i$ is displacement vector for any point on the corresponding boundary Ω_i and $\mathbf{u}_{\upsilon_i}$ is displacement vector for vertex υ_i. The relations in Eq. (13.6) are imposed by discretizing the RVE using a periodic mesh such that opposite boundaries are discretized using the same mesh distribution. A python script is used to find the matching nodes on opposite faces and the relations of Eq. (13.6) are imposed to the matching nodes using equation constraint in Abaqus for each degree of freedom of all nodes on boundary surfaces.

CHAPTER 14: RESULTS

To eliminate the impact of randomness of the arrangement of constituents on the calculated values of $\tan\delta$, the values of $\tan\delta$ presented in this section are ensemble averages. The ensemble averages $\langle\tan\delta\rangle$ are obtained from

$$\langle\tan\delta\rangle = \frac{1}{M}\sum_{J=1}^{M}\left(\tan\delta\right)_J, \tag{14.1}$$

where M is the number of samples in the ensemble and $\left(\tan\delta\right)_J$ is the value of $\tan\delta$ calculated using the J^{th} RVE. To ensure enough number of RVE samples are available in the ensemble, we incrementally increase the size of the ensemble. If the value of ensemble average of $\tan\delta$ does not change by increasing the size of ensemble, the ensemble average is converged and the ensemble contains enough number of samples. We use the following convergence criterion

$$\left|\frac{\langle\tan(\delta)\rangle^{M} - \langle\tan(\delta)\rangle^{M+1}}{\langle\tan(\delta)\rangle^{M}}\right| < \text{Tol} = 0.01\%, \tag{14.2}$$

where $\langle\cdot\rangle^{M}$ denotes an ensemble average value obtained using M samples. As an example, the ensemble average of the maximum value of $\tan\delta$ versus the number of samples in the ensemble are shown in Fig. 14.1. These results are obtained for a three–dimensional RVE with a inclusion volume fraction of $v_f = 0.10$ under mixed boundary conditions. This graph shows that the convergence criterion is satisfied by an ensemble containing 25 samples. In this paper, the reported values of $\tan\delta$ are the ensemble averages obtained from an ensemble with 100 samples for two–dimensional RVEs and 50 samples for three–dimensional RVEs.

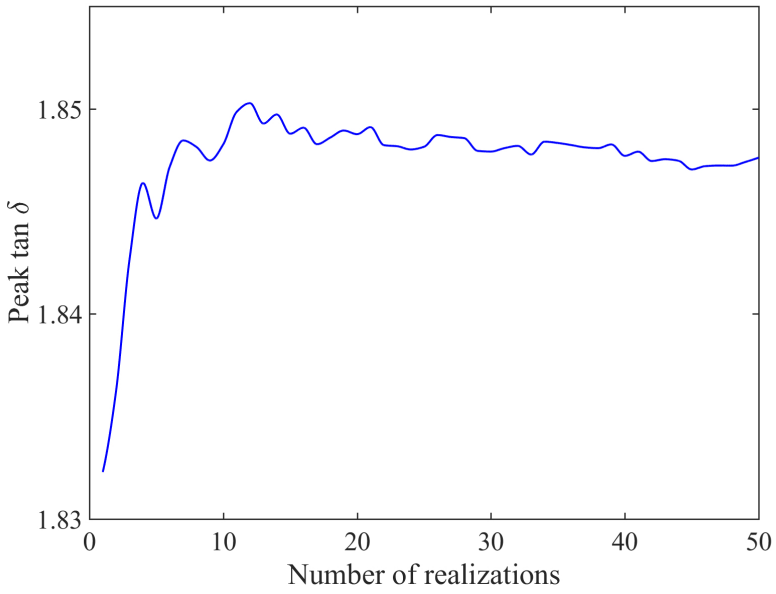

Figure 14.1: Ensemble average of peak $\tan\delta$ versus realization number for $v_f = 0.10$.

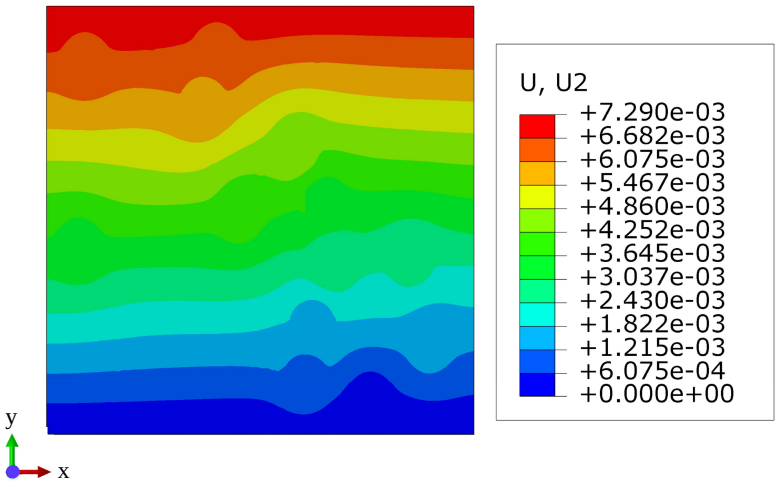

Figure 14.2: Deformation of RVE under applied loading.

14.1 Interaction between inclusions

The analytical methods mentioned above assume that the inclusions are at large distances from each other so that they don't interact with each other. This assumption is only valid when inclusions volume fraction is low and hence there is considerable distance between any two inclusions. In practice, when inclusion volume fraction in-

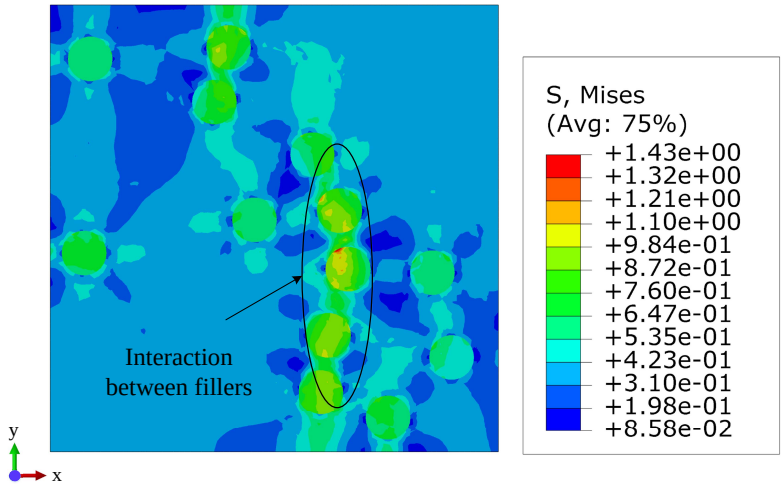

Figure 14.3: Mises stress distribution in a 2D RVE indicating interaction between inclusions.

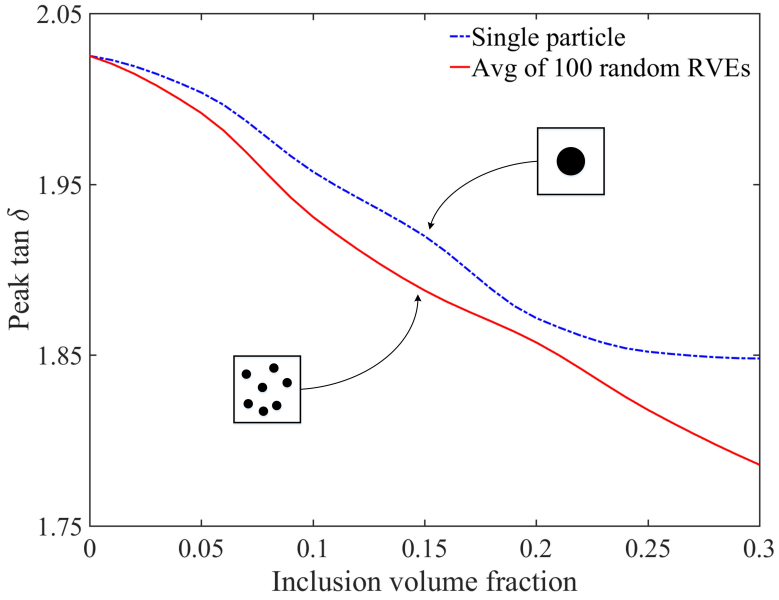

Figure 14.4: Comparison of peak $\tan\delta$ values for RVEs with single inclusion versus RVEs with random particles distribution.

creases inclusions get close to each other which results in interaction between stress fields of individual inclusions. The deformation and Mises stress distribution in a 2D RVE are shown in Fig. 14.2 and Fig. 14.3 show; respectively. As shown in Fig. 14.3, the interaction between particles lead to stress concentration in the regions between particles. Such an interaction affects the mechanical properties of composite ma-

terials. We also studied the effect of interaction between inclusions by comparing the values of peak $\tan\delta$ for RVEs including only one inclusion at their center versus RVEs with similar inclusion volume fraction but including several small inclusions randomly distributed in the matrix. The peak $\tan\delta$ results for these cases are shown in Fig. 14.4. The peak $\tan\delta$ for the RVEs with random distribution is obtained by averaging the results obtained from 100 RVEs. As Fig. 14.4 shows, at low volume fraction the peak $\tan\delta$ of both RVEs are close to each other. By increase in the inclusions volume fraction the difference between the value of peak $\tan\delta$ between the two RVEs increases. Such difference between the results is due to the interaction between the inclusions. Due to such interaction between inclusions, the analytical homogenization approach cannot be used for obtaining the damping properties of polymer composites with high inclusion volume fractions.

14.2 Two–dimensional analysis of $\tan\delta$

The average values of $\tan\delta$ under different vibration frequencies for a two–dimensional RVE under mixed boundary conditions are shown in Fig. 14.5a. These graphs show that damping is significantly influenced by the vibration frequency. At low frequencies the value of $\tan\delta$ is close to zero indicating that stress is in phase with the applied strain and no energy damping is occurring. Then value of $\tan\delta$ increases as frequency increases until reaching its maximum value at a frequency of about 10^{-2}/s. Further increase in the vibration frequency leads to a reduction in the damping capability of polymer composite and $\tan\delta$ goes to zero for frequencies greater than 10^{2}/s. Moreover, the graphs of Fig. 14.5a show that increasing the inclusion volume fraction slightly reduces the maximum value of $\tan\delta$. The frequency at which peak $\tan\delta$ occurs as a function of inclusion volume fraction is shown in Fig. 14.5b. This graph shows that by increasing the volume fraction the maximum damping occurs at a lower frequency. Comparison of results from FEM with analytical methods is shown in Fig. 14.6. It is very clear that, analytical methods gives accurate predictions

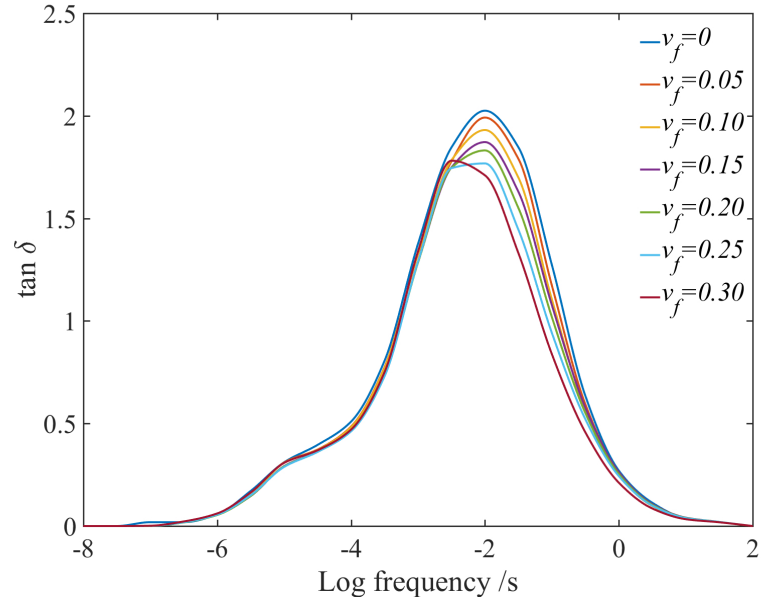

(a)

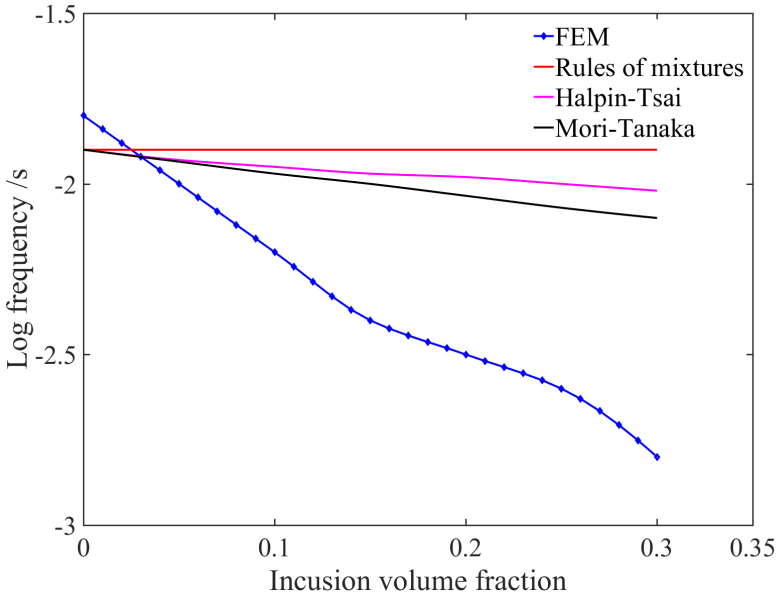

(b)

Figure 14.5: (a) $\tan\delta$ values for 2D system with mixed boundary conditions at varying frequencies, and (b) the frequency at which peak $\tan\delta$ occurs versus inclusion volume fraction.

only for very low volume fraction. As inclusion volume fraction increases predictions deviate drastically. In all analytical methods Mori-Tanaka gives closest predictions

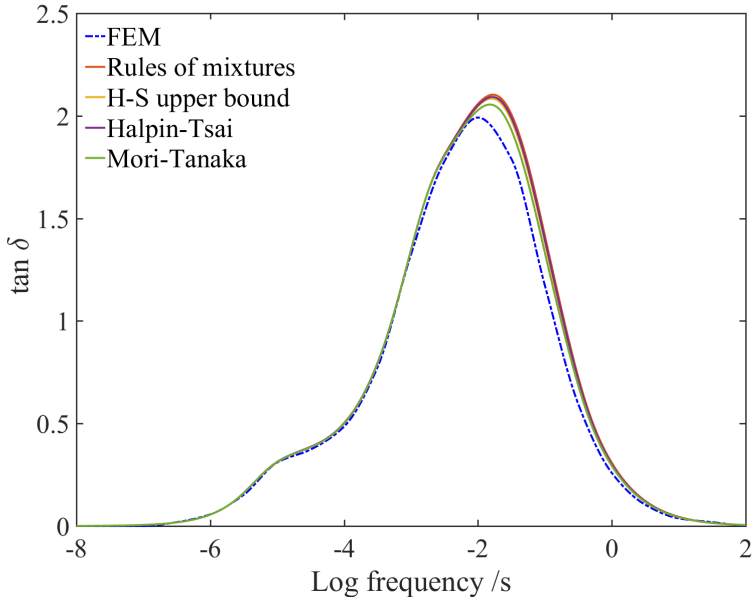

(a)

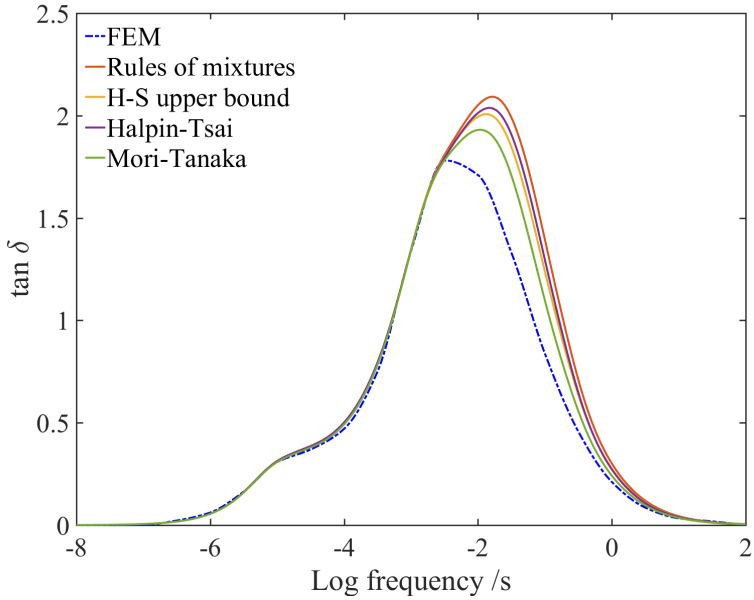

(b)

Figure 14.6: Comparison of FEM $\tan\delta$ values for 2D system with analytical methods for inclusion volume fraction of (a) $v_f = 0.05$ and (b) $v_f = 0.30$.

as it considers shape of inclusions. But it gives very accurate answers for prediction of $\tan\delta$ for few inclusions but looses its accuracy for large number of inclusions as it does not consider interactions between inclusions.

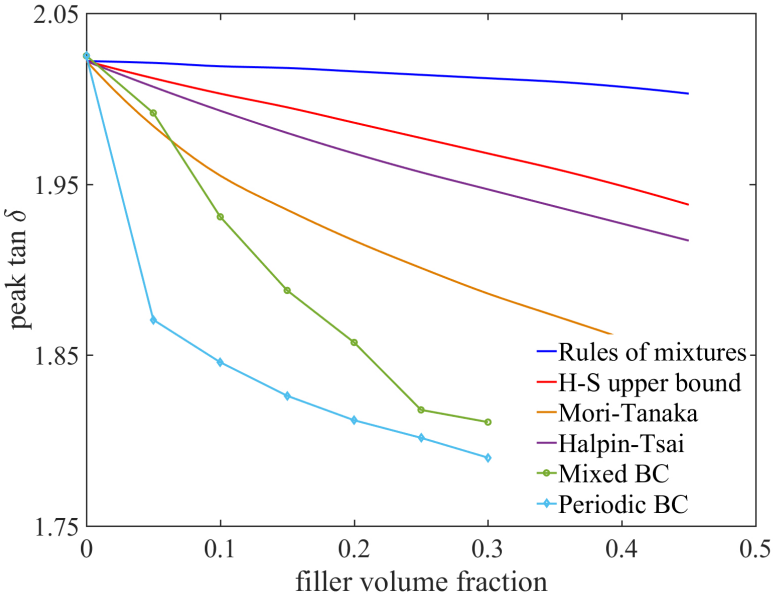

Figure 14.7: Comparison of peak $\tan\delta$ values for 2D system with mixed boundary conditions and periodic boundary conditions for different volume fractions.

14.3 Effect of boundary conditions

The maximum value of $\tan\delta$ obtained using mixed and periodic boundary conditions (PBCs) are shown in Fig. 14.7 and compared with analytical methods. In the absence of inclusions the maximum $\tan\delta$ predicted using periodic boundary conditions is about 6% lower than that obtained using mixed boundary condition. As the inclusion volume fraction increases the $\tan\delta$ obtained from the two boundary conditions approach each other. Although the results obtained from the PBCs are in general slightly less than those obtained from mixed boundary conditions, however, the values predicted by the two boundary conditions are close to each other and both mixed and periodic boundary conditions can be used for the purpose of calculating $\tan\delta$. Mori-Tanaka method gives very accurate predictions for small number of inclusions but gives huge error for large number of inclusions. This is basically because of the fact that, analytical methods don't consider interactions between particles. When number of particles are low, interaction between any two particle is very weak

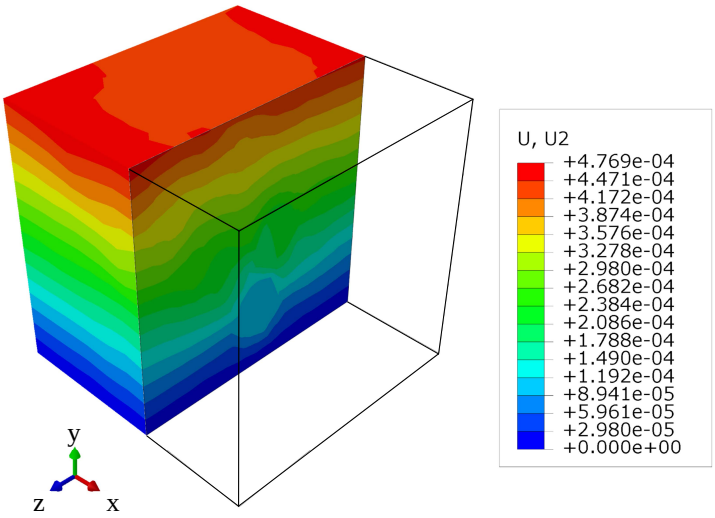

Figure 14.8: Deformation of 3D RVE under applied loading.

and hence analytical methods give correct predictions, but as number of particles increases, interaction forces increases and predictions introduce huge errors.

14.4 Three-dimensional analysis of $\tan\delta$

We conduct three–dimensional analysis to study the damping of composites with spherical inclusions. An example of the deformation of a 3D RVE under applied loading is shown in Fig. 14.8 The values of $\tan\delta$ obtained using mixed boundary conditions are shown in Fig. 14.9a. Similar to the results of two–dimensional analysis, by increasing the vibrational frequency the value of $\tan\delta$ increases until it reaches its peak value after which further increase in the input frequency leads to a reduction in the value of $\tan\delta$. Increase in inclusion volume fraction results in a decrease in the the peak value of $\tan\delta$. The maximum value of $\tan\delta$ in the absence of inclusions is more than that obtained from two–dimensional analysis, indicating that damping is higher under plane strain conditions.

The impact of boundary conditions on the peak value of $\tan\delta$ is studied and the peak values of $\tan\delta$ obtained from these boundary conditions are presented in Fig. 14.9b. Similar to the plane stress case, RVEs with periodic boundary condi-

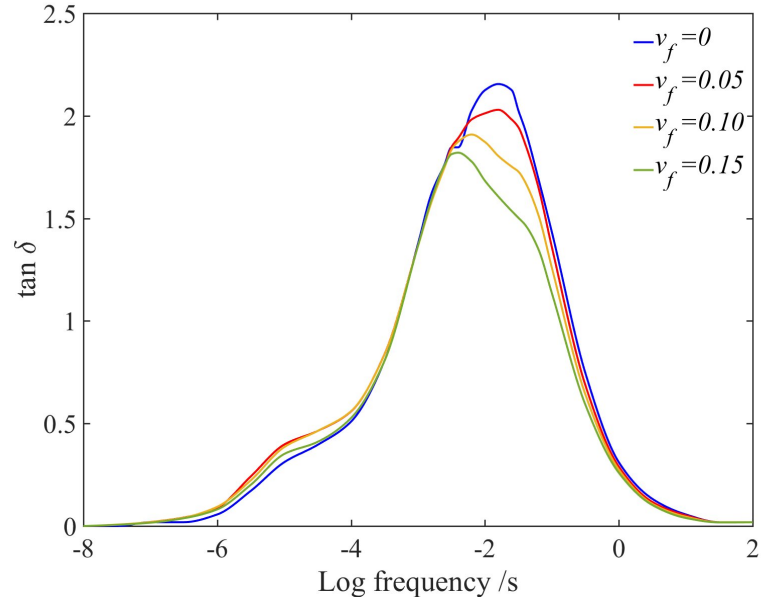

(a)

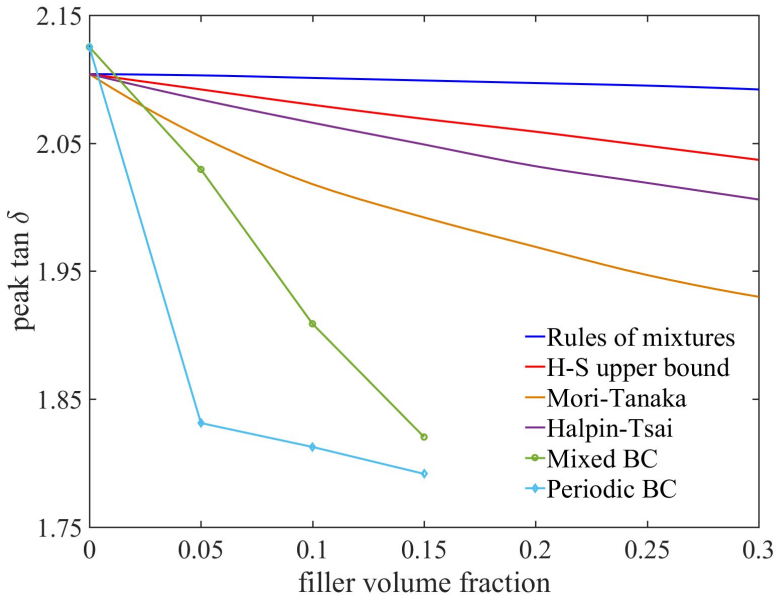

(b)

Figure 14.9: (*a*) $\tan\delta$ values for 3D system with mixed boundary conditions at varying frequencies and (*b*) Comparison of peak $\tan\delta$ values for 3D system with mixed boundary conditions and periodic boundary conditions for different inclusion volume fractions.

tions demonstrate a lower $\tan\delta$ value, but the maximum difference between the peak $\tan\delta$ obtained from the two boundary conditions is about 5%, hence using periodic

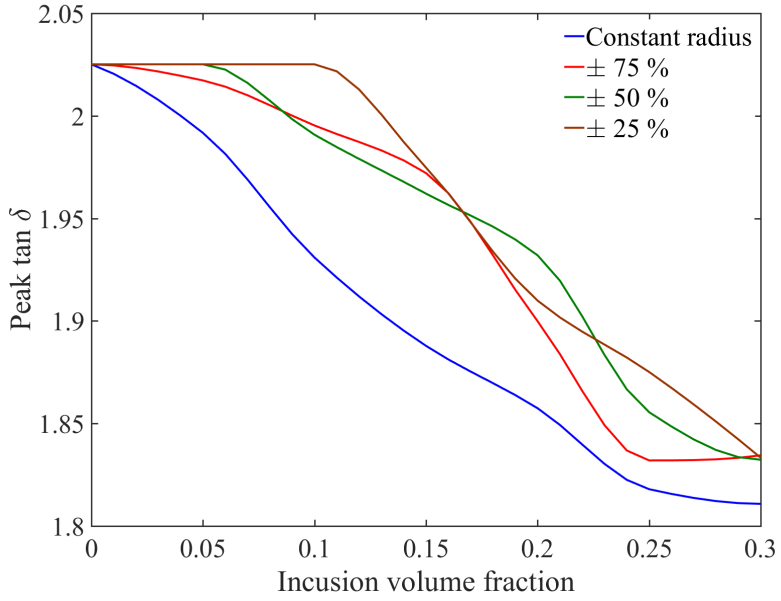

Figure 14.10: Comparison of $\tan\delta$ values for 2D system with mixed boundary conditions for different variation in radius of inclusions for different inclusion volume fractions.

or mixed boundary condition leads to similar predictions for $\tan\delta$. Again similar behavior is observed with comparison to predictions of analytical methods.

14.5 Effect of variation in the size of inclusions on damping properties

In practice it is not possible to use inclusions of the same particle size, hence it is necessary to understand the effect of variation in inclusions size on $\tan\delta$ at constant inclusion volume fractions. For this purpose, we use normal distribution function to create inclusions with different radius in the RVE. We generate four cases where in case one radius of inclusions are same and that is equal to mean value of normal distribution function. In case two, radius of inclusions is varied by $\pm 25\%$. Similarly in case three and four radius of inclusions is varied by $\pm 50\%$ and $\pm 75\%$ respectively.

To avoid inclusions which are too small or too large the maximum and minimum radius of inclusions are limited to 25% and 175% of it's mean value. All the RVEs generated have multiple number of inclusions so the effects of inclusions interactions

are considered. Results for all four cases are shown in Fig. 14.10. These results show that the peak value of $\tan\delta$ is not very sensitive to the size of inclusions as long as the number of inclusions in both cases are comparable.

CHAPTER 15: SENSITIVITY ANALYSIS

We conduct sensitivity analysis (SA) to understand how the prediction of the damping properties of polymer composites are impacted by the uncertainty in the input parameters of material properties of matrix and inclusions. In this paper two types of sensitivity analysis are conducted. The first set of analysis is performed with respect to uncertainty in the instantaneous Young's modulus of polymer and inclusion and the second set of sensitivity analysis is conducted with respected to the relaxation time of matrix. Since the matrix material presented in Table 12.1 has multiple relaxation times, the sensitivity analysis of relaxation time is conducted only on the relaxation time which is associate with the largest value of relaxation modulus, i.e $\tau = 3.162$ s. This relaxation time is chosen since its corresponding modulus has the most impact on the instantaneous configuration of the matrix.

The sensitivity analysis is conducted by preparing RVEs with different material properties. For each inclusion volume fraction 100 RVEs are generated. The instantaneous Young's modulus of the matrix and inclusion are randomly chosen in the range of 0.5 MPa to 900 MPa for matrix and 32 GPa to 96 GPa for inclusions. The value of the relaxation time of the matrix is varied by 50% while keeping all the other parameters fixed. Different schemes have been developed in the past for the generation of input variables over a specific range. These include deterministic sampling, random sampling, stratified sampling [249–251]. In deterministic sampling input parameters are selected in regular intervals. Although this is a very straight forward approach but the number of required samples increases exponentially. This disadvantage can be overcome by using a random sampling technique such as Monte Carlo. Monte Carlo scheme provide an efficient technique for the generation of random input variables,

however using Monte Carlo approach can lead to artificial correlations in the input and output parameters [250]. To remove the issue of undesired correlations, stratified sampling method has been developed. In stratified sampling method the sampling space is divided into separate groups called strata. Random samples are drawn from each strata group. This technique is further extended to Latin Hypercube Sampling (LHS) where the range of each variable is divided into equal intervals and a sample is selected from each interval [251]. In this paper, to overcome the issue of undesired correlations between input parameters, we use LHS to generate random values for the Young's modulus of matrix and inclusions. Python package pyDOE [252] is used to generate sample points using LHS with two variables and 100 sample points for each variable.

15.1 Results of sensitivity analysis

The scatter plots of peak value of $\tan\delta$ versus the Young's modulus of inclusions and matrix at different volume fractions are shown in Fig. 15.1 to Fig. 15.6. The data of these figures show that as the inclusions become stiffer the peak value of $\tan\delta$ increases whereas when matrix becomes stiffer the peak value of $\tan\delta$ decreases.

15.2 Regression analysis

In order to understand results better, regression analysis is conducted on obtained data. In simple words, regression analysis is nothing but study of how parameters are dependent of each other. In our case, the material properties are independent parameter and peak value of $\tan\delta$ is dependent parameter. Therefore our aim is to come up with an equation which will give us relationship between these dependent and independent parameters. The most common and easiest type of relationship is linear relationship. Linear regression lines are fitted to the scatter data points using the following equations

$$\bar{y} = c + m\bar{x}, \tag{15.1}$$

where intercept c and slope m are given by

$$c = \bar{y} - m\bar{x}, m = \frac{S_{xy}}{S_{xx}}, S_{xx} = \sum_{j=1}^{N} x_j^2 - N\bar{x}^2, S_{xy} = \sum_{j=1}^{N} x_j y_j - N\bar{x}\bar{y}, \tag{15.2}$$

where x_i and y_i represent inputs and outputs parameters, i.e the Young's modulus and the peak of $\tan\delta$, $\bar{x}$ and $\bar{y}$ are mean values of x_i and y_i and N is the number of observations. The intercept c and slope m corresponding to uncertainty in the Young's modulus of filler and matrix are presented in Table 15.1 and Table 15.2, respectively.

The 95% confidence interval (CI) is calculated using

$$y_C = y_{\text{fitted}} \pm t_\alpha(SE)\sqrt{\frac{1}{N} + \frac{(x-\bar{x})^2}{SS_x}}, \tag{15.3}$$

and the 95% prediction interval (PI) is computed by

$$y_P = y_{\text{fitted}} \pm t_\alpha(SE)\sqrt{1 + \frac{1}{N} + \frac{(x-\bar{x})^2}{SS_x}}, \tag{15.4}$$

where, y_{fitted} is fitted value using regression, t_α is the coefficient for 95% level and SE is the residual standard error. The expected bounds of the regression function are depicted by the confidence interval lines, while the width of the confidence interval provides an indication of the quality of the fitted regression function. The width of the prediction interval is always wider than the CIs as the PIs takes into consideration the uncertainty in knowing the value of the population as well as the data scatter.

As shown in Table 15.1 the slope of regression lines of peak $\tan\delta$ versus inclusion's Young's modulus is always positive and increases from 0.5×10^{-6} to 3×10^{-6} as inclusion volume fraction increases from 0.05 to 0.30. This shows that at a specific volume percentage, composites with stiffer inclusions have higher damping capabilities. On the other hand, the intercept values of the regression lines decreases from

Table 15.1: The intercept and slope of linear regression line for peak $\tan\delta$ versus Young's modulus of inclusions

Filler volume fraction (V_f)	0.05	0.10	0.15	0.20	0.25	0.30
Intercept	1.9104	1.7132	1.6568	1.4855	1.5492	1.2572
Slope$\times 10^{-6}$	0.5	1.0	2.0	2.0	2.0	3.0

Table 15.2: The intercept and slope of linear regression line for peak $\tan\delta$ versus Young's modulus of matrix

Filler volume fraction (V_f)	0.05	0.10	0.15	0.20	0.25	0.30
Intercept	1.9788	1.8899	1.8548	1.7855	1.8643	1.6343
Slope$\times 10^{-4}$	-0.7	-2.0	-2.0	-3.0	-4.0	-4.0

1.9104 to 1.2576 as the inclusion volume fraction increases indicating that composites with lower inclusion volume fractions have higher damping capabilities.

The values of slope and intercept presented in Table 15.2 show that as the matrix get stiffer the values of both slope and intercept reduces. The value of slope is negative for all the inclusion volume fractions and reduces from -0.7×10^{-4} to -4×10^{-4}. This shows that increase in the stiffness of matrix adversely affect the damping capability of composite and its adverse effects are more severe for composites with higher inclusion volume fractions. The figures also show the regions with 95% confidence intervals and 95% prediction intervals . The area which lies between the red lines depicts the 95% CIs while the 95% PIs are depicted by the area between the magenta lines. The likely location of the true population parameter can be inferred from the CIs, while the PIs provide an indication regarding the distribution of values and where the next data point can be expected.

The effect of relaxation time on the peak value of $\tan\delta$ is shown in Fig. 15.7. As expected when the relaxation time of polymer increases the damping capability of polymer improves. The plot of Fig. 15.7 shows that for the matrix used in this paper the peak value of damping is linearly related to the relaxation time.

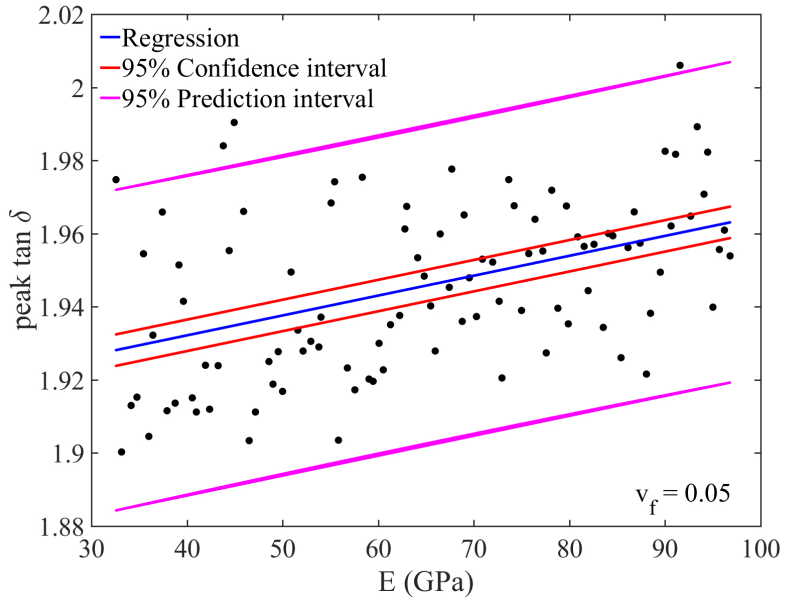

(a)

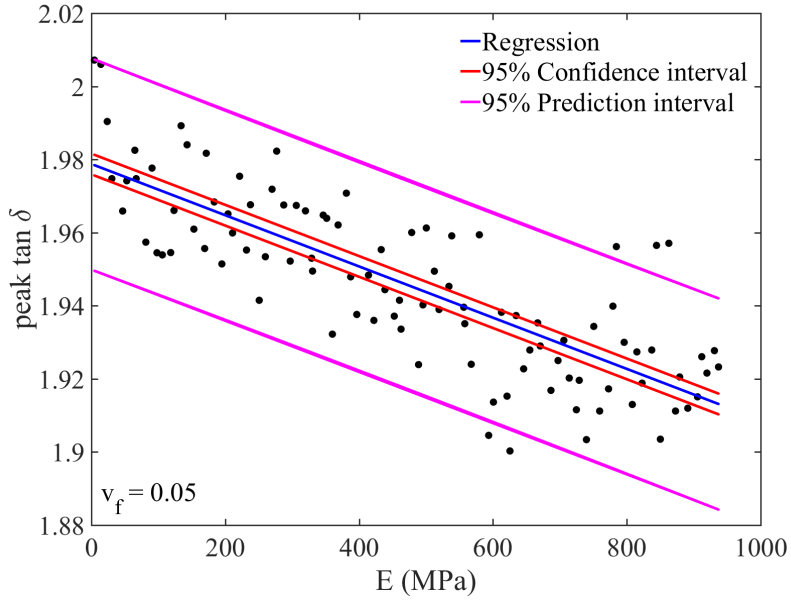

(b)

Figure 15.1: Peak tan δ versus Young's modulus of (a) inclusions and (b) matrix for inclusion volume fraction of 0.05 .

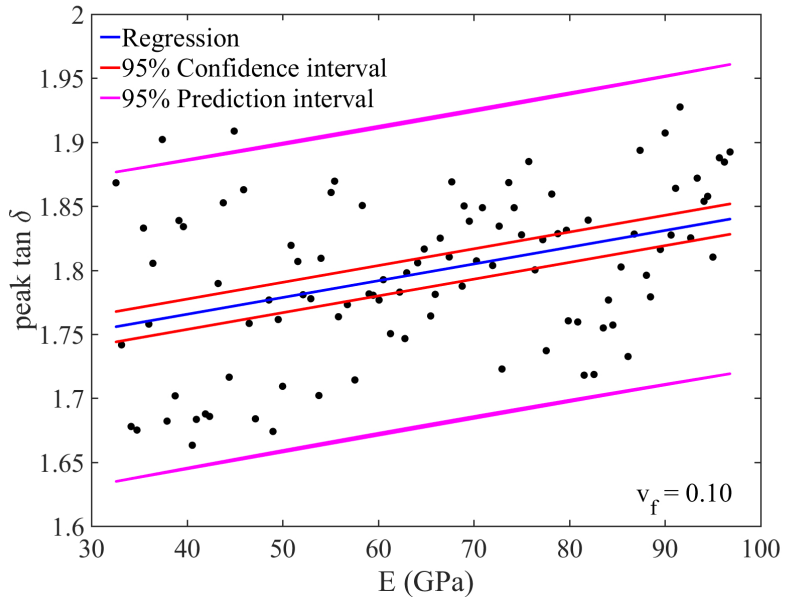

(a)

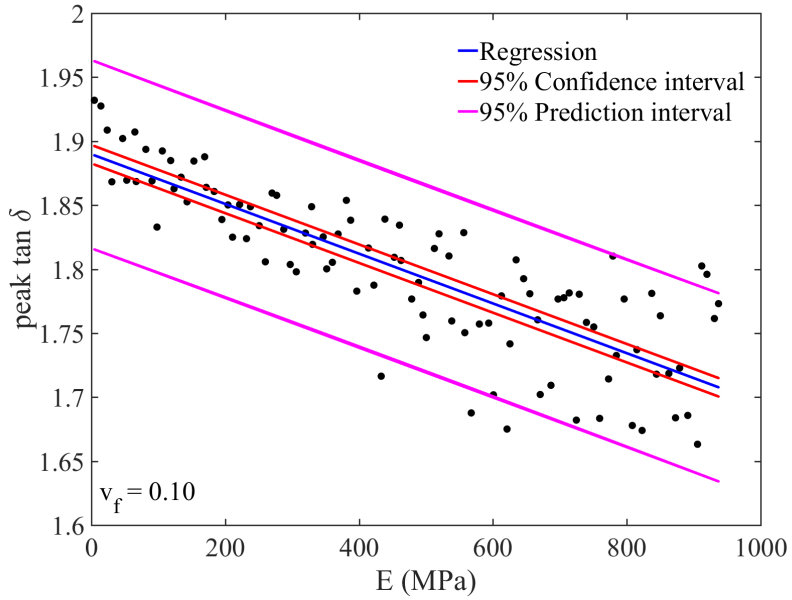

(b)

Figure 15.2: Peak tan δ versus Young's modulus of (a) inclusions and (b) matrix for inclusion volume fraction of 0.10 .

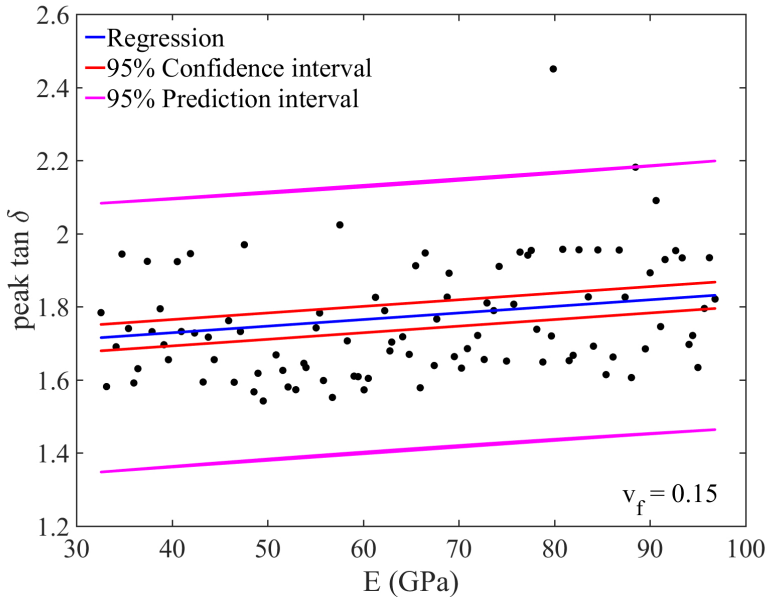

(a)

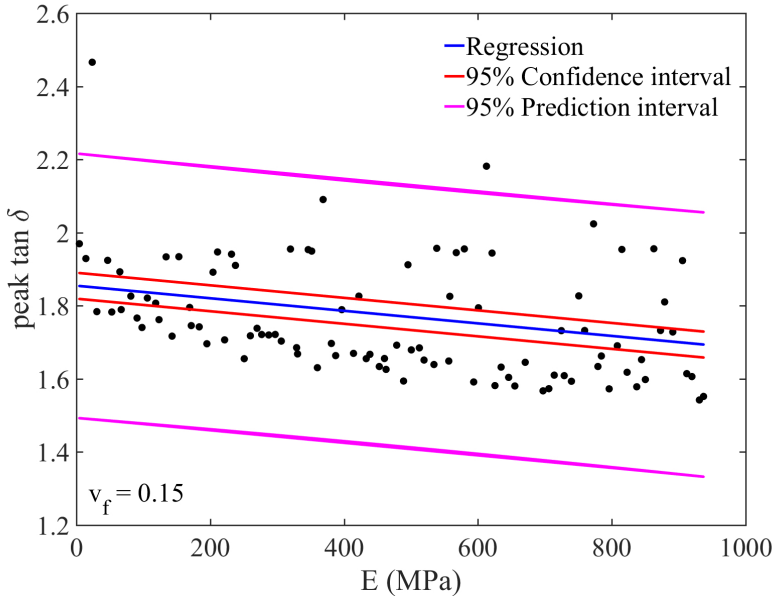

(b)

Figure 15.3: Peak tan δ versus Young's modulus of (a) inclusions and (b) matrix for inclusion volume fraction of 0.15 .

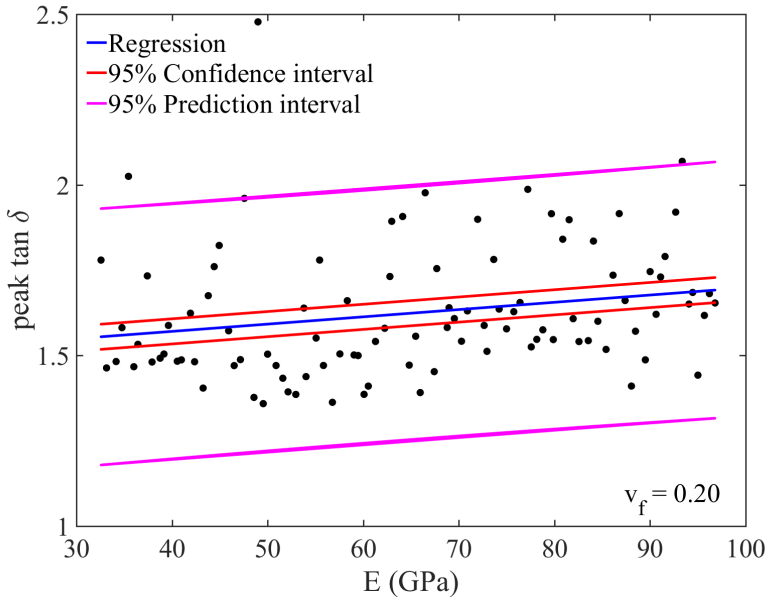

(a)

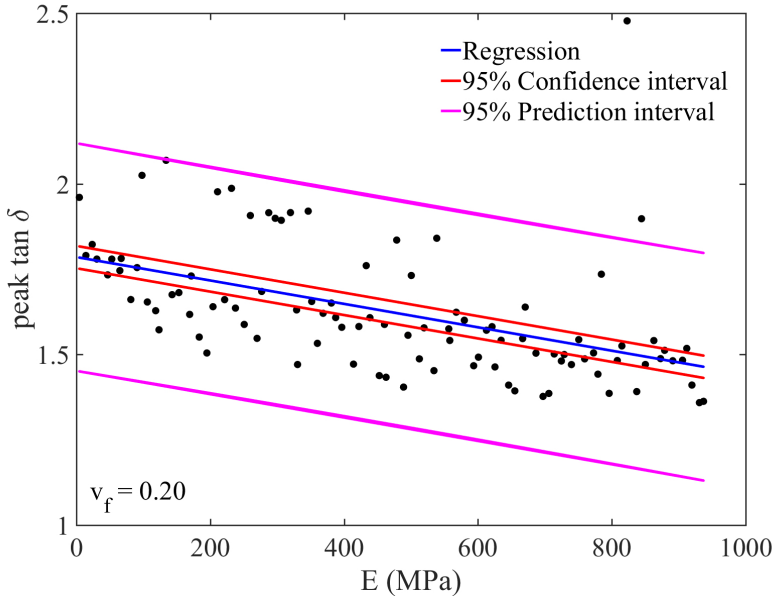

(b)

Figure 15.4: Peak tan δ versus Young's modulus of (a) inclusions and (b) matrix for inclusion volume fraction of 0.20 .

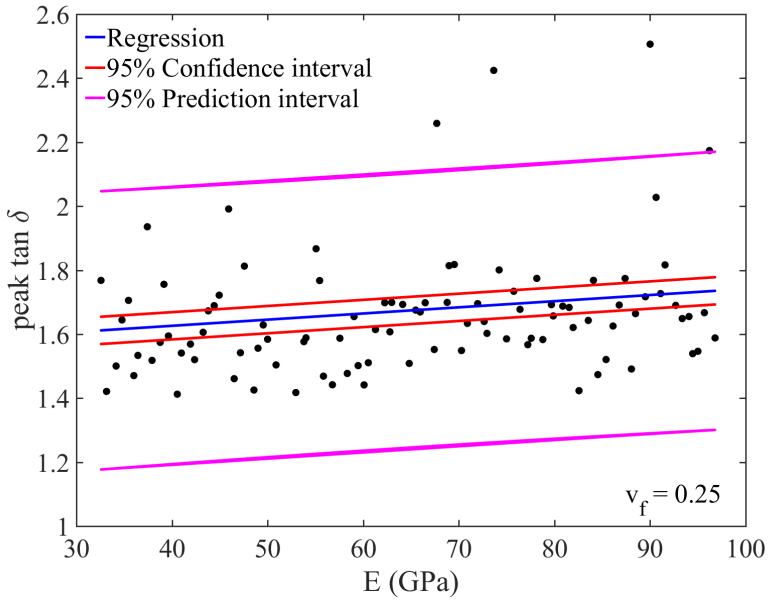

(a)

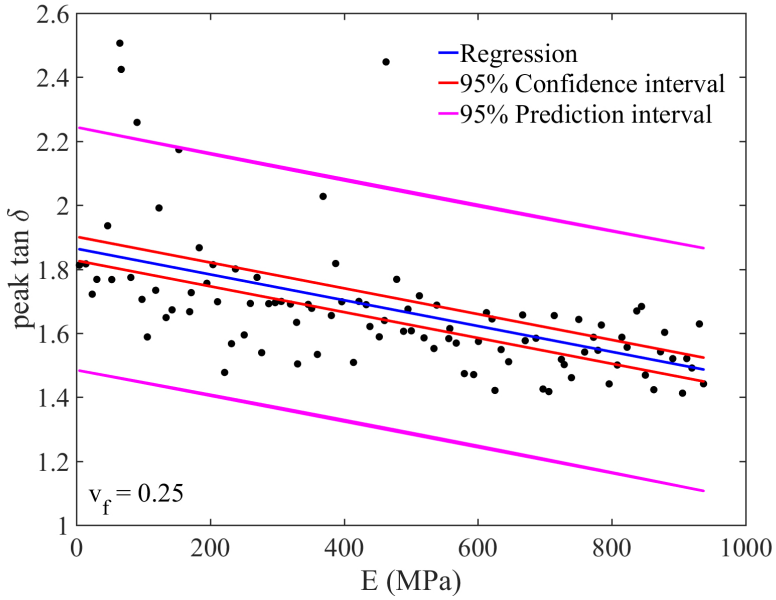

(b)

Figure 15.5: Peak tan δ versus Young's modulus of (a) inclusions and (b) matrix for inclusion volume fraction of 0.25 .

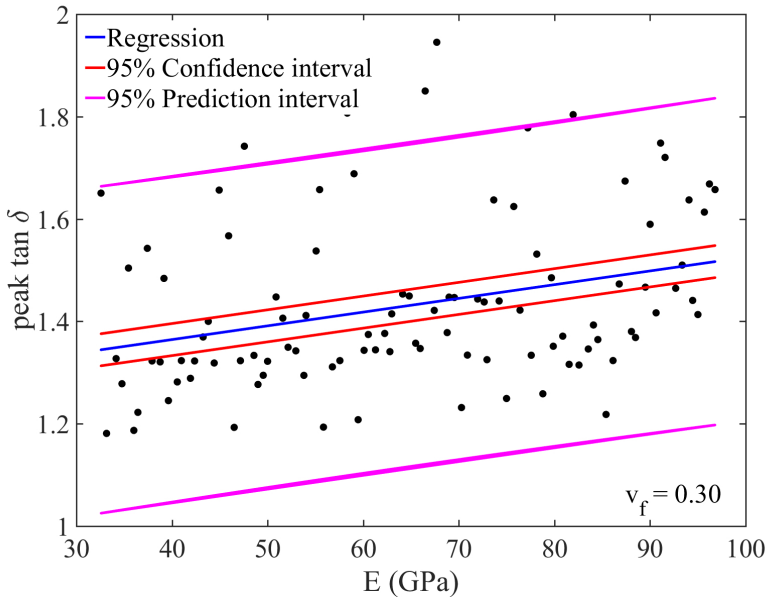

(a)

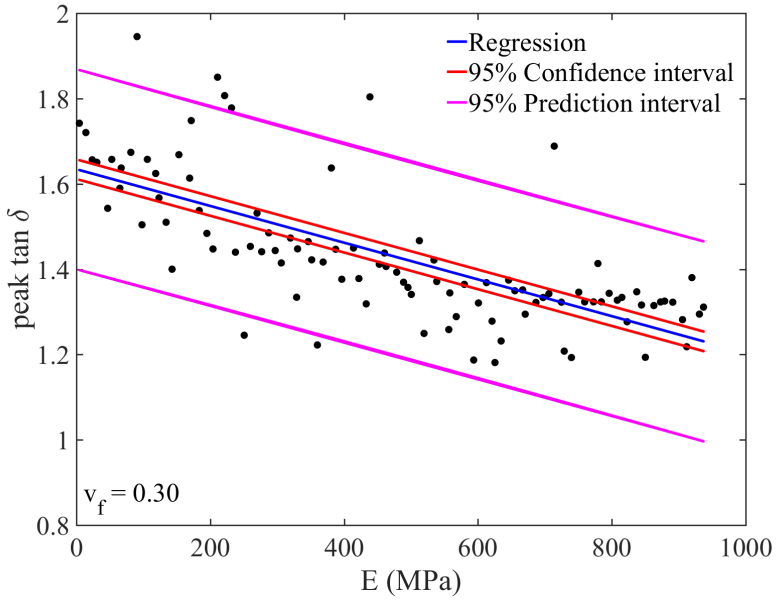

(b)

Figure 15.6: Peak tan δ versus Young's modulus of (a) inclusions and (b) matrix for inclusion volume fraction of 0.30 .

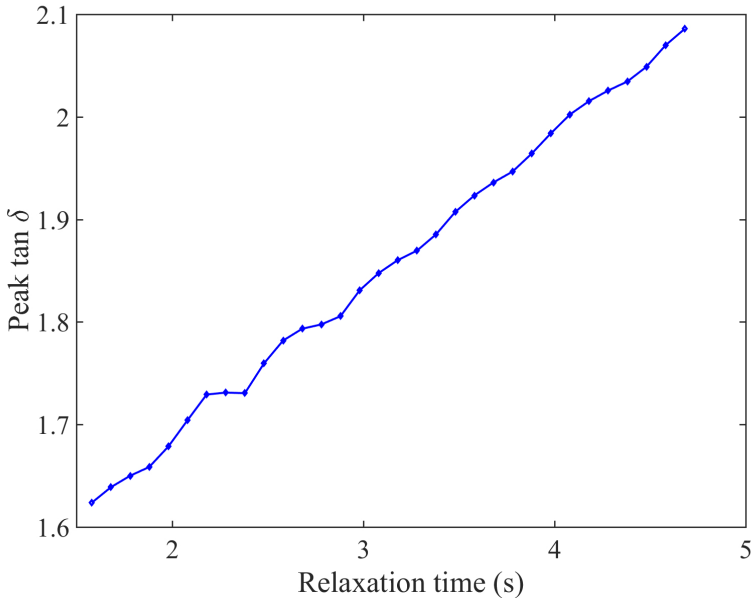

Figure 15.7: Peak $\tan\delta$ versus relaxation modulus of matrix.

CHAPTER 16: CONCLUSIONS

New constitutive model for polyurea was presented using superposition of hyper-elastic and viscoelastic behavior. Four parameter Ogden model and three parameters Mooney-Rivlin model was used for modeling the hyper-elastic part. It was found that four parameter Ogden model is better in predicting the quasi-static response of polyurea than three parameter Mooney-Rivlin model. The most important reason for better accuracy of the Ogden model is more number of parameters which gives it more flexibility. SLS model and K-BKZ model were used to model viscoelastic behavior. New constitutive model using 'Ogden + SLS' model is very effective in predicting stress-strain curve for polyurea under a wide range of strain rates, i. e. for tension from 0.09 to 294 /s and for compression from 0.0016 to 9000 /s. 'Ogden + K-BKZ' model is also effective in predicting the stress-strain curve for compression response but not suitable for tension response. This new model can be easily incorporated into commercial finite element software.

We used finite element modeling to study the damping property of polymer composites with elastic inclusions. The computations were done on representative volume elements which include several inclusions. The modelings were conducted using mixed and periodic boundary condition. For each model, the values of $\tan\delta$ under different vibration frequencies were calculated. Both periodic and mixed boundary conditions give similar results. Results show that the vibration frequency significantly impacts the value of $\tan\delta$. Moreover, the finite element modelings indicate that by increasing the inclusion volume fraction the damping capability of polymers composites reduces. Some analytical methods such as Mori-Tanaka gives accurate predictions for damping properties of composite for small inclusion volume fractions. But for high inclusion

volume fractions use of analytical methods is not recommended as predicted properties deviate by a marginal amount.

Sensitivity analysis showed that as inclusions get stiffer the value of peak $\tan\delta$ increases whereas as matrix gets stiffer the value of peak $\tan\delta$ decreases. Furthermore, the relaxation time of the polymer matrix plays a significant role on the damping capability of polymer and an increase in the relaxation time of material results in an increase in $\tan\delta$.

APPENDIX A: Kachanov-Rabotnov damage model

One of the most widely used creep damage model is Kachanov-Rabotnov damage model and can be given as [10],

$$\dot{\varepsilon}^c_{ij} = \frac{3}{2} A \left(\frac{\sigma_{eq}}{1-\omega} \right)^n t^m \left(\frac{\mathbf{S}_{ij}}{\sigma_{eq}} \right), \tag{A.1}$$

where, A, n and m are material constant. $\dot{\varepsilon}^c_{ij}$,σ_{eq}, and $\mathbf{S}_{ij}$ are creep strain rate, von Misses stress and deviotaric stress respectively.

Damage variable D is evaluated by equation,

$$\dot{D} = B \frac{\sigma_r^{\xi_R}}{(1+\phi)(1+D)^\phi} t^m, \tag{A.2}$$

where, B, ξ_R, and ϕ are material constants. σ_r is rapture stress, which can be given as,

$$\sigma_r = \alpha \sigma_1 + (1-\alpha)\sigma_{eq}, \tag{A.3}$$

where, α is multi-axiality parameter. For uniaxial condition α is zero. All material parameters have to be determined by careful creep test experiments. Many researchers used this model to predict creep in different materials such as, Nickel and Titanium based alloys [253, 254], Ti-6Al-2Cr-2Mo alloy [255], P91 steel [256, 257], P92 steel [258] etc. Although model predicts creep very well, as material reaches failure the damage rate obtained by Kachanov-Rabotnov model reached infinity. This makes it computationally expensive to use with any numerical method as time step required for integration needs to be very small.

On the other hand Liu-Morakami model does not suffer from this issue and hence

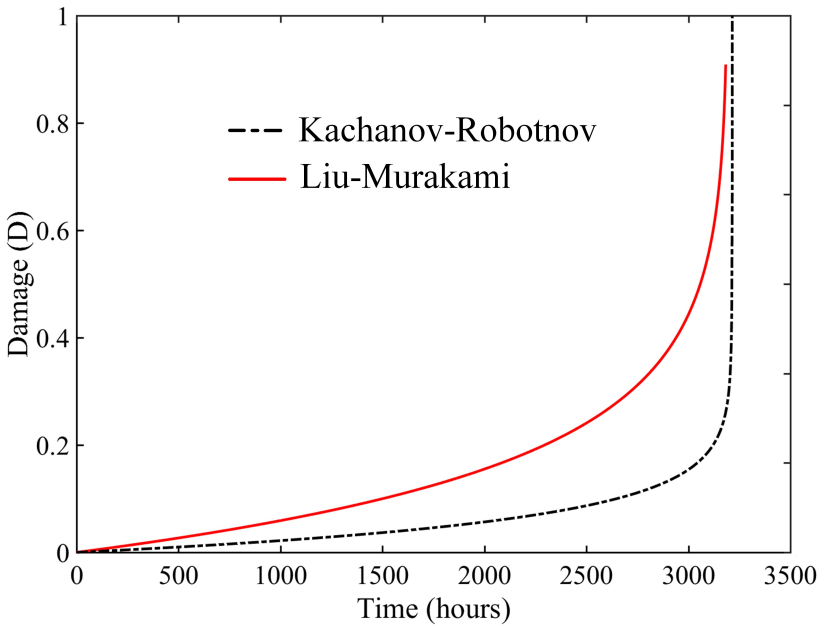

Figure A.1: Comparison of evolution of damage parameter D for Liu-Morakami and Kachanov-Rabotnov model.

more stable for using in numerical simulation. Fig. A.1 shows the comparison of evolution of damage parameter D for Liu-Morakami and Kachanov-Rabotnov model. Due to this reason we chose Liu-Morakami model over Kachanov-Rabotnov model in this study.

APPENDIX B: Convergence analysis

Convergence is an important part of any numerical solution. As peridynamic model is non-local formulation, convergence in case of peridynamics is somewhat different than finite elements. In case of peridynamics, horizon size δ and size of PD node r are two important parameters on which accuracy of solution depends up on. Therefore, two types of convergences can be checked in peridynamics.

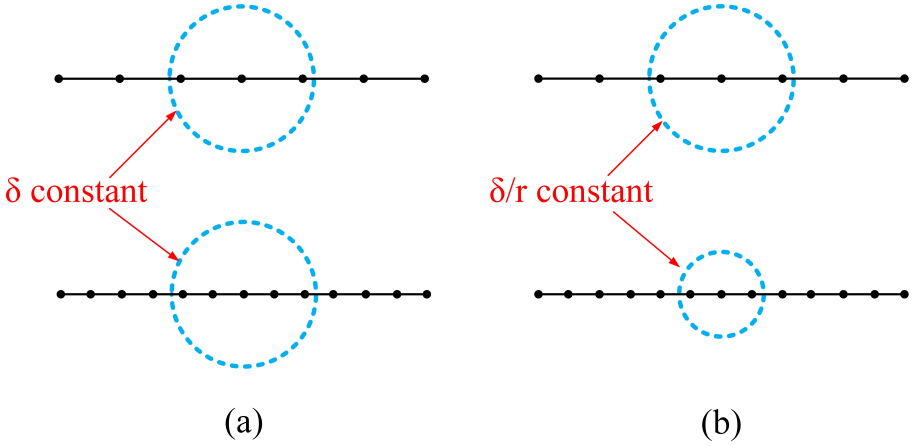

Figure B.1: Schematic of (a) m convergence and (b) δ convergence.

1. m convergence: δ is fixed and m goes to ∞, where $m = \frac{\delta}{r}$. This case is shown in Fig. B.1a. As value of δ is fixed and m is increasing, means value of r in decreasing, implying finer mesh. This increases number of PD nodes inside horizon resulting in increasing computational time exponentially. We chose the fixed value of $\delta = 0.4$ cm and values of r and m are given in Table B.1.

2. δ convergence: m is fixed and δ goes to 0. This case is shown in Fig. B.1b. As value of δ also decreases keeping number of PD nodes inside the horizon fixed, this results in increasing computational time only due to more number of PD

nodes inside whole domain. We chose the fixed value of $m = 4$ and values of r and δ are given in Table B.2.

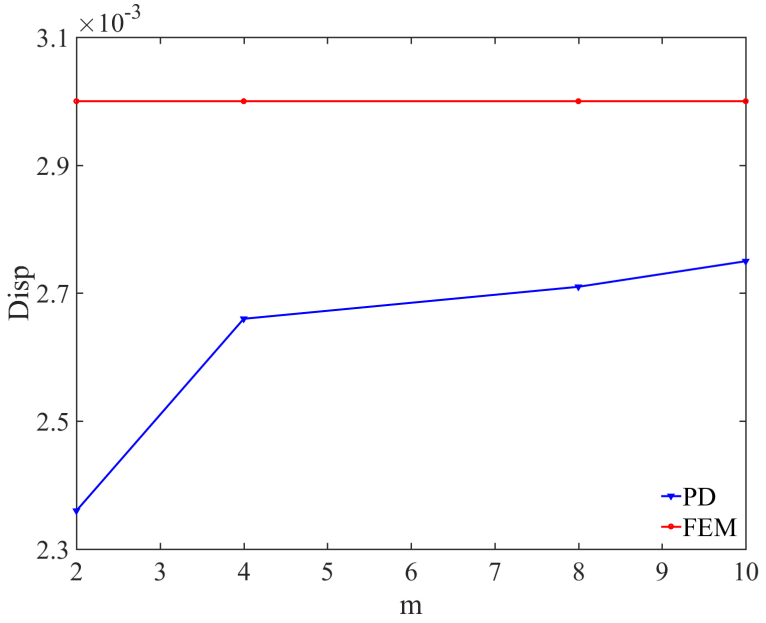

(a)

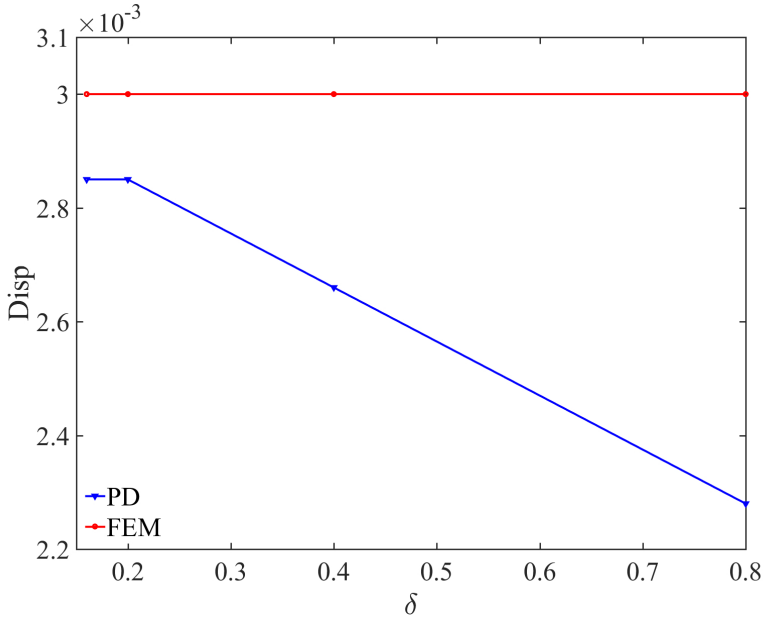

(b)

Figure B.2: Results of (a) m convergence and (b) δ convergence.

Table B.1: Parameters used for m convergence with fixed value of $\delta = 0.4$ cm.

r	m
0.2	2
0.1	4
0.05	8
0.04	10

Table B.2: Parameters used for δ convergence with fixed value of $m = 4$.

r	δ
0.2	0.8
0.1	0.4
0.05	0.2
0.04	0.16

Results of both convergence studies are shown in Fig. B.2. It can be seen that, as value of m increases, solution from peridynamics approaches the FEM solution. On the other hand, as value of δ decreases, PD solution approaches the finite element solution. Here solution from ABAQUS can be considered as exact solution as problem is static problem with simple geometry.

APPENDIX C: Details of derivations of equations for angular frequency in peridynamic zone

Eq. (6.4) can be written as,

$$\rho\ddot{u}_k = F_{k+3} + F_{k+2} + F_{k+1} + F_{k-1} + F_{k-2} + F_{k-3}, \tag{C.1}$$

where F_{k+3} is force exerted by $(k+3)^{th}$ PD node on k^{th} PD node and so on. Hence for n^{th} time step, we can denote same equation of motion as,

$$\begin{aligned}\rho\ddot{u}_k = c_0\frac{(u_{k+3,n} - u_{k,n})}{|x_{k+3,n} - x_{k,n}|}\frac{V_{k+3}}{2} + c_0\frac{(u_{k+2,n} - u_{k,n})}{|x_{k+2,n} - x_{k,n}|}V_{k+2} + c_0\frac{(u_{k+1,n} - u_{k,n})}{|x_{k+1,n} - x_{k,n}|}V_{k+1} \\ + c_0\frac{(u_{k-1,n} - u_{k,n})}{|x_{k-1,n} - x_{k,n}|}V_{k-1} + c_0\frac{(u_{k-2,n} - u_{k,n})}{|x_{k-2,n} - x_{k,n}|}V_{k-2} + c_0\frac{(u_{k-3,n} - u_{k,n})}{|x_{k-3,n} - x_{k,n}|}\frac{V_{k-3}}{2},\end{aligned} \tag{C.2}$$

here volume of PD node is multiplied by fraction of volume of PD node inside horizon $\delta = 3h$. As mesh is uniform, volume of all PD nodes is same and can be given by,

$$V_{k+3} = V_{k+2} = V_{k+1} = V_{k-1} = V_{k-2} = V_{k-3} = Ah. \tag{C.3}$$

Also, from Eq. (2.13) we know that c_0 can be given as,

$$c_0 = \frac{2E}{\delta^2 A} = \frac{2E}{(3h)^2 A} = \frac{2E}{9Ah^2}. \tag{C.4}$$

By substituting Eq. (C.4) and Eq. (C.3) in Eq. (C.2), along with Eq. (6.5) we get,

$$\frac{\rho}{\tau^2}(u_{k,n+1} - 2u_{k,n} + u_{k,n-1}) = \frac{2E}{9Ah^2}\left[\frac{(u_{k+3,n} - u_{k,n})}{3h}\frac{Ah}{2} + \frac{(u_{k+2,n} - u_{k,n})}{2h}Ah \right.$$
$$\left. + \frac{(u_{k+1,n} - u_{k,n})}{h}Ah + \frac{(u_{k-1,n} - u_{k,n})}{h}Ah + \frac{(u_{k-2,n} - u_{k,n})}{2h}Ah + \frac{(u_{k-3,n} - u_{k,n})}{3h}\frac{Ah}{2}\right]. \tag{C.5}$$

As we substitute solution from Eq. (6.3) in to Eq. (C.5), amplitude A_0 will cancel out from both sides of equation, along with $e^{i\omega(\tau r)}$ and $e^{-i\omega(kh/v)}$ and we are left with,

$$e^{i\omega\tau} - 2 + e^{i\omega\tau} = \frac{E\tau^2}{27\rho h^2}\left[e^{-3i\omega h/v} + 3e^{-2i\omega h/v} + 6e^{-i\omega h/v} + 6e^{i\omega h/v} + 3e^{2i\omega h/v} + e^{3i\omega h/v} - 20\right]. \tag{C.6}$$

Using property $e^{i\theta} = \cos(\theta) + i\sin(\theta)$, we get

$$2\cos(\omega\tau) - 2 = \frac{E\tau^2}{27\rho h^2}\left[2\cos\left(\frac{3\omega h}{v}\right) + 6\cos\left(\frac{2\omega h}{v}\right) + 12\cos\left(\frac{\omega h}{v}\right) - 20\right], \tag{C.7}$$

further simplifying above equation using trigonometric property, $\cos(x) = 1 - 2\sin^2\left(\frac{x}{2}\right)$ we get,

$$\sin^2\left(\frac{\omega\tau}{2}\right) = \frac{E\tau^2}{27\rho h^2}\left[\sin^2\left(\frac{3\phi}{2}\right) + 3\sin^2\phi + 6\sin^2\left(\frac{\phi}{2}\right)\right], \tag{C.8}$$

here, $\phi = \frac{\omega h}{v}$. Which is Eq. (6.6) in section 6.1.

APPENDIX D: Details of derivations of equations for reflected and transmitted wave amplitudes for non-uniform mesh

For the case of non-uniform mesh, equation of motion for PD node at $k = 0$ can be written using Eq. (6.16) as,

$$\rho\ddot{u}_{0,n+1} = c_0\Bigg[\frac{u_{-3,n} - u_{0,n}}{3h}\frac{Ah}{2} + \frac{u_{-2,n} - u_{0,n}}{2h}Ah + \frac{u_{-1,n} - u_{0,n}}{h}Ah + \frac{u^*_{1,n} - u_{0,n}}{h}Ah + \frac{u^*_{2,n} - u_{0,n}}{2h}Ah + \frac{u^*_{3,n} - u_{0,n}}{3h}\frac{Ah}{2}\Bigg], \tag{D.1}$$

where u^*_1, u^*_2 and u^*_3 are displacements of three ghost nodes respectively. Value of k for three ghost nodes can be given as $k^*_1 = {}^{h}/_{H}$, $k^*_2 = {}^{2h}/_{H}$ and $k^*_3 = {}^{3h}/_{H}$.

By substituting the solution from Eq. (6.17b) in above equation along with Eq. (6.5), we get,

$$\frac{\rho(1-\beta)}{\tau^2}\Big[e^{i\omega\tau(n+1)} - 2e^{i\omega\tau(n)} + e^{i\omega\tau(n-1)}\Big] = \frac{E}{H}\Big[\alpha e^{i\omega(\tau n - {}^{H}/_{V})} - 2\alpha e^{i\omega\tau(n)} + e^{i\omega(\tau n + {}^{h}/_{v}({}^{H}/_{h}))} - \beta e^{i\omega(\tau n - {}^{h}/_{v}({}^{H}/_{h}))}\Big], \tag{D.2}$$

with canceling $e^{i\omega\tau(n)}$ from both sides of above equation and rearranging we get,

$$(1-\beta)\Big[e^{i\omega\tau} - 2 + e^{i\omega\tau}\Big] = \frac{2E\tau^2}{\rho h^2}\Big[\alpha\left\{e^{-3i\Phi^h/_H} + 3e^{-2i\Phi^h/_H} + 6e^{-i\Phi^h/_H}\right\} + \left\{e^{3i\phi} + 3e^{2i\phi} + 6e^{i\phi} - 20\right\} - \beta\left\{e^{-3i\phi} + 3e^{-2i\phi} + 6e^{-i\phi} - 20\right\}\Big]. \tag{D.3}$$

Using property $e^{i\theta} = \cos(\theta) + i\sin(\theta)$ and substituting $\phi = \frac{\omega h}{v}$ and $\Phi = \frac{\omega H}{V}$ we get,

$$(1-\beta)\Big[2\cos(\omega\tau) - 2\Big] = \frac{2E\tau^2}{\rho h^2}\Bigg[\alpha\left\{e^{-3i\Phi^h/H} + 3e^{-2i\Phi^h/H} + 6e^{-i\Phi^h/H}\right\} + \left\{e^{3i\phi} + 3e^{2i\phi} + 6e^{i\phi} - 20\right\} - \beta\left\{e^{-3i\phi} + 3e^{-2i\phi} + 6e^{-i\phi} - 20\right\}\Bigg]. \tag{D.4}$$

By further simplifying above equation using trigonometric property, $\cos(x) = 1 - 2\sin^2\left(\frac{x}{2}\right)$ we get expression for angular velocity as,

$$\sin^2\left(\frac{\omega\tau}{2}\right) = \frac{-E\tau^2}{108(1-\beta)\rho h^2}\Bigg[\alpha\left\{e^{-3i\Phi^h/H} + 3e^{-2i\Phi^h/H} + 6e^{-i\Phi^h/H}\right\} + \left\{e^{3i\phi} + 3e^{2i\phi} + 6e^{i\phi} - 20\right\} - \beta\left\{e^{-3i\phi} + 3e^{-2i\phi} + 6e^{-i\phi} - 20\right\}\Bigg]. \tag{D.5}$$

Now by equating Eq. (D.5) with Eq. (6.12), which is expression for angular velocity in FEM region we get,

$$\sin^2\left(\frac{\Phi}{2}\right) + \frac{(H/h)^2}{108(1-\beta)}\Bigg[\alpha\left\{e^{-3i\Phi^h/H} + 3e^{-2i\Phi^h/H} + 6e^{-i\Phi^h/H}\right\} + \left\{e^{3i\phi} + 3e^{2i\phi} + 6e^{i\phi} - 20\right\} - \beta\left\{e^{-3i\phi} + 3e^{-2i\phi} + 6e^{-i\phi} - 20\right\}\Bigg] = 0, \tag{D.6}$$

which indeed is Eq. (6.21). We have to mention here, ϕ in Eq. (6.12) becomes Φ in this case as per our nomenclature. As a final step, Eq. (D.6) is solved simultaneously with Eq. (6.18) for α and β along with Eq. (6.19) for the case of $\delta = 3h$.

APPENDIX E: Conversion of time domain response to frequency domain response using Fourier Transform

It is important to convert time domain response in to frequency domain to get clear understanding of visco-elastic material's behavior. It can be achieved by taking Fourier transform of time domain response. In this appendix we will see how Eq. (12.13) which represents the shear modulus of visco elastic material in frequency domain is obtained from Eq. (12.12) which represents the shear modulus of in time domain.

The shear modulus of visco elastic material in time domain is given by Eq. (12.12), which is

$$G(t) = G_\infty + \sum_{j=1}^{N} G_j e^{-t/\tau_j}, \tag{E.1}$$

where t represents time. Fourier transform of Eq. (E.1) is to be taken to convert it to frequency domain response. Following is the step by step procedure for the same.

$$\begin{aligned}
G^*(\omega) &= i\omega \int_0^\infty G(t) e^{-i\omega t} dt, \\
&= i\omega \int_0^\infty \left[G_\infty + \sum_{j=1}^{N} G_j e^{-t/\tau_j} \right] e^{-i\omega t} dt, \\
&= i\omega \int_0^\infty G_\infty e^{-i\omega t} dt + i\omega \int_0^\infty \sum_{j=1}^{N} G_j e^{-t/\tau_j} e^{-i\omega t} dt, \\
&= i\omega G_\infty \int_0^\infty e^{-i\omega t} dt + i\omega \sum_{j=1}^{N} G_j \int_0^\infty e^{-t/\tau_j} e^{-i\omega t} dt, \\
&= i\omega G_\infty \int_0^\infty e^{-i\omega t} dt + i\omega \sum_{j=1}^{N} G_j \int_0^\infty e^{-t(i\omega + \frac{1}{\tau_j})} dt,
\end{aligned}$$

$$
\begin{aligned}
G^*(\omega) &= i\omega G_\infty \left[\frac{-e^{-i\omega t}}{i\omega}\right]_0^\infty + i\omega \sum_{j=1}^{N} G_j \left[\frac{-e^{-t(i\omega+\frac{1}{\tau_j})}}{i\omega+\frac{1}{\tau_j}}\right]_0^\infty, \\
&= i\omega G_\infty \left[\frac{-(e^{-\infty}-e^0)}{i\omega}\right] + i\omega \sum_{j=1}^{N} G_j \left[\frac{-(e^{-\infty}-e^0)}{i\omega+\frac{1}{\tau_j}}\right]_0^\infty, \\
&= G_\infty + i\omega \sum_{j=1}^{N} \frac{G_j}{i\omega+\frac{1}{\tau_j}}, \\
&= G_\infty + i\omega \sum_{j=1}^{N} \frac{G_j\tau_j}{(1+i\omega\tau_j)},
\end{aligned}
$$

which is Eq. (12.13).

REFERENCES

[1] F. Bobaru, M. Yang, L. F. Alves, S. A. Silling, E. Askari, and J. Xu, "Convergence, adaptive refinement, and scaling in 1D peridynamics," *International Journal for Numerical Methods in Engineering*, vol. 77, no. 6, pp. 852–877, 2009.

[2] K. Naumenko and H. Altenbach, *Modeling of creep for structural analysis*. Springer Science & Business Media, 2007.

[3] T. Hyde, M. Saber, and W. Sun, "Testing and modelling of creep crack growth in compact tension specimens from a P91 weld at 650 C," *Engineering Fracture Mechanics*, vol. 77, no. 15, pp. 2946–2957, 2010.

[4] C. J. Hyde, T. Hyde, W. Sun, and A. Becker, "Damage mechanics based predictions of creep crack growth in 316 stainless steel," *Engineering Fracture Mechanics*, vol. 77, no. 12, pp. 2385–2402, 2010.

[5] Q. Meng and Z. Wang, "Creep damage models and their applications for crack growth analysis in pipes: A review," *Engineering Fracture Mechanics*, 2016.

[6] X. Lin and R. Smith, "Finite element modelling of fatigue crack growth of surface cracked plates: Part I: The numerical technique," *Engineering Fracture Mechanics*, vol. 63, no. 5, pp. 503–522, 1999.

[7] X. Lin and R. Smith, "Finite element modelling of fatigue crack growth of surface cracked plates: Part II: Crack shape change," *Engineering Fracture Mechanics*, vol. 63, no. 5, pp. 523–540, 1999.

[8] J. F. Wen, S. T. Tu, J. M. Gong, and W. Sun, "Creep fracture mechanics parameters for internal axial surface cracks in pressurized cylinders and creep crack growth analysis," *International Journal of Pressure Vessels and Piping*, vol. 88, no. 11-12, pp. 452–464, 2011.

[9] J. Lemaitre and R. Desmorat, *Engineering damage mechanics: ductile, creep, fatigue and brittle failures*. Springer Science & Business Media, 2005.

[10] L. M. Kachanov, "Rupture time under creep conditions," *International Journal of Fracture*, vol. 97, no. 1-4, pp. 11–18, 1999.

[11] Y. N. Rabotnov, "Creep problems in structural members," 1969.

[12] S. Murakami and Y. Liu, "Mesh-dependence in local approach to creep fracture," *International Journal of Damage Mechanics*, vol. 4, no. 3, pp. 230–250, 1995.

[13] Y. Liu and S. Murakami, "Damage localization of conventional creep damage models and proposition of a new model for creep damage analysis," *JSME International journal series A solid mechanics and material engineering*, vol. 41, no. 1, pp. 57–65, 1998.

[14] S. Murakami, Y. Liu, and M. Mizuno, "Computational methods for creep fracture analysis by damage mechanics," *Computer Methods in Applied Mechanics and Engineering*, vol. 183, no. 1-2, pp. 15–33, 2000.

[15] M. Yatomi, K. Nikbin, and N. O'Dowd, "Creep crack growth prediction using a damage based approach," *International Journal of Pressure Vessels and Piping*, vol. 80, no. 7-8, pp. 573–583, 2003.

[16] M. Yatomi, C. M. Davies, and K. M. Nikbin, "Creep crack growth simulations in 316H stainless steel," *Engineering Fracture Mechanics*, vol. 75, no. 18, pp. 5140–5150, 2008.

[17] C. S. Oh, N. H. Kim, S. H. Min, and Y. J. Kim, "Finite element damage analyses for predictions of creep crack growth," in *ASME 2010 Pressure Vessels and Piping Division/K-PVP Conference*, pp. 331–335, American Society of Mechanical Engineers, 2010.

[18] S. Murakami, M. Kawai, and H. Rong, "Finite element analysis of creep crack growth by a local approach," *International Journal of Mechanical Sciences*, vol. 30, no. 7, pp. 491–502, 1988.

[19] T. Hyde, M. Saber, and W. Sun, "Creep crack growth data and prediction for a P91 weld at 650 C," *International Journal of Pressure Vessels and Piping*, vol. 87, no. 12, pp. 721–729, 2010.

[20] T. Hyde, R. Li, W. Sun, and M. Saber, "A simplified method for predicting the creep crack growth in P91 welds at 650 C," *Proceedings of the Institution of Mechanical Engineers, Part L: Journal of Materials: Design and Applications*, vol. 224, no. 4, pp. 208–219, 2010.

[21] T. H. Hyde, B. S. Ali, and W. Sun, "Analysis and design of a small, two-bar creep test specimen," *Journal of Engineering Materials and Technology*, vol. 135, no. 4, p. 041006, 2013.

[22] T. H. Hyde, B. S. Ali, and W. Sun, "On the determination of material creep constants using miniature creep test specimens," *Journal of Engineering Materials and Technology*, vol. 136, no. 2, p. 021006, 2014.

[23] C. S. Oh, N. H. Kim, Y. J. Kim, C. Davies, K. Nikbin, and D. Dean, "Creep failure simulations of 316H at 550 C: Part I–a method and validation," *Engineering Fracture Mechanics*, vol. 78, no. 17, pp. 2966–2977, 2011.

[24] N. H. Kim, C. S. Oh, Y. J. Kim, C. M. Davies, K. Nikbin, and D. W. Dean, "Creep failure simulations of 316H at 550 C: Part II–effects of specimen geometry and loading mode," *Engineering Fracture Mechanics*, vol. 105, pp. 169–181, 2013.

[25] J. H. Song, H. Wang, and T. Belytschko, "A comparative study on finite element methods for dynamic fracture," *Computational Mechanics*, vol. 42, no. 2, pp. 239–250, 2008.

[26] V. Pandey, I. Singh, B. Mishra, S. Ahmad, A. Rao, and V. Kumar, "Creep crack simulations using continuum damage mechanics and extended finite element method," *International Journal of Damage Mechanics*, p. 1056789517737593, 2017.

[27] N. Moes, J. Dolbow, and T. Belytschko, "A finite element method for crack growth without remeshing," *International Journal for Numerical Methods in Engineering*, vol. 46, pp. 131–150, 1999.

[28] P. Kauppila, R. Kouhia, J. Ojanperä, T. Saksala, and T. Sorjonen, "A continuum damage model for creep fracture and fatigue analyses," *Procedia Structural Integrity*, vol. 2, pp. 887–894, 2016.

[29] ansys, *ANSYS user's manual : version 5.6.* Canonsburg, PA : ANSYS, 2007.

[30] T. Rabczuk and T. Belytschko, "Cracking particles: a simplified meshfree method for arbitrary evolving cracks," *International Journal for Numerical Methods in Engineering*, vol. 61, no. 13, pp. 2316–2343, 2004.

[31] T. Rabczuk and T. Belytschko, "A three-dimensional large deformation meshfree method for arbitrary evolving cracks," *Computer Methods in Applied Mechanics and Engineering*, vol. 196, no. 29-30, pp. 2777–2799, 2007.

[32] T. Chau Dinh, G. Zi, P. S. Lee, T. Rabczuk, and J. H. Song, "Phantom-node method for shell models with arbitrary cracks," *Computers & Structures*, vol. 92, pp. 242–256, 2012.

[33] P. Areias, T. Rabczuk, and D. Dias-da Costa, "Element-wise fracture algorithm based on rotation of edges," *Engineering Fracture Mechanics*, vol. 110, pp. 113–137, 2013.

[34] P. Areias, M. Msekh, and T. Rabczuk, "Damage and fracture algorithm using the screened poisson equation and local remeshing," *Engineering Fracture Mechanics*, vol. 158, pp. 116–143, 2016.

[35] P. Areias, T. Rabczuk, and M. Msekh, "Phase-field analysis of finite-strain plates and shells including element subdivision," *Computer Methods in Applied Mechanics and Engineering*, vol. 312, pp. 322–350, 2016.

[36] S. A. Silling, "Reformulation of elasticity theory for discontinuities and long-range forces," *Journal of the Mechanics and Physics of Solids*, vol. 48, no. 1, pp. 175–209, 2000.

[37] S. A. Silling, M. Epton, O. Weckner, J. Xu, and E. Askari, "Peridynamic states and constitutive modeling," *Journal of Elasticity*, vol. 88, no. 2, pp. 151–184, 2007.

[38] J. Rouse, W. Sun, T. Hyde, and A. Morris, "Comparative assessment of several creep damage models for use in life prediction," *International Journal of Pressure Vessels and Piping*, vol. 108, pp. 81–87, 2013.

[39] X. Wang and A. Tabarraei, "Phonon thermal conductivity of monolayer MoS2," *Applied Physics Letters*, vol. 108, no. 19, p. 191905, 2016.

[40] A. Tabarraei and X. Wang, "Anomalous thermal conductivity of monolayer boron nitride," *Applied Physics Letters*, vol. 108, no. 18, p. 181904, 2016.

[41] X. Wang and A. Tabarraei, "Strain engineering of thermal conductivity of two-dimensional MoS2 and h-BN," *MRS Advances*, vol. 1, no. 32, pp. 2297–2302, 2016.

[42] A. Tabarraei, X. Wang, and D. Jia, "Effects of hydrogen adsorption on the fracture properties of graphene," *Computational Materials Science*, vol. 121, pp. 151–158, 2016.

[43] A. Tabarraei, X. Wang, and S. Shadalou, "Mechanical properties of monolayer molybdenum disulfide," in *ASME 2014 International Mechanical Engineering Congress and Exposition*, p. V009T12A070, American Society of Mechanical Engineers, 2014.

[44] A. Tabarraei and X. Wang, "A molecular dynamics study of nanofracture in monolayer boron nitride," *Materials Science and Engineering: A*, vol. 641, pp. 225–230, 2015.

[45] X. Wang, A. Tabarraei, and D. E. Spearot, "Fracture mechanics of monolayer molybdenum disulfide," *Nanotechnology*, vol. 26, no. 17, p. 175703, 2015.

[46] M. S. Elapolu, A. Tabarraei, X. Wang, and D. E. Spearot, "Fracture mechanics of multi–layer molybdenum disulfide," *Engineering Fracture Mechanics*, 2019.

[47] T. Bittencourt, P. Wawrzynek, A. Ingraffea, and J. Sousa, "Quasi-automatic simulation of crack propagation for 2D LEFM problems," *Engineering Fracture Mechanics*, vol. 55, no. 2, pp. 321–334, 1996.

[48] G. Dhondt, "Automatic 3-D mode I crack propagation calculations with finite elements," *International Journal for Numerical Methods in Engineering*, vol. 41, no. 4, pp. 739–757, 1998.

[49] T. Belytschko and T. Black, "Elastic crack growth in finite elements with minimal remeshing," *International Journal for Numerical Methods in Engineering*, vol. 45, no. 5, pp. 601–620, 1999.

[50] T. Belytschko, Y. Y. Lu, and L. Gu, "Element-free Galerkin methods," *International Journal for Numerical Methods in Engineering*, vol. 37, no. 2, pp. 229–256, 1994.

[51] L. B. Lucy, "A numerical approach to the testing of the fission hypothesis," *The Astronomical Journal*, vol. 82, pp. 1013–1024, 1977.

[52] J. J. Monaghan, "Why particle methods work," *SIAM Journal on Scientific and Statistical Computing*, vol. 3, no. 4, pp. 422–433, 1982.

[53] W. Benz and E. Asphaug, "Simulations of brittle solids using smooth particle hydrodynamics," *Computer Physics Communications*, vol. 87, no. 1-2, pp. 253–265, 1995.

[54] W. K. Liu, S. Jun, and Y. F. Zhang, "Reproducing kernel particle methods," *International Journal for Numerical Methods in Fluids*, vol. 20, no. 8-9, pp. 1081–1106, 1995.

[55] S. A. Silling and E. Askari, "A meshfree method based on the peridynamic model of solid mechanics," *Computers & structures*, vol. 83, no. 17, pp. 1526–1535, 2005.

[56] M. Bessa, J. Foster, T. Belytschko, and W. K. Liu, "A meshfree unification: reproducing kernel peridynamics," *Computational Mechanics*, vol. 53, no. 6, pp. 1251–1264, 2014.

[57] S. A. Silling, M. Zimmermann, and R. Abeyaratne, "Deformation of a peridynamic bar," *Journal of Elasticity*, vol. 73, no. 1-3, pp. 173–190, 2003.

[58] S. A. Silling and E. Askari, "Peridynamic modeling of impact damage," *PVP*, vol. 489, pp. 197–205, 2004.

[59] W. Gerstle, N. Sau, and S. Silling, "Peridynamic modeling of concrete structures," *Nuclear Engineering and Design*, vol. 237, no. 12, pp. 1250–1258, 2007.

[60] J. Xu, A. Askari, O. Weckner, H. Razi, and S. Silling, "Damage and failure analysis of composite laminates under biaxial loads," in *48th AIAA Structures, Structural Dynamics, and Materials Conf*, 2007.

[61] Y. D. Ha and F. Bobaru, "Characteristics of dynamic brittle fracture captured with peridynamics," *Engineering Fracture Mechanics*, vol. 78, no. 6, pp. 1156–1168, 2011.

[62] F. Bobaru and W. Hu, "The meaning, selection, and use of the peridynamic horizon and its relation to crack branching in brittle materials," *International Journal of Fracture*, pp. 1–8, 2012.

[63] Y. D. Ha and F. Bobaru, "Studies of dynamic crack propagation and crack branching with peridynamics," *International Journal of Fracture*, vol. 162, no. 1, pp. 229–244, 2010.

[64] C. Wu and B. Ren, "A stabilized non-ordinary state-based peridynamics for the nonlocal ductile material failure analysis in metal machining process," *Computer Methods in Applied Mechanics and Engineering*, vol. 291, pp. 197–215, 2015.

[65] W. Hu, Y. D. Ha, and F. Bobaru, "Peridynamic model for dynamic fracture in unidirectional fiber-reinforced composites," *Computer Methods in Applied Mechanics and Engineering*, vol. 217, pp. 247–261, 2012.

[66] J. Amani, E. Oterkus, P. Areias, G. Zi, T. Nguyen Thoi, and T. Rabczuk, "A non-ordinary state-based peridynamics formulation for thermoplastic fracture," *International Journal of Impact Engineering*, vol. 87, pp. 83–94, 2016.

[67] Y. D. Ha, J. Lee, and J. W. Hong, "Fracturing patterns of rock-like materials in compression captured with peridynamics," *Engineering Fracture Mechanics*, vol. 144, pp. 176–193, 2015.

[68] Y. Wang, X. Zhou, and X. Xu, "Numerical simulation of propagation and coalescence of flaws in rock materials under compressive loads using the extended non-ordinary state-based peridynamics," *Engineering Fracture Mechanics*, vol. 163, pp. 248–273, 2016.

[69] S. A. Silling, "Introduction to peridynamics and thoughts on corrosion modeling.," tech. rep., Sandia National Laboratories (SNL-NM), Albuquerque, NM (United States), 2014.

[70] D. De Meo, L. Russo, and E. Oterkus, "Modeling of the onset, propagation, and interaction of multiple cracks generated from corrosion pits by using peridynamics," *Journal of Engineering Materials and Technology*, vol. 139, no. 4, p. 041001, 2017.

[71] D. De Meo and E. Oterkus, "Finite element implementation of a peridynamic pitting corrosion damage model," *Ocean Engineering*, vol. 135, pp. 76–83, 2017.

[72] Z. Chen and F. Bobaru, "A peridynamic model for corrosion damage," *Handbook of Peridynamic Modeling*, p. 437, 2016.

[73] A. Agwai, I. Guven, and E. Madenci, "Predicting crack initiation and propagation using XFEM, CZM and peridynamics: A comparative study," in *Electronic Components and Technology Conference (ECTC), 2010 Proceedings 60th*, pp. 1178–1185.

[74] S. Silling, O. Weckner, E. Askari, and F. Bobaru, "Crack nucleation in a peridynamic solid," *International Journal of Fracture*, vol. 162, pp. 219–227, 2010.

[75] B. Kilic and E. Madenci, "Prediction of crack paths in a quenched glass plate by using peridynamic theory," *International Journal of Fracture*, vol. 156, pp. 165–177, 2009.

[76] Y. Ha and F. Bobaru, "Characteristics of dynamic brittle fracture captured with peridynamics," *Engineering Fracture Mechanics*, vol. 78, pp. 1156–1158, 2011.

[77] Y. Ha and F. Bobaru, "Studies of dynamic crack propagation and crack branching with peridynamics," *International Journal of Fracture*, vol. 162, pp. 229–244, 2010.

[78] Z. Cheng, G. Zhang, Y. Wang, and F. Bobaru, "A peridynamic model for dynamic fracture in functionally graded materials," *Composite Structures*, vol. 133, pp. 529–546, 2015.

[79] F. Bobaru and G. Zhang, "Why do cracks branch? a peridynamic investigation of dynamic brittle fracture," *International Journal of Fracture*, vol. 196, no. 1-2, pp. 59–98, 2015.

[80] E. Askari, F. Bobaru, R. Lehoucq, M. Parks, S. Silling, and O. Weckner, "Peridynamics for multiscale materials modeling," *Journal of Physics: Conference Series*, vol. 125, p. 012078, 2008.

[81] S. A. Silling and F. Bobaru, "Peridynamic modeling of membranes and fibers," *International Journal of Non-Linear Mechanics*, vol. 40, no. 2-3, pp. 395–409, 2005.

[82] B. Kilic, A. Agwai, and E. Madenci, "Peridynamic theory for progressive damage prediction in center-cracked composite laminates," *Composite Structures*, vol. 90, pp. 141–151, 2009.

[83] W. Hu, Y. D. Ha, and F. Bobaru, "Modeling dynamic fracture and damage in a fiber-reinforced composite lamina with peridynamics," *International Journal for Multiscale Computational Engineering*, vol. 9, no. 6, 2011.

[84] W. Hu, Y. Ha, and F. Bobaru, "Peridynamic model for dynamic fracture in unidirectional fiber-reinforced composites," *Computer Methods in Applied Mechanics and Engineering*, vol. 217-220, pp. 247–261, 2012.

[85] J. Xu, A. Askari, O. Weckner, and S. Silling, "Peridynamic analysis of impact damage in composite laminates," *Journal of Aerospace Engineering*, vol. 21, pp. 187–194, 2008.

[86] A. Askari, J. Xu, and S. Silling, "peridynamic analysis of damage and failure in composites," in *44TH AIAA Aerospace Sciences Meeting and Exhibit, AIAA2006-8*, pp. 1–12.

[87] Z. Chen and F. Bobaru, "Peridynamic modeling of pitting corrosion damage," *Journal of the Mechanics and Physics of Solids*, vol. 78, pp. 352–381, 2015.

[88] S. Jafarzadeh, Z. Chen, and F. Bobaru, "Peridynamic modeling of repassivation in pitting corrosion of stainless steel," *Corrosion*, vol. 74, no. 4, pp. 393–414, 2017.

[89] S. Jafarzadeh, Z. Chen, and F. Bobaru, "Peridynamic modeling of intergranular corrosion damage," *Journal of The Electrochemical Society*, vol. 165, no. 7, pp. C362–C374, 2018.

[90] E. Oterkus, I. Guven, and E. Madenci, "Fatigue failure model with peridynamic theory," in *Thermal and Thermomechanical Phenomena in Electronic Systems (ITherm), 2010 12th IEEE Intersociety Conference on*, pp. 1–6, IEEE, 2010.

[91] G. ZHANG and F. Bobaru, "Modeling the evolution of fatigue failure with peridynamics," *Romanian Journal of Technical Sciences-Applied Mechanics*, vol. 66, pp. 20–39, 2016.

[92] G. Zhang, Q. Le, A. Loghin, A. Subramaniyan, and F. Bobaru, "Validation of a peridynamic model for fatigue cracking," *Engineering Fracture Mechanics*, vol. 162, pp. 76–94, 2016.

[93] Y. Hu and E. Madenci, "Peridynamics for fatigue life and residual strength prediction of composite laminates," *Composite Structures*, vol. 160, pp. 169–184, 2017.

[94] P. Demmie and S. Silling, "An approach to modeling extreme loading of structures using peridynamics," *Journal of Mechanics of Materials and Structures*, vol. 2, pp. 1921–1945, 2007.

[95] S. Silling and E. Askari, "A meshfree method based on the peridynamic model of solid mechanics," *Computers and Structures*, vol. 83, pp. 1526–1535, 2005.

[96] K. Dayal and K. Bhattacharya, "Kinetics of phase transformations in the peridynamic formulation of continuum mechanics," *Journal of the Mechanics and Physics of Solids*, vol. 54, pp. 1811–1842, 2006.

[97] X. Song and N. Khalili, "A peridynamics model for strain localization analysis of geomaterials," *International Journal for Numerical and Analytical Methods in Geomechanics*, vol. 43, no. 1, pp. 77–96, 2019.

[98] J. T. Foster, S. A. Silling, and W. W. Chen, "Viscoplasticity using peridynamics," *International Journal for Numerical Methods in Engineering*, vol. 81, no. 10, pp. 1242–1258, 2010.

[99] A. Pathrikar, M. M. Rahaman, and D. Roy, "A thermodynamically consistent peridynamics model for visco-plasticity and damage," *Computer Methods in Applied Mechanics and Engineering*, 2019.

[100] S. Oterkus, E. Madenci, and A. Agwai, "Peridynamic thermal diffusion," *Journal of Computational Physics*, vol. 265, pp. 71–96, 2014.

[101] S. Casolo and V. Diana, "Modelling laminated glass beam failure via stochastic rigid body-spring model and bond-based peridynamics," *Engineering Fracture Mechanics*, vol. 190, pp. 331–346, 2018.

[102] S. S. Kulkarni, X. Wang, and A. Tabarraei, "State based peridynamic formulation for modeling of metal creep," in *ASME 2019 International Mechanical Engineering Congress and Exposition*, p. in press, American Society of Mechanical Engineers, 2019.

[103] F. Bobaru and M. Duangpanya, "The peridynamic formulation for transient heat conduction," *International Journal of Heat and Mass Transfer*, vol. 53, no. 19-20, pp. 4047–4059, 2010.

[104] F. Bobaru and M. Duangpanya, "A peridynamic formulation for transient heat conduction in bodies with evolving discontinuities," *Journal of Computational Physics*, vol. 231, pp. 2764–2785, 2012.

[105] S. Oterkus, E. Madenci, and A. Agwai, "Fully coupled peridynamic thermomechanics," *Journal of the Mechanics and Physics of Solids*, vol. 64, pp. 1–23, 2014.

[106] Z. Xu, G. Zhang, Z. Chen, and F. Bobaru, "Elastic vortices and thermally-driven cracks in brittle materials with peridynamics," *International Journal of Fracture*, vol. 209, no. 1-2, pp. 203–222, 2018.

[107] G. Hattori, J. Trevelyan, and W. M. Coombs, "A non-ordinary state-based peridynamics framework for anisotropic materials," *Computer Methods in Applied Mechanics and Engineering*, vol. 339, pp. 416–442, 2018.

[108] Y. Zhang and P. Qiao, "An axisymmetric ordinary state-based peridynamic model for linear elastic solids," *Computer Methods in Applied Mechanics and Engineering*, vol. 341, pp. 517–550, 2018.

[109] M. Behzadinasab, T. J. Vogler, A. M. Peterson, R. Rahman, and J. T. Foster, "Peridynamics modeling of a shock wave perturbation decay experiment in granular materials with intra-granular fracture," *Journal of Dynamic Behavior of Materials*, pp. 1–14, 2018.

[110] C. T. Nguyen and S. Oterkus, "Peridynamics formulation for beam structures to predict damage in offshore structures," *Ocean Engineering*, vol. 173, pp. 244–267, 2019.

[111] R. L. S. Silling, "Convergence of peridynamics to classical elasticity theory," *Journal of Elasticity*, vol. 93, pp. 13–37, 2008.

[112] K. Zhou and Q. Du, "Mathematical and numerical analysis of linear peridynamic models with nonlocal boundary conditions," *SIAM Journal on Numerical Analysis*, vol. 48, pp. 1759–1780, 2010.

[113] B. Alali and R. Lipton, "Multiscale dynamics of heterogeneous media in the peridynamic formulation," *Journal of Elasticity*, vol. 106, pp. 71–103, 2012.

[114] Y. Mikata, "Analytical solutions of peristatic and peridynamic problems for a 1D infinite rod," *International Journal of Solids and Structures*, vol. 49, no. 21, pp. 2887–2897, 2012.

[115] P. Lindsay, M. Parks, and A. Prakash, "Enabling fast, stable and accurate peridynamic computations using multi-time-step integration," *Computer Methods in Applied Mechanics and Engineering*, vol. 306, pp. 382–405, 2016.

[116] S. Kulkarni and A. Tabarraei, "An analytical study of wave propagation in a peridynamic bar with nonuniform discretization," *Engineering Fracture Mechanics*, vol. 190, pp. 347–366, 2018.

[117] S. S. Kulkarni, A. Tabarraei, and X. Wang, "Study of spurious wave reflection at the interface of peridynamics and finite element regions," in *ASME 2018 International Mechanical Engineering Congress and Exposition*, pp. V009T12A054–V009T12A054, American Society of Mechanical Engineers, 2018.

[118] V. Mutnuri and S. Gopalakrishnan, "A comparative study of wave dispersion between discrete and continuum linear bond-based peridynamics systems: 1D framework," *Mechanics Research Communications*, 2018.

[119] E. Madenci, A. Barut, and M. Futch, "Peridynamic differential operator and its applications," *Computer Methods in Applied Mechanics and Engineering*, vol. 304, pp. 408–451, 2016.

[120] B. Kilic and E. Madenci, "Coupling of peridynamic theory and the finite element method," *Journal of Mechanics of Materials and Structures*, vol. 5, no. 5, pp. 707–733, 2010.

[121] E. Oterkus, E. Madenci, O. Weckner, S. Silling, P. Bogert, and A. Tessler, "Combined finite element and peridynamic analyses for predicting failure in a stiffened composite curved panel with a central slot," *Composite Structures*, vol. 94, no. 3, pp. 839–850, 2012.

[122] G. Lubineau, Y. Azdoud, F. Han, C. Rey, and A. Askari, "A morphing strategy to couple non-local to local continuum mechanics," *Journal of the Mechanics and Physics of Solids*, vol. 60, no. 6, pp. 1088–1102, 2012.

[123] W. Liu and J. W. Hong, "A coupling approach of discretized peridynamics with finite element method," *Computer Methods in Applied Mechanics and Engineering*, vol. 245, pp. 163–175, 2012.

[124] U. Galvanetto, T. Mudric, A. Shojaei, and M. Zaccariotto, "An effective way to couple FEM meshes and peridynamics grids for the solution of static equilibrium problems," *Mechanics Research Communications*, vol. 76, pp. 41–47, 2016.

[125] A. Shojaei, T. Mudric, M. Zaccariotto, and U. Galvanetto, "A coupled meshless finite point/peridynamic method for 2d dynamic fracture analysis," *International Journal of Mechanical Sciences*, vol. 119, pp. 419–431, 2016.

[126] J. Lee, S. E. Oh, and J. W. Hong, "Parallel programming of a peridynamics code coupled with finite element method," *International Journal of Fracture*, vol. 203, no. 1-2, pp. 99–114, 2017.

[127] H. Li, H. Zhang, Y. Zheng, H. Ye, and M. Lu, "An implicit coupling finite element and peridynamic method for dynamic problems of solid mechanics with crack propagation," *International Journal of Applied Mechanics*, vol. 10, no. 04, p. 1850037, 2018.

[128] M. Zaccariotto, T. Mudric, D. Tomasi, A. Shojaei, and U. Galvanetto, "Coupling of fem meshes with peridynamic grids," *Computer Methods in Applied Mechanics and Engineering*, vol. 330, pp. 471–497, 2018.

[129] G. Fang, S. Liu, M. Fu, B. Wang, Z. Wu, and J. Liang, "A method to couple state-based peridynamics and finite element method for crack propagation problem," *Mechanics Research Communications*, 2019.

[130] Z. P. Bažant, "Spurious reflection of elastic waves in nonuniform finite element grids," *Computer Methods in Applied Mechanics and Engineering*, vol. 16, no. 1, pp. 91–100, 1978.

[131] R. Rahman and J. Foster, "Onto resolving spurious wave reflection problem with changing nonlocality among various length scales," *Communications in Nonlinear Science and Numerical Simulation*, vol. 34, pp. 86–122, 2016.

[132] A. Tabarraei, X. Wang, A. Sadeghirad, and J. Song, "An enhanced bridging domain method for linking atomistic and continuum domains," *Finite Elements in Analysis and Design*, vol. 92, pp. 36–49, 2014.

[133] A. Sadeghirad and A. Tabarraei, "A damping boundary condition for coupled atomistic–continuum simulations," *Computational Mechanics*, vol. 52, no. 3, pp. 535–551, 2013.

[134] H. Ren, X. Zhuang, Y. Cai, and T. Rabczuk, "Dual-horizon peridynamics," *International Journal for Numerical Methods in Engineering*, vol. 108, no. 12, pp. 1451–1476, 2016.

[135] H. Ren, X. Zhuang, and T. Rabczuk, "Dual-horizon peridynamics: A stable solution to varying horizons," *Computer Methods in Applied Mechanics and Engineering*, vol. 318, pp. 762–782, 2017.

[136] X. Wang, *Multiscale modeling of the properties of two-dimensional materials*. PhD thesis, The University of North Carolina at Charlotte, 2017.

[137] X. Wang, S. S. Kulkarni, and A. Tabarraei, "Concurrent coupling of peridynamics and classical elasticity for elastodynamic problems," *Computer Methods in Applied Mechanics and Engineering*, vol. 344, pp. 251–275, 2019.

[138] X. Wang, S. S. Kulkarni, and A. Tabarraei, "Seamless coupling of peridynamics and finite element method in commercial software of finite element to solve elasto-dynamics problems," in *ASME 2019 International Mechanical Engineering Congress and Exposition*, p. in press, American Society of Mechanical Engineers, 2019.

[139] MATLAB, *version 9.2.0 (R2017a)*. Natick, Massachusetts: The MathWorks Inc., 2017.

[140] Q. V. Le, W. K. Chan, and J. Schwartz, "A two-dimensional ordinary, state-based peridynamic model for linearly elastic solids," *International Journal for Numerical Methods in Engineering*, vol. 98, no. 8, pp. 547–561, 2014.

[141] G. Taubin, "Estimation of planar curves, surfaces, and nonplanar space curves defined by implicit equations with applications to edge and range image segmentation," *IEEE Transactions on Pattern Analysis & Machine Intelligence*, no. 11, pp. 1115–1138, 1991.

[142] W. C. Xie, *Dynamic stability of structures*. Cambridge University Press, 2006.

[143] N. Nikabdullah, M. A. Azizi, R. Alebrahim, and S. Singh, "The application of peridynamic method on prediction of viscoelastic materials behaviour," in *AIP Conference Proceedings*, vol. 1602, pp. 357–363, AIP, 2014.

[144] M. Azizi, A. Ihsan, and A. Mohamed, "The peridynamic model of viscoelastic creep and recovery," *Multidiscipline Modeling in Materials and Structures*, vol. 11, no. 4, pp. 579–597, 2015.

[145] J. Nocedal and S. J. Wright, "Conjugate gradient methods," *Numerical optimization*, pp. 101–134, 2006.

[146] A. Day, "An introduction to dynamic relaxation," *The Engineer*, vol. 219, 1965.

[147] J. Otter, "Computations for prestressed concrete reactor pressure vessels using dynamic relaxation," *Nuclear Structural Engineering*, vol. 1, no. 1, pp. 61–75, 1965.

[148] A. K. Welsh, "Discussion on dynamic relaxation," *Proceedings of the Institution of Civil Engineers*, vol. 37, pp. 723–735, 1967.

[149] A. C. Cassell, P. J. Kinsey, and D. J. Sefton, "Cylindrical shell analysis by dynamic relaxation.," *Proceedings of the Institution of Civil Engineers*, vol. 39, no. 1, pp. 75–84, 1968.

[150] T. Rabczuk and H. Ren, "A peridynamics formulation for quasi-static fracture and contact in rock," *Engineering Geology*, vol. 225, pp. 42–48, 2017.

[151] M. Papadrakakis, "A method for the automatic evaluation of the dynamic relaxation parameters," *Computer Methods in Applied Mechanics and Engineering*, vol. 25, no. 1, pp. 35–48, 1981.

[152] P. Underwood, "Dynamic relaxation," *Computational Method for Transient Analysis*, vol. 1, pp. 245–265, 1983.

[153] B. Kilic and E. Madenci, "Structural stability and failure analysis using peridynamic theory," *International Journal of Non-Linear Mechanics*, vol. 44, pp. 845–854, 2009.

[154] B. Kilic and E. Madenci, "An adaptive dynamic relaxation method for quasi-static simulations using the peridynamic theory," *Theoretical and Applied Fracture Mechanics*, vol. 53, no. 3, pp. 194–204, 2010.

[155] D. Huang, G. Lu, and P. Qiao, "An improved peridynamic approach for quasi-static elastic deformation and brittle fracture analysis," *International Journal of Mechanical Sciences*, vol. 94, pp. 111–122, 2015.

[156] E. Emmrich and O. Weckner, "The peridynamic equation and its spatial discretisation," *Mathematical Modelling and Analysis*, vol. 12, no. 1, pp. 17–27, 2007.

[157] R. W. Macek and S. A. Silling, "Peridynamics via finite element analysis," *Finite Elements in Analysis and Design*, vol. 43, no. 15, pp. 1169–1178, 2007.

[158] E. Madenci and E. Oterkus, *Peridynamic theory and its applications*, vol. 17. Springer, 2014.

[159] J. Mitchell, S. Silling, and D. Littlewood, "A position-aware linear solid constitutive model for peridynamics," *Journal of Mechanics of Materials and Structures*, vol. 10, no. 5, pp. 539–557, 2015.

[160] Q. Le and F. Bobaru, "Surface corrections for peridynamic models in elasticity and fracture," *Computational Mechanics*, pp. 1–20, 2017.

[161] M. Tupek, J. Rimoli, and R. Radovitzky, "An approach for incorporating classical continuum damage models in state-based peridynamics," *Computer Methods in Applied Mechanics and Engineering*, vol. 263, pp. 20–26, 2013.

[162] S. A. Silling and R. Lehoucq, "Peridynamic theory of solid mechanics," in *Advances in Applied Mechanics*, vol. 44, pp. 73–168, Elsevier, 2010.

[163] Z. P. Bažant and Z. Celep, "Spurious reflection of elastic waves in nonuniform meshes of constant and linear strain unite elements," *Computers & Structures*, vol. 15, no. 4, pp. 451–459, 1982.

[164] S. N. Butt, J. J. Timothy, and G. Meschke, "Wave dispersion and propagation in state-based peridynamics," *Computational Mechanics*, pp. 1–14, 2017.

[165] S. Xiao and T. Belytschko, "A bridging domain method for coupling continua with molecular dynamics," *Computer methods in applied mechanics and engineering*, vol. 193, no. 17, pp. 1645–1669, 2004.

[166] P. A. Guidault and T. Belytschko, "On the l2 and the h1 couplings for an overlapping domain decomposition method using lagrange multipliers," *International Journal for Numerical Methods in Engineering*, vol. 70, no. 3, pp. 322–350, 2007.

[167] P.-A. Guidault and T. Belytschko, "Bridging domain methods for coupled atomistic–continuum models with l2 or h1 couplings," *International journal for numerical methods in engineering*, vol. 77, no. 11, pp. 1566–1592, 2009.

[168] C. W. Roeder and J. F. Stanton., "Elastomeric bearings: State of the art," *Journal of Structural Engineering*, vol. 109, pp. 2853–2871, 1983.

[169] M. D. Rao., "Recent applications of viscoelastic damping for noise control in automobiles and commercial airplanes," *Journal of Sound and Vibration*, vol. 262, pp. 457–474, 2003.

[170] C. S. Tsai and H. H. Lee., "Applications of viscoelastic dampers to high-rise buildings," *Journal of Structural Engineering*, vol. 119, pp. 1222–1233, 1993.

[171] T. Duncan., "Applications of nanotechnology in food packaging and food safety: Barrier materials, antimicrobials and sensors," *Journal of Colloid and Interface Science*, vol. 363, pp. 1–24, 2011.

[172] F. Hussain, M. Hojjati, M. Okamoto, and R. E. Gorga, "Polymer-matrix nanocomposites, processing, manufacturing, and application: An overview," *Journal of Composite Materials*, vol. 40, no. 17, pp. 1511–1575, 2006.

[173] M. Grujicic, W. Bell, B. Pandurangan, and T. He, "Blast-wave impact-mitigation capability of polyurea when used as helmet suspension-pad material," *Materials & Design*, vol. 31, no. 9, pp. 4050–4065, 2010.

[174] S. N. Raman, T. Ngo, P. Mendis, and T. Pham, "Elastomeric polymers for retrofitting of reinforced concrete structures against the explosive effects of blast," *Advances in Materials Science and Engineering*, vol. 2012, 2012.

[175] A. Amirkhizi, J. Isaacs, J. McGee, and S. Nemat-Nasser, "An experimentally-based viscoelastic constitutive model for polyurea, including pressure and temperature effects," *Philosophical Magazine*, vol. 86, no. 36, pp. 5847–5866, 2006.

[176] T. El Sayed, W. Mock, A. Mota, F. Fraternali, and M. Ortiz, "Computational assessment of ballistic impact on a high strength structural steel/polyurea composite plate," *Computational Mechanics*, vol. 43, no. 4, pp. 525–534, 2009.

[177] K. J. Knox, M. I. Hammons, T. T. Lewis, and J. R. Porter, "Polymer materials for structural retrofit," *Force Protection Branch, Air Expeditionary Forces Technology Division, Air Force Research Laboratory, Tyndall AFB, Florida*, 2000.

[178] C. Roland, J. Twigg, Y. Vu, and P. Mott, "High strain rate mechanical behavior of polyurea," *Polymer*, vol. 48, no. 2, pp. 574–578, 2007.

[179] S. S. Sarva, S. Deschanel, M. C. Boyce, and W. Chen, "Stress–strain behavior of a polyurea and a polyurethane from low to high strain rates," *Polymer*, vol. 48, no. 8, pp. 2208–2213, 2007.

[180] R. Bogoslovov and C. Roland, "Viscoelastic effects on the free retraction of rubber," *Journal of Applied Physics*, vol. 102, no. 6, p. 063531, 2007.

[181] J. Shim and D. Mohr, "Using split hopkinson pressure bars to perform large strain compression tests on polyurea at low, intermediate and high strain rates," *International Journal of Impact Engineering*, vol. 36, no. 9, pp. 1116–1127, 2009.

[182] J. Shim and D. Mohr, "Rate dependent finite strain constitutive model of polyurea," *International Journal of Plasticity*, vol. 27, no. 6, pp. 868–886, 2011.

[183] J. Yi, M. Boyce, G. Lee, and E. Balizer, "Large deformation rate-dependent stress–strain behavior of polyurea and polyurethanes," *Polymer*, vol. 47, no. 1, pp. 319–329, 2006.

[184] C. Gamonpilas and R. McCuiston, "A non-linear viscoelastic material constitutive model for polyurea," *Polymer*, vol. 53, no. 17, pp. 3655–3658, 2012.

[185] C. Li and J. Lua, "A hyper-viscoelastic constitutive model for polyurea," *Materials Letters*, vol. 63, no. 11, pp. 877–880, 2009.

[186] S. S. Kulkarni and A. Tabarraei, "A nonlinear visco-hyper elastic constitutive model for modelling behavior of polyurea at large deformations," in *ASME 2019 International Mechanical Engineering Congress and Exposition*, p. in press, American Society of Mechanical Engineers, 2019.

[187] R. Adams and D. Bacon, "Effect of fiber–orientation and laminate geometry on properties of CFRP," *Journal of Composite Materials*, vol. 7, pp. 402–28, 1973.

[188] S. Hwang and R. Gibson, "Micromechanical modeling of damping in discontinuous fiber composites using a strain energy/finite element approach," *Journal of engineering materials and technology*, vol. 109, no. 1, pp. 47–52, 1987.

[189] M. Kaliske and H. Rothert, "Damping characterization of unidirectional fibre reinforced polymer composites," *Composites Engineering*, vol. 5, no. 5, pp. 551–567, 1995.

[190] L. Brinson and W. Lin, "Comparison of micromechanics methods for effective properties of multiphase viscoelastic composites," *Composite Structures*, vol. 41, no. 3, pp. 353–367, 1998.

[191] T. Mori and K. Tanaka, "Average stress in matrix and average elastic energy of materials with misfitting inclusions," *Acta Metallurgica*, vol. 21, no. 5, pp. 571–574, 1973.

[192] J. C. Halpin, *Primer on Composite Materials Analysis, (revised).* CRC Press, 1992.

[193] L. C. Brinson and W. G. Knauss., "Finite element analysis of multiphase viscoelastic solids," *Journal of Applied Mechanics*, vol. 59, pp. 730–737, 1992.

[194] J. A. Moore, R. Ma, A. G. Domel, and W. K. Liu., "An efficient multiscale model of damping properties for filled elastomers with complex microstructures," *Composites: Part B*, vol. 62, pp. 262–270, 2014.

[195] M. Kamiński and D. Sokołowski, "Dual probabilistic homogenization of the rubber-based composite with random carbon black particle reinforcement," *Composite Structures*, vol. 140, pp. 783–797, 2016.

[196] D. Sokołowski and M. Kamiński, "Computational homogenization of carbon/polymer composites with stochastic interface defects," *Composite Structures*, vol. 183, pp. 434–449, 2018.

[197] C. S. Lyrintzis., "The unfolding model for the representation of the mesophase layer in composites," *Journal of Applied Polymer Science*, vol. 30, pp. 621–645, 1985.

[198] J. L. Thomason., "The interface region in glass fibre-reinforced epoxy resin composites: 2, water absorption, voids and the interface," *Composites*, vol. 26, pp. 477–485, 1995.

[199] K. Mai, E. Mäder, and M. Mühle, "Interphase characterization in composites with new non-destructive methods," *Composites Part A: Applied Science and Manufacturing*, vol. 29, no. 9-10, pp. 1111–1119, 1998.

[200] M. Munz, H. Sturm, E. Schulz, and G. Hinrichsen, "The scanning force microscope as a tool for the detection of local mechanical properties within the interphase of fibre reinforced polymers," *Composites Part A: Applied Science and Manufacturing*, vol. 29, no. 9-10, pp. 1251–1259, 1998.

[201] S. S. Kulkarni, A. Tabarraei, and P. P. Ghag, "A finite element approach for study of wave attenuation characteristics of epoxy polymer composite," in *ASME 2018 International Mechanical Engineering Congress and Exposition*, pp. V009T12A042–V009T12A042, American Society of Mechanical Engineers, 2018.

[202] S. Shukla, A. Tabarraei, and S. S. Kulkarni, "A finite element study of the impact of interphase on the damping properties of polymer composites," in *ASME 2018 International Mechanical Engineering Congress and Exposition*, American Society of Mechanical Engineers, 2018.

[203] S. S. Kulkarni and A. Tabarraei, "A study on damping properties of polymer composites with randomly distributed fillers," in *ASME 2019 International Mechanical Engineering Congress and Exposition*, p. in press, American Society of Mechanical Engineers, 2019.

[204] S. Shukla, S. S. Kulkarni, and A. Tabarraei, "Study of the effect of carbon nano-tube waviness and volume fraction on the damping property of a polymer composite," in *ASME 2019 International Mechanical Engineering Congress and Exposition*, p. in press, American Society of Mechanical Engineers, 2019.

[205] S. S. Kulkarni and T. K. Bhandakkar, "Study of the effect of large deformation through a finite deformation based constitutive model for metallic glasses," in *ASME 2018 International Mechanical Engineering Congress and Exposition*, pp. V009T12A010–V009T12A010, American Society of Mechanical Engineers, 2018.

[206] J. Bonet and R. D. Wood, *Nonlinear continuum mechanics for finite element analysis*. Cambridge university press, 1997.

[207] E. M. Arruda and M. C. Boyce, "A three-dimensional constitutive model for the large stretch behavior of rubber elastic materials," *Journal of the Mechanics and Physics of Solids*, vol. 41, no. 2, pp. 389–412, 1993.

[208] M. Mooney, "A theory of large elastic deformation," *Journal of Applied Physics*, vol. 11, no. 9, pp. 582–592, 1940.

[209] R. Rivlin, "Large elastic deformations of isotropic materials. iv. further developments of the general theory," *Philosophical Transactions of the Royal Society of London A: Mathematical, Physical and Engineering Sciences*, vol. 241, no. 835, pp. 379–397, 1948.

[210] O. Yeoh, "Some forms of the strain energy function for rubber," *Rubber Chemistry and Technology*, vol. 66, no. 5, pp. 754–771, 1993.

[211] R. W. Ogden, "Large deformation isotropic elasticity–on the correlation of theory and experiment for incompressible rubberlike solids," in *Proc. R. Soc. Lond. A*, vol. 326, pp. 565–584, The Royal Society, 1972.

[212] R. Brown, *Physical testing of rubber*. Springer Science & Business Media, 2006.

[213] H. Brinson and L. C. Brinson, *Polymer engineering science and viscoelasticity*. Springer, 2016.

[214] B. Bernstein, E. Kearsley, and L. Zapas, "A study of stress relaxation with finite strain," *Rubber Chemistry and Technology*, vol. 38, no. 1, pp. 76–89, 1965.

[215] F. J. Lockett, *Nonlinear viscoelastic solids*. Academic Press, 1972.

[216] C. Truesdell and W. Noll, "The non-linear field theories of mechanics," in *The non-linear field theories of mechanics*, pp. 1–579, Springer, 2004.

[217] B. Bernstein, E. Kearsley, and L. Zapas, "A study of stress relaxation with finite strain," *Transactions of the Society of Rheology*, vol. 7, no. 1, pp. 391–410, 1963.

[218] L. J. Zapas, "Viscoelastic behavior under large deformations," *J Res Natl Bur Stand A*, vol. 70, pp. 525–532, 1966.

[219] V. Shim, L. Yang, C. Lim, and P. Law, "A visco-hyperelastic constitutive model to characterize both tensile and compressive behavior of rubber," *Journal of Applied Polymer Science*, vol. 92, no. 1, pp. 523–531, 2004.

[220] L. Yang, V. Shim, and C. Lim, "A visco-hyperelastic approach to modelling the constitutive behaviour of rubber," *International Journal of Impact Engineering*, vol. 24, no. 6, pp. 545–560, 2000.

[221] L. Yang and V. Shim, "A visco-hyperelastic constitutive description of elastomeric foam," *International Journal of Impact Engineering*, vol. 30, no. 8, pp. 1099–1110, 2004.

[222] H. Pouriayevali, Y. Guo, and V. Shim, "A visco-hyperelastic constitutive description of elastomer behaviour at high strain rates," *Procedia Engineering*, vol. 10, pp. 2274–2279, 2011.

[223] H. Pouriayevali, Y. Guo, and V. Shim, "A constitutive description of elastomer behaviour at high strain rates–a strain-dependent relaxation time approach," *International Journal of Impact Engineering*, vol. 47, pp. 71–78, 2012.

[224] MATLAB, *MATLAB curve fitting toolbox (R2017a)*. Natick, Massachusetts: The MathWorks Inc., 2017.

[225] Z. Hashin and S. Shtrikman., "The variational approach to the thory of the elastic behaviour of multiphase materials," *Journal of Mechanics and Physics of Solids*, vol. 11, pp. 127–140, 1963.

[226] Z. Hashin., "Viscoelastic behavior of heterogeneous media," *Journal of Applied Mechanics*, vol. 32, pp. 630–636, 1965.

[227] R. Hill., "Elastic properties of reinforced solids: Some theoretical principles," *Journal of the Mechanics and Physics of Solids*, vol. 11, pp. 357–372, 1963.

[228] T. Mori and K. Tanaka., "Average stress in matrix and average elastic energy of materials with misfitting inclusions," *Acta Metallurgica*, vol. 21, pp. 571–574, 1973.

[229] S. Kari, H. Berger, and U. Gabbert, "Numerical evaluation of effective material properties of randomly distributed short cylindrical fibre composites," *Computational Materials Science*, vol. 39, no. 1, pp. 198–204, 2007.

[230] Y. Pan, L. Iorga, and A. A. Pelegri, "Numerical generation of a random chopped fiber composite rve and its elastic properties," *Composites Science and Technology*, vol. 68, no. 13, pp. 2792–2798, 2008.

[231] M. Silani, H. Talebi, S. Ziaei-Rad, P. Kerfriden, S. P. Bordas, and T. Rabczuk, "Stochastic modelling of clay/epoxy nanocomposites," *Composite Structures*, vol. 118, pp. 241–249, 2014.

[232] A. A. Gusev, "Representative volume element size for elastic composites: a numerical study," *Journal of the Mechanics and Physics of Solids*, vol. 45, no. 9, pp. 1449–1459, 1997.

[233] A. Gusev, M. Heggli, H. R. Lusti, and P. J. Hine, "Orientation averaging for stiffness and thermal expansion of short fiber composites," *Advanced Engineering Materials*, vol. 4, no. 12, pp. 931–933, 2002.

[234] M. Schneider, "The sequential addition and migration method to generate representative volume elements for the homogenization of short fiber reinforced plastics," *Computational Mechanics*, pp. 1–17, 2016.

[235] E. Ghossein and M. Lévesque, "Random generation of periodic hard ellipsoids based on molecular dynamics: A computationally-efficient algorithm," *Journal of Computational Physics*, vol. 253, pp. 471–490, 2013.

[236] V. Salnikov, D. Choï, and P. Karamian-Surville, "On efficient and reliable stochastic generation of rves for analysis of composites within the framework of homogenization," *Computational Mechanics*, vol. 55, no. 1, pp. 127–144, 2015.

[237] M. Faessel, C. Delisée, F. Bos, and P. Castéra, "3D modelling of random cellulosic fibrous networks based on x-ray tomography and image analysis," *Composites Science and Technology*, vol. 65, no. 13, pp. 1931–1940, 2005.

[238] L. Mishnaevsky, "Micromechanical analysis of nanocomposites using 3D voxel based material model," *Composites Science and Technology*, vol. 72, no. 10, pp. 1167–1177, 2012.

[239] DS Simulia Corp., *Abaqus 6.13 theory manual*.

[240] S. S. Kulkarni and A. Tabarraei, "Study of damping properties of polymer matrix composites through wave propagation," in *ASME 2017 International Mechanical Engineering Congress and Exposition*, pp. V001T03A018–V001T03A018, American Society of Mechanical Engineers, 2017.

[241] S. S. Kulkarni and A. Tabarraei, "A stochastic analysis of the damping property of filled elastomers," *Macromolecular Theory and Simulations*, vol. 28, no. 2, p. 1800062, 2019.

[242] R. Smit, W. Brekelmans, and H. Meijer, "Prediction of the mechanical behavior of nonlinear heterogeneous systems by multi-level finite element modeling," *Computer Methods in Applied Mechanics and Engineering*, vol. 155, no. 1-2, pp. 181–192, 1998.

[243] J. Segurado and J. LLorca., "A computational micromechanics study of the effect of interface decohesion on the mechanical behavior of composites," *Acta Materialia*, vol. 53, pp. 4931–4942, 2005.

[244] O. Van der Sluis, P. Schreurs, W. Brekelmans, and H. Meijer, "Overall behaviour of heterogeneous elastoviscoplastic materials: effect of microstructural modelling," *Mechanics of Materials*, vol. 32, no. 8, pp. 449–462, 2000.

[245] V. D. Nguyen, E. Béchet, C. Geuzaine, and L. Noels, "Imposing periodic boundary condition on arbitrary meshes by polynomial interpolation," *Computational Materials Science*, vol. 55, pp. 390–406, 2012.

[246] Z. Liu, J. Moore, S. Aldousari, H. Hedia, S. Asiri, and W. K. Liu., "A statistical descriptor based volume-integral micromechanics model of heterogeneous material with arbitrary inclusion shape," *Comput Mech*, vol. 55, pp. 963–981, 2015.

[247] Y. Jiang, X. Shi, and K. Qiu, "A micromechanics-based incremental damage model for carbon black filled rubbers," *Composites Part B: Engineering*, vol. 75, pp. 11–16, 2015.

[248] A. Anthoine., "Derivation of the in-plane elastic characteristics of masonry through homogenization theory," *International Journal of Solids and Structures*, vol. 32, pp. 137–163, 1995.

[249] M. D. Mckay, R. J. Beckman, and W. J. Conover., "A comparison of three methods for selecting values of input variables in the analysis of output from a computer code," *Technometrics*, vol. 21, pp. 239–245, 1979.

[250] R. Y. Rubinstein and D. P. Kroese., *Simulation and the Monte Carlo method*. John Wiley and Sons, 2011.

[251] D. E. Huntington and C. S. Lyrintzis., "Improvements to and limitations of latin hypercube sampling," *Probabilistic Engineering Mechanics*, vol. 13, pp. 245–253, 1998.

[252] "pydoe: Design of experiments for python." http://pythonhosted.org/pyDOE. Accessed: 13 Sep 2016.

[253] A. Becker, T. Hyde, and L. Xia, "Numerical analysis of creep in components," *The Journal of Strain Analysis for Engineering Design*, vol. 29, no. 3, pp. 185–192, 1994.

[254] T. Hyde, L. Xia, and A. Becker, "Prediction of creep failure in aeroengine materials under multi-axial stress states," *International Journal of Mechanical Sciences*, vol. 38, no. 4, pp. 385–403, 1996.

[255] O. J. Gonçalves Filho, "Closed-form solution for the isothermal creep rupture behaviour of a two-bar structure under constant load," *International Journal of Solids and Structures*, vol. 32, no. 21, pp. 3087–3104, 1995.

[256] T. Hyde, W. Sun, A. Becker, and J. Williams, "Creep properties and failure assessment of new and fully repaired p91 pipe welds at 923 k," *Proceedings of the Institution of Mechanical Engineers, Part L: Journal of Materials: Design and Applications*, vol. 218, no. 3, pp. 211–222, 2004.

[257] T. Hyde and W. Sun, "Creep failure behaviour of a circumferential p91 pipe weldment with an anisotropic weld metal subjected to internal pressure and end load," *Proceedings of the Institution of Mechanical Engineers, Part L: Journal of Materials: Design and Applications*, vol. 220, no. 3, pp. 147–162, 2006.

[258] D. Tanner, M. Puliyaneth, W. Sun, and T. Hyde, "Creep damage modelling of P92 pipe weld at 675Â° C," *Materials Science and Technology*, vol. 30, no. 1, pp. 6–11, 2014.

VITA

Shank S. Kulkarni obtained PhD degree in Mechanical engineering at University of North Carolina at Charlotte, USA, under guidance of Prof. Alireza Tabarrai. His research mainly focuses on computational solid mechanics with specialization in material modeling, finite element method, and peridynamics. He obtained his Master's degree in Mechanical engineering from Indian Institute of Technology, Bombay with specialization in Design in 2013. Also, he obtained a Bachelor's degree in Mechanical engineering from University of Pune, India in 2010. He has industry experience of more than two years for working in design and development department of Whirlpool corporation. He also completed a summer internship in Dassault systems in Johnston, Rode Island, USA. In his free time he creates short movies for his YouTube channel 'Shank Kulkarni'.